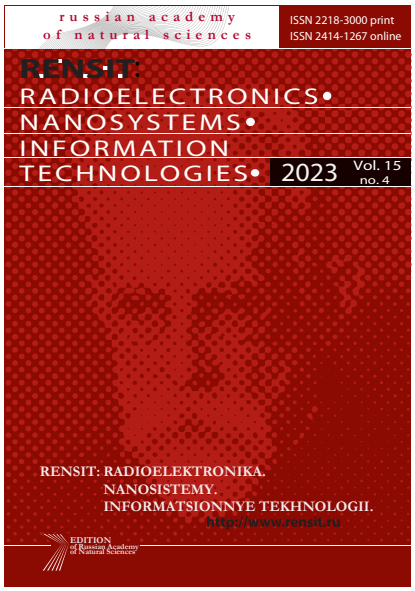

RENSIT:
RadioElectronics. NanoSystems. Information Technologies

Journal "Radioelectronics. Nanosystems. Information Technologies" (abbr. RENSIT)
publishes original articles, reviews and brief reports, not previously published, on topical problems in **radioelectronics (including biomedical) and fundamentals of information, nano- and biotechnologies and adjacent areas of physics and mathematics.**

Designed for **researchers, graduate students, physics students of senior courses and teachers**.
It turns out **2 times a year** (that includes 2 issues)

Authors of journal are academicians, corresponding members and foreign members of Russian Academy of Natural Sciences (RANS) and their colleagues,
as well as other russian and foreign authors on presentation of their manuscripts by the members of RANS, which can be obtained by authors before sending articles to editors.
And also after its receiving - on recommendation of a member of editorial board of journal, or another member of Academy of Natural Sciences, that gave her opinion on article at request of editor.
The editors will accept articles in both **Russian and English** languages.

Articles are internally peer reviewed (**double-blind peer review**) by members of the Editorial Board.
Some articles undergo external review, if necessary.

Journal RENSIT is included in the **DB SCOPUS, EBSCO Publishing,** in the international abstracts database - **Ulrich's International Periodicals Directory**,(USA, New York, http://www.ulrichsweb.com), in the **AJ and DB VINITI RAS** (http://www.viniti.ru), and DB **Russian Science Citation Index (RSCI** http://elibrary.ru/project_risc.asp). Included in the **List of Higher Attestation Comission** (No. 2204 dated July 17, 2023: K1 in 18 groups of specialties) **of Science and Higher Education Ministry of the Russian Federation**.
Full-text content is posted in the DB of the **Russian Scientific Electronic Library**
- information resource on the Internet http://elibrary.ru and is available for registered users.
And also - in Open Access **CyberLeninka NEB** of Russian Federation http://cyberleninka.ru..

On journal's website http://www.rensit.ru posted metadata publications
and **RENSIT: Radioelectronics. Nanosystems. Infomation Technologies - english version** (cover-to-cover translation) of journal, which is a party to **CrossRef.**

The founder - the **Russian Academy of Natural Sciences**
Publisher - Publishing Center of the Russian Academy of Natural Sciences
Publisher Address: 29/16, Sivtsev Vrazhek lane, Moscow 119002, Russian Federation

CONTENTS

RUSSIAN ACADEMY OF NATURAL SCIENCES

DEPARTMENT OF RADIOELECTRONICS, NANOPHYSICS AND INFORMATION TECHNOLOGIES PROBLEMS

RENSIT:

RADIOELECTRONICS. NANOSYSTEMS. INFORMATION TECHNOLOGIES.
2023, Vol. 15, no. 4

FOUNDED IN **2009**
4 ISSUES PER YEAR
MOSCOW

ISSN 2414-1267
The journal on-line is registered by the Ministry of Telecom and Mass Cjmmunications of the Russian Federation. Certificate El. no. FS77-60275 on 19.12.2014

EDITORIAL BOARD ADDRESS
218-219 of., 7 b., 11, Mokhovaya str., 125009 MOSCOW, RUSSIAN FEDERATION,
TEL. **+7 495 629 3368**
FAX **+7 495 629 3678** FOR GRACHEV

DOI: 10.17725/rensit.2023.15.341

About direct radiation of ultrashort electromagnetic pulses and fractal space-time geometry

Alexander A. Potapov

Kotelnikov Institute of Radioengineering and Electronics of Russian Academy of Sciences, http://www.cplire.ru/
Moscow 125009, Russian Federation
Jinan University, JNU-IREE RAS Joint Laboratory of Information Technology and Fractal Processing of Signals, https://jnu.edu.cn/
Guangzhou 510632, China

E-mail: potapov@cplire.ru

Elena R. Men'kova

All-Russian Research Institute for Optical and Physical Measurements, http://www.vniiofi.ru/
Moscow 119361, Russian Federation
E-mail: menkova@vniiofi.ru

Received August 26, 2023, peer-reviewed September 01, 2023, accepted September 08, 2023, published December 06, 2023.

Abstract: **Theoretical and experimental investigations of propagation of ultrashort electromagnetic pulses (US EMP) are needed to develop new technologies of creation of modern special engineering. The analytical method of field calculation of travelling antenna waves taking into account reflection of fracture and redistribution of currents in wires because of losses of radiation energy from fractures is considered. The calculations of V-antenna, the field of radiation of a horn system and the pulse radiation of the antenna with a reflector are presented. Experimental investigations of UWB EMP propagation carried out on the basis of the theory developed by S.A. Podosenov are the base of creation of modern radiotechnical complexes. Simultaneously the main conceptions of space-time fractal geometry of deterministic structures are introduced.**

Keywords: **ultrashort pulses, antenna structures, fractal, space-time, new technologies**
UDC 530.1+621.396

Acknowledgments: The authors are grateful to K.Yu. Sakharov, A.V. Sukhov, O.V. Mikheev, and V.A. Turkin of the laboratory of generation and measurement of parameters of electromagnetic pulses FGBU "VNIIOFI" for a number of usual conversations and helpful comments.

For citation: Alexander A. Potapov, Elena R. Men'kova. About direct radiation of ultrashort electromagnetic pulses and fractal space-time geometry. *RENSIT: Radioelectronics. Nanosystems. Information Technologies,* 2023, 15(4):341-354e. DOI: 10.17725/rensit.2023.15.341.

This article is dedicated to the bright memory of Stanislav Alexandrovich Podosenov (1.09.1937 – 1.03.2022) who made a great contribution to development of modern and classical theory of radiation of pulse electromagnetic fields

Contents

1.INTRODUCTION

This work is dedicated to the bright memory of Ph.D. (phys.-math. sci.) Stanislav Alexandrovich Podosenov (1.08.1937-1.03.2022). He graduated from the Physical Department of the M.V. Lomonosov Moscow State University in 1963 (the chair of statistical physics and quantum mechanics, the chairman was academician N.N. Bogolubov). His speciality is the theoretical physicist. He is a winner of the prize of RF Government 2002 in the field of science and engineering. He made a great contribution to development of modern and classical field radiation of pulse electromagnetic fields appreciated by the world scientific community. In 1972 S.A. Podosenov (at the University of Peoples Friendship, in the theoretical physics chair of prof. Ya.P. Terletskiy) defended his Ph.D. thesis. The speciality is theoretical and mathematical physics. The subject is "Relativistic mechanics of deformable medium in the tetrade formulation." The thesis is connected with the scientific school of known prof. of MSU D.D Ivanenko, V.I. Rodichev and academician L.I. Sedov.

Ultrashort pulses (US) of electromagnetic field have wide practical application in radiophysics, radiolocation, metrology, nuclear physics (for explosion investigations), antenna engineering, medicine etc.

In radiolocation US pulses of electromagnetic field are used for transmission of energy and information. Transmission of information by means of US EMP is realized during the short time intervals. This permits to diminish power of radio communication means, their dimensions and mass and consequently their cost. Application of US EMP for information transmission diminishes harmful influence of electromagnetic field on environment. It is possibly to transmit information concerning sizes, location and structure of the object by means of reflected US EMP. That permits rapid and exact determination of necessary target characteristics [1-5]. At pulse duration 10^{-10} *s* the resolution of the order of a few centimeters can be achieved.

US pulses of electromagnetic field are widely applied in the field of ensuring of the unity of measurements – state verification schemes, state special standards, reference and working measuring instruments and standard settings [6-9].

S.A. Podosenov began working at the laboratory of generation and measurement of parameters of electromagnetic pulses VNIIOFI in 1989 jointly with prof. A.A. Sokolov. The problem of creation of the theory of pulse radiation from fieldforming systems was set by prof. A.A. Sokolov. By means of formulae derived by S.A. Podosenov one can calculate the radiation field applying computers that do not have big power [10].

In the laboratory of generation and measurement of parameters of electromagnetic pulses VNIIOFI works for creation new measurement technologies and application of US EMP to investigate physical processes in heterogeneous media [11-47] and pulse interaction strip lines in printed circuit boards are successfully carried out [12].

Measurement technologies are successfully applied to struggle with electromagnetic terrorism [17]. Experimental investigations of influence of US EMP in the systems of monitoring of access to rooms are important [20,39]. Measuring complex for investigation of electromagnetic environment, when propagating of US EMP indoors, was created [41]. Methods and means of monitoring of electromagnetic radiation in ultrashort duration range [45,46] are used to investigate stability of video supervision systems against power US EMP [43], in particular, when investigating of functioning of typical complex security system devices [44].

Ultrashort pulse standard radiators are used for metrological ensurance of telecommunication techniques [22]. Measuring instruments for test of radioelectronic equipment for US EMP impact resistance are developed [26]. Investigations of functioning of personal computers in condition of US EMP impact are carried out [30]. When creating of means of resistance ensurance of information systems for impact of ultrawide band electromagnetic radiation (UWB EMP) investigations of functioning of local computer networks in conditions of UWB EMP impact are of great importance [33]. Investigation of US EMP propagation has great importance to estimate resistance of on-board computers in conditions of impact of US electromagnetic fields [38].

At the laboratory of generation and measurement of parameters of electromagnetic pulses VNIIOFI works for creation of new methods and measuring instruments of US EMP parameters in the picosecond

range are successfully carried out [48]. On the basis of US EMP application in VNIIOFI the measuring system for express-diagnostics of electromagnetic parameters of radio absorbing materials in the range of 0.1…4.0 GHz having great practical importance was created [49].

US electromagnetic pulses are applied in medicine. Using of electromagnetic radiation assists to effective therapy when treatment of cancer diseases. Ultrawide band pulse periodic microwave radiation on mouse tumors was investigated in vivo [50]. Using of such radiation in combination anticancer therapy permitted to get inhibition of the growth rate of Lewis lung carcinoma on 70-80% as compared with the only action of chemotherapy drug (cyclophosphamide).

Miniature appliances operating on the basis of US EMP permit contactless controlling of pulsations of inner human organs that essentially improves diagnostics.

Such pulses can be effectively applied to transmit energy and information. This permits qualitative improvement of technical and ecological characteristics of radioelectronic devices and decreasing of their cost. Information transmitting by means of US EMP has profit as compared with methods of modulation of radio waves because energy is radiated during very short time interval.

The purpose of this work is brief representation of mathematical apparatus created by S.A. Podosenov. On the basis of this one it is possibly to calculate fields from travelling current waves taking into account fracture reflections and the basis of fractal space-time geometry of deterministic structures created jointly with prof. A.A. Potapov.

2.ANALYTICAL METHOD OF FIELD CALCULATION FROM TRAVELLING CURRENT WAVES TAKING INTO ACCOUNT FRACTURE REFLECTIONS

When creating the theory of pulse radiation from fieldforming systems S.A. Podosenov got a set of integro-differential equations for charge and current densities of charged metallic bodies and wires locating in external heterogeneous and nonstationary electromagnetic field. Created new simple calculation method of pulse radiation in time domain is based on direct finding of tensor of electromagnetic field from travelling current waves of arbitrary form.

Line fractures are the secondary radiation sources of anisotropic TEM waves. Energy losses stipulated for radiation have to change the amplitude and form of the signal passing through the fractures of transmission lines. The method of predetermined currents was modified taking into account the fracture reflection coefficients. Rounded wires were replaced by fractures (**Fig. 1**).

Reflection and transmission coefficients of current pulses from line fractures depending on parameters of pulse and time of their transmission through fractures permit to determine the form of reflected and transmitted pulses as compare with incident ones.

The simple method of analytical calculation of radiation from travelling current waves propagating on the curvilinear wires proposed by S.A. Podosenov can be applied to calculate radiation of V-antenna, linear one and the antenna constituted with rectilinear cuts.

This new analytical method of field calculation from travelling current waves with fractures takes into account redistribution of currents in wires stipulated for losses of fracture radiation energy. The correlation between transmission coefficient γ and reflection coefficient β and fracture angles and wire geometry is determined. The radiation field from angles is described with spherical TEM waves with

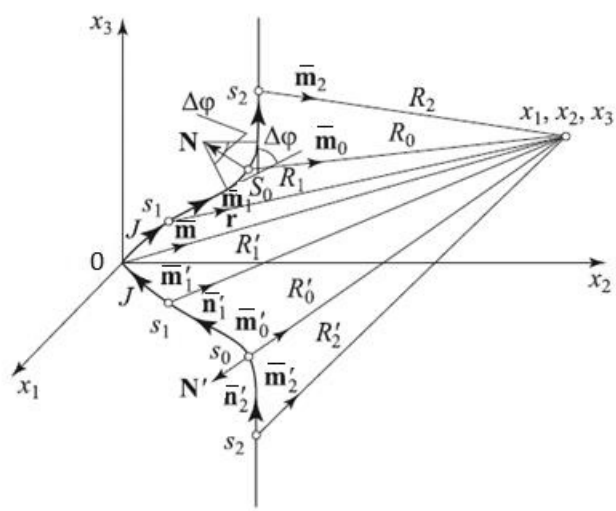

Fig. 1. *Geometry of symmetrical sections with fractures.* $\vec{m}_0$ *is the unit vector directed from the fracture to the observation point,* R_0 *is the distance from the fracture to the observation point,* s_1 *and* s_2 *are the distances from the antenna excitation point along the wire to points 1 and 2,* R_1 *and* R_2 *are the distances from points 1 and 2 to the observation point.*

centres on fractures. Proposed calculation method is close with the experiment.

The main formulae for calculation of electric and magnetic radiation fields at known reflection β and transmission γ coefficients through fractures in the vector form are presented below [1]:

$$\begin{aligned}\vec{E} = \frac{\eta_0}{4\pi}\Bigg\{&\gamma\cdot\frac{J(t-s_0/c-R_0/c)}{R_0}\left(\frac{\vec{n}_1-\vec{m}_0}{1-\vec{m}_0\cdot\vec{n}_1}-\frac{\vec{n}_2-\vec{m}_0}{1-\vec{m}_0\cdot\vec{n}_2}\right)+\\ &+\beta\cdot\frac{J(t-s_0/c-R_0/c)}{R_0}\left(\frac{\vec{n}_1-\vec{m}_0}{1-\vec{m}_0\cdot\vec{n}_1}+\frac{\vec{n}_1+\vec{m}_0}{1+\vec{m}_0\cdot\vec{n}_1}\right)+\\ &+\gamma\cdot\frac{J(t-s_2/c-R_2/c)}{R_2}\frac{\vec{n}_2-\vec{m}_2}{1-\vec{m}_2\cdot\vec{n}_2}-\frac{J(t-s_1/c-R_1/c)}{R_1}\frac{\vec{n}_1-\vec{m}_1}{1-\vec{m}_1\cdot\vec{n}_1}+\\ &+\gamma\cdot\frac{J(t-s_0/c-R'_0/c)}{R'_0}\cdot\left(\frac{\vec{m}'_0+\vec{n}'_1}{1+\vec{m}'_0\cdot\vec{n}'_1}-\frac{\vec{m}'_0+\vec{n}'_2}{1+\vec{m}'_0\cdot\vec{n}'_2}\right)+\\ &+\beta\cdot\frac{J(t-s_0/c-R'_0/c)}{R'_0}\cdot\left(\frac{\vec{m}'_0+\vec{n}'_1}{1+\vec{m}'_0\cdot\vec{n}'_1}-\frac{\vec{m}'_0-\vec{n}'_1}{1-\vec{m}'_0\cdot\vec{n}'_1}\right)+\\ &+\gamma\cdot\frac{J(t-s_2/c-R'_2/c)}{R'_2}\frac{\vec{n}'_2+\vec{m}'_2}{1+\vec{m}'_2\cdot\vec{n}'_2}-\frac{J(t-s_1/c-R'_1/c)}{R'_1}\frac{\vec{n}'_1+\vec{m}'_1}{1+\vec{m}'_1\cdot\vec{n}'_1}\Bigg\},\end{aligned} \tag{1}$$

$$\begin{aligned}\vec{H} = \frac{1}{4\pi}\Bigg\{&\gamma\cdot\frac{J(t-s_0/c-R_0/c)}{R_0}\left(\frac{\vec{m}_0\times\vec{n}_1}{1-\vec{m}_0\cdot\vec{n}_1}-\frac{\vec{m}_0\times\vec{n}_2}{1-\vec{m}_0\cdot\vec{n}_2}\right)+\\ &+\beta\cdot\frac{J(t-s_0/c-R_0/c)}{R_0}\left(\frac{\vec{m}_0\times\vec{n}_1}{1-\vec{m}_0\cdot\vec{n}_1}+\frac{\vec{m}_0\times\vec{n}_1}{1+\vec{m}_0\cdot\vec{n}_1}\right)+\\ &+\gamma\cdot\frac{J(t-s_2/c-R_2/c)}{R_2}\frac{\vec{m}_2\times\vec{n}_2}{1-\vec{m}_2\cdot\vec{n}_2}-\frac{J(t-s_1/c-R_1/c)}{R_1}\frac{\vec{m}_1\times\vec{n}_1}{1-\vec{m}_1\cdot\vec{n}_1}+\\ &+\gamma\cdot\frac{J(t-s_0/c-R'_0/c)}{R'_0}\cdot\left(\frac{\vec{m}'_0\times\vec{n}'_1}{1+\vec{m}'_0\cdot\vec{n}'_1}-\frac{\vec{m}'_0\times\vec{n}'_2}{1+\vec{m}'_0\cdot\vec{n}'_2}\right)+\\ &+\beta\cdot\frac{J(t-s_0/c-R'_0/c)}{R'_0}\cdot\left(\frac{\vec{m}'_0\times\vec{n}'_1}{1+\vec{m}'_0\cdot\vec{n}'_1}+\frac{\vec{m}'_0\times\vec{n}'_1}{1-\vec{m}'_0\cdot\vec{n}'_1}\right)+\\ &+\gamma\cdot\frac{J(t-s_2/c-R'_2/c)}{R'_2}\frac{\vec{m}'_2\times\vec{n}'_2}{1+\vec{m}'_2\cdot\vec{n}'_2}-\frac{J(t-s_1/c-R'_1/c)}{R'_1}\frac{\vec{m}'_1\times\vec{n}'_1}{1+\vec{m}'_1\cdot\vec{n}'_1}\Bigg\},\end{aligned} \tag{2}$$

where $\eta_0 = (\mu_0/\varepsilon_0)^{1/2}$ is the wave impedance of vacuum [51-57].

3. CALCULATION OF PULSE RADIATION OF ANTENNA BASIC STRUCTURES

On the basis of the method proposed by S.A. Podosenov pulse radiation of the main for US EMP radiation fieldforming systems: *V*-antenna (**Fig. 2***a*) [58], a radiation field of a horn system (Fig. 2*b*) [59], and pulse radiation of an antenna with a reflector (Fig. 2*c*) [60] are calculated.

3.1. Calculation of V-antenna

Solution of problems connected with investigation of nonstationary radiation is necessary to ensure defense of electronics from nonstationary electromagnetic fields. The investigation of fields from non-sinusoidal current waves in near zone is needed. *V*-antenna radiates a spherical electromagnetic wave and has high sensibility and widebandness that permits measuring nanosecond EMP.

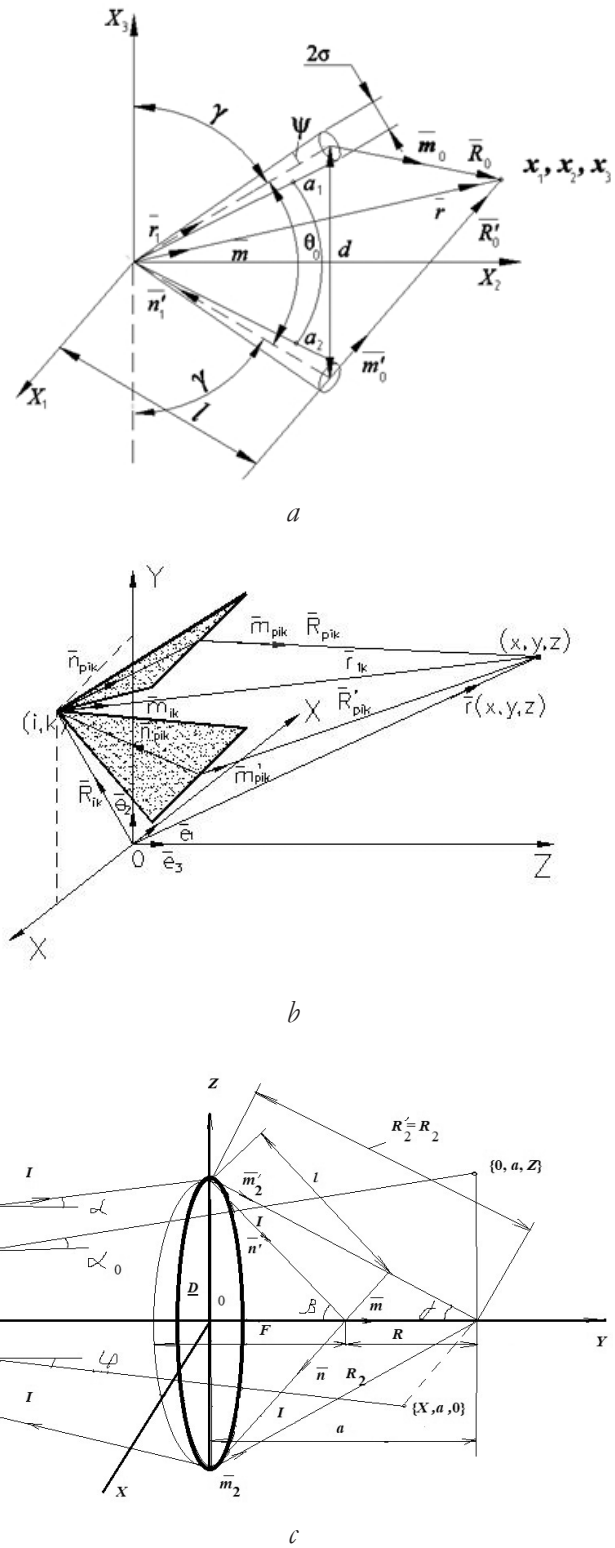

Fig. 2. *Calculation of concrete antenna basis structures: V-antenna (a), radiation of a horn system (b), image of V-antenna in a reflector (c).*

Let us consider radiation of *V*-antenna formed with two thin cones originated from one point with the angle θ_0 between axes (Fig. 2*a*).

We will consider two cases:

a) Infinite antenna

Infinite *V*-antenna radiates TEM wave. Formulae for calculation radiation fields have the vector form [1,58]:

$$\vec{E} = -\frac{\eta_0}{4\pi}\frac{J\left(t-r/c\right)}{r}\left(\frac{\vec{n}-\vec{m}}{1-\vec{m}\cdot\vec{n}}+\frac{\vec{n}'+\vec{m}}{1+\vec{m}\cdot\vec{n}'}\right), \quad (3)$$

$$\vec{H} = -\frac{1}{4\pi}\frac{J\left(t-r/c\right)}{r}\left(\frac{\vec{m}\times\vec{n}}{1-\vec{m}\cdot\vec{n}}+\frac{\vec{m}\times\vec{n}'}{1+\vec{m}\cdot\vec{n}'}\right), \quad (4)$$

where $\vec{m}$ and $\vec{n}$ are the unit vectors, t is the time, c is the light velocity in vacuum, J is the current value.

b) Finite antenna

Let *V*-antenna with finite length has an arm l. We will consider that the current in such an antenna propagates on a line with a fracture at the end on 180° and flows further to the load. The antenna is matched with the generator load. We will take into account reflections only one time.

One can represent formulae for calculation of radiation fields in the vector form [1,58]:

$$\begin{aligned}\vec{E} = -\frac{\eta_0}{4\pi}\Bigg\{&\frac{J\left(t-r/c\right)}{r}\left(\frac{\vec{n}_1-\vec{m}}{1-\vec{n}_1\cdot\vec{m}}+\frac{\vec{n}'_1+\vec{m}}{1+\vec{n}'_1\cdot\vec{m}}\right)+\\ &+\frac{J\left(t-2l/c-r/c\right)}{r}\left(\frac{\vec{n}_1+\vec{m}}{1+\vec{n}_1\cdot\vec{m}}+\frac{\vec{n}'_1-\vec{m}}{1-\vec{n}'_1\cdot\vec{m}}\right)-\\ &-\frac{J\left(t-l/c-R_0/c\right)}{R_0}\left(\frac{\vec{n}_1-\vec{m}_0}{1-\vec{n}_1\cdot\vec{m}_0}+\frac{\vec{n}_1+\vec{m}_0}{1+\vec{n}_1\cdot\vec{m}_0}\right)-\\ &-\frac{J\left(t-l/c-R'_0/c\right)}{R'_0}\cdot\left(\frac{\vec{n}'_1-\vec{m}'_0}{1-\vec{n}'_1\cdot\vec{m}'_0}+\frac{\vec{n}'_1+\vec{m}'_0}{1+\vec{n}'_1\cdot\vec{m}'_0}\right),\end{aligned} \quad (5)$$

$$\begin{aligned}\vec{H} = -\frac{1}{4\pi}\Bigg\{&\frac{J\left(t-r/c\right)}{r}\left(\frac{\vec{m}\times\vec{n}_1}{1-\vec{m}\cdot\vec{n}_1}+\frac{\vec{m}\times\vec{n}'_1}{1+\vec{m}\cdot\vec{n}'_1}\right)+\\ &+\frac{J\left(t-2l/c-r/c\right)}{r}\left(\frac{\vec{m}\times\vec{n}_1}{1+\vec{m}\cdot\vec{n}_1}+\frac{\vec{m}\times\vec{n}'_1}{1-\vec{m}\cdot\vec{n}'_1}\right)-\\ &-\frac{2J\left(t-l/c-R_0/c\right)}{R_0}\left(\frac{\vec{m}_0\times\vec{n}_1}{\left(1-\vec{n}_1\cdot\vec{m}_0\right)\left(1+\vec{n}_1\cdot\vec{m}_0\right)}\right)-\\ &-\frac{2J\left(t-l/c-R'_0/c\right)}{R'_0}\left(\frac{\vec{m}'_0\times\vec{n}'_1}{\left(1-\vec{n}'_1\cdot\vec{m}'_0\right)\left(1+\vec{n}'_1\cdot\vec{m}'_0\right)}\right)\Bigg\}.\end{aligned} \quad (6)$$

Here $2l/c$ is the phase shift of spherical waves. It is equal to time of interaction propagation to ends of the antenna and back. It follows from formulae (5) and (6) that radiation contains the sum of four spherical waves. The first two ones originate from the centre with the phase shift $2l/c$ that is equal to time of interaction propagation to ends of the antenna and back. Two other waves are formed from antenna ends at the moment of signal coming from the excitation point [55-58].

3.2. Calculation of a radiation field of a horn system

Knowing the induced electric current on the horn surface one can determine the radiation field created with the horn.

Finding of the horn radiation field in time domain is come down to the theory of radiation of travelling wave wire antenna. The antenna form can be arbitrary. The radiating system with the radiation field based on the theory [59] is presented schematically in Fig. 2*b*.

Let in plane *YOX* the coordinates of the excitation points of the horn system are specified. $\vec{R}'_{i,k}$ is the radius-vector connecting the origin and the excitation point of the cell with numbers {*i, k*}. We will substitute each horn on *N V*-antennae and let *p* is the number of the antenna in {*i, k*} cell. Electric radiation field of *V*-antenna with number *p* locating in the horn with numbers {*i, k*} in the observation point {*x, y, z*} in the time moment *t* has the form [1,59]:

$$\begin{aligned}\vec{E}_{p,i,k} = -\frac{\eta_0}{4\pi}\Bigg\{&\frac{J_p\left(t-r_{i,k}/c\right)}{r_{i,k}}\left(\frac{\vec{n}_{p,i,k}-\vec{m}_{i,k}}{1-\vec{m}_{i,k}\cdot\vec{n}_{p,i,k}}+\frac{\vec{n}'_{p,i,k}+\vec{m}_{i,k}}{1+\vec{m}_{i,k}\cdot\vec{n}'_{p,i,k}}\right)-\\ &-\frac{J_p\left(t-l_p/c-R_{p,i,k}/c\right)}{R_{p,i,k}}\left(\frac{\vec{n}_{p,i,k}-\vec{m}_{p,i,k}}{1-\vec{m}_{p,i,k}\cdot\vec{n}_{p,i,k}}+f\frac{\vec{n}_{p,i,k}+\vec{m}_{p,i,k}}{1+\vec{m}_{p,i,k}\cdot\vec{n}_{p,i,k}}\right)-\\ &-\frac{J_p\left(t-l_p/c-R'_{p,i,k}/c\right)}{R'_{p,i,k}}\left(\frac{\vec{n}'_{p,i,k}+\vec{m}'_{p,i,k}}{1+\vec{m}'_{p,i,k}\cdot\vec{n}'_{p,i,k}}+f\frac{\vec{n}'_{p,i,k}-\vec{m}'_{p,i,k}}{1-\vec{m}'_{p,i,k}\cdot\vec{n}'_{p,i,k}}\right)+\\ &+f\frac{J_p\left(t-2l_p/c-r_{i,k}/c\right)}{r_{i,k}}\left(\frac{\vec{n}'_{p,i,k}-\vec{m}_{i,k}}{1-\vec{m}'_{i,k}\cdot\vec{n}'_{p,i,k}}+\frac{\vec{n}_{p,i,k}+\vec{m}_{i,k}}{1+\vec{m}_{i,k}\cdot\vec{n}_{p,i,k}}\right)\Bigg\},\end{aligned} \quad (7)$$

where $R_{p,i,k}$ and $R'_{p,i,k}$ are the distances from the ends of straight and back wires of number *p* cell {*i, k*} to the observation point, and $\vec{m}_{p,i,k}$ and $\vec{m}'_{p,i,k}$ are the corresponding unit vectors directed from the wire ends to the observation point.

Let the current at the ends of the horn of *V*-antenna is completely absorbed that is equivalent to zero reflection coefficient *f*. Reflection of the current at the end of the horn is equivalent to presence of fractures at the end of the horn of *V*-antenna on 180° and the reflection coefficient *f* is equal to unit. In practice reflection coefficient *f* is the function of time and its value is in the range between zero and unit. Resulting formula for the calculation

of the radiation field from the horn system has the form

$$\vec{E}(t,x,y,z)=\sum_{k=1}^{v}\sum_{i=1}^{u}\sum_{p=1}^{N}\vec{E}_{p,i,k}(t,x,y,z), \qquad (8)$$

where u is the number of horizontal horns, and v is the number of vertical ones.

A horn antenna array can be considered as superposition of radiators, its field is additive in accordance with the numbers of horns. Experimental results of the field calculation of the systems containing 36, 64 and 144 horns carried out confirm correctness of the theory [56].

3.3. Calculation of pulse radiation of an antenna with a reflector

When calculating the radiation field of an antenna with a reflector the radiation field of the parabolic mirror is substituted with the radiation field of V-antenna reflected in a mirror. The method permits to determine the field at any distance from the reflector.

As the excitation point of V-antenna is in the focus of the parabolic reflector then the image of the excitation point in the mirror will be imaginary and it will be located in the infinitely remoted point behind the mirror. The ends of the exiting antenna and its mirror imagination will be coincided each other and they will be located at the generatrix of the mirror. The distance between the ends is equal to the mirror diameter (Fig. 2*a*).

Thus, instead of V-antenna – reflector system we obtain two V-antennae with different opening angles θ_0. The antenna opening angle substituting the reflector will tend to zero. Field superposition of these antennae gives the search field.

The symmetrical parts of the antenna with a fracture formed by crossing of two rectilinear parts are presented in Fig. 1. The beginning of the rectilinear section is located on the distance s_1 measured along the wire, the end is located on the distance s_2 and the fracture is located on the distance s_0 from the excitation point of the antenna. Omitting simple but cumbersome transformations we present the general expression for determination of the full electric field for points with arbitrary coordinates $\{x, y, z\}$ [1,60]:

$$\begin{aligned}E_{tz}=\frac{1}{2f_g\pi}\Bigg\{&\frac{V(t-R/c)}{2R}\cdot\Bigg(\frac{\sin\beta+z/R}{1+\frac{(y-\cot\beta D/2)\cos\beta+z\sin\beta}{R}}+\\&+\frac{\sin\beta-z/R}{1+\frac{(y-\cot\beta D/2)\cos\beta-z\sin\beta}{R}}\Bigg)-\\&-\frac{V(t-l/c-R_2/c)}{2R_2}\cdot\frac{\sin\beta-\frac{z-D/2}{R_2}}{1+\frac{y\cos\beta+(D/2-z)\sin\beta}{R_2}}-\\&-\frac{V(t-l/c-R'_2/c)}{2R'_2}\cdot\frac{\sin\beta+\frac{z+D/2}{R'_2}}{1+\frac{y\cos\beta+(D/2+z)\sin\beta}{R'_2}}-\\&-\frac{4V(t-2F/c-y/c+(D/2c)\cot\beta)}{D}\cdot\frac{1+k^2-p^2}{1+2k^2-2p^2+2k^2p^2+k^4+p^4}+\\&+\frac{V(t-l/c-R_2/c)}{2R_2}\cdot\frac{D/2-z}{R_2-y}+\frac{V(t-l/c-R'_2/c)}{2R'_2}\cdot\frac{D/2+z}{R'_2-y}\Bigg\}.\end{aligned} \qquad (9)$$

On the basis of the theory developed by S.A. Podosenov experimental investigations of propagation of UWB pulse signals were carried out. These investigations confirmed its correctness. The main formulae were checked up experimentally in the laboratory of generation and measurement of parameters of electromagnetic pulses VNIIOFI. Obtained results are matched with theoretical results [60]. Experimental investigations were carried out using nonsymmetrical strip lines. Strip transducer was located in heterogeneous field of GTEM-cell. GTEM-cell is a section of matched cone line with a flat inner electrode and rectangular external one. By means of it one can create TEM waves with a homogeneous field in a cross section in the area between electrodes. A spherical TEM wave is formed in GTEM-cell. Such a cell has a transmittance bandwidth 5 GHz by level 3 dB. In investigation a pulse generator with front 70 ps and amplitude 5.3 V was used. The method proposed by S.A. Podosenov can be used for calculation of pulse interaction of strip lines in print circuit boards.

The theory of interaction of line two-wire transmission line with external electromagnetic field was experimentally confirmed and applied for calculation of interaction of transmission lines with nonstationary heterogeneous electromagnetic fields. It was ascertained that two-wire (strip) lines can be used both for measurement of local intensity of electromagnetic pulses and for measurement of space heterogeneities of pulse electromagnetic fields.

4. ABOUT FRACTAL GEOMETRY OF SPACE-TIME OF DETERMINISTIC STRUCTURES

S.A. Podosenov interested in not only theory of radiation of pulse electromagnetic fields. Many works of S.A. Podosenov were devoted to investigations in the field of the relativity theory – investigation of space-time and classical fields of bound structures. In particularly, jointly with prof. A.A. Potapov he investigated fractal space-time geometry of deterministic structures [4,5,53]. Briefly essence of this problem consists in following.

Usually when describing properties of arbitrary deformed systems in the form of continuum that in general case can be represented by fractals [2,3] either the field of 4-velocities (Euler's view point) or the continuum motion law establishing the connection between Euler and Lagrangian variables is prescribed. Space-time is considered either flat in the case of the special relativity theory (SRT) or the Riemannian one in the case of the general relativity theory (GRT). In other words it is considered that any external non-gravitational fields do not curve space-time of fractal deterministic structures. Its space-time geometry is remained flat. Only "space sections" are bent. Geometry of that in general case is not a Euclidian one. Such a view point is the most spread in scientific literature on the relativity theory and it is supported by majority of investigators.

V.I. Rodichev's [61] and A.A. Vlasov's [62] works differ from the standard interpretation. In [62, p. 326-327] considering the theory of growth of crystal, plasma and biological structures keeping their similarity the author concluded that growth of such structures (fractals!) is possible in non-Eucledian space-time.

Our approach is based on the development of Rodichev's and Vlasov's ideas. It consists in following. Let in a flat Minkowsky space-time with signature (+ - - -) continuum is at rest. In some moment force field of any nature switches on (except the gravitational one) and continuum begins moving. In accordance with the classical version space-time properties remain unchanged.

Our version depends on the location of the observer. If the observer considers motion of the medium from inertial reference frame (IRF) then for him fractal space-time geometry will be unchanged. For the observer connected with moving continuum that is being in noninertial reference frame (NRF) properties of fractal space-time in general case can be changed. We admit that applying of a force field for the observer locating in NRF can change space-time properties transforming it in a curved one in the world tube.

Thus, for the NRF observer after application of the force field continuum will move in some space-time. We want to determine the structure of this space-time in accordance with the specified structure of a force field and the continuum characteristics: a deformation velocity tensor $\Sigma_{\mu\nu}$, an angular velocity tensor $\Omega_{\mu\nu}$, a first curvature tensor of world lines of medium particles F_μ.

For moving continuum in four-dimensional space-time with signature (+ - - -) the expansion is right

$$\nabla_\mu V_\nu = \Sigma_{\mu\nu} + \Omega_{\mu\nu} + V_\mu F_\nu, \tag{10}$$

where V_μ is the field of 4-velocity satisfying the normalization condition

$$g_{\mu\nu} V^\mu V^\nu = 1, \tag{11}$$

$g_{\mu\nu}$ is the metric tensor in the Euler frame of reference,

$$\Sigma_{\mu\nu} = \nabla_{(\mu} V_{\nu)} - V_{(\mu} F_{\nu)}, \tag{12}$$

$$\Omega_{\mu\nu} = \nabla_{[\mu} V_{\nu]} - V_{[\mu} F_{\nu]}, \tag{13}$$

$$F_\mu = V^\nu \nabla_\nu V_\mu. \tag{14}$$

Parentheses arounds indices are the symmetry sigh, and square brackets are the alternation sign. Greek indices are changed from zero to three, latin ones are changed from unit to three.

One can interpret expansion (10) from two view points.

1. We consider that the field of 4-velocity V_μ is known, for example, as a result of integration of relativistic Euler's or Navier-Stokes's equation at specified flat metric. In this case the continuum characteristics $\Sigma_{\mu\nu}$, $\Omega_{\mu\nu}$, F_μ can be obtained in accordance with formulae (12-14), and expansion (10) is a mathematical identity.
2. We consider functions $\Sigma_{\mu\nu}$, $\Omega_{\mu\nu}$, F_μ are specified. In this case expansion (10) turns into a system of differential equations relatively V_ν and $g_{\mu\nu}$. As the number of equations of system (10) and (11) exceeds the number of unknown functions, integrability conditions should be fulfilled. Relation (15) will be an integrability condition for components of 4-velocity

$$\frac{\partial^2 V_\nu}{\partial x^\varepsilon \partial x^\sigma} = \frac{\partial^2 V_\nu}{\partial x^\sigma \partial x^\varepsilon}. \quad (15)$$

To obtain the connection between geometrical and kinematic characteristics of continuum we will calculate expression (16) in an explicit form

$$2\nabla_{[\varepsilon} V_{\sigma]} V_\nu = 2\partial_{[\varepsilon}\partial_{\sigma]} V_\nu + \\ + \left(\frac{\partial \Gamma^\mu_{\varepsilon\nu}}{\partial x^\sigma} - \frac{\partial \Gamma^\mu_{\sigma\nu}}{\partial x^\varepsilon} + \Gamma^\mu_{\sigma\rho}\Gamma^\rho_{\varepsilon\nu} - \Gamma^\mu_{\varepsilon\rho}\Gamma^\rho_{\sigma\nu} \right) V_\mu, \quad (16)$$

where $\Gamma^\mu_{\varepsilon\nu}, \Gamma^\mu_{\sigma\nu}, \Gamma^\mu_{\sigma\rho}, \Gamma^\rho_{\varepsilon\nu}, \Gamma^\mu_{\varepsilon\rho}, \Gamma^\rho_{\sigma\nu}$ – are the Christoffel's symbols expressed by the metric coefficients. From expression (16) taking into account (10-15) the structure equation of deterministic fractal has the form:

$$R^\mu_{\varepsilon\sigma,\nu} V_\mu = 2\nabla_{[\varepsilon}\Sigma_{\sigma]\nu} + 2\nabla_{[\varepsilon}\Omega_{\sigma]\nu} + 2\nabla_{[\varepsilon}(V_{\sigma]} F_\nu). \quad (17)$$

Integration of system (10) and (17), where $R^\mu_{\varepsilon\sigma,\nu}$ is the Riemann-Christoffel's curvature tensor, gives the solution of the problem about space-time geometry where NRF with prescribed structure is realized.

Transition into the rotating reference frame (deterministic fractal) as it is proved in [1,53,63-66], also results in pseudo-Riemannian space-time geometry.

However variety of fractals can not be described only by Riemannian geometry. In [1,63] the structure equation for spaces of metric connectivity with the curvature tensor differed from zero was obtained.

Thus, at the early 2000s owing to our works first a new problem area arose. It was called "Fractal geometry of space-time of deterministic structures" [1,4,5,53,63-66].

In our works [53,67-70] the Hausdorff-Colombeau measure for negative fractal dimensions was introduced. Space-time is modelled as multifractal subset with positive and negative fractal measurements. The axiomatic quantum field theory in space-time with negative fractal dimensions is proposed. We showed that fractal nature of quantum space-time with negative Hausdorff-Colombeau dimensions can solve the problem of cosmological constant.

Works concerning the rotor Mössbauer experiment [71,72] were one of the last works of S.A. Podosenov.

5.CONCLUSION

Theory of pulse radiation from field-forming systems developed by S.A. Podosenov is the base for the analytical calculation of radiation from travelling current waves.

A new analytical method of field calculation in time domain permitting to determine electromagnetic fields from complex structures both in near zone and far one is proposed.

Developed method of analytical calculation of fields from travelling current waves taking into account reflections from fractures and redistribution of currents in wires due to loss of radiation energy was experimentally confirmed.

Simple analytical relations for calculation of antenna constructions of main basic structures are presented. Developed mathematical apparatus can be used for calculation of fields in EMP simulators and calculation of *V*-antenna, radiation field of a horn system, and for the calculation of pulse radiation of an antenna with a reflector. Ordinary personal computer can be used for these calculations.

An investigation of propagation of UWB pulses confirmed correctness of the theory. Presented method has a great practice value and can be used to calculate of pulse interaction of strip lines in printed circuit boards.

The theory of interaction of a linear two-wire transmission line with an external electromagnetic field created by S.A. Podosenov was confirmed experimentally. It was used for calculation of interaction of transmission lines with nonstationary heterogeneous electromagnetic fields. Two-wire (strip) lines can be used both for the measurement of local EMP field strength and for the measurement of space heterogeneities of pulse electromagnetic fields.

Besides that at the early 2000s owing to our works first a new problem area arose. It was called "Fractal geometry of space-time of deterministic structures" [1,4,5,53,63-66] for problems of electrodynamics. In our works [53,63-66] Hausdorff-Colombeau measure concerning negative fractal dimensions was introduced. Space-time is modelled as a multifractal subset with positive and negative fractal measurements. The axiomatic quantum field theory in space-time with negative fractal dimension is proposed.

REFERENCES

1. Podosenov SA, Potapov AA, Sokolov AA. *Impul'snaya electrodinamika sverkhshirokopolosnykh radiosistem i polia sviazannykh structur* [Pulse electrodynamics of ultrawide band radiosystems and fields of bound structures]. Ed. by A.A. Potapov. Moscow, Radiotekhnika Publ., 2003, 720 p.
2. Potapov AA. *Fraktaly v radiofizike i radiolokatsii* [Fractals in radiophysics and radiolocation]. Moscow, Logos Publ., 2002, 664 p.
3. Potapov AA. *Fraktaly v radiofizike i radiolokatsii. Topologiya vyborki* [Fractals in radiophysics and radiolocation. Topology of sampling]. 2nd edition. Moscow, Universitetskaya kniga Publ., 2005, 848 p.
4. Podosenov SA, Potapov AA. O fractal'noy geometrii prostranstva–vremeni determinirovannykh structur [About space–time fractal geometry of deterministic structures]. *Thes. of rep. of the 1st sci.–tech. conf. "Radiooptic technologies in instrumentation"* (Sochi, 9–12 Sept. 2003). Moscow, Publ. house N.E. Bauman MGTU, 2003, p. 62–63.
5. Podosenov SA, Potapov AA. Fractal'naya geometryia prostranstva–vremeni determinirovannykh structur. [Fractal geometry of space–time of deterministic structures]. *Proc of Int. interdisciplinary symposium "Fractals and applied synergy FAPS–03"* (Moscow, 17–20 Nov. 2003). Moscow, Publ. house MGOU, 2003, p. 250–253.
6. GOST 8.540–2015. State system for ensuring the uniformity of measurements. State verification scheme for means of measuring the impulse electric and magnetic field strengths with the pulse rise time over the range 0.1–10.0 ns. Moscow, Standartinform Publ., 2019.
7. GOST 8.540–93. State system for ensuring the uniformity of measurements. State verification shedule for means measuring maximum values of impulse electric and magnetic field strength. Moscow, Izdatel'stvo standartov Publ., 1995.
8. Sakharov KYu, Mikheev OV, Turkin VA, Sukhov AV, Dobrotvorskii MI. Get 148–2013: State Primary Special Standard of Units of Electric and Magnetic Pulse Field Strengths with Pulse Rise Time in the Range from 0.1 to 10.0 ns. *Measurement Techniques,* 2019, 61(10):967-972. DOI: 10.1007/s11018-019-01534-z.
9. Sakharov KYu, Mikheev OV, Turkin VA, Sukhov AV, Aleshko AI, Rodin RA. GET 178–2016: State Primary Special Standard of the Units of the Intensity of Pulsed Electric and Magnetic Fields with Length of Pulse Front in the Range from 10 to 100 psec. *Measurement Techniques,* 2018, 61(6):521-527. DOI: 10.1007/s11018-018-1461-y.
10. Podosenov SA, Sokolov AA. *Izluchenie i izmerenie impul'snykh electromagnitnykh poley* [Radiation and measurement of pulse electromagnetic fields]. Moscow, Sputnik+Publ., 2000, 249 p.
11. Sokolov AA, Sakharov KYu, Kravchenko VF. Possibility of application of UWB short electromagnetic pulses for physical process investigation in inhomogeneous media. *Proc. of the I-st International Workshop on "Mathematical Modeling of Physical Processes in Inhomogeneous Media",* Guanjuato, Mexico, 20-22 March 2001, p. 84-86.
12. Sakharov KYu, Aleshko AI, Sokolov AA, Podosenov SA. Poloskovyi datchik kak sredstvo issledovanyia vozdeistvyia SSHP EMI na pechatnye platy. [The strip transducer as a mean for investigation of UWB EMP impact on printed circuit boards]. *Thes. of rep. of the Vth All–Russian sci.–tech. conf. "Metrological ensurance of defense and safety in RF"*, Mytischi, 13–15 Sept. 2004, Moscow, 2004.
13. Sakharov KYu, Mikheev OV, Sokolov AA, Turkin VA. Antennas for beaming and receiving short ultrawide band electromagnetic impulses. *Proc. of Int. Conf. in Blanes "Information and Telecommunication Technologies in Intelligent Systems",* Barcelona, Spain 22-29 May 2004, p. 37-39.
14. Podosenov SA, Sakharov KYu, Sokolov AA. Calculation of Energy Evolved in the Loads of Strip Transmission Line in Action of Pulse Electromagnetic Field. *Book of Abstracts, Euroem,* Magdeburg, 2004, p. 27.
15. Podosenov SA, Sakharov KYu, Sokolov AA. Influence of Earth Surface on TEM Horn Array Transient Radiation. *Book of Abstracts, Euroem,* Magdeburg, 2004, p. 27-28.
16. Dobrotvorsky MI, Sakharov KYu, Mikheev OV, Turkin VA, Aleshko AI. Malogabaritnyi avtonomnyi izmeritel' maksimal'nykh znacheniy napriazhennosti electricheskogo polia sverkhkorotkikh electromagnitnykh impul'sov

[Compact standalone meter of maximal values of electric field strength of ultrashort electromagnetic pulses]. *Thes. of rep. of All–Russian sci.–tech. conf. "Methods and measuring instruments in the field of electromagnetic compatibility of technical means. Measurement EMC–2004",* N. Novgorod, 2004, p. 49–50.

17. Sakharov KYu. Izmeritel'nye tekhnologii v bor'be s electromagnitnym terrorizmom. [Measurement technologies in the struggle with electromagnetic terrorism]. *Mir izmereniy* [World of measurements], 2015, 10:12 (in Russ.).
18. Sakharov KYu. Printzipy sozdaniya pervichnogo etalona sverkhkorotkikh electromagnitnykh impul'sov. [Principles of creation of primary standard of ultrashort electromagnetic pulses]. *Tekhnologii electromagnitnoi sovmestimosti* [Technologies of electromagnetic compatibility], 2005, 3(14):12–16 (in Russ.).
19. Sakharov KYu. Vybor poleobrazuiuschei sistemy etalona sverkhkorotkikh electromagnitnykh impul'sov. [Selection of the standard fieldforming system of ultrashort electromagnetic pulses]. *Tekhnologii electromagnitnoi sovmestimosti* [Technologies of electromagnetic compatibility], 2005, 3(14):17-26 (in Russ.).
20. Akbashev BB, Aleshko AI, Mikheev OV, Sakharov KYu, Semin VV, Sokolov AA, Turkin VA. Eksperimental'nye issledovaniya vozdeistviya sverkhkorotkikh electromagnitnykh imoul'sov na sistemu kontrolia dostupa v pomescheniya [Experimental investigations of impact of ultrashort electromagnetic pulses in the system of monitoring of access to rooms]. *Tekhnologii electromagnitnoi sovmestimosti* [Technologies of electromagnetic compatibility], 2005, 1:1-6 (in Russ.).
21. Sakharov KYu, Sokolov AA, Mikheev OV, Aleshko AI. Eksperimental'nye resul'taty po generirovaniiu impul'sov electromagnitnogo polia s dlitel'nost'iu fronta v desiatki pikosekund. [Experimental results on generation of standard pulses of electromagnetic field with front duration in tens picoseconds] *Tekhnologii electromagnitnoi sovmestimosti* [Technologies of electromagnetic compatibility], 2006, 1:7-8 (in Russ.).
22. Sakharov KYu. Novye resul'taty issledovaniya kharakteristik sverkhkorotkoimpul'snogo etalonnogo izluchatelia dlia metrologicheskogo obespecheniya telecommunikatsionnykh tekhnologiy. [New results of investigation of characteristics of ultrashort pulse standard radiator for metrological ensurance of telecommunication technologies]. *Col. sci. proc. "Projection of telecommunication and information systems".* Ed. by L.N. Kechiev. Moscow, MIEM Publ., 2006, p. 15-18.
23. Sakharov KYu. O vybore metoda rascheta etalonnykh poleobrazuiuschikh system dlia vysokotochnogo vosproizvedeniya sverkhkorotkikh etalonnykh electromagnitnykh impul'sov. [About selection of calculation method of standard fieldforming systems for high precision reproduction of ultrashort standard electromagnetic pulses.] *Col. sci. proc. "Proektirovanie telekommunikatsionnykh i informatsionnykh sistem"* [Projection of telecommunication and information systems]. Ed. by L.N. Kechiev. Moscow, MIEM Publ., 2006, p. 60–62.
24. Sakharov KYu. *Izluchateli sverkhkorotkikh electromagnitnykh impul'sov i metody izmereniya ikh parametrov* [Radiators of ultrashort electromagnetic pulses and methods of measurement of their parameters]. Moscow, MIEM Publ., 2006, 159 p.
25. Turkin VA, Sakharov KYu, Sokolov AA, Mikheev OV, Kuznetsov EV. Izluchateli sverkhkorotkikh electromagnitnykh impul'sov dlia ispytaniy tekhnicheskikh sredstv. [Radiators of ultrashort electromagnetic pulses for testing of technical means]. *Tekhnologii electromagnitnoi sovmestimosti* [Technologies of electromagnetic compatibility], 2006, 2:10-16 (in Russ.).
26. Mikheev OV, Turkin VA, Sakharov KYu, Sokolov AA, Kuznetsov EV. Sredstva izmereniy dlia ispytaniy radioelectronnoi apparatury na stoykost' k vozdeystviiu sverkhkorotkikh electromagnitnykh impul'sov. [Measuring instruments for testing of testing of radioelectronicc apparatus for impact resistance of ultrashort electromagnetic pulses]. *Tekhnologii electromagnitnoi sovmestimosti* [Technologies of electromagnetic compatibility], 2006, 2:17-21 (in Russ.).
27. Aleshko AI, Sokolov AA, Sakharov KYu, Turkin VA, Kornev AN. Datchik napriazhennosti

elektricheskogo polia sverkhkorotkikh electromagnitnykh impul'sov so sverkhvysokoy chastotoy povtoreniya. [Transducer of electric field strength of ultrashort electromagnetic pulses with ultrahigh repetition rate]. *Tekhnologii electromagnitnoi sovmestimosti* [Technologies of electromagnetic compatibility] 2006, 2:22-26 (in Russ.).

28. Dobrotvorsky MI, Sakharov KYu, Mikheev OV, Turkin VA. Sistema registratsii sverkhkorotkikh impul'sov. [System of registration of ultrashort pulses]. *Tekhnologii electromagnitnoi sovmestimosti* [Technologies of electromagnetic compatibility], 2006, 2:27-30 (in Russ.).
29. Denisov MYu, Sakharov KYu, Mikheev OV, Turkin VA, Ugolev VL. Malogabaritnyi avtonomnyi izmeritel' amplitudy sverkhkorotkikh electromagnitnykh impul'sov. [Compact standalone meter of amplitude of ultrashort electromagnetic pulses]. *Tekhnologii electromagnitnoi sovmestimosti* [Technologies of electromagnetic compatibility], 2006, 2:31-36 (in Russ.).
30. Sakharov KYu, Mikheev OV, Turkin VA, Kornev AN, Dolbnia SN, Pevnev AV, Akbasev BB. Issledovanie funktsionirovaniia personal'nykh kompiuterov v usloviiakh vozdeystvia sverkhkorotkikh electromagnitnykh inpul'sov. [Investigation of functioning of personnel computers in conditions of impact of ultrashort electromagnetic pulses]. *Tekhnologii electromagnitnoi sovmestimosti* [Technologies of electromagnetic compatibility], 2006, 2:44-49 (in Russ.).
31. Podosenov SA, Sakharov KYu, Sokolov AA. Vliianie poverkhnosti zemli na rasprostranenie sverkhkorotkikh inpul'sov electromagnitnogo polia. [Influence of the Earth surface on propagation of ultrashort electromagnetic pulses]. *Tekhnologii electromagnitnoi sovmestimosti* [Technologies of electromagnetic compatibility], 2006, 2:50-53 (in Russ.).
32. Boroday PN, Tiapin MS, Myrova LO, Sakharov KYu. Sredstva obespecheniia stoykosti informatsionnykh system k vozdeystviiu izlucheniy SSHP EMI [Mean of ensurance of information system resistance to impact of UWB EMP radiation]. *Tekhnologii electromagnitnoi sovmestimosti* [Technologies of electromagnetic compatibility], 2006, 2:59-70 (in Russ.).
33. Sakharov KYu, Sokolov AA, Mikheev OV, Turkin VA, Kornev AN, Dolbnia SN, Pevnev AV. Issledovanie funktsionirovaniya lokal'noy vychislitel'noy seti v usloviiakh vozdeystviia sverkhkorotkikh electromagnitnykh impul'sov [Investigation of functioning of local computer net in conditions of impact of ultrashort electromagnetic pulses]. *Tekhnologii electromagnitnoi sovmestimosti* [Technologies of electromagnetic compatibility], 2006, 3:36-45 (in Russ.).
34. Evtikheev NN, Sakharov KYu, Sokolov AA, Aleshko AI, Zasovin EA, Cherepanov AK. Biconicheskaya antenna kak bazovaya structura dlia izluchenia ispytatel'nykh i etalonnykh sverkhkorotkikh electromagnitnykh impul'sov v nestatsionarnykh zadachakh EMS. [Biconical antenna as a base structure for radiation of test and standard ultrashort electromagnetic pulses in nonstationary EMC problems]. *Tekhnologii electromagnitnoi sovmestimosti* [Technologies of electromagnetic compatibility], 2006, 4:3-9 (in Russ.).
35. Sokolov AA, Sakharov KYu, Mikheev OV, Turkin VA, Aleshko AI. Radiators of ultrashort electromagnetic pulses. *Proc. of the 3-rd Int. Conf. on "Ultrawideband and Ultrashort Impulse Signals UWBUSIS"*. Sevastopol, 2006, p. 203-205.
36. Evtikheev NN, Sakharov KYu, Sokolov AA, Aleshko AI, Zasovin EA, Cherepanov AK. Biconicheskaya antenna kak bazovaya structura dlia izluchenia ispytatel'nykh i etalonnykh sverkhkorotkikh electromagnitnykh impul'sov v zadachakh EMS. [Biconical antenna as a base structure for radiation of test and standard ultrashort electromagnetic pulses in EMC problems]. *Proc of 15th Int. conf. on radiolocation and radio communication.* Moscow, MEI Publ., 2007, p. 226-237.
37. Sakharov KYu, Evtikheev NN, Sokolov AA, Zasovin EA, Cherepanov AK. Antenny dlia izluchenia sverkhkorotkikh electromagnitnykh impul'sov [Antennae for radiation of ultrashort electromagnetic pulses]. *Proc of 15th Int. conf. on radiolocation and radio communication.* Moscow, MEI Publ., 2007, p. 487-489.
38. Mikhailov VA, Sakharov KYu, Turkin VA, Mikheev OV, Simakin SV, Larionenko AV. Otsenka stoikosti bortovykh vychislitel'nykh mashin v usloviiakh vozdeystvia sverkhkorotkikh

electromagnitnykh poley. [Resistance rating of onboard computers in conditions of impact of ultrashort electromagnetic fields]. *Tekhnologii electromagnitnoi sovmestimosti* [Technologies of electromagnetic compatibility], 2008, 4(27):12-19 (in Russ.).

39. Akbashev BB, Sakharov KYu, Mikheev OV, Turkin VA, Aleshko AI, Katkov BG, Berdyshev AV. Issledovanie rasprostraneniia sverkhkorotkikh electromagnitnykh impul'sov v pomescheniiakh [Investigation of propagation of ultrashort electromagnetic pulses indoors]. *Tekhnologii electromagnitnoi sovmestimosti* [Technologies of electromagnetic compatibility], 2009, 1(28):41-47 (in Russ.).
40. Sakharov KYu, Tikhomirov SV, Turkin VA, Mikheev OV, Sukhov AV, Aleshko AI. Etalonnyi kompleks sverkhkorotkikh electromagnitnykh impul'sov s dlitel'nost'iu fronta 20 ps [Standard complex of ultrashort electromagnetic pulses with 20 ps front duration]. I*zmeritel'naya tekhnika* [Measurement Techniques], 2010, 7:57-59 (in Russ.).
41. Sakharov KYu, Iankovskiy BD, Miliaev AP, Morev VL, Turkin VA, Mikheev OV. Ismeritel'nyi compleks dlia issledovania electromagnitnoy obstanovki pri rasprostranenii sverkhkorotkikh electromagnitnykh impul'sov v pomescheniiakh zdania [Measuring complex for investigation of electromagnetic environment when propagating ultrashort electromagnetic pulses indoors]. *Tekhnologii electromagnitnoi sovmestimosti* [Technologies of electromagnetic compatibility], 2009, 3(30):18-21 (in Russ.).
42. Shunin OA, Belov AS, Dobrynin MK, Kashin AV, Sakharov KYu, Turkin VA, Mikheev OV. Issledovanie radiopogloschaiuschikh materialov s pomoschiu sverkhkorotkikh electromagnitnykh impul'sov [Investigation of radioabsorpting materials by means of ultrashort electromagnetic pulses]. *Tekhnologii electromagnitnoi sovmestimosti* [Technologies of electromagnetic compatibility], 2009, 3(30):38-46 (in Russ.).
43. Akbashev BB, Batonov NM, Sakharov KYu, Mikheev OV, Turkin VL, Eriashev DI, Lafishev MA, Sukhov AV. Ustoichivost' system videonabludenia k vozdeistviiu moschnykh sverkhkorotkikh electromagnitnykh impul'sov [Resistance of videoobservation systems to impact of power ultrashort electromagnetic pulses]. *Tekhnologii electromagnitnoi sovmestimosti* [Technologies of electromagnetic compatibility], 2011, 2(37):24-28 (in Russ.).
44. Akbashev BB, Batonov NM, Sakharov KYu, Mikheev OV, Turkin VL, Eriashev DI, Lafishev MA, Sukhov AV. Eksperimental'nye issledovaniia funktsionirovaniia ustroystv tipovoy kompleksnoy sistemy bezopasnosti v usloviiakh vozdeystviia sverkhkorotkikh electromagnitnykh impul'sov [Experimental investigations of functioning of devices of typical complex safety system in condition of impact of ultrashort electromagnetic pulses]. *Tekhnologii electromagnitnoi sovmestimosti* [Technologies of electromagnetic compatibility], 2011, 2(37):30-37 (in Russ.).
45. Sakharov KYu, Turkin VA, Mikheev OV, Sukhov AV, Dnischenko VN. Metody i sredstva monitoringa electromagnitnykh izlucheniy v sverkhkorotkoimpul'snom diapazone dlitel'nostey [Methods and means of monitoring of electromagnetic radiation in ultrashort pulse range of durations]. *4th Int. radioelectronic forum "Applied radioelectronics. State and perspectives of development" IRF-2011. Col. sci. proc. in 3 vol. Vol. I Conf. "Integrated information radioelectronic systems and technologies" Part 2*. Khar'kov, ANPRE, KHNURE Publ., 2011, p. 237-240.
46. Sakharov KYu, Turkin VA, Mikheev OV, Sukhov AV, Lafishev MA, Eriashev DI. Apparatura dlia monitoringa electromagnitnykh izlucheniy v sverkhkorotkoimpul'snom diapazone dlitel'nostey [Apparatus for monitoring of electromagnetic radiation in ultrashort pulse range of duration]. *Tekhnologii electromagnitnoi sovmestimosti* [Technologies of electromagnetic compatibility], 2011, 4:58-61 (in Russ.).
47. Sakharov KYu, Turkin VA, Mikheev OV, Sukhov AV. Ustroistvo dlia izmerenia parametrov electromagnitnogo impul'sa so sverkhkorotkoy dlitel'nost'iu fronta [Device for measurement of electromagnetic pulse parameters with ultrashort front duration]. *RF Patent № 2468375 C1*. Publ. bul."Izobretenia, Poleznye modeli" [Inventions. Useful models] № 33, 27.11.2012.
48. Sukhov AV. Metody i sredstva izmereniy parametrov sverkhkorotkikh electromagnitnykh impul'sov v pikosekundnom diapazone [Methods and measuring instruments of parameters of

ultrashort electromagnetic pulses in picosecond range]. *Thes. … Ph. D.* (tech. sci.). Moscow, FGUP "VNIIOFI" Publ., 2016.

49. Sakharov KYu, Turkin VA, Mikheev OV. A measuring system for characterization of radar-absorbent materials by ultra-short electromagnetic pulses sounding over the range 0.1 – 4.0 GHz. *Proc. of 14th Conf. on Microwave Techniques COMITE 2015,* Pardubice, Czech Republic, 21-23 April 2015, p. 1-4.
50. Zinovev SV, Evdokimov AN, Sakharov KYu, Turkin VA, Aleshko AI, Ivanov AV. Opredelenie terapevticheskoy znachimosti vozdeystviia impul'snogo shirokopolosnogo electromagnitnogo SVCH-izslucheniia na modeliakh eksperimental'noy onkologii [Determination of therapeutic value of ultra-wideband pulsed electromagnetic microwave radiation on models of experimental oncology]. *Meditsinskaya fizika* [Medical physics], 2015, 3:62-67 (in Russ.).
51. Podosenov SA, Potapov AA, Men'kova ER. Novyi analiticheskiy metod rascheta electromagnitnykh poley ot beguschikh voln toka [New analytical method of calculation of electromagnetic fields from travelling current waves]. *Nelineinyi mir* [Nonlinear world], 2007, 5(12):725-739 (in Russ.).
52. Potapov AA, Podosenov SA, Foukzon J, and Men'kova ER. New Method for Calculating Pulsed Electromagnetic Fields from Traveling Current Waves in Complex Wire Structures. *Phys. of Wave Phenomena*, 2011, 19(2):112-123.
53. Podosenov SA, Potapov AA, Foukzon J, Men'kova ER. *Negolonomnye, fraktal'nye i sviazannye structury v reliativistskikh sploshnykh sredakh, electrodinamike, kvantovoy mekhanike i kosmologii* [Nonholonomic, Fractal and Bound Structures in Relativistic Continua, Electrodynamics, Quantum Mechanics and Cosmology] in three books. Ed. By A.A. Potapov. Moscow, LENAND Publ., 2016, 1128 p.
54. Sakharov KYu, Podosenov SA, Turkin VA, Mikheev OV, Men'kova ER, Sukhov AV, Aleshko AI. Ispol'zovanie metoda zadannykh tokov dlia rascheta vo vremennoy oblasti parametrov impul'snykh electromagnitnykh poley s dlitel'nost'iu fronta do 10 ps [Use of the method of predetermined currents to calculate the parameters of pulsed electromagnetic fields in the time domain] *Izmeritel'naya tekhnika* [Measurement Techniques], 2015, 11:55-58 (in Russ.).
55. Podosenov SA, Svekis YGu, Sokolov AA. Transient Radiation of Traveling Waves by Wire Antennas. *IEEE Trans.*, 1995, AP-37(3):367-383.
56. Podosenov SA, Sokolov AA. Linear Two-Wire Transmission Line Coupling to an External Electromagnetic Field, Part I: Theory. *IEEE Trans.*, 1995, AP-37(4):559-566.
57. Podosenov SA, Sakharov KYu, Svekis YaG, and Sokolov AA. Linear Two-Wire Transmission Line Coupling to an External Electromagnetic Field, Part II: Specific cases, experiment. *IEEE Trans.*, 1995, AP-37(4):566-574.
58. Podosenov SA, Sokolov AA, Al'betkov SV. Exitation of a V-Antenna by a Pulse Electromagnetic Field. *IEEE Trans.*, 1996, AP-38(1):31-42.
59. Mikheev OV, Podosenov SA, Sakharov KYu, Sokolov AA, Turkin VA. Approximate Calculation Methods for Radiation of a TEM-Horn Array. *IEEE Trans.*, 2001, AP-43(1):67-74.
60. Mikheev OV, Podosenov SA, Sakharov KYu, Sokolov AA, Svekis YaG, Turkin VA. New Method for Calculating Pulse Radiation from an Antenna with a Reflector. *IEEE Trans.*, 1997, AP-39(1):48-54.
61. Rodichev VI. *Teoriia tiagoteniya v ortogonal'nom repere.* [Gravity theory in orthogonal benchmark]. Moscow, Nauka Publ., 1974, 184 p.
62. Vlasov AA. *Statisticheskie funktsii raspredeleniia.* [Statistical distributional functions]. Moscow, Nauka Publ., 1966, 356 p.
63. Podosenov SA. *Prostranstvo, vremia i klassicheskie polia sviazannykh struktur* [Space, time and classical fields of bound structures]. Moscow, Company "Sputnik+" Publ., 2000, 445 p.
64. Podosenov SA, Foukzon J, and Potapov AA. A Study of the Motion of a Relativistic Continuous Medium. *Gravitation and Cosmology,* 2010, 16(4):307-312.
65. Podosenov SA, Foukzon J, Potapov AA, and Men'kova ER. Electrodynamics in Noninertial Reference Frames. *Journal of Appl. Math. and Phys.,* 2016, 4(4):806-843. URL: http://www.scirp.org/journal/jamp.

66. Podosenov SA, Potapov AA, Foukzon J, Men'kova ER. Metric and structure equations in relativistic continua. *RENSIT: Radioelectronika. Nanosistemy. Informatsionnye tekhnologii* [RENSIT: Radioelectronics. Nanosystems. Information technologies], 2019, 11(2):113-124, doi: 10.17725/rensit.2019.11.113.
67. Foukzon J, Men'kova E, and Potapov A. The Solution Cosmological Constant Problem. *Journal of Modern Phys.,* 2019, 10:729-794. DOI: 10.4236/jmp.2019.107053.
68. Foukzon J, Menkova ER, Potapov AA, and Podosenov SA. *Quantum Field Theory in Fractal Space-Time with Negative Hausdorff-Colombeau Dimensions. The Solution Cosmological Constant Problem*. 2019, https://arxiv.org/abs/1004.0451.
69. Foukzon J, Men'kova ER, Potapov AA. The Solution Cosmological Constant Problem. Quantum Field Theory in Fractal Space-Time with Negative Hausdorff-Colombeau Dimensions and Dark Matter Nature. *Journal of Physics: Conf. Ser.,* 2019, 1391:ID 012058. DOI: 10.1088/1742-6596/1391/1/012058.
70. Foukzon J, Men'kova ER, Potapov AA. Singular general relativity using the Colombeau approach. I. Distributional Schwarzschild geometry from nonsmooth regularization via horizon. *Physics Essays,* 2020, 33(2):180-199. DOI: 10.4006/0836-1398-33.2.180.
71. Podosenov SA., Foukzon J, Men'kova ER. Comment on "The Mössbauer rotor experiment and the general theory of relativity" [Ann. Physics 368 (2016) 258-266]. *Annals of Physics*, 2020, 413:168047. DOI: 10.1016/j.aop.2019.168047.
72. Podosenov SA, Foukzon J, Men'kova ER. Erratum to Comment on "The Mössbauer rotor experiment and the general theory of relativity" [Ann. Physics 368 (2016) 258-266]. *Annals of Physics,* 2020, 423:168329. DOI: 10.1016/j.aop.2020.168329.

DOI: 10.17725/rensit.2023.15.355

The investigation of resonators with longitudinal and lateral electric fields with various shear dimensions

Boris D. Zaitsev, Alexander P. Semyonov, Andrey A. Teplykh, Irina A. Borodina

Kotel'nikov Institute of Radioengineering and Electronics of RAS, Saratov Branch, http://cplire.ru/
Saratov 410019, Russian Federation

E-mail: zai-boris@yandex.ru, alex-sheib@yandex.ru, teplykhaa@mail.ru, borodinaia@yandex.ru

Received November 24, 2023, peer-reviewed November 30, 2023, accepted December 03, 2023, published December 06, 2023.

Abstract: **The influence of the diameter of a disk resonator with a radial electric field made on the basis of PZT-19 piezoceramics and the shear dimensions of a resonator with a lateral electric field (LFE) based on PZTNV-1 piezoceramics on their main characteristics, such as the frequencies of parallel and serial resonances and maximum values of the real parts of electrical impedance and admittance has been studied experimentally and theoretically.**

Keywords: **radial oscillations, resonators with a lateral electric field, resonators with a longitudinal electric field, parallel resonance, series resonance, electrical impedance and admittance**

UDC: 534.231, 534.6.08

Acknowledgments: The work was carried out with the financial support of the Ministry of Education and Science of the Russian Federation (state assignment FFWZ-2022-0002).

For citation: Boris D. Zaitsev, Alexander P. Semyonov, Andrey A. Teplykh, Irina A. Borodina. The investigation of resonators with longitudinal and lateral electric fields with various shear dimensions. *RENSIT: Radioelectronics. Nanosystems. Information Technologies,* 2023, 15(4):355-360e. DOI: 10.17725/rensit.2023.15.355.

Contents

1. INTRODUCTION

Piezoelectric resonators are widely used in various fields of science and technology, both as passive components of electronic equipment [1] and as various sensors. These sensors are used to study the properties of various liquids [2-8] and films [9-10], to analyze various gases in the air [11-15], to record specific biological reactions in aqueous environments [16-18], to create micro-movement detectors [19], etc.

It was previously shown that changing the electrical boundary conditions near the free side of a piezoelectric resonator with a lateral electric field affects its parameters [19]. However, in practice during measuring the characteristics of resonators of this type in a wide frequency range, there are often the resonances the nature of which is either unclear or difficult to analyze theoretically. In addition, it should be noted that the features of excited oscillations in resonators must be analyzed not only theoretically, but also the theoretical data must be confirmed by experimental results. In this work, the features of mechanical vibrations in a disk resonator with a longitudinal exciting electric field and in a rectangular resonator

with a lateral electric field are studied when their shear dimensions change.

The purpose of this work is to investigate the influence of the shear dimensions of a piezoceramic disk resonator with a longitudinal electric field and a piezoceramic rectangular resonator with a lateral electric field on their main characteristics.

2. EXPERIMENTAL PROCEDURE AND EXPERIMENTAL RESULTS

2.1. The study of a disk resonator with a longitudinal electric field

To carry out the research, a disk resonator with a longitudinal electric field based on piezoceramics PZTNV-1 (Aurora-ELMA LLC, Volgograd) with a diameter of D = 21.9 mm and a thickness of 1.945 mm was used. During the entire experiment, the diameter of the disk resonator was changed by mechanical processing from 21.9 mm to 14 mm in steps of ~1 mm. For each value of the disk resonator diameter, the frequency dependences of the real and imaginary parts of the electrical impedance were measured. From the measured frequency dependences, the maximum values of the real parts of the electrical impedance and admittance, as well as the resonant frequencies of parallel and series resonances were determined. The dependences of the resonant frequencies of parallel (f_{par}) and series (f_{ser}) resonances on the resonator diameter (D) are presented in **Fig. 1**. The maximum values of the real parts of the electrical impedance (R_{max}) and

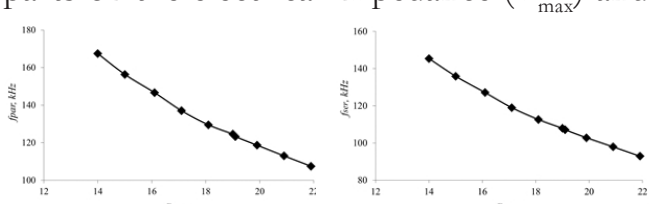

Fig. 1. *Experimental dependences of the frequencies of parallel fpar (left) and serial fser (right) resonances on the diameter of disk D of a resonator with longitudinal electric field made on the basis of PZTNV-1 piezoceramics*

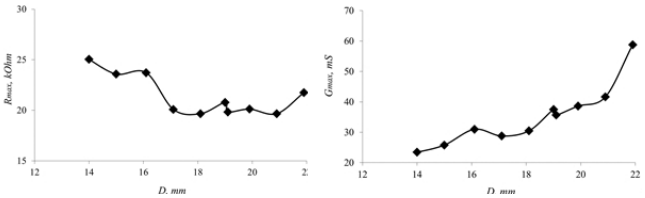

Fig. 2. *Experimental dependences of the maximum values of the real parts of the electrical impedance Rmax (left) and admittance Gmax (right) on the diameter of the disk D of the resonator with longitudinal electric field made on the basis of piezoceramics PZTNV-1.*

admittance (G_{max}) as function of diameter D are shown in **Fig. 2**. Fig. 1 shows that as the diameter decreases, the frequency of both parallel and series resonances increases. The total relative change in these values is 56% and 57%, respectively. The maximum value of the real part of the electrical impedance (R_{max}) does not change as the disk diameter decreases from 22 to 17 mm, but then increases slightly as the diameter decreases from 17 to 14 mm (Fig. 2 (left)). The total relative change in this value is 25% when the disk diameter changes from 17 to 14 mm. The maximum value of the real part of the electrical admittance (G_{max}) decreases from 60 to 20 mS with a decrease in the resonator diameter from 22 to 14 mm (Fig. 2 (right)). The total relative change in the maximum value of the real part of the electrical admittance is 60%. Such a change in the characteristics of the disk resonator, especially the resonant frequency of the parallel resonance, with a decrease in its diameter indicates the excitation of mechanical vibrations of the radial type.

2.2. The investigation of a resonator with a lateral electric field

The resonator with the lateral electric field was manufactured in laboratory conditions from a rectangular PZT-19 piezoceramic plate with a thickness of 2.566 mm and shear dimensions of 19.9×17.86 mm². Two rectangular aluminum electrodes with

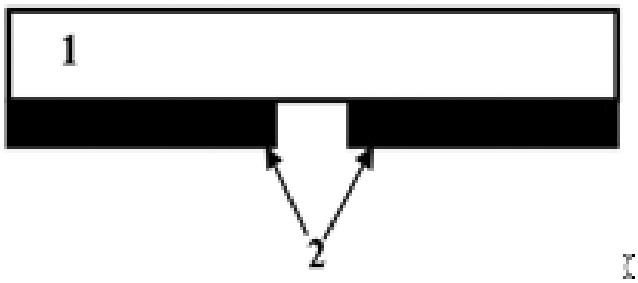

Fig. 3. *Layout of the resonator with lateral electric field: 1 – plate of piezoceramics PZT-19, 2 – electrodes.*

dimensions of 19.9×6.9 mm2 and a gap of 4 mm between them were applied to one side of the piezoceramic plate (**Fig. 3**). The polar axis of the piezoelectric was oriented perpendicular to the gap. During the experiment, the largest shear dimension (H) of the piezoceramic plate along the gap was changed by mechanically grinding from 19.9 to 14.8 mm with a step of ~1-2 mm. This process allowed to maintain the parallelism of opposite faces and the integrity of the resonator electrodes. For each plate length (H) of the resonator probe, the frequency dependences of the real and imaginary parts of the electrical impedance were measured in the operating range of 50-300 kHz. From these dependencies, the values of the resonant frequencies and the maximum values of the real parts of the electrical impedance corresponding to each length of the resonator were determined for the three observed resonances in a given frequency range. The dependences of the maximum value of the real part of the electrical impedance and the resonant frequency of the parallel resonance on the length of the resonator for the three observed resonances are presented in **Figs 4, 5, 6.** Figs 4, 5, 6 show that as the plate length decreases from 19.9 to 14.8 mm, an increase in the resonant frequency is clearly observed for the three observed parallel resonances in the selected operating range. The maximum value of the real parts of the electrical impedance

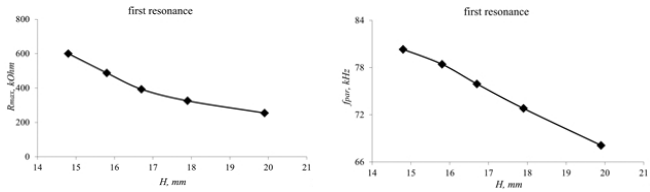

Fig. 4. *Experimental dependences of the maximum value of the real part of the electrical impedance R_{max} (left) and the frequency of parallel resonance f_{par} (right) on the length H of the piezoceramic plate of the resonator with lateral electric field for the first observed resonance.*

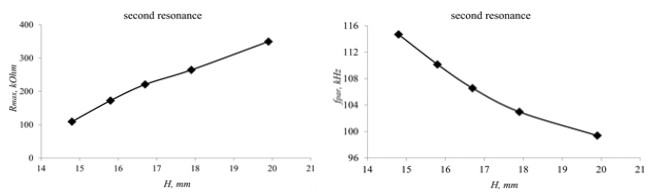

Fig. 5. *Experimental dependences of the maximum value of the real part of the electrical impedance R_{max} (left) and the frequency of parallel resonance f_{par} (right) on the length H of the piezoceramic plate of the resonator with lateral electric field for the second observed resonance.*

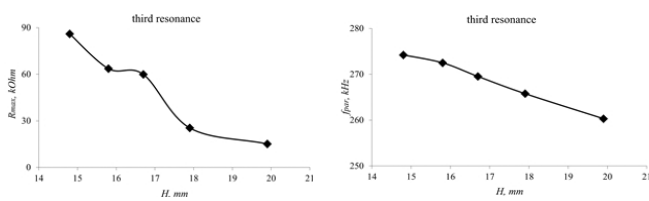

Fig. 6. *Experimental dependences of the maximum value of the real part of the electrical impedance R_{max} (left) and the frequency of parallel resonance f_{par} (right) on the length H of the piezoceramic plate of the resonator with lateral electric field for the third observed resonance*

increases with decreasing plate length for the first and third resonances (Figs. 4, 6) and decreases for the second resonance (Fig. 5). Relative changes in these values are presented in **Table 1**.

Table 1

Relative changes in the resonant frequency and the maximum value of the real part of the electrical impedance of the resonator with lateral electric field for each

Value	First resonance	Second resonance	Third resonance
f_{par}	18%	15%	5%
R_{max}	136%	69%	460%

3. THEORETICAL ANALYSIS OF THE INFLUENCE OF THE SHEAR DIMENSIONS OF RESONATORS ON THEIR CHARACTERISTICS

Theoretical analysis of the characteristics of the resonator with longitudinal electric field for various values of its diameter was carried out using a two-dimensional finite element method [10]. The dependences of the resonant frequencies of parallel and series resonances (**Fig. 7**) and the maximum values of the real parts of the electrical impedance and admittance (**Fig. 8**) on the diameter of the resonator were plotted. Comparison of dependencies in Fig. 1 and Fig. 7, and ones in Fig. 2 and Fig. 8 indicates good agreement between the theoretical data and the experimental results. During the calculations, the material constants for the PZTNV-1 piezoceramics were taken from the reference book [20]. A similar theoretical analysis for the resonator with lateral electric field was not carried out, since the two-dimensional finite element method used does not allow taking into account the size of the resonator in the third dimension, which changed during the experiment.

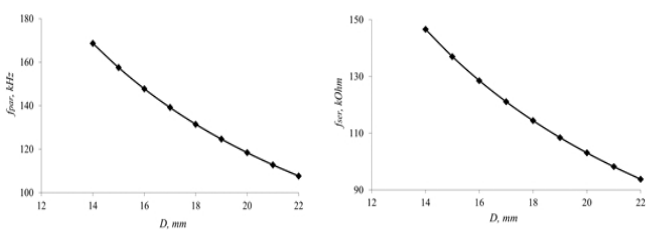

Fig. 7. *Theoretical dependences of the frequencies of parallel f_{par} (left) and series f_{ser} (right) resonances on the diameter of the disk D of the resonator with longitudinal electric field made on the basis of PZTNV-1 piezoceramics.*

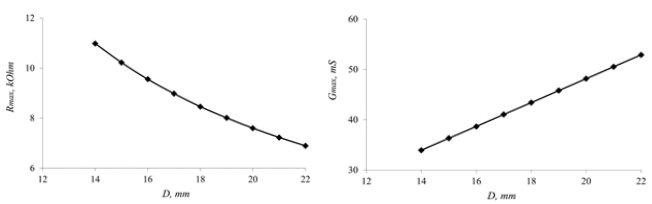

Fig. 8. *Theoretical dependences of the maximum values of the real parts of the electrical impedance R_{max} (left) and admittance G_{max} (right) on the diameter of the disk D of the resonator with longitudinal electric field made on the basis of piezoceramics PZTNV-1.*

4. CONCLUSION

The influence of the diameter of a resonator with a longitudinal electric field, made of PZTNV-1 piezoceramics, on its main characteristics, such as the resonant frequencies of parallel and series resonances and the maximum values of the real parts of the electrical impedance and admittance, has been studied experimentally and theoretically. It has been established that a change in the characteristics of a disk resonator with a decrease in its diameter indicates the excitation of mechanical vibrations of the radial type, which is confirmed by theoretical analysis. Theoretical analysis was carried out using the finite element method. In addition, the influence of the shear dimensions of a resonator with lateral electric field made on the basis of PZT-19 piezoceramics on its characteristics was experimentally studied. These characteristics are the parallel resonance frequency and the maximum value of the real part of the electrical impedance. It has been shown that decreasing the length of the resonator with lateral electric field from 19.9 to 14.8 mm leads to an increase in the frequencies of all observed parallel resonances. In this case, the maximum value of the real part of the electrical impedance increases with decreasing plate length for the first and third resonances and decreases for the second one.

REFERENCES

1. Khomenko I.V., Kosykh A.V., Quartz resonators and self-oscillators. Omsk: Publishing house. Omsk State Technical University, 2018, 160 p. (in Russian).

2. Zao Z., Qian Z., Wang B., Kuznetsova I., Ma T., Yong Y.-K. Design considerations for frequency shifts in a laterally finite FBAR sensor in contact with the Newtonian liquid // IEEE Trans. on Ultrasonics, Ferroelectrics and Frequency Control, 2020, v.67, #11, pp. 2402-2412, https://doi.org/10.1109/TUFFC.2020.3006186
3. McCann D.F., McCann J.M., Parks J.M., Frankel D.J., M. Pereira da Cunha and Vetelino J.F. A lateral-field-excited LiTaO3 high frequency bulk acoustic wave sensor // IEEE Trans. on Ultras., Ferroel., and Freq. Contr., 2006, vol. 56, no. 4, pp. 779–787.
4. Zaitsev B.D., Shikhabudinov A.M., Teplykh A.A., Kuznetsova I.E. Liquid sensor based on a piezoelectric lateral electric field-excited resonator // Ultrasonics, 2015, vol. 63, pp. 179–183.
5. Borodina I.A., Zaitsev B.D., Teplykh A.A. Influence of the conductivity of a liquid contacting with a lateral electric field excited resonator based on PZT ceramics on its characteristics // Ultrasonics, 2020, vol. 102, 106059, DOI: 10.1016/j.ultras.2019.106059
6. Zaitsev B.D., Semyonov A.P., Teplykh A.A., Borodina I.A. A new liquid sensor based on a piezoelectric resonator with a radial electric field // Ultrasonics, 2022, vol. 119, 106603, https://doi.org/10.1016/j.ultras.2021.106603,
7. Zaitsev B.D., Borodina I.A., Teplykh A.A. Compact liquid analyzer based on a resonator with a lateral excitation electric field // Ultrasonics, 2022, vol. 126, 106814, https://doi.org/10.1016/j.ultras.2022.106814,
8. Semyonov A., Zaitsev B., Teplykh A. and Borodina I. The Effect of Glycerol-Based Suspensions on the Characteristics of Resonators Excited by a Longitudinal Electric Field // Sensors. 2023. vol. 23, P. 608
9. Kuznetsova I.E., Zaitsev B.D., and Shikhabudinov A.M. Elastic and viscosity properties of nanocomposite films based on low – density polyethylene // IEEE Transactions on Ultrasonics, Ferroelectrics, and Frequency Control, 2010, vol. 57, № 9, pp. 2099 – 2102.
10. Teplykh Andrey, Zaitsev Boris, Semyonov Alexander and Borodina Irina The Study of the Acoustic Characteristics of Chitosan Acetate Film Using a Radial Electric Field Excited Resonator // Sensors, 2023, vol. 23, P. 1808, https://doi.org/10.3390/s23041808
11. Kuznetsova I., Zaitsev B., Krasnopolskaya L., Teplykh A., Semyonov A., Avtonomova A., Ziangirova M., Smirnov A., Kolesov, V. Influence of humidity on the acoustic properties of mushroom mycelium films used as sensitive layers for acoustic humidity sensors // Sensors. 2020. vol. 20, P. 2711
12. Zaitsev B.D., Teplykh A.A., Fedorov F.S., Grebenko A.K., Nasibulin A.G., Semyonov A.P., Borodina I.A. Evaluation of Elastic Properties and Conductivity of Chitosan Acetate Films in Ammonia and Water Vapors Using Acoustic Resonators // Sensors, 2020, vol. 20, pp. 2236; doi:10.3390/s20082236.
13. Liu K., Zhang C. Volatile organic compounds gas sensor based on quartz crystal microbalance for fruit freshness detection: A review, Food Chem., 2021, 334, 127615.doi:10.1016/j.foodchem.2020.127615.
14. Wang L. Metal-organic frameworks for QCM-based gas sensors: A review,

Sensors Actuators, A Phys., 2020, 307, 111984. doi:10.1016/j.sna.2020.111984

15. Gorbachev I., Smirnov A., Ivanov G., Avramov I., Datsuk E., Venelinov T., Bogdanova E., Anisimkin V., Kolesov V, Kuznetsova I. Langmuir-Blodgett films of arachidic and stearic acids as sensitive coatings for chloroform HF SAW sensors // Sensors, 2023, vol.23, p.100, 10.3390/s23010100.
16. Guliy O.I., Zaitsev B.D., Semyonov A.P., Alsowaidi A.K.M., Teplykh A.A., Karavaeva O.A., Borodina I.A. Microbial acoustic sensor test-system based on a piezoelectric resonator with a lateral electric field for kanamycin detection in liquid // Ultrasonics, 2022, vol. 120, 106651, https://doi.org/10.1016/j.ultras.2021.106651,
17. Hartz Jequil S. R., Emanetoglu Nuri W., Howell Caitlin, and John F. Vetelino Lateral field excited quartz crystal microbalances for biosensing applications, Biointerphases, May 2020. DOI: 10.1116/6.0000144
18. Gorbachev I.A., Smirnov A.V. Biosensor based on Langmuir-Blodgett film with alcohol oxidase enzyme // Radioelektronika, Nanosistemy, Informacionnye Tehnologii, 2023. V.15.#3, p. 307-316e, https://doi.org/10.17725/rensit.2023.15.307
19. Zaitsev B.D., Semyonov A.P., Teplykh A.A., Borodina I.A. The sensor for measuring the micro-displacements based on the piezoelectric resonator with lateral electric field // Ultrasonics, 2019, vol. 99, https://doi.org/10.1016/j.ultras.2019.105973
20. Piezoceramic transducers. Measurement methods and calculation of parameters. Reference book. Edited by S. I. Pugachev. Leningrad, 1984, 256 p. (in Russ.)

DOI: 10.17725/rensit.2023.15.361

Sensors for liquid level and analysis of thermodynamic processes during its freezing based on bulk acoustic waves

Vladimir I. Anisimkin, Iren E. Kuznetsova, Andrey V. Smirnov

Kotel'nikov Institute of Radioengineering and Electronics of RAS, http://www.cplire.ru/
Moscow 125009, Russian Federation

E-mail: anis@cplire.ru, kuziren@yandex.ru, andre-smirnov-v@yandex.ru

Received December 01, 2023, peer-reviewed December 03, 2023, accepted December 05, 2023, published December 06, 2023.

Abstract: **A fundamental property of longitudinal bulk acoustic waves (BAW) is their inability to propagate in a gaseous medium due to strong absorption in the MHz range and, on the contrary, their ability to propagate in liquids. Based on this property, a liquid level sensor based on BAW is proposed. For these purposes, for the first time, it was used not to measure changes in the velocity and attenuation of waves, but to change the time of their propagation from the emitter to the receiver. It is shown that this acoustic parameter is ideal for such measurements, since it weakly depends on temperature, but depends on the aggregate state of the propagation medium. A technique has been developed for non-contact research of exo-, endo- and isothermal processes accompanying liquid-ice and ice-liquid phase transitions. With its help, the isothermal nature of the water-ice phase transition under normal conditions was experimentally demonstrated.**

Keywords: **bulk acoustic waves, liquid, liquid level, exo-, endo- and isothermal processes, water-ice phase transition**

PACS: 43.35.Yb

Acknowledgments: The work was carried out within the framework of the state assignment of the V.A. Kotel'nikov Institute of Radioengineering and Electronics of RAS.

For citation: Vladimir I. Anisimkin, Iren E. Kuznetsova, Andrey V. Smirnov. Sensors for liquid level and analysis of thermodynamic processes during its freezing based on bulk acoustic waves. *RENSIT: Radioelectronics. Nanosystems. Information Technologies,* 2023, 15(4):361-366e. DOI: 10.17725/rensit.2023.15.361.

Contents

1. INTRODUCTION

The determination of the liquid level in closed tanks is an important technical problem [1,2]. Its solution is important both for the implementation of biological liquid sensors and for industrial applications in the field of nuclear energy, gas industry, etc. Various approaches are used to solve this problem. These approaches are based on the use of fiber optic sensors [3,4], a laser beam reflected from the liquid/glass structure [5], acoustic waves excited by a laser or by a piezoelectric transducer placed on the tank wall [6,7]. Depending on the problem being solved, these sensors can be placed either inside the liquid itself [8,9] or outside [6,7]. One of the most actively used methods is the use of acoustic waves. In the case of direct measurements, acoustic pulses reflected from the liquid-gas interface are

used to obtain information about the position of the liquid level [10]. In this case, an acoustic wave is generated by a transducer placed at the bottom of the tank, passes through the tank walls and liquid, is reflected from the liquid-gas interface and returns to the trigger transducer. The delay time of the reflected signal provides the necessary information. Other methods are based on the transmission of an acoustic wave through the tank wall and liquid in the horizontal direction [10]. In this case, the output signal appears if the liquid level exceeds the distance between the input and output sensors.

This paper explores the possibility of determining the presence of liquid using longitudinal bulk acoustic waves. The technique is based on the fundamental property of longitudinal bulk acoustic waves (BAW), namely, their inability to propagate in a gaseous medium due to strong absorption in the MHz range and, conversely, their ability to propagate in liquids. The possibility of using BAW to analyze thermodynamic processes occurring during liquid freezing was also investigated.

2. DESIGN OF THE LIQUID LEVEL SENSOR BASED ON BAW AND THE OBTAINED RESULTS

Fig. 1 shows the design of a liquid level sensor based on longitudinal bulk acoustic

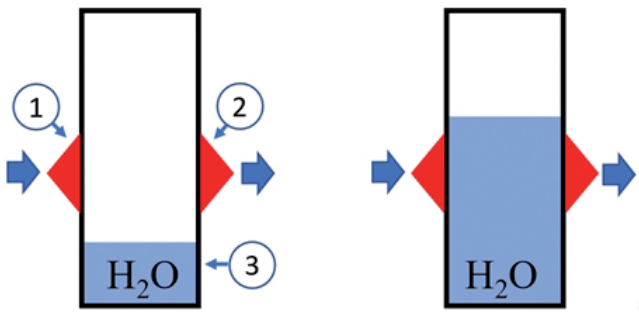

Fig. 1. *Schematic representation of an experimental sample based on longitudinal volumetric acoustic waves, intended for recording the liquid level. 1 – emitter, 2 – receiver, 3 – cell.*

waves (BAW). The sensor consists of an emitter, a liquid cell and an ultrasound receiver at frequencies from 1 to 37 MHz. The distance between the transducers was 5.3 mm. The impulse responses are shown in **Fig. 2**. In the absence of liquid (the cell is filled with air), the output signal of the sensor at the sample exit is zero due to the high absorption of ultrasound in the air (Fig. 2*a*). When the liquid reaches a certain level and blocks the path of propagation of the ultrasonic beam, the longitudinal wave begins to propagate from the emitter to the receiver, and the signal $S_{12}(\tau_L)$ is recorded at the sensor output, the delay of which τ_L(lq) corresponds to the velocity of the longitudinal wave V_L(lq) in this liquids (Fig. 2*b*). Based on the delay of the acoustic signal, its amplitude

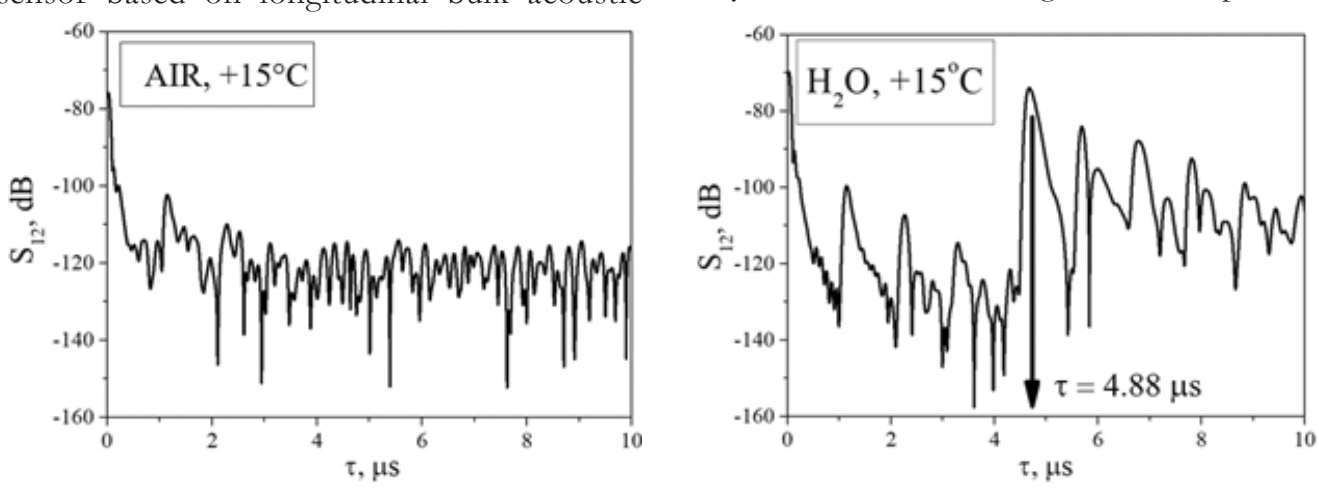

a *b*

Fig. 2. *Pulse responses at the output of the experimental sample for recording the liquid level, measured using an E5061B quadripole analyzer operating in the amplitude-time format. (a) – low liquid level (Fig. 1, left), (b) – high liquid level (Fig. 1, right). The distance between the converters is 5.3 mm.*

and the size of the cell, the velocity V_L and attenuation of longitudinal (L) BAW in water were determined: $V_L(H_2O)$ = 1480 km/s and attenuation coefficient $\alpha_L(H_2O)$ = 1.9 dB/mm (at 30 MHz). The results obtained coincide with the literature values [11].

3. SENSOR FOR NON-CONTACT STUDY OF EXO-, ENDO- AND ISOTHERMAL PROCESSES ACCOMPANYING PHASE TRANSITIONS LIQUID-ICE AND ICE-LIQUID

The experimental technique for non-contact study of exo-($\Delta T > 0$), endo-($\Delta T < 0$) and iso($\Delta T = 0$)thermal processes accompanying liquid-ice and ice-liquid phase transitions was based on the sample shown in **Fig. 3.** It consisted of a silicon rod (10×10×50 mm^3), a cell made of thermal insulating material (Teflon) (diameter 5 mm, height 10 mm, thickness 1.5 mm) and two ceramic transducers glued to the rod with salol. A sample of the liquid, the phase transition of which was being studied, was injected with a syringe through the upper surface of the cell, after which this surface was isolated from the external environment (covered). Heat transfer through the side walls of the cell was also prevented by the poor thermal conductivity of Teflon, so that the liquid was in contact only with the upper surface of the silicon. The nature of the phase transition of liquid into ice was controlled by the change in temperature ΔT of the test sample as the sample cooled.

The sample, together with the rod and transducers, cooled to a temperature below the phase transition temperature, was probed at a certain distance from the silicon end with a bulk acoustic wave with known sensitivity to temperature. The change in liquid temperature ΔT during the ice formation process (if any) was transmitted practically unchanged to the internal regions of the silicon rod due to its high temperature conductivity, which led to a change in the speed ΔV and phase $\Delta\varphi$ of the probing acoustic wave. The value of ΔT was determined from the known relation [12]

$$\Delta T = (1/TCV)(\Delta V/V) = (1/TCV)(\Delta\varphi/\varphi), \quad (1)$$

where TCV is the temperature coefficient of the velocityof the probing wave in silicon, close to the temperature coefficient of delay of the wave TCD (known), V, φ are the velocity and phase of this wave (known), ΔV, $\Delta\varphi$ are changes in velocity and phase, which are measured using a network analyzer KEYSIGHT E5061B in phase mode.

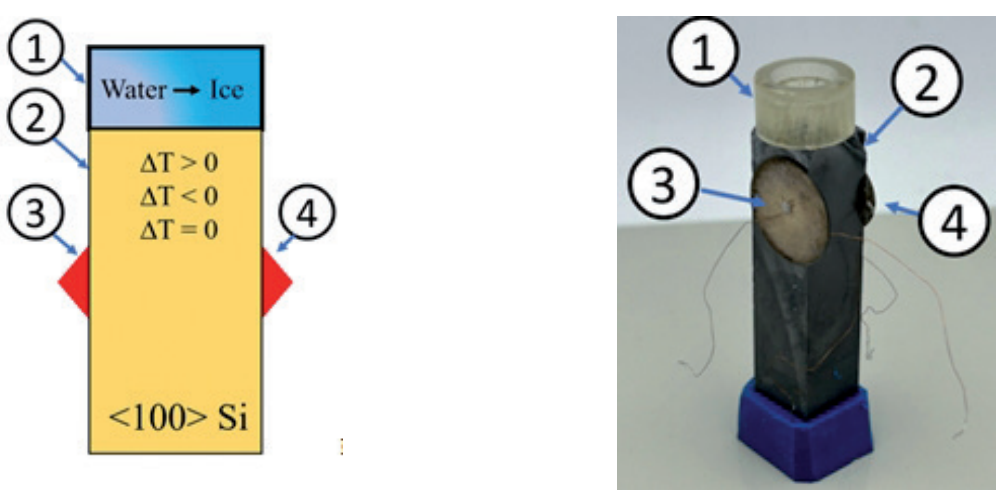

a *b*

Fig. 3. *Schematic representation (a) and photograph (b) of an experimental sample for non-contact study of exo-($\Delta T > 0$), endo-($\Delta T < 0$) and iso-($\Delta T = 0$)thermal processes accompanying liquid-ice phase transitions-liquid. 1 – test sample, 2 – silicon rod, 3 – emitter, 4 – receiver.*

To account for temperature changes in the adhesions between the transducers and the rod, as well as in transducers that are pressed piezoceramics, similar measurements were previously carried out without the test sample and the values of the output signals with and without the test liquids were subtracted. Distilled water was used as the test liquid. Salol was used to glue ceramic converters to a silicon rod. The measurement accuracy, which was mainly determined by the quality of the acoustic contact (bonding) between the piezoelectric transducers and the silicon rod, is estimated to be ±1°C.

Fig. 4 shows the measurement results. The experiment used ceramic transducers of longitudinal body waves at 10 MHz with a wavelength $\lambda = V_L/f = 0.85$ mm. Since the length of the rod in the direction of wave propagation was $L = 10$ mm, the total phase shift between the transducers was $\varphi_0 = 360°(L/\lambda) = 360°(10\text{ mm}/0.85\text{ mm}) = 4235°$.

The measurement procedure was as follows. At the first stage, the temperature delay coefficient TCD of a longitudinal acoustic wave was measured in a silicon rod with ceramic transducers and gluing in the absence of a test liquid: when the sample was cooled,

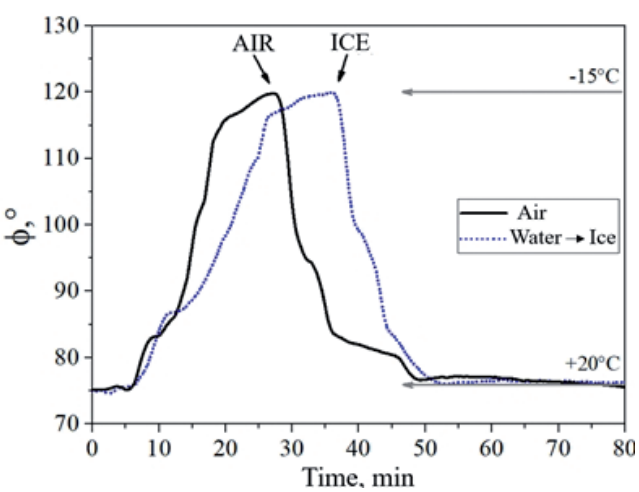

Fig. 4. *Phase responses of longitudinal acoustic waves measured in air (black line) and during the water-ice phase transition (blue dashed line).*

for example, from $T = +20°$C to $T = -15°$C, the phase change was $\Delta\varphi = 53.1°$ (Fig. 4, solid line). Therefore, the TCD of the rod with ceramic converters and gluing was equal to $(1/\Delta T)(\Delta\varphi/\varphi_0) = (1/35°\text{C})(51.13°/4235°) = +345$ ppm/°C. For comparison, the same coefficient for longitudinal BAW in silicon without converters and gluing is an order of magnitude lower and amounts to only +32.7 ppm/°C [13].

At the second stage, a similar change in the phase of the wave was measured when a rod with water on its upper surface was cooled. Water was transformed into ice, which gave an additional change in phase $\Delta\varphi$ by –0.16° compared to a clean rod (Fig. 4, dotted line). Hence, the additional temperature change associated with the water-ice phase transition is $\Delta T = (1/\text{TC}D)(\Delta\varphi/\varphi_0) = (1/345\text{ppm/°C})(-0.16°/4235°) = -0.1°$C or the value, close to zero ($\Delta T \approx 0°$C) – the water-ice phase transition, as it should be, is isothermal [11].

Thus, non-contact studies of thermal processes accompanying liquid-ice and ice-liquid phase transitions under conditions of thermal contact of the object under study only with the measuring element are possible using volumetric acoustic waves. The measurement accuracy is low (±1°C) and is mainly determined by the quality of the acoustic contact of the piezoelectric transducers with the silicon rod and thermal losses. To minimize the bonding effect, measurements with pure silicon should be carried out immediately before testing each liquid, and to minimize thermal loss, piezoelectric transducers should be located in close proximity to the interface with the substance being tested. Approbation of the methodology has shown that the phase transition process for distilled water, as it should be, is isothermal ($\Delta T \approx 0°$C), However, small values of the accompanying

temperature variations ΔT are determined with low accuracy ±1°C.

More reliable measurements of ΔT using the developed method are possible only for phase transitions that are accompanied by more significant temperature changes $|\Delta T| \geq 5$°C.

4. CONCLUSION

The propagation of longitudinal bulk acoustic waves in liquids with much less attenuation than in gaseous media makes it possible to record the excess or fall of the liquid level relative to a given value.

Temperature changes in the velocity of the bulk acoustic wave probing the silicon rod in depth make it possible to record the nature of the thermal processes accompanying the phase transition on the surface of the rod. The disadvantage of using bulkacoustic waves to detect liquid-ice phase transitions is the need to take into account temperature changes in electromechanical transducers and gluing the transducers to a liquid cell.

REFERENCES

1. Skladnev DA, Sorokin VV, Karlov SP, Anisimkin VI. Methods for Studying Parameters Biogenic Metal Nanoparticles, Formed in situ. *RENSIT: Radioelectronics. Nanosystems. Information Technologies*, 2022, 14(4):393-414e. DOI: 10.17725/rensit.2022.14.393.
2. Gorbachev IA, Smirnov AV. Biosensor based on Langmuir-Blodgett film with alcohol oxidase enzyme. *RENSIT: Radioelectronics. Nanosystems. Information Technologies*, 2023, 15(3):307-316e. DOI: 10.17725/rensit.2023.15.307.
3. Shi J, Xu Z, Li X, Bai H, Guo C, Niu P, Yao J. A High-Resolution Liquid-Level Sensor Based on Fabry-Perot Interferometer With Fiber Laser Intracavity Sensing. *IEEE Sensors Journal,* 2023, 23(15):16938-16943. DOI: 10.1109/JSEN.2023.3288223.
4. He R, Teng C, Kumar S, Marques C, Min R. Polymer Optical Fiber Liquid Level Sensor: A Review. *IEEE Sensors Journal,* 2022, 22(2):1081-1091. DOI: 10.1109/JSEN.2021.3132098.
5. Suemori K, Komatsu Y, Nobeshima T. Flange-type liquid-level sensor based on laser light reflection. *Sensors International,* 2023, 4:100230. DOI: 10.1016/j.sintl.2023.100230.
6. Kim H, Balagopal B, Kerrigan S, Garcia N, Chow M-Y, Bourham M, Fang T, Jiang X. Noninvasive liquid level sensing with laser generated ultrasonic waves. *Ultrasonics,* 2023, 130:106926. DOI: 10.1016/j.ultras.2023.106926.
7. Sakharov VE, Kuznetsov SA, Zaitsev BD, Kuznetsova IE, Joshi SG. Liquid level sensor using ultrasonic Lamb waves. *Ultrasonics,* 2003, 41(4):319-322. DOI: 10.1016/S0041-624X(02)00459-6.
8. Hercik R, Machacek Z, Byrtus R, Koziorek J. Identification of the Physical Dependencies of Accurate Oil Level Measurement for Automotive Applications. *Applied Sciences* (Switzerland), 2023, 13(13):7707. DOI: 10.3390/app13137707.
9. Rhee C, Yu SI, Kim DW, Bae IH, Shin J, Jeong SY, Kim YM, Shin SG. Density profile modeling for real-time estimation of liquid level in anaerobic digester using multiple pressure meters. *Chemosphere,* 2021, 277:130299. DOI: 10.1016/j.chemosphere.2021.130299.
10. Lynnworth LC. *Ultrasonic measurements for process control.* New York, Academic Press, 1989.
11. Kikoin IK, Kikoin AK. *Senior Physics 1.* Moscow, Mir Publ., 1987.

12. Slobodnik AJ. The temperature coefficients of acoustic surface wave velocity and delay on lithium niobate, lithium tantalate, quartz, and tellurium dioxide. *Phys. Sci. Res. Pap.,* 1972, 477.
13. Ono S, Wasa K, Hayakawa S. Surface acoustic wave properties in ZnO-SiO_2O-Si layered structure. *Wave Electronics,* 1977, 3(1):35-49.

DOI: 10.17725/rensit.2023.15.367

Method for determining spacecraft motion parameters based on ultra-long-baseline radio interferometric measurements

Igor L. Afonin, Alexander L. Polyakov, Yuri N. Tyschuk, Vladislav V. Golovin, Gennadiy V. Slyozkin

Sevastopol State Technical University, http://www.sevsu.ru/

Sevastopol 299053, Russian Federetion

E-mail: igor_afonin@inbox.ru, al_polyakov@inbox.ru, y.tyschuk@gmail.com, v_golovin@mail.ru, g.slyozkin@mail.ru

Received August 14, 2023, peer-reviewed August 21, 2023, accepted August 28, 2023, published December 06, 2023.

Abstract: **The proposed method for measuring current navigational parameters of spacecrafts makes it possible to control them to a certain extent using a single ground-based automated station. With this the following specifics of a single-station control are taken into account: location of spacecraft spatial-time monitoring stations, geometrical interpretation of these measurements, difficulties in processing of the received information and proper selection of radio equipment required for performing such measurements. The proposed method for trajectory tracking is based on the ultra-long-baseline interferometry. Measuring base here is the distance between a ground-based radio complex and onboard radio complex of the reference spacecraft that is constantly visible by the ground-based monitoring station. Onboard radio complex can include an array of spacecrafts traveling either along elongated elliptical orbit with an apogee height of more than twenty thousand kilometers or along a 36000 km high geostationary orbit. Application of the proposed method will help extend capabilities of the space monitoring system in terms of prompt clarification of public and private catalogues of spacecrafts orbiting the Earth.**

Keywords: **navigation, ballistic-navigational support, spacecraft, space source, radio system, trajectory tracking, radio interferometer**

UDC 656.61.052:621.396

For citation: Igor L. Afonin, Alexander L. Polyakov, Yuri N. Tyschuk, Vladislav V. Golovin, Gennadiy V. Slyozkin. Method for determining spacecraft motion parameters based on ultra-long-baseline radio interferometric measurements. *RENSIT: Radioelectronics. Nanosystems. Information Technologies,* 2023, 15(4):367-376e. DOI: 10.17725/rensit.2023.15.367.

Contents

1. INTRODUCTION

When developing highly complex systems, a number of fundamental issues arise, the solution of which determines the appearance of the system and ways to further enhance it. Developing a trajectory radio interferometric system involves the following fundamental steps: elaboration of the trajectory tracking method for spacecrafts (SC); due consideration of specifics associated with gathering and processing information about current navigational parameters (ICNP) of spacecrafts; ensuring synchronization of remote time scales at the radio interferometer monitoring stations.

Synchronization of time scales in the proposed method is achieved by the use of a geostationary SC in order to reduce the errors associated with the movement of the SC relative to the reference points.

Signal exchange procedure is to be structured in such a way as to mainly eliminate the delays associated with the formation and propagation of signals. In this case, the synchronization accuracy will depend on the parameters of the

onboard radio complex (RC), type of signal, and accuracy of time interval measurements.

Signal exchanged between the stations of an ultra-long baseline interferometer (ULBI) must be a broadband noise-like signal (BNLS) synchronized with frequency and time reference standards.

Stability of onboard RC oscillators the ground-based RC oscillators shall ensure such coherent accumulation time at the output of the ground-based RC receiver that would achieve the desired signal-to-noise ratio.

Time delays of the space source (SS) required to calculate the clock difference must be measured using correlation signal processing similar to that used in radio interferometry, which yields the highest measurement accuracy.

2. MAIN PART

Considering relatively simple design (in particular, for synchronization of radio signals), it seems appropriate to place the onboard RC of the spacecraft ULBI system on the geostationary orbit [2,3]. Geometric interpretation of the proposed trajectory tracking method is the double difference in the propagation time of radio signals from the SC, reference SC and reference SS (see **Fig. 1**). Then ULBI measurements can be represented as

$$\Delta T = \Delta T_{SC} - \Delta T_{SC0} = (t_1 - t_2) - (t_3 - t_4),$$

where $\Delta T_{SC} = (t_1 - t_2)$ is time difference between t_1 (signal propagation time between ground RC and target SC) and t_2 (time between target SC and reference SC).

$$\Delta T_{SC} = t_1 - t_2 = (B\cos\alpha)/c,$$

where α is an angle between the baseline and direction of the target SC; c is the speed of light, $c = 2.99792458 \cdot 10^8$ m/s; B is the measurement baseline; $\Delta T_{SC0} = (t_3 - t_4)$ is the time difference of signal propagation between the ground-based RC and reference SS, and between reference SS and reference SC.

ΔT_{SC0} can be calculated using the following formula

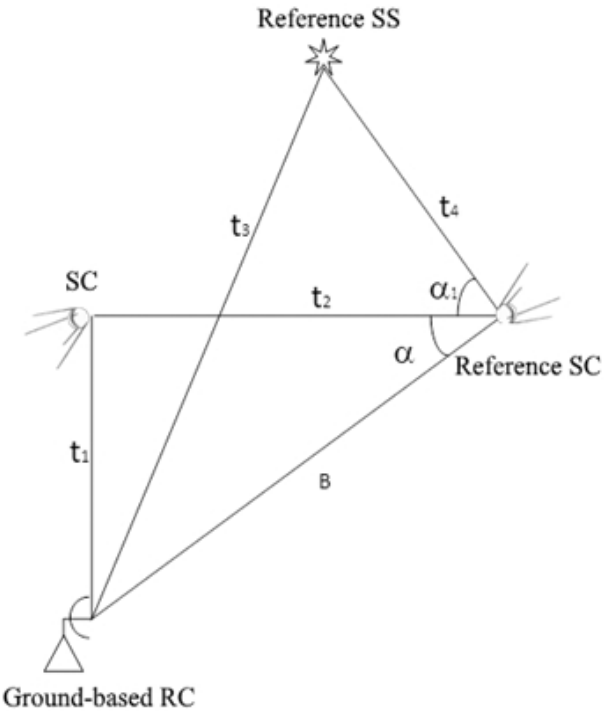

Fig. 1. *Geometrical interpretation of the trajectory interferometric system.*

$$\Delta T_{SC0} = t_3 - t_4 = B\cos(\alpha - \alpha\_1)/c,$$

where α_1 is an angle between direction of the reference SC to the target SC and direction of the reference SC to the reference SS.

With a sufficient degree of accuracy for measurement error ΔT, the following approximation will hold true

$$\Delta T = -\frac{\alpha_1 B}{c}\sin\alpha. \quad (1)$$

Therefore the ratio for calculating an angular inclination of the SC relative to the reference SC (as projected onto the baseline) according to the ΔT measurement will be as follows

$$\alpha_1 = \frac{c\Delta T}{B\sin\alpha}. \quad (2)$$

It can be seen from expression (2) that measurement error for angle α_1 is proportionally dependent on ΔT measurement error and for a given accuracy it will decrease as the value of $B\sin\alpha$ increases. To achieve the highest possible accuracy in spacecraft trajectory measurements, it is desirable that the baseline length B and angle α are as large as possible.

Given the fact that the reference SC is located on the geostationary orbit, the proposed trajectory measurement method helps achieve the measurement baseline that significantly exceeds the maximum possible baseline when only ground-based RCs are used in ULBI measurements.

At the same time, if trajectory measurements are made from one baseline, then SC localization area on the celestial sphere is represented by a strip, width of which is determined by the error α_1 (along the baseline projection). When two intersecting baselines are used (with the second baseline represented by the distance between the ground-based RC and the reference SS or reference SC) the spacecraft localization area is determined by the intersection of the strips described above. Moreover, if we introduce the following notations: α_1' are the errors of measuring the angular position of the SC along the first baseline, α_2 are the errors of measuring the angular position of the SC along the second baseline, and α_3 is the angle of baseline direction intersection, then the maximum distances between the boundaries of the localization area, measured by two orthogonal directions (arbitrarily considering the direction α_1 as the first one) will be determined by the following values:

— α_1 in the first direction;

— $[\alpha_1 + \alpha_1 \cos\alpha_3]/\sin\alpha_3$ in the second direction.

The minimum uncertainty of the SC localization area in both directions will be when the baseline directions are orthogonal, i.e.

$\alpha_3 = \pi/2$.

ULBI measurements from two intersecting baselines yielding the angular position of the object on the celestial sphere are supplemented by the measurement of the third coordinate, i.e. distance to the SC. In this case, a complete spatial definition of the SC is achieved, which is very valuable for the operation of space systems. In the limiting case, use of even two such triples of measurements makes it possible to solve the navigational problem of SC control.

Creation of a trajectory radio interferometer is largely dependent on proper selection of the RCs used for measurements and, in particular, their antenna systems. This is due to the fact that not only the coordinate-spatial characteristics of the SC are measured, but also the spatiotemporal characteristics of the reference SS.

Signal-to-noise ratio in ULBI measurements is determined by the expression

$$h = \sqrt{\frac{2\Delta f T}{k T_n}} \pi o_1 o_2 S_s, \quad (3)$$

where o_1, o_2 are the diameters of the antennas used, with surface area utilization factors equal to 0.5; S_s is spectral flux density of a point source (radio emission from a SS or SC); Δf is registration band; T is signal accumulation time; T_N is noise temperature of the ground-based RC; k is the Boltzmann constant.

It is clear from expression (3) that RCs with large diameter antennas are required in order to increase the signal-to-noise ratio. However, in the proposed trajectory radio interferometric system, one of the monitoring stations is located on board the reference SC. Therefore, increasing the size of the antenna of this RC is a complex and expensive task. In this regard, it seems appropriate to increase the diameter of the antenna of ground-based RCs. Of particular interest in this case are the RCs, which are already involved in SC control operations.

The analysis performed gives us grounds to assert that it is appropriate to use a RT-70 antenna for a trajectory radio interferometric system.

RT-70 antenna [4] is located at the point with coordinates 45°11'N and 33°11'E and it is of full-revolving Gregory type with a quasi-parabolic main mirror of 70 m and a field of view of 0° to 360° in azimuth plane and 6° to 90° in elevation plane. Main specifications of

the monitoring station equipped with the RT-70 antenna are given in [4,5].

Before we start reviewing astrophysical aspects affecting selection of the SS, we will briefly analyze parameters and specifics of the RT-70 antenna application for receiving SS signals, while taking into account the data in **Table 1**.

For estimates in the spectral measurement mode, we will set the radial velocity resolution ΔV = 1 km/s, from which the spectral resolution and corresponding analysis bandwidth depending on the frequency will be calculated by the following formula

$$\Delta v = \Delta v_L = v\frac{\Delta V}{c}.$$

In this measurement mode, typical integration time is approximately 1 hour. For continuum estimates, it would be appropriate to set an integration constant of 1 s. We will use two analysis bandwidth options: B1 = 5 MHz (available at the moment, for example, at a frequency of 6 GHz) and prospective B2, the provision of which is quite realistic. Time required for a point source to pass through the radiation pattern was estimated from the expression

$$t_{\min} = \frac{\Delta\Theta}{15},$$

where $\Delta\Theta$ is beamwidth, measured in arcminutes. Calculation results for the limiting parameters of radio astronomical values are given in Table 1.

As expected for this antenna, the limiting parameters of the radio astronomical values are adequate. We will also find out how well the ground-based RC is matched in terms of spatial resolution and sensitivity resolution. For the purpose of estimation, we will use a 5-cm wave because the best parameters of the system are achieved at this wavelength [4].

Table 1

Calculation results of limiting parameters of radio astronomical values for RT-70

Operating frequency, MHz	B2, MHz	S_{min}, Jy		T_{min}, K		t, s	Δv_L, kHz	TL_{min}, K
		B1	B2	B1	B2			
740	20	0.10	0.05	0.10	0.05	165	2.5	0.07
930	50	0.05	0.02	0.05	0.02	130	3.1	0.04
1668	100	0.03	0.006	0.04	0.01	75	5.6	0.02
5008	100	0.02	0.005	0.04	0.01	25	16.7	0.01
5885	100	0.02	0.005	0.04	0.01	20	19.6	0.01

Number of sources that are identifiable by a ground-based RC along a hemisphere is approximately estimated by the formula

$$N(\mathrm{r}) = 0.1\frac{2\pi}{\Delta\Theta^2} = 10^6.$$

Based on the analysis of the available statistical data for the sources, as well as their spectra, and models of the Universe, it is known that the number of sources with flux densities of 5 to 20 mJy does not exceed $N(d) = 10^7 \ldots 10^6$ which is close to the value of $N(r)$, which indicates almost optimal matching of the instrument in terms of sensitivity and resolution. Some excess of sensitivity is not harmful, because for studies of, for example, lines or pulsars, the "entanglement" effect is not so dangerous due to availability of such additional criteria for distinguishing such as frequency and time.

Thus, the use of the RT-70 antenna for the ground-based RC of the trajectory radio interferometric system makes it possible to use galactic and extragalactic SSs as reference objects and, moreover, will ensure reception and processing of uncontrolled radiation signals from onboard equipment to obtain trajectory and identification information about the SC [6].

The main difference between the proposed method for gathering information about the current navigation parameters of SCs and existing systems is the use of a satellite channel for reception and transmission of information between the ground-based RC and the reference SC, as well as between the ground-based RC and target SC, and between the reference SC and target SC. Moreover, data from the reference SSs and from the reference SC also come via satellite communication channels. Given that these channels, in addition to information about the space-time position of the SS, the reference

and target SC of the ULBI system, also transmit program-command and telemetry information used for controlling the SCs involved, tense energy relation arise both along the Earth to SC path and SC to the Earth path. This circumstance necessitates the analysis of the specifics associated with collection of information about current navigation parameters (ICNP) in the ULBI system including selection of the main parameters, as well as energy calculation of the entire trajectory radio interferometric system, and optimization of areas serviced by the reference SC.

To obtain information about the current navigation parameters of the SC, it is appropriate to use uncontrolled radiation signals (URS) (leaking through the waveguide radiation paths of permanently functioning blocks of onboard equipment: master oscillators, local oscillators, etc.) from these SCs. Then the reference SC must ensure transmission of the following 6 channels to the ground-based RC: a command radio link to the target (controlled) SC, a trajectory radio link from the target SC, a special (according to functional layout) radio link from the target SC, a command radio link to the reference SC, a trajectory radio link from the reference SC, as well as radio links for receiving signals from the reference SS.

To serve as a reference SC we find it suitable to use a geostationary satellite with a 11/14 GHz repeater transponder (**Fig. 2**)[7].

Radio signals received by the onboard antenna pass through a preliminary low-noise amplifier (LNA) and a band-pass channel filter used to separate the transponders and to decouple the receiving path from the transmitting path of the SC. Additional amplification and clipping is performed to bring the signals in each transponder to the proper level. Gain control is carried out via a command radio link from a ground-based RC. The signals are then transported down the frequency and amplified by the traveling-wave tube (TWT) amplifier. If there are several signals at the TWT input, non-linear distortions in the frequency band may occur. To avoid this, the input power level is reduced to the required level by means of an adjustable amplifier (AA). An amplitude limiter (AL) can be installed at the input of the TWT amplifier (TWTA) to prevent the amplifier from being overloaded by the peak value of the signal.

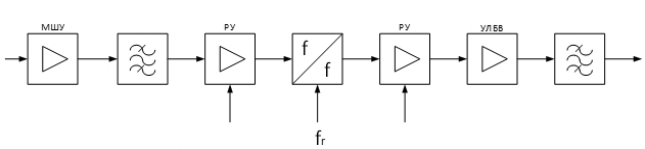

Fig. 2. *Block diagram of a repeater transponder on the reference SC.*

Thus, the onboard RC of a reference SC is a complex radio device, which can be modelled by an inertial nonlinear system with distributed parameters [7]. Such systems are extremely time consuming to analyze, so we will use a simplified model featuring localized linear inertial part (band-pass filter), nonlinear inertia-free part (limiter) and the nonlinear inertial part (source of amplitude-phase conversion). Each of these parts and all of them together cause a number of effects that lead to a decrease in the noise immunity and throughput of the RC.

We are to calculate the frequency parameters of the six-channel signal of the RC onboard the reference SC. According to the well-known technique [7], we will first calculate the minimum frequency band needed to transmit single-channel information at a rate of $\nu = 4.5$ Mbps by using the double phase-shift modulation (PSM). This band is equal to

$$\Delta f_{\min} = 1.5\frac{v}{2} = 3.375 \cdot 10^6.$$

We will assume that the allowable energy loss of the model in relation to the signal energy to the noise power spectral density Δh is equal to 0.7. This loss corresponds to Δa equivalent value, by which the signal amplitude must be reduced to account for additional losses. Values $\Delta a/a$ and Δh are related by the following formula [8]

$$\frac{\Delta\alpha}{\alpha}=\frac{1}{10^{-\frac{\Delta h}{20}}}. \quad (4)$$

Now it is possible to formulate requirements that a filter must adhere to in order to achieve the calculated value of $\Delta a/a$. Attenuation $\delta_k(\Omega)$ of a k^{th}-order filter at the normalized frequency Ω depending on $\Delta a/a$ is calculated by the following formula [7]

$$\delta_k(\Omega)=-20\lg\frac{\Delta\alpha}{0.84\alpha}. \quad (5)$$

At $\Delta h = 0.7$, formulas (4) and (5) will give us the following results

$$\frac{\Delta\alpha}{\alpha}=1\div10^{\frac{-0.7}{20}}=0.077,$$

$$\delta_k(\Omega)=-20\lg\frac{0.077}{0.84}=20.8\ dB.$$

Attenuation of 20.8 dB is achievable by using a 4th-order Butterworth filter at a relative frequency Ω of 1.7 [9].

After having selected characteristics of the filters that provide proper filtering of the channels, it is possible to lay out channeling arrangement in the frequency spectrum of the transponder and size of the guard bands. We will denote frequency band of each channel as Δf, filtering band as Δf_p, and the value equal to ($\Delta f_p + \Delta f/2$) as δf. In [8], the following formulas are given to calculate these values

$$\Delta f = A\Delta F - C\delta f, \quad (6)$$

where $A = 2/(n + 1)$, $C = 2(n – 1)/(n + 1)$; n is number of channels; ΔF is frequency band of the transponder being part of RC onboard the reference SC.

To account for frequency response unevenness at the ends of the transponder spectrum, we will take ΔF as 32 MHz. At the ends of the transponder spectrum, narrow-band channels for transmitting service information can be placed, for which the unevenness of the magnitude response and phase response in the channel band will be less significant.

Parameter δf can be calculated as follows [7]

$$\delta f=-\frac{1}{2(1-C\Omega)}\times\left(2f_0+C\Omega f_0-A\Omega\Delta F+\right.$$
$$\left.+\sqrt{\left(2f_0+C\Omega f_0-A\Omega\Delta F\right)^2+4A\Omega\Delta ff_0\left(1+C\Omega\right)}\right), \quad (7)$$

where f_0 is central frequency of the modem that is equal to 20 MHz.

Inserting Ω = 1.7 into (6) and (7) gives us δf = 3.4 MHz , Δf = 4 MHz, Δf_p = 1.6 MHz. It is known [7] that the standard intermediate frequency in the satellite channel is 70 MHz, and f_0 = 20 MHz is the intermediate frequency of the modem at which the signals are filtered. The modems are fitted with frequency converters, in which the signal spectrum translation is carried out.

Location of subchannels in the frequency transponder of the onboard RC on the reference SC relative to the intermediate frequency (or "frequency plan") is shown in Fig. 3.

Distance between the carriers is 5.6 MHz, and the bandwidth allocated to each of the six data transmission subchannels is 4 MHz. Guard bands are placed at the ends of the transponder spectrum, in one of which a relatively narrow-band service communication channel is located at a frequency of 87.6 MHz.

Thus, using one transponder of the reference SC, it is possible to create an information system for ULBI (ground-based RC — onboard RC) with a total speed of about 30 Mbps. Noise immunity of such system depends, on the one hand, on the coding algorithms, modulation, and signal processing, and, on the other hand, on the parameters and statistical characteristics of the signal and noises in the radio channel.

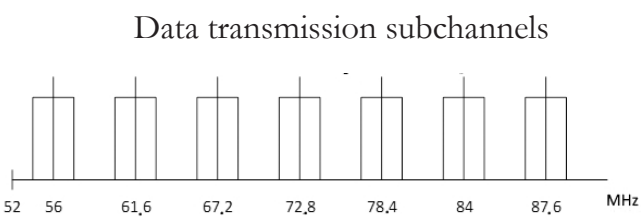

Fig. 3. *Frequency plan of the six-channel complex.*

Accuracy of synchronization of the remote clocks via a satellite radio communication signal also depends on the signal used, its processing methods and signal-to-noise ratio at the ends of the satellite link. This physically understandable commonness made it possible to develop a unified method for analyzing noise immunity and potential synchronization accuracy of ULBI.

Fig. 4 shows a diagram describing how current navigation parameters of the SC are collected and processed.

Onboard RC is placed on the geostationary orbit within visibility area of the ground RC. The reference SS is located in the same area. Flight control center (FCC) receives all information flows from the ground RC with subsequent processing of these information flows. At the same time, FCC generates command and program information for controlling the target and reference SCs, as well as navigation information for the ground and onboard RCs to ensure this control.

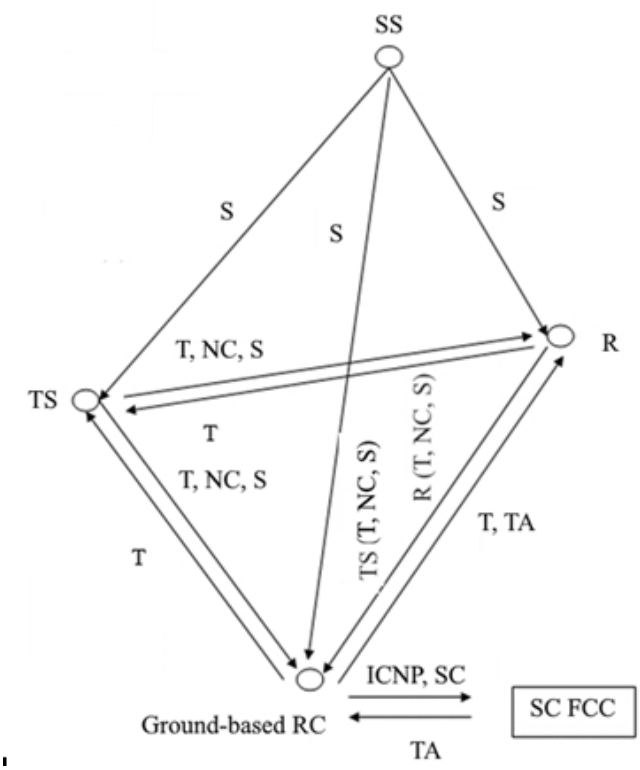

Fig. 4. *Collection and processing of ICNP of SC.*

Given the existing requirements for such systems [13,14], the reliability of information reception is:

— radio astronomy of 10^{-3};

— command-trajectory and telemetry of 10^{-6};

— service communication - 10^{-6}.

where *SS* is space source; *R* is reference spacecraft; *TS* is target spacecraft; *T* is trajectory signal of the onboard *RC; NC* is non-controlled radiation signal from the onboard *RC; S* is space source signal; *TA* is target assignment for *RC* antennas.

Specified reliability is to be ensured when working in sessions throughout 95% of the year.

Information is exchanged via an onboard RC combined with a system of the Luch type of a geostationary SC in the 11/14 GHz band.

Main technical specifications of the Luch system are given in [7,14].

Further calculations were made for an onboard RC equipped with the Luch system.

We decided to use Luch-type SC as a reference SC where onboard RC is placed, with SC being located on the geostationary orbit with location points of 80°E, 90°E, 95°E, which is suitable for the previously selected region where ground-based RC will be located. [7,16]

In this case, the ground-based RC is in the service area with field level of –2 to –3 dB, which makes it possible to thoroughly study these three options for placement of the reference SC.

The next step of the study is to calculate the radiation power flux density of the earlier selected reference SCs at the location of the ground-based ULBI RC, while considering instability of the position of the SC and its antennas. This step is applicable not only to the target SCs, but also to geostationary reference SCs, which not only shift relative to the calculated location point, but also experience oscillatory movements, thus altering the exposure level onto the Earth's surface. This effect is especially strong at the border of the

Table 2

Input data

Parameter	Value
Roll angle, deg.	0.42
Pitch angle, deg.	0.33
Yaw angle, deg.	1.16
Longitude shift angle, deg.	0.3
Latitude shift angle, deg.	1.55
Angle of initial rotation of the antenna, deg.	0
Antenna gain	1000
Antenna pattern opening angle at –3 dB level, deg.	5
Antenna beam shape	sinx/x
Onboard transmitter power, W	15
Losses in antenna and waveguide transmission line during transmission, dB	2

service areas. Input data for the calculation are given in **Table 2.**

To account for this specific effect, calculations were made according to the technique described in [15].

For each given point, the values of the SC power flux density near the Earth's surface were calculated at its normal position in the orbit (W_{nom}), as well as the lowest (W_{min}) and largest (W_{max}) values arising from fluctuations in the position of the SC and onboard antenna within the specified parameters.

Calculations were performed for the "clear sky" conditions (without intense rains), which, as shown by special studies of attenuation statistics on ULBI satellite lines, corresponds to 95% of the time of the year.

Table 3 shows calculation results for the ground-based RC with coordinates 43°11'20" and 33°11'13" (Evpatoria).

To ensure fairness of further research it seems reasonable to choose a reference ULBI SC with average values of the power flux density near the Earth's surface, i.e. with coordinates 90°E (western beam) at standardized aiming point positions of the onboard antennas.

Table 3

Calculation results

Location	Signal levels, dB W/m²		
	W_{min}	W_{nom}	W_{max}
80°	–126.9	–125.8	–125.1
90°	–129.1	–121.6	–126.6
95°	–131.6	–129.7	–128.1

Energy calculation of the radio link of the ULBI trajectory measurement system was carried out for the single-signal operating mode of the onboard RC.

Analysis of the discrepancy between the results of preliminary and final calculations showed that $W_{nom} \approx (1 \pm 2)$ dB, i.e. the calculation accuracy satisfies the existing requirements for similar systems [7]. In this case, the last calculation should be considered more reliable (see Table 2), however, it is necessary to take into account from Table 3 the magnitude of the decrease in W_{nom} down to W_{min} (resulting from antenna holding and aiming errors at the center of the service area) and adjust the final results accordingly in order to perform the worst-case calculations in the future.

Optimization of the service areas of the reference SC is of particular importance for the ULBI trajectory system. The calculations performed showed that at the currently accepted aiming points of the antennas of the onboard RC Luch, the requirements for service areas of the ULBI trajectory system are fulfilled only by the western beam of the reference SC located at 90°E.

However, even this aiming point is not optimal for passing target SCs, therefore, in the proposed system we find it suitable to provide for the possibility of using another reference SC.

3. CONCLUSIONS

Analysis of the obtained results leads to two important conclusions:

1. Selection of any of the above aiming points for all SCs makes it possible to have only one reference SC suitable for the ULBI trajectory system.

2. It is impossible to find such a single aiming point, at which at least two reference SCs could

be used simultaneously for the needs of the system.

Thus, to make it possible for the ULBI trajectory system to use 2 or 3 SCs for operation, it is necessary to make arrangements to ensure that position of the onboard RC antennas can be adjusted by a command from the ground-based RC. At the same time, optimization of the aiming points of reference SCs makes it possible to double the number of target SCs suitable for use in the ULBI trajectory system.

However as noted earlier, to ensure operation of such system it is necessary to achieve the required accuracy of synchronization of time scales in the ground-space radio interferometer.

REFERENCES

1. Polyakov AL, Rachinsky AP, Lomonosov SE, Morgun AA. Analysis of possibilities of increasing the efficiency of space situation monitoring and analysis system for navigational support of spacecraft control. *Navigation, Control and Communication Systems,* 2007, 1:7-11. Kyiv, Central Research Institute for Navigation and Control.
2. Kozelkov SV. Application of planetary radar for spacecraft navigation tasks. *Information Processing Systems: Collection of Scientific Works,* 1999, 1(5):139-142. Kharkov, National Academy of Sciences, PANM, Kharkov University of Science and Technology.
3. Kozelkov SV, Bogdanovsky AN, Pashkov DP, Polyakov AL. Method of planning the observation of space objects by optical-electronic means. *Navigation, Control and Communication Systems*, 2007, 2:3-6. Kyiv, CNDI of Navigation and Control.
4. Gusev LI, Molotov EP. Ground-based network for tracking deep-space satellites and high-apogee artificial satellites. *Cosmic Bulletin*, 1995, 2(1):11-13.
5. Vinitsky AS (ed.). *Radio systems of interplanetary spacecraft.* Moscow, Radio i Svyaz' Publ., 1993, 328 p.
6. Polyakov AL, Afonin IL, Tyshchuk YN, Polyakov DA. Method of identification of spacecraft. *Journal of Radioelectronics* [*electronic journal*]. 2020, №5. Access mode: http://jre.cplire.ru/jre/may20/10/text.pdf. DOI: 10.30898/1684-1719.2020.5.10 (access date 10.12.2022).
7. Kaidanovskii NM. Construction of satellite data transmission systems for radio interferometers with ultra-long bases: *Thesis Doctor of Engineering Sciences,* Saint Petersburg, Institute of Applied Astronomy RAS Publ.,1998, 281 p.
8. Koyama Y. Automated Remote Operation System for the Key Stone Project VLBJ Network. *Tactical Warning and Attack Assessment'96*. Kashima, Japan, 1996, pp. 139-143.
9. Abolitz AK. Energy relations in frequency division transmission through a nonlinear repeater. *Elektrosvyaz'*, 1967. 3:19-23 (in Russ.).
10. Okunev YB. *Theory of Phase-Difference Modulation.* Moscow, Svyaz' Publ., 1979, 216 p.
11. Kazarinov YuM (ed.). *Radiotekhnicheskie sistemy* [Radio technical systems]. Moscow, Vysshaya shkola Publ., 1990, 496 p.
12. Kantor LYa (ed.). *Spravochnik po sputnikovoy svyazi i veshchaniyu* [Handbook on Satellite Communications and Broadcasting]. Moscow, Radio i svyaz' Publ., 1986, 287 p.
13. Silvestrov SD, Lazarev VM, Kornienko AI, Panshin MI. T*ochnost' izmereniya parametrov dvizheniya kosmicheskikh apparatov radiotekhnicheskimi metodami* [Accuracy of Spacecraft Motion Parameters Measurements by Radio Engineering Methods]. Moscow, Sovetskoe Radio Publ., 1990, 320 p.
14. Livshits II, Rozhkov VM, Ryabov BA. Ispol'zovanie ISZ dlya svyazi v diapazone

millimetrovykh voln [Using ISZ for Communications in the Millimeter Wave Range]. *Zarubezhnaya radioelektronika*, 1987, 5:41-49 (in Russ.).

15. Mashbitz LM. *Zony obsluzhivaniya sistem sputnikovoy svyazi* [Zones of Satellite Communications Systems]. Moscow: Radio i svyaz' Publ., 1982. 152 p.
16. Makshanov AV, Musaev AA, Stepanyuk OM. Metody statisticheskoy regulyarizatsii v zadachakh navigatsionnogo opredeleniya orbit KA [Methods of statistical regularization in tasks of navigational determination of SC orbits]. *Kosmicheskie issledovaniya*, 1984, 22(3):468-471 (in Russ.).

DOI: 10.17725/rensit.2023.15.377

Design of Slot Antenna based on Ansoft HFSS Software

Mohanad Abdulhamid
AL-Hikma University, https://hiuc.edu.iq/
P.O. Box 20468-11345, Baghdad, Iraq
E-mail: moh1hamid@yahoo.com

Received Juli 15, 2023, peer-reviewed Juli 22, 2023, accepted Juli 29, 2023, published December 06, 2023.

Abstract: **A micro-strip fed slot antenna array for application in the 2.4 GHz industrial, scientific and medical (ISM) band is implemented using the Ansoft HFSS software. Standard formulas are used to calculate different antenna parameters. The proposed antenna is designed to work at 2.4 GHz frequency band. A half power beam width (HPBW) of 57°. A bandwidth of around 7.7% is attained. This may have been brought about by poor impedance matching and a high level of surface waves. A way of improving the bandwidth would have been to use proximity coupling feeding method which offers the highest bandwidth and is somewhat easy to model and has low spurious radiation. However, its fabrication would have been more difficult. A directivity of 2.01 dB is achieved. This is a fairly high though directivity increase could have been studied through use of different substrate material and thickness. Adjusting length and width of narrow slot loop antenna will influence on the resonance frequency and bandwidth. By using HFSS software, the characteristics of antenna are investigated and analyzed, including voltage standing wave ratio(VSWR), return loss and far field radiation patterns.**

Keywords: **MIMO, spatial multiplexing, algebraic codes, precoding, Golden code, maximum likelihood, ML, MMSE**

UDC 621.396.67

For citation: Mohanad Abdulhamid. Design of Slot Antenna based on Ansoft HFSS Software. *RENSIT: Radioelectronics. Nanosystems. Information Technologies,* 2023, 15(3):377-384e. DOI: 10.17725/rensit.2023.15.377.

Contents

1. INTRODUCTION

An antenna is generally a bidirectional device, that is, the power through the antenna can flow in both directions, coupling electromagnetic energy from the transmitter to free space and from free space to the receiver, and hence it works as a transmitting as well as a receiving device, that is, by reciprocity. Transmission lines are used to transfer electromagnetic energy from one point to another within a circuit and this mode of energy transfer is generally known as guided wave propagation. An antenna can be thought of as a mode transformer which transforms a guided-wave field distribution into a radiated-wave field distribution.

A slot antenna consists of a metal surface, usually a flat plate, with a hole or slot cut out. When the plate is driven as an antenna by a driving frequency, the slot radiates electromagnetic waves in a way similar to a dipole antenna. The shape and size of the slot, as well as the driving frequency, determine the radiation distribution pattern. A slot antenna's main advantages are its size, design simplicity, robustness, mechanically robust when mounted on rigid surfaces, compatible with monolithic microwave integrated circuit (MMIC) designs and convenient adaptation to mass production using PC board technology. Unique features of these antennas are horizontal polarization and omnidirectional gain around the azimuth. Slot antennas exhibit wider bandwidth which is approximately 10-20%, lower dispersion and lower radiation loss compared to micro-strip antennas. The slot antennas can be fed by micro-strip line, slot line or Coplanar Waveguide (CPW). In this paper, the design of slot antenna is fed by micro-strip line.

In a conventional micro-strip line-fed slot antenna, a narrow rectangular slot is cut in the ground plane and the slot is excited by a micro-strip feed line with a short or an open termination. With this feed configuration, a good impedance match has been achieved with a narrow slot, and a bandwidth of approximately 7.7% has been obtained. However, as the width of the slot increases, the radiation resistance of the slot antenna also increases proportionately. This, in turn, reduces the impedance bandwidth of the antenna, even though the size of the slot is larger. There is a possibility of increasing the bandwidth of a wide slot antenna by terminating the open end of the feed line within the width of the slot, although substantial bandwidth improvement has not been achieved. The conventional feeding structures of conventional transverse slot antennas are center feeding and offset feeding. The center feed has a larger value of radiation impedance than an offset feed. It means that the bandwidth of a center feed antenna is less than for an offset

fed antenna. Some works discuss the design of slot antenna can be found in [1-6].

2. DESIGN METHODOLOGY

A rectangular slot is chosen as the basis of the design because of its ease of fabrication and analysis. The micro-strip line is used as the feeding method as it is easy to fabricate, simple to match by controlling the inset feed position and rather simple to model. The antenna is designed to work in the 2.4 GHz ISM band which has a frequency range of 2.5-2.6 GHz, a center frequency of 2.58 GHz, and a bandwidth of 100 MHz.

2.1. Design Procedure

The Flame Retardant (FR4) Glass Epoxy, whose loss tangent is 0.002, is chosen as the dielectric material substrate.

To commence the design procedure assumes, specific information had to be included: dielectric constant of the substrate ε_r, the resonant frequency f_r and the height of the substrate, h.

$\varepsilon_r = 4.3$, $f_r = 2.4$ GHz, $h = 1.6$ mm.

For an efficient radiator, the practical width that leads to good radiation efficiencies is

$$W = 0.1\ \lambda_g = 7 \text{ mm}, \quad (1)$$

where λ_g is the dielectric wavelength.

The initial values (at low frequencies) of the effective dielectric constant are referred to as the static values, and they are calculated as

$W / h > 2$,

$$\varepsilon_{reff} = \frac{\varepsilon_r + 1}{2} + \frac{\varepsilon_r - 1}{2}\left[1 + 12\frac{h}{W}\right]^{-\frac{1}{2}} = 3.27. \quad (2)$$

The actual length of the slot is determined by solving L as,

$$L = 0.5\ \lambda_g = 35 \text{ mm}. \quad (3)$$

For efficient transfer of power from a transmission line to the slot antenna, the input impedance of the slot antenna needed to be matched to the characteristic impedance of the transmission line. It is observed that impedance seen by a transmission line attached to the radiating edge increased as one moved towards the center of the slot. Therefore, depending on the characteristic impedance of the transmission line, an appropriate point on the slot is chosen through calculation as the feed point. An off-the center feed is used with distance from the edge calculated as:

$$0.05\ \lambda_g = 3.5 \text{ mm}. \quad (4)$$

2.2. Ground Plane

As part of the antenna, the ground plane should be infinite in size as for slot antenna but in reality this is not easy to apply besides a small size of ground plane is desired. In practice, it has been found that the micro-strip impedance with finite ground plane width is practically equal to the impedance value with infinite width ground plane, if the ground width > $3W$. The size of the ground plane is chosen as 100 mm length by 97.5 mm width.

2.3. Microstrip Discontinuities

Surface waves are electromagnetic waves that propagate on the dielectric interface layer of the microstrip. The propagation modes of surface waves are practically transverse electric (TE) and transverse magnetic (TM). Surface waves are generally at any discontinuity of the microstrip. Once generated, they travel and radiate, coupling with other microstrip of the circuit, decreasing

isolation between different networks and signal attenuation. Surface waves are a cause of crosstalk, coupling, and attenuation in a multi-microstrip circuit. For this reason surface waves are always an undesired phenomenon.

A discontinuity in a microstrip is caused by an abrupt change in geometry of the strip conductor, and electric and magnetic field distributions are modified near the discontinuity. The altered electric field distribution gives rise to a change in capacitance, and the changed magnetic field distribution to a change in inductance.

2.4. Micro-strip feed and distance between elements

For the 2-element array of **Fig. 1** to implement an even number of in-phase slot elements, the feed network needed to be carefully designed. The distance from the 50-ohm Sub-Miniature version A (SMA) source to each slot element needed to be identical or multiples of λ. Unequal line lengths would have produced phase shifts, which would yield fixed beams that would be scanned away from the broadside. The 50-ohm micro-strip line is fed using a 50-ohm SMA. In the design of an effective in-phase radiator, the distance between the slot elements needed to be optimized to yield a peak gain. A separation distance of $\lambda/2$ as providing the optimal gain. In the design, this separation is used as 35 mm.

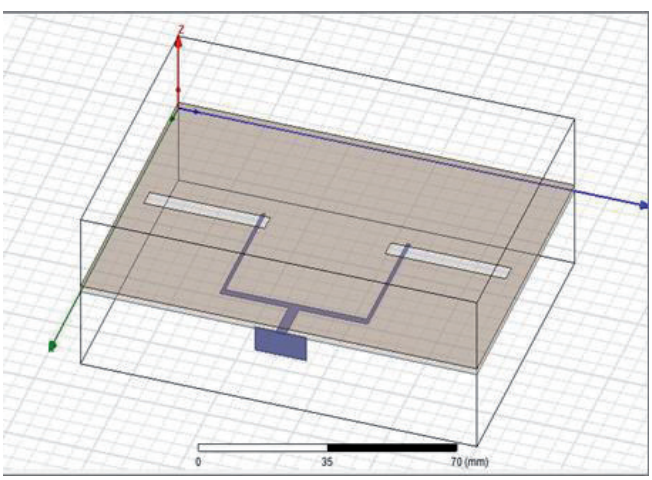

Fig. 1. *2-element slot antenna HFSS model.*

2.5. Matching Microstrip Lines to Source

The characteristic impedance of a transmission line of the micro-strip feed was designed with respect to the source impedance. The characteristic impedance of the transmission line from the source with respect to the source impedance was

$$Z_0 = Z_s,\ Z_0 = 50 \text{ ohms}. \tag{5}$$

2.6. Quarter-Wave Transformer

For the input impedance of a transmission line of length L with a characteristic impedance Z_0 and connected to a load with impedance Z_A:

$$Z_{in}(-L) = Z_o\left[\frac{Z_A + jZ_o\tan(\beta L)}{Z_o + jZ_A\tan(\beta L)}\right], \tag{6}$$

When the length of the transformer is a quarter wavelength

$$Z_{in}\left(L = \frac{\lambda}{4}\right) = \frac{Z_o^2}{Z_A}. \tag{7}$$

Hence by using a transmission line with a characteristic impedance of 50-ohms, the 50 ohm inset feed line is matched to

$$Z_0 = \sqrt{50 \cdot 50} = 50 \ ohms,$$

where Z_0 = characteristic impedance of the quarter-wavelength transformer.

This ensured that no power would be reflected back to the SMA feed point as it tried to deliver power to the antenna.

The length of the quarter wavelength transformer is calculated as

$$L = \lambda_g/4 = 17.5 \text{ mm}. \quad (8)$$

2.7. Simulation

The antenna array is designed using the Ansoft HFSS 13.0 software. HFSS is a 3*D* full wave electromagnetic field simulator. HFSS uses a numerical technique called the Finite Element Method (FEM). This is a procedure where a structure is subdivided into many smaller subsections called finite elements. The finite elements used by HFSS are tetrahedra, and the entire collection of tetrahedra is called a mesh. A solution is found for the fields within the finite elements, and these fields are interrelated so that Maxwell's equations are satisfied across inter-element boundaries yielding a field solution for the entire, original, structure. Once the field solution has been found, the generalized S-matrix solution is determined. It can calculate and plot both the near and far field radiation and compute important antenna parameters such as gain and radiation efficiency. This software is used to vary the sizes of the slot. Fig. 1 illustrates the 2-element slot antenna HFSS model.

3. HFSS SIMULATION RESULTS AND ANALYSIS

3.1. VSWR Plot

Fig. 2 shows the VSWR plot for the designed antenna. The value of the VSWR should lie between 1 and 2. VSWR is used as an efficiency measure for transmission lines, electrical cables that conduct radio frequency signals, used for purposes such as connecting radio transmitters and receivers with their antennas.

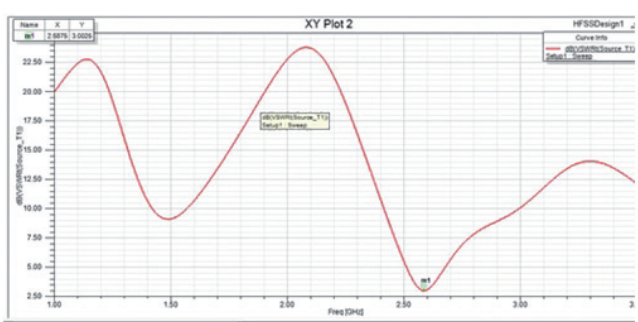

Fig. 2. *VSWR Plot.*

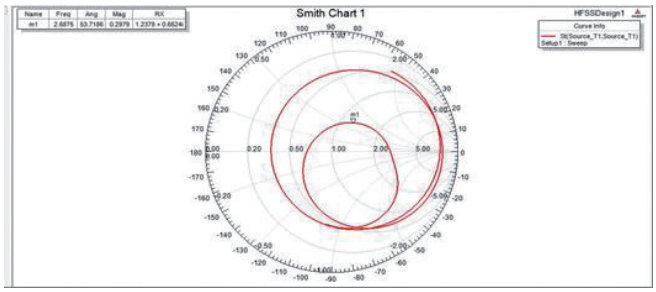

Fig. 3. *Smith Chart for the slot antenna array.*

3.2. Smith Chart

The smith chart is a graphical representation of the normalized characteristic impedance. It provides the information about the impedance match of the radiating slot. The smith chart for the designed slot antenna array shown in **Fig. 3**, shows an input impedance of 50.78 + 10.5*i* ohms at resonant frequency 2.58 GHz. The magnitude of the input impedance is 51.85 which showed that accurate matching is not achieved. This is due to shifting of the inset feed position away from the edge of the ground plane.

3.3. Reflection coefficient and bandwidth

Fig. 4 shows the reflection coefficient [S11] of the proposed antenna in dB. S11 gives the reflection coefficient at the inset feed position where the input to the micro-strip slot antenna is applied. It should be less than –10 dB for an acceptable operation. It shows that the

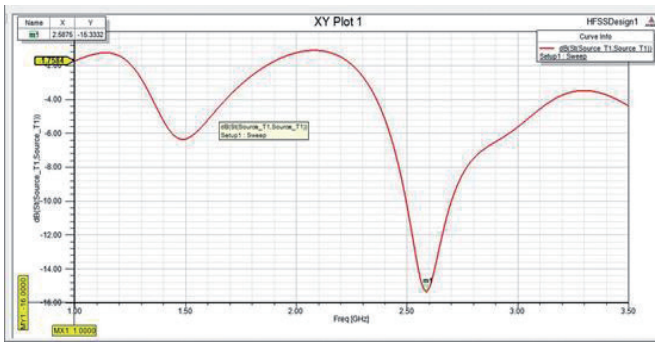

Fig. 4. *Return loss S11 obtained for the slot antenna array.*

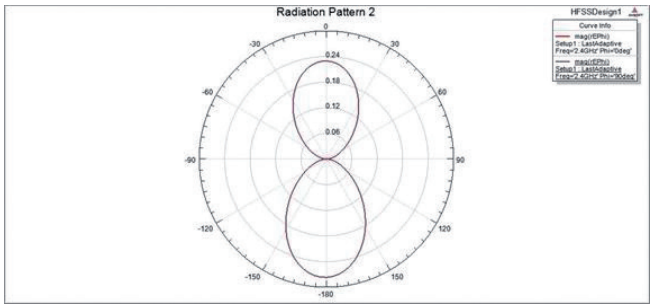

Fig. 5. *Radiation pattern of E-total at 2.58 GHz xz plane (Φ = 0°).*

proposed antenna had a frequency of resonance of 2.58 GHz.

The simulated impedance bandwidth of about 200 MHz (2.5022-2.7023 GHz) is achieved at −10 dB reflection coefficient (VSWR ≤ 2). The reflection coefficient value that is achieved at this resonant frequency was equal to –15.33 dB. This reflection coefficient value suggested that there is good matching at the frequency point below the –10 dB region.

3.4. Variation of slot length and width

Dimensions calculated in the design procedure are used to create a 2-element slot antenna array. In order to shift the S11 minima towards the desired center frequency, the length and width of the slot are varied.

At designed frequency of 2.58 GHz, the width of slot antenna is varied in five values beginning from 5.0 mm to 7.0 mm by step up 0.5 mm, and length is adjusted for match impedance. The simulation results of return loss S11, resonance frequency and bandwidth are tabulated in **Table 1**. It shows that the changing in width of slot antenna will affect the resonance frequency. When the width of slot is increased, the resonance frequency will decrease and bandwidth is wider. Therefore, if we increase the width of slot, the length of slot should be decreased in order to achieve the same resonance frequency and wider bandwidth.

Table 1
Simulation results of slot antenna by adjusting width

Width, mm	Resonance frequency, GHz	Return loss S11, dB	Bandwidth, MHz
5.0	2.71	-10.5	165
5.5	2.68	-14.9	173
6.0	2.64	-25.5	188
6.5	2.62	-18.74	195
7.0	2.58	-15.33	200

3.5. Radiation Pattern

The radiation patterns in the E-plane, Φ = 0° and Φ = 90° are shown in **Fig. 5** and **Fig. 6**, respectively.

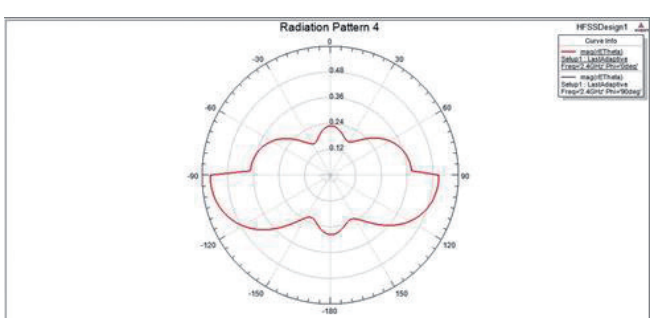

Fig. 6 *Radiation pattern of E-total at 2.58 GHz yz plane (Φ = 90°).*

Table 2

Summary of antenna parameters

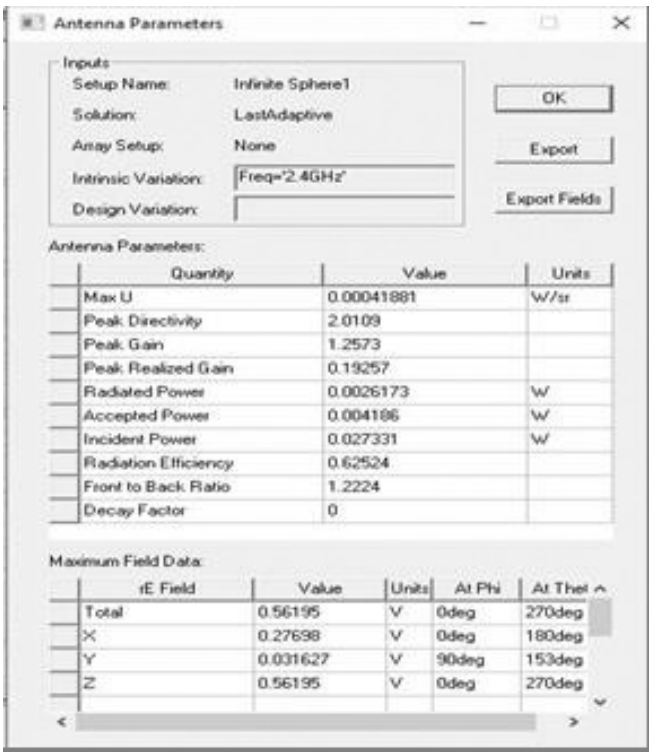

3.6. Other antenna parameters

Table 2 shows a summary of the antenna parameters from the HFSS software. The directivity and efficiency are 2.0109 and 62.5%, which gave a gain of the antenna as 1.25. The front to back ratio is 1.2224.

The **Fig. 7** shows E-plane and H-plane from which the antenna has two main lobes which were 180° out of phase with each other. It is used to determine the half-power beam widths for the radiation patterns as the peaks and 3 dB points below them could easily be picked.

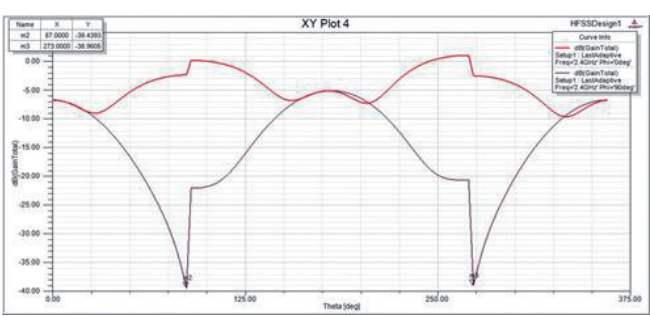

Fig. 7. *E-Plane and H-Plane patterns in rectangular coordinates.*

4. CONCLUSION

A modified slot antenna fed by a 50 Ω micro-strip line was presented in the paper. In addition, the size of the implemented antenna array can be increased. Moreover, the two rectangular slots are embedded on the ground plan to increase antenna gain. With optimized antenna geometry, the implemented antenna offers a bandwidth of 7.7%. By properly calculating slot dimensions and tuning the dimension parameters with simulation software, improvements can be made on the gain, bandwidth and radiation pattern. The implemented antenna is feasible for use as a low profile, low cost antenna for wireless applications in the ISM band.

REFERENCES

1. Ochieng E. *A 2.4 GHz slot antenna array*. Graduation Project, University of Nairobi, Kenya, 2016.
2. Kim J, Ahn C. Small dual-band slot antenna using capacitor loading. *Microwave and Optical Technology Letter*, 2017, 59(9):2126-2131.
3. Kulkarni S, Kasabegoudar V. Bandwidth enhancement of compact circular slot antenna for UWB applications. *Global Journal of Researches in Engineering* (F), 2017, 17(1), Version 1.0.
4. Parvathy A, Thomaskutty M. A printed tree fractal based cross slot antenna for 2.45 GHz. *Procedia Computer Science*, 2017, 115:80-86.

5. Kuma S, Shanmuganantham T. Design of clover slot antenna for biomedical applications. *Alexandria Engineering Journal,* 2017, 56(3):313-317.
6. Fernandez M, Espinosa H, Thiel D, Arrinda A. Wearable slot antenna at 2.45 GHz for off-body radiation: Analysis of efficiency, frequency shift, and body absorption. *Bioelectromagnetics*, 2018, 39(1):25-34.

DOI: 10.17725/rensit.2023.15.385

Spintronics of non-magnetic chiral media on the example of the Seebeck effect

Vyacheslav K. Ignatjev, Sergey V. Perchenko, Dmitry A. Stankevich

Volgograd State University, https://volsu.ru/

Volgograd 400062, Russian Federation

E-mail: vkignatjev@yandex.ru, perchenko@volsu.ru, dimon50002004@yandex.ru

Received July 12, 2023, peer-reviewed July 16, 2023, accepted July 19, 2023, published December 06, 2023.

Abstract: **Spin transport in chiral materials is considered as the main direction for the spintronics development. Experimental work on the study of the spin Seebeck effect shows that in chiral materials it is possible to achieve effective generation of spin-polarized current at distances up to several millimeters. In the presented work, we develop a theoretical approach to describe the spin Seebeck effect based on the spin Hamiltonian for conduction electrons in a chiral medium. Taking into account this Hamiltonian, the equation of electron spin dynamics averaged over the polycrystalline sample is obtained. In the approximation of ideal Fermi-gas and local-quasi-equilibrium distribution, the spin density operator of conduction electrons is constructed. It is shown that averaging over randomly oriented crystallites does not destroy spin ordering at strong spin-orbit interaction, and the temperature gradient generates spin polarization directed predominantly along the temperature gradient. Spin polarization by the described in the paper mechanism does not require external magnetic fields and remanent magnetization and therefore does not interfere with the operation of micro- and nano-sized structures of spintronics. Since the spin Seebeck effect is reciprocal with the spin Peltier effect, the theoretical approach presented in this work can form the basis of new methods for controlling heat flow in spintronics systems.**

Keywords: **spintronics, spin Seebeck effect, spin-orbit interaction, chiral crystal, polycrystalline conductor**

PACS: 67.57.Lm, 72.25.Ba, 75.76.+j

Acknowledgments: The research was carried out of the funds of the Russian Science Foundation grant № 22-22-20035 (https://rscf.ru/en/project/22-22-20035/), as well as the funds of the Volgograd region budget resources.

For citation: Vyacheslav K. Ignatjev, Sergey V. Perchenko, Dmitry A. Stankevich. Spintronics of non-magnetic chiral media on the example of the Seebeck effect. *RENSIT: Radioelectronics. Nanosystems. Information Technologies,* 2023, 15(4):385-392e. DOI: 10.17725/rensit.2023.15.385.

Contents

1. INTRODUCTION

The most important branch of modern spintronics is the generation of spin fluxes in conductors and semiconductors in order to use them in various kinds of microelectronics devices [1]. Conventional methods based on spin-dependent scattering in materials

with strong spin-orbit interaction, such as platinum, provide a ratio of spin-polarized current of less than a percent with coherence lengths on the order of tens of nanometers. This is sufficient for research on spin effects in nanostructures, but not for information and biotechnology. It was shown in [2] that under conditions of inhomogeneous torsion in the steady-state case, the average spin of conduction electrons is oriented predominantly along the charge current density vector. The maximum value of the spin-orbit interaction is observed when the torsion axis is orthogonal to the current density vector and full spin polarization can be achieved. However, this method is energy-consuming. The efficiency of spin polarization drops rapidly with increasing frequency of control actions. This fact also limits the application of controlling spin polarization dynamics by electrical and mechanical actions in modern nanoelectronics.

At the initial stage of spintronics, the spin Seebeck effect (SSE) was considered as a way to efficiently generate spin-polarized current at distances of up to a few millimeters [3]. This effect, consisting in the temperature-gradient-induced generation of spin current, was originally discovered in conducting ferromagnetic metals [4]. The authors explained this effect by magnon and phonon degrees of freedom [5]. Subsequently, the spin Seebeck effect was found in non-magnetic materials [6-8]. The theoretical model of SSE in paramagnetic dielectric material was experimentally confirmed [9]. The microscopic theory of temperature-gradient-driven spin transport in ferromagnets has shown that a temperature gradient is equivalent to an electric field for spin current generation [10]. Similar conclusions are drawn in [11].

It should be noted that the experimentally investigated SSE is essentially a magneto-thermal-galvanic effect. It is seen in paramagnetic materials in an external magnetic field or in magnetized ferromagnets. The vector of magnetic induction or residual magnetization sets the specific direction in an isotropic matter. In this case, controlling spin polarization by magnetic influence is even slower and more energy consuming than the electrical and mechanical control proposed in [2], where the selected direction sets the torsion vector. A general model of the spin Seebeck effect in non-magnetic materials is currently lacking.

New possibilities for efficient generation of spin currents in spintronics devices are opened by the experimentally detected activation of SSE in nonmagnetic materials by the flow of chiral phonons [8]. According to the authors, chiral phonons possessing angular momentum break the symmetry of the material and create the possibility of spin current generation in the presence of a temperature gradient. Such symmetry breaking exists without external influences in enantiopure chiral crystals such as WSe_2. Currently, the application of chiral media is considered as the main direction for the development of spintronics [12]. To effectively control large spin current densities the control element must be bulk, rather than thin-film. Therefore, the model of SSE in non-magnetic polycrystalline structures is of interest.

2. MODEL BUILDING

Let us consider the thermally induced polarization of the conduction electron spin in a homogeneous and isotropic polycrystalline metal. The interaction of the collective electron with the crystal field is chosen in the form of a spin-orbit interaction with lattice ions, that is, relativ-istic corrections in the second order in magnitude $1/c$, where c is the speed of light.

The spin-orbit addition to the electron energy in the field of a crystallite containing N identical ions with effective charge $+Ze$ and coordinates $\mathbf{r}_l$ has the form [13]

$$\hat{V} = \frac{\hbar e}{2m^2c^2}\left[\mathbf{E}\times\hat{\mathbf{p}}\right]\hat{\mathbf{s}}, \quad \mathbf{E}(\mathbf{r}) = -\frac{eZ}{4\pi\varepsilon_0}\sum_{l=1}^{N}\frac{\mathbf{r}-\mathbf{r}_l}{\left|\mathbf{r}-\mathbf{r}_l\right|^3}. \qquad (1)$$

Here, m is the mass of an electron with charge $-e$, $\hbar$ is the Dirac constant (reduced Planck constant), ε_0 is the electric constant. The value of the effective charge Z can be estimated by equating the coordinate of the maximum of the hydrogen-like radial wave function to the covalent radius of the atom. For example, for platinum the atomic radius is $1.39\cdot10^{-10}$ m, which for a 6s shell corresponds to $Z \approx 22.45$.

Let us construct the spin Hamiltonian of the perturbation (1) for the conduction electron by averaging it over the coordinates [14]. The wave function of the conduction electron with wave vector $\mathbf{k}$ is expressed as a Wannier function [15]

$$\psi_{\mathbf{k}}(\mathbf{r}) = \frac{1}{\sqrt{N}}\sum_{n=1}^{N}\Psi(\mathbf{r}-\mathbf{R}_n)\exp(i\mathbf{k}\mathbf{R}_n),$$

Here, $\Psi(\mathbf{r})$ is the atomic function of the electron, $\mathbf{R}_n$ is the translation vector. Replacing the variables $\mathbf{r}-\mathbf{r}_l \to \mathbf{r}$ we obtain

$$\hat{V}_{\mathbf{k}} = -\frac{\hbar^2e^2Z\hat{\mathbf{s}}_{\mathbf{k}}}{8\pi\varepsilon_0m^2c^2N}\sum_{n,m,l=1}^{N}\exp\left(i\mathbf{k}\left(\mathbf{R}_n-\mathbf{R}_m\right)\right)\times$$

$$\times\left\langle\Psi\left(\mathbf{r}+\mathbf{r}_l-\mathbf{R}_m\right)\left|\frac{\hat{\mathbf{l}}}{r^3}\right|\Psi\left(\mathbf{r}+\mathbf{r}_l-\mathbf{R}_n\right)\right\rangle.$$

In the nearest neighbor approximation we retain in the right-hand side only the summands for which $\mathbf{R}_n-\mathbf{r}_l=\mathbf{R}_m-\mathbf{r}_l=0$, or $\mathbf{R}_n-\mathbf{r}_l=\mathbf{a}_\nu$ and $\mathbf{R}_m-\mathbf{r}_l=0$, or $\mathbf{R}_n-\mathbf{r}_l=0$ and $\mathbf{R}_m-\mathbf{r}_l=\mathbf{a}_\nu$, where $\mathbf{a}_\nu$ is the vector drawn to the nearest neighbor node. In the first order of smallness in $\mathbf{k}\mathbf{a}_\nu$ we obtain

$$\hat{V}_{\mathbf{k}} = \hat{\mathbf{s}}_{\mathbf{k}}(\mathbf{I}_0+\mathbf{I}_1+\mathbf{I}_{\mathbf{k}}), \quad \mathbf{I}_0 = -\frac{\hbar^2e^2Z}{8\pi\varepsilon_0m^2c^2}\left\langle\Psi\left|\frac{\hat{\mathbf{l}}}{r^3}\right|\Psi\right\rangle,$$

$$\Psi_\nu(\mathbf{r}) = \Psi(\mathbf{r}+\mathbf{a}_\nu), \ \mathbf{I}_1 = -\frac{\hbar^2e^2Z}{4\pi\varepsilon_0m^2c^2}\mathrm{Re}\sum_\nu\left\langle\Psi_\nu\left|\frac{\hat{\mathbf{l}}}{r^3}\right|\Psi\right\rangle, \ (2)$$

$$\mathbf{I}_{\mathbf{k}} = -\frac{\hbar^2e^2Z}{4\pi\varepsilon_0m^2c^2}\mathrm{Im}\sum_\nu(\mathbf{k}\mathbf{a}_\nu)\left\langle\Psi_\nu\left|\frac{\hat{\mathbf{l}}}{r^3}\right|\Psi\right\rangle.$$

For s-electrons the vectors $\mathbf{I}_0$, $\mathbf{I}_1$, $\mathbf{I}_{\mathbf{k}}$ are zero. The conduction bands overlap in metals and part of the conduction electrons can be formed by collectivization of p-electrons.

Let us consider the macroscopic area of a polycrystalline metal. For any state of the electron one can choose the direction of the quantization axis (z-axis) so that the projection of its orbital momentum on this axis has a certain value $l_z = l$. The electron energy in an atom under an electric field depends on the projection of its orbital momentum on the direction of the field [14]. Therefore, the orientation of atomic orbitals is determined by the orientation of the crystallo-physical axes of the crystallite, and we can consider that the vectors $\mathbf{I}_0$ and $\mathbf{I}_1$, in relations (2) are written in the coordinate system associated with the symmetry axes of the crystallite.

Let us introduce the laboratory coordinate system associated with the instruments that set the conduction current and measure the spin components. Therefore, the wave vector and spin vector of the conduction electrons should be considered as specified in the laboratory coordinate system. The components of vectors and tensors in the laboratory system will be denoted by non-primed indices, but in the coordinate system, associated with the crystal axes, by primed these.

The vectors $\mathbf{I}_0$ and $\mathbf{I}_1$ are converted to the laboratory coordinate system as follows $I_\alpha = p_{\alpha\alpha'}\cdot I_{\alpha'}$, where $p_{\alpha\alpha'}$ is the unitary rotation matrix. It is convenient to express the rotation matrix through Euler angles:

$$p_{ij} = \begin{bmatrix} \cos(\alpha)\cos(\gamma)-\sin(\alpha)\cos(\beta)\sin(\gamma) & -\cos(\alpha)\sin(\gamma)-\sin(\alpha)\cos(\beta)\cos(\gamma) & \sin(\alpha)\sin(\beta) \\ \sin(\alpha)\cos(\gamma)+\cos(\alpha)\cos(\beta)\sin(\gamma) & -\sin(\alpha)\sin(\gamma)+\cos(\alpha)\cos(\beta)\cos(\gamma) & -\cos(\alpha)\sin(\beta) \\ \sin(\beta)\sin(\gamma) & \sin(\beta)\cos(\gamma) & \cos(\beta) \end{bmatrix},$$

Here, $0 \le \alpha \le 2\pi$ is the precession angle, $0 \le \beta \le \pi$ is the nutation angle, $0 \le \gamma \le 2\pi$ is the angle of proper rotation. Then for a macroscopically isotropic conductor averaging over random crystallite orientations leads to averaging over random uniformly distributed Euler angles.

Let us average the vectors $\mathbf{I}_0$ and $\mathbf{I}_1$ over random crystallite orientations. In an isotropic polycrystal $\langle \mathbf{I}_0 \rangle = \langle \mathbf{I}_1 \rangle = 0$. For a symmetric crystal in which each nearest neighbor with vector $\mathbf{a}_\nu$ corresponds to a neighbor with vector $\mathbf{a}_{-\nu} = -\mathbf{a}_\nu$, the last relation of formula (2) takes the form

$$\mathbf{I}_\mathbf{k} = -\frac{\hbar^2 e^2 Z}{4\pi\varepsilon_0 m^2 c^2} \mathrm{Im} \sum_{\nu>0} (\mathbf{k}\mathbf{a}_\nu) \langle \Psi_\nu - \Psi_{-\nu} | \frac{\hat{\mathbf{l}}}{r^3} | \Psi \rangle. \quad (3)$$

In a symmetric crystal, the function $\Psi_\nu - \Psi_{-\nu}$ has parity opposite to the parity of the function Ψ. Therefore, all summands in (6) for the undeformed crystal are zero.

At distortion $r'_\alpha = r_\alpha + u_\alpha(\mathbf{r})$ we obtain in (3) $\Psi(\mathbf{r}') = \Psi(\mathbf{r}) + r_\beta \frac{\partial \Psi}{\partial r_\alpha} \frac{\partial u_\alpha}{\partial r_\beta}$, $\hat{l}'_\alpha = \hat{l}_\alpha - i\varepsilon_{\alpha\beta\gamma}\left(u_\beta \frac{\partial}{\partial r_\gamma} - r_\beta \frac{\partial u_\delta}{\partial r} \frac{\partial}{\partial r_\delta} \right)$. Here, $\varepsilon_{\alpha\beta\gamma}$ is the Levi-Civita tensor. For inhomogeneous torsional strain along the $\mathbf{n}$ axis of the form $\mathbf{\Omega}(\mathbf{r}) = \mathbf{n}(\mathbf{rn})\omega$, we obtain

$$I_{\mathbf{k}\alpha} = -\frac{\hbar^2 e^2 Z\omega}{4\pi\varepsilon_0 m^2 c^2} \varepsilon_{\alpha\beta\gamma} n_\beta n_\delta k_\sigma a_{\nu\sigma} \times \\ \times \mathrm{Im} \langle \Psi_\nu - \Psi_{-\nu} | \frac{r_\gamma \hat{l}_\delta}{r^3} | \Psi \rangle, \quad (4)$$

Here, the summation over ν by nearest neighbor pairs is implied.

3. SPINTRONICS OF CHIRAL MEDIA

The product of the value ω by the distance $\mathbf{a}_\nu$ to the nearest neighbor in the direction of the torsion axis $\mathbf{n}$ characterizes the torsion of the unit cell, i.e., the rotation angle of its crystallographic planes relative to its neighbors. Such torsion exists in chiral crystals such as WSe_2 and layered hybrid perovskites [10]. Therefore, in can be considered that vector $\mathbf{n}$, as well as vectors $\mathbf{a}_\nu$ are set in the system of crystallophysical axes, and vector $\mathbf{k}$ – in the laboratory system. Then formula (4) can be written in the form

$$\langle I_{\mathbf{k}\alpha} \rangle = -\frac{\hbar^2 e^2 Z\omega}{4\pi\varepsilon_0 m^2 c^2} \langle p_{\alpha\alpha'} p^{-1}_{\sigma'\sigma} \rangle \varepsilon_{\alpha'\beta'\gamma'} n_{\beta'} n_{\delta'} k_\sigma a_{\nu\sigma'} \times \\ \times \mathrm{Im} \langle \Psi_\nu - \Psi_{-\nu} | \frac{r_{\gamma'} \hat{l}_{\delta'}}{r^3} | \Psi \rangle. \quad (5)$$

Let us denote $\mathbf{s}_\mathbf{k}(t) = \langle \hat{\mathbf{s}}_\mathbf{k}(t) \rangle = \mathrm{Sp}(\hat{\mathbf{s}}_\mathbf{k}(t)\hat{\rho}(t))$, where $\hat{\rho}(t)$ is the density operator. Then

$$\frac{d\mathbf{s}_\mathbf{k}}{dt} = \left\langle \frac{d\hat{\mathbf{s}}_\mathbf{k}}{dt} \right\rangle + \mathrm{Sp}\left(\hat{\mathbf{s}}_\mathbf{k} \frac{d\hat{\rho}}{dt} \right). \quad (6)$$

The dynamics of the conduction electron spin caused by the perturbation (2) is described by equation [14]

$$\frac{d\hat{s}_{\mathbf{k}\alpha}}{dt} = \frac{i}{\hbar} \left[\hat{V}_\mathbf{k}, \hat{s}_\alpha \right] = \varepsilon_{\alpha\beta\gamma} I_{\mathbf{k}\beta} \hat{s}_{\mathbf{k}\gamma}, \\ \left\langle \frac{d\hat{\mathbf{s}}_\mathbf{k}}{dt} \right\rangle = \left[\langle \mathbf{I}_\mathbf{k} \rangle \times \mathbf{s}_\mathbf{k} \right] + \left\langle \left[\delta\mathbf{I}_\mathbf{k} \times \delta\hat{\mathbf{s}}_\mathbf{k} \right] \right\rangle, \quad (7) \\ \delta\mathbf{I}_\mathbf{k} = \mathbf{I}_\mathbf{k} - \langle \mathbf{I}_\mathbf{k} \rangle, \quad \delta\hat{\mathbf{s}}_\mathbf{k} = \hat{\mathbf{s}}_\mathbf{k} - \langle \hat{\mathbf{s}}_\mathbf{k} \rangle.$$

In the steady-state, when $d\hat{\rho}/dt = 0$, only the first summand in the righthand side of equation (6) remains and equation (7) takes the form

$$\frac{d\mathbf{s}_\mathbf{k}}{dt} = \left[\langle \mathbf{I}_\mathbf{k} \rangle \times \mathbf{s}_\mathbf{k} \right] + \left\langle \left[\delta\mathbf{I}_\mathbf{k} \times \delta\hat{\mathbf{s}}_\mathbf{k} \right] \right\rangle. \quad (8)$$

The modulus of the average spin is not conserved because of the second summand in the right-hand side of (8). Therefore, it can be considered as relaxational and written in the form $-(\mathbf{s}_\mathbf{k} - \mathbf{s}^e_\mathbf{k})/\tau$. Here, $\mathbf{s}^e_\mathbf{k}$ is the equilibrium value of the sample average spin, τ is the longitudinal relaxation time.

In the absence of influences, a quasi-equilibrium distribution is established with a density operator [16]

$$\hat{\rho}^q(t)=\exp\left\{-\Phi(t)-\int_V\theta(t,\mathbf{r})\hat{h}_{\mathbf{k}}(t,\mathbf{r})d^3r\right\},$$
$$\Phi(t)=\ln\mathrm{Sp}\exp\left\{-\int_V\theta(t,\mathbf{r})\hat{h}_{\mathbf{k}}(t,\mathbf{r})d^3r\right\}. \quad (9)$$

Here, $\theta(t,\mathbf{r})=1/(k_BT(t,\mathbf{r}))$, k_B is the Boltzmann constant, $T(t,\mathbf{r})$ is the local temperature, $\hat{h}_{\mathbf{k}}(t,\mathbf{r})$ is the density operator of the Hamiltonian, satisfying the relations [17]

$$\hat{H}_{\mathbf{k}}(t)=\int_V\hat{h}_{\mathbf{k}}(t,\mathbf{r})d^3r,\quad \frac{\partial\hat{h}_{\mathbf{k}}(t,\mathbf{r})}{\partial t}=-\mathrm{div}\,\hat{\mathbf{q}}_{\mathbf{k}}(t,\mathbf{r}), \quad (10)$$

Here, $\hat{\mathbf{q}}_{\mathbf{k}}(t,\mathbf{r})$ is the flux density operator of the Hamiltonian.

We used the ideal Fermi gas approximation for conduction electrons. The applicability of this model to conduction electrons in metals is justified by the fact that the thermodynamics of the Fermi-system is determined by its microscopic structure only near the Fermi-surface and is completely independent of what happens outside the range of order k_BT. As a result, the denser the Fermi-gas in the metal, the more ideal it is [18]. Experimental studies of the temperature dependence of the electron heat capacity in metals show that it corresponds well to the model of an ideal Fermi-gas with a scalar effective mass m^*. For most metals, the effective mass of the conduction electron is close to the mass of the free electron $m^* \approx m$. Such a model allows us to describe the collective of electrons with wave vector $\mathbf{k}$ by its density operator and put $\hat{\mathbf{q}}_{\mathbf{k}}(t,\mathbf{r})=\hbar\mathbf{k}\hat{h}_{\mathbf{k}}(t,\mathbf{r})/m^*$. Then, from (9) and (10) we obtain

$$\frac{d\hat{\rho}^q}{dt}=-\hat{\rho}^q\left\{\frac{d\Phi}{dt}+\int_V\frac{\partial\theta}{\partial t}\hat{h}_{\mathbf{k}}d^3r-\right.$$
$$\left.-\int_V\mathrm{div}(\theta\hat{\mathbf{q}}_{\mathbf{k}})d^3r+\int_V\hat{\mathbf{q}}_{\mathbf{k}}\,\mathrm{grad}\,\theta d^3r\right\}. \quad (11)$$

Analytical averaging of equation (5) gives $\langle\mathbf{I}_{\mathbf{k}}\rangle=J\mathbf{k}$, where

$$J=\frac{\hbar^2e^2Z\omega}{24\pi\varepsilon_0m^2c^2}\mathrm{Im}\langle\Psi_\nu-\Psi_{-\nu}|\frac{(\mathbf{n}\hat{\mathbf{l}})[\mathbf{a}_\nu\times\mathbf{n}]\mathbf{r}}{r^3}|\Psi\rangle.$$

Let us substitute the ratio (11) into the second summand in the right-hand side of equation (6), restricting to summands proportional to $\partial\theta/\partial\mathbf{r}$. Taking into account (10), we obtain

$$\frac{d\mathbf{s}_{\mathbf{k}}}{dt}=J[\mathbf{k}\times\mathbf{s}_{\mathbf{k}}]-\frac{\mathbf{s}_{\mathbf{k}}-\mathbf{s}^e_{\mathbf{k}}}{\tau}-\frac{\hbar}{m^*}\langle\hat{\mathbf{s}}_{\mathbf{k}}\hat{H}_{\mathbf{k}}\rangle^e\mathbf{k}\frac{\partial\theta}{\partial\mathbf{r}} \quad (12)$$

In the absence of a magnetic field, the unperturbed Hamiltonian of an ideal Fermi-gas does not depend on spin variables, so

$$\langle\hat{\mathbf{s}}_{\mathbf{k}}\hat{H}_{\mathbf{k}}\rangle^e=\langle\hat{\mathbf{s}}_{\mathbf{k}}\rangle^e\langle\hat{H}_{\mathbf{k}}\rangle^e=\mathbf{s}^e_{\mathbf{k}}H(\mathbf{k}).$$

Let us introduce the spin density operator of conduction electrons

$$\hat{\mathbf{s}}(t)=\int_V\hat{\mathbf{s}}(t,\mathbf{r})d^3r,$$
$$\hat{\mathbf{s}}(t,\mathbf{r})=\frac{1}{8\pi^3}\int\hat{\mathbf{s}}_{\mathbf{k}}(t)f(\mathbf{k},\mathbf{r})d^3k, \quad (13)$$
$$f(\mathbf{k},\mathbf{r})=\left[\exp\left(\left(H(\mathbf{k})-F(\mathbf{r})\right)\theta(\mathbf{r})\right)+1\right]^{-1}.$$

For an isotropic Fermi-gas $H(\mathbf{k})=\hbar^2k^2/(2m^*)$. The Fermi energy in (13) is found as $F(\mathbf{r})=\hbar^2k_F^2(\mathbf{r})/(2m^*)$, $k_F^3(\mathbf{r})=6\pi^2n_e(\mathbf{r})$, Here, $n_e(\mathbf{r})$ is the conduction electron density. The first summand in the right-hand side of equation (12) is zero when averaging of the form (13).

The steady-state in (8) corresponds to the orientation of $\mathbf{s}_{\mathbf{k}}$ along the vector $\mathbf{k}$. Averaging the perturbation (1) by quantum state and by random orientations, we obtain that the addition to the energy of states when spin is oriented parallel or antiparallel to the vector $\mathbf{k}$ is $\pm\hbar Jk/2$. Then

$$\mathbf{s}^e=\frac{1}{16\pi^3}\int\frac{\mathbf{k}}{k}\left\{f\left(H(k^2)-\frac{\hbar Jk}{2}\right)-\right.$$
$$\left.-f\left(H(k^2)+\frac{\hbar Jk}{2}\right)\right\}d^3k=0.$$

The wave vector average of the last summand in the right part (12) is equal to

$$\frac{\hbar^2 J}{16\pi^3 m^*}\int k\frac{df}{dH}\frac{\mathbf{k}}{k}H\left(k^2\right)\left(\mathbf{k}\frac{\partial\theta}{\partial\mathbf{r}}\right)d^3k = \\ =\frac{3F\left(\mathbf{r}\right)J}{2\pi}n_e\left(\mathbf{r}\right)\frac{\partial\theta}{\partial\mathbf{r}},$$

and the steady-state spin polarization is parallel to the temperature gradient

$$\mathbf{s}\left(\mathbf{r}\right)=\frac{3F\left(\mathbf{r}\right)J\tau}{2\pi k_B}\frac{n_e\left(\mathbf{r}\right)}{T^2\left(\mathbf{r}\right)}\frac{\partial T}{\partial\mathbf{r}}. \quad (14)$$

4. CONCLUSION

Formula (14) describes the well-known longitudinal spin Seebeck effect, when the direction of spin polarization is determined by the temperature gradient even in the absence of a charge current. Of course, the temperature gradient will also create the classical (charge) Seebeck effect in the conductor. Therefore, if a conductor is connected in a closed circuit, a charge current with longitudinal spin polarization will appear in it. The charge current in the conductor can also be generated by an external current source, which opens up the possibility of rapid electrical control of spin polarization. The high efficiency of such control is due to the fact that in chiral media the torsion of the unit cell can reach several radians, which is many orders of magnitude more than can be obtained by mechanical stresses [2] without irreversible destruction. The possibility of spin polarization generation at a distance of several millimetres in polycrystalline chiral media was shown in [19].

Spin polarization by the mechanism described in this work does not require external magnetic fields and residual magnetization and therefore does not interfere with the work in micro- and nano-sized spintronics structures. The energy required for spin polarization by the proposed mechanism comes from the heat fluxes in the medium due to the temperature gradient. However, the functioning of spintronics devices, as well as any microelectronics devices, is always accompanied by the generation of heat fluxes and temperature gradients. In this sense, the energy expended for spin polarization by the proposed mechanism in spintronics systems is "free".

In addition, the Seebeck spin effect is reciprocal with the Peltier spin effect. Reciprocity relations for them, at least in magnetic dielectrics, have been experimentally verified [20]. General reciprocity relations between Peltier and Seebeck spin effects, including for conducting media in the presence of mechanical strain, were obtained in [21]. This suggests that the dynamical effect (12) presented in this work may form the basis for new methods of heat flow control in spintronics systems.

REFERENCES

1. Hirohataa A, Yamadab K, Nakatanic Y, Prejbeanud I-L, Dienyd B, Pirroe P, Hillebrandse B. Review on spintronics: Principles and device applications. *Journal of Magnetism and Magnetic Materials*, 2020, 509, 166711, 1-28; https://dx.doi.org/10.1016/j.jmmm.2020.166711.
2. Ignatiev VK, Lebedev NG, Perchenko SV, Stankevich DA. Controlling the dynamics of spin polarization of conduction electrons by electrical and mechanical action. *RENSIT: Radioelectronics. Nanosystems. Information Technologies*, 2023, 15(2):133-138e. DOI: 10.17725/rensit.2023.15.133.
3. Sadamichi Maekawa, Sergio O. Valenzuela, Eiji Saitoh, and Takashi

Kimura (Eds.). *Spin Current*. Oxford, University Press, 2012, 461 p.

4. Uchida K, Takahashi S, Harii K, Ieda J, Koshibae W, Ando K, Maekawa S, Saitoh E. Observation of the spin Seebeck effect. *Nature*, 2008, 455, 778-781; doi: 10.1038/nature07321.
5. Adachi H, Uchida K, Saitoh E, Maekawa S. Theory of the spin Seebeck effect. *Reports on Progress in Physics,* 2013, 76(3):036501; https://dx.doi.org/10.1088/0034-4885/76/3/036501.
6. Capps J, Marinescu DC, Manolescu A. Spin Seebeck effect in an (In,Ga)As quantum well with equal Rashba and Dresselhaus spin-orbit couplings. *Phys. Rev. B.,* 2016, 93:085307; https://dx.doi.org/10.1103/PhysRevB.93.085307.
7. Yamada K, Kurokawa Y, Kogiso K, Yuasa H, Shima M. Observation of Longitudinal Spin Seebeck Voltage in YIG Films Chemically Prepared by Co-Precipitation and Spin Coating. *IEEE Trans. on Mag.*, 2019, 55(2):4500104; https://dx.doi.org/10.1109/TMAG.2018.2865199.
8. Kyunghoon Kim, Eric Vetter, Liang Yan, Cong Yang, Ziqi Wang, Rui Sun, Yu Yang, Andrew H. Comstock, Xiao Li, Jun Zhou, Lifa Zhang, Wei You, Dali Sun & Jun Liu. Chiral-phonon-activated spin Seebeck effect. *Nature Materials,* 2023, 22:322-328; https://dx.doi.org/10.1038/s41563-023-01473-9.
9. Oyanagi K, Takahashi S, Kikkawa T, Saitoh E. Mechanism of paramagnetic spin Seebeck effect. *Phys. Rev. B,* 2023, 107:014423; https://dx.doi.org/10.1103/PhysRevB.107.014423.
10. Takezoe Y, Hosono K, Takeuchi A, Tatara G. Theory of spin transport induced by a temperature gradient. *Phys. Rev. B*, 2010, 82:094451; https://dx.doi.org/10.1103/PhysRevB.82.094451.
11. Bebenin NG. Effect of electric current on the spin polarization of electrons in materials with inhomogeneous magnetization. *Journal of Experimental and Theoretical Physics*, 2022, 161(5):737-745; doi: 10.31857/S004445102205011X.
12. Yu T, Luo Z, Bauer GEW. Chirality as generalized spin–orbit interaction in spintronics. *Physics Reports*, 2023, 1009, 1-115; https://dx.doi.org/10.1016/j.physrep.2023.01.002.
13. Berestetskii VB., Pitaevskii LP., Lifshitz EM. Teoreticheskaya fizika. T. IV. Kvantovaya electrodinamika [Course of Theoretical Physics, Vol. 4, Quantum Electrodynamics]. Moscow, Fizmatlit Publ., 2002, 720 p.
14. Landau LD., Lifshitz EM. Teoreticheskaya fizika. T. III. Kvantovaya mehanika. Nerelyativ-istskaya teoriya [Course of Theoretical Physics, Vol. 3, Quantum Mechanics. Non-relativistic Theory]. Moscow, Fizmatlit Publ., 2004, 800 p.
15. Madelung O. Teoiriya tverdogo tela [Theory of solid states]. Moscow, Nauka Publ., 1980, 416 p.
16. Leontovich MA. Vvedenie v termodinamiku, statisticheskaya fizika. Moscow, Nauka Publ., 1983, 416 p.
17. Ahiezer AI, Peletminskij SV. Metody statisticheskoj fiziki. Moscow, Nauka Publ., 1977, 368 p.
18. Kvasnikov IA. Teoriya ravnovesnyh sistem: Statisticheskaya fizika. Moscow, Editorial URSS Publ., 2002, 240 p.
19. Shishidoa H, Sakai R, Hosaka Y, Togawaa Y. Detection of chirality-induced spin polarization over millimeters in polycrystalline bulk samples of chiral disilicides $NbSi_2$ and $TaSi_2$. *Appl.*

Phys. Lett., 2021, 119(18):182403; doi: 10.1063/5.0074293.

20. Sola A, Basso V, Kuepferling M, Dubs C, Pasquale M. Experimental proof of the reciprocal relation between spin Peltier and spin Seebeck effects in a bulk YIG/Pt bilayer. *Scientific Reports,* 2019, 9(1):2047.

21. Ignatjev VK. Sootnosheniya vzaimnosti dlya otkrytykh nelineynykh sistem v peremennykh polyakh [Reciprocity relations for open nonlinear systems in variable fields]. *Zhurnal tekhnicheskoy fiziki* [Technical Physics], 2022, 67(1):92-103; http://dx.doi.org/10.21883/TP.2022.01.52539.126-21, (in Russ.).

DOI: 10.17725/rensit.2023.15.393

New compounds of boron nitride with atoms in the $sp+sp^2$ hybridized state formed on the basis of the BN-L_{4-8} layer

Dmitry S. Ryashentsev, Anna K. Kudryavtseva

Chelyabinsk State University, https://www.csu.ru/

Chelyabinsk 454001, Russian Federation

E-mail: ryashentsev_dmitry@mail.ru, tsipyshevaanna@yandex.ru

Received August 11, 2023, peer-reviewed August 18, 2023, accepted August 25, 2023, published December 06, 2023.

Abstract: **The density functional theory (DFT) method was used to determine the crystal structures and electronic properties of new layered polymorphic varieties of boron nitride with a graphyne-like structure. The structures of new graphyne-like monolayers consist of boron and nitrogen atoms in the sp- and sp^2-hybridized state and were model-built from a layer of graphene-like boron nitride BN-L_{4-8} by partial replacement of atoms in the three-coordinated (sp^2-hybridized) state by atoms in the two-coordinated state (sp-hybridized). As a result of theoretical analysis, the possibility of the existence of seven $sp+sp^2$ new structures of boron nitride was established: one α-type, three β-types and three γ-types, differing in the proportion of atoms in the sp-hybridized state and their spatial arrangement. However, two of the three structural varieties with a minimum content of atoms in the sp-hybridized state (γ-type) turned out to be unstable and, in the process of geometric optimization, were transformed into structures of graphene-like layers of boron nitride. The structure of the BN-L_{4-8}-γ2 layer passed into the structure of the original graphene-like layer BN-L_{4-8}, while the structure of the BN-L_{4-8}-γ3 layer passed into the structure of the graphene-like layer BN-L_{4-6-8}, where there are no atoms in the sp-hybridized state. The sublimation energies of the new polymorphic varieties range from 16.23 eV/(BN) to 16.70 eV/(BN). The band gap varies from 3.777 eV to 3.878 eV.**

Keywords: **polymorphism, boron nitride, crystal structure, ab initio calculations, electronic properties**

UDC 538.911+538.915

Acknowledgments: The study was supported by the Russian Foundation for Basic Research (Project № 23-23-00140).

For citation: Dmitry S. Ryashentsev, Anna K. Kudryavtseva. New compounds of boron nitride with atoms in the $sp+sp^2$ hybridized state formed on the basis of the BN-L_{4-8} layer. *RENSIT: Radioelectronics. Nanosystems. Information Technologies*, 2023, 15(4):393-400e. DOI: 10.17725/rensit.2023.15.393.

Contents

1. INTRODUCTION

Boron nitride compounds are isoelectronic and isostructural analogues of carbon compounds, and their crystal structure can be similar to that of graphite and diamond [1–2]. Theoretically predicted hybrid carbon materials, consisting of atoms with different hybridization of electron orbitals. The most interesting are

sp+sp^2 carbon materials, consisting of carbon atoms in two- and three-coordinated states, which were called graphynes [3–6]. Boron and nitrogen atoms in BN, as well as carbon atoms in carbon materials, can be in various sp, sp^2, or sp^3 hybridized states [7–9]. Therefore, the existence of hybrid sp+sp^2 compounds of boron nitride, similar to graphyne compounds, consisting of carbon atoms is theoretically possible [10–11]. The structure of BN-graphyne compounds can theoretically be built from three main polymorphic varieties of graphene-like boron nitride: BN-L_6; BN-$L_{4\text{-}8}$ and BN-$L_{4\text{-}6\text{-}12}$ [12,13], by partial replacement of atoms in the three-coordinate state with atoms in the two-coordinate state. Earlier, in [14,15], the structure and electronic properties of a number of new polymorphic varieties of boron nitride with a graphyne-like layer structure, formed on the basis of hexagonal boron nitride BN-L_6, were theoretically studied. Polymorphic varieties of such hybrid compounds differ in the ratio of atoms in different hybridized states, the degree of deformation of their structure, and the value of the band gap, as a result of which their properties may differ. In this article, the structure and electronic properties of new polymorphic layered varieties of boron nitride with a graphyne-like structure, modeled from a BN-$L_{4\text{-}8}$ graphene-like layer, are theoretically studied.

2. MATERIALS AND METHODS

As the initial structures for modeling the graphyne-like layers of boron nitride, we took the graphyne layers described in [5,6]. A number of new structural varieties of graphyne-like boron nitride can be obtained by considering the gradual transformation of the structure of graphene-like boron nitride BN-$L_{4\text{-}8}$, in which all atoms are in the state of sp^2 hybridization to graphyne-like (sp+sp^2), where the number of atoms in the sp-hybridized state maximum. Depending on the structure, the graphyne-like layers can be divided into three groups (α, β and γ), differing in the proportion of atoms in the sp-hybridized state. To construct an α-graphyne-like layer, it is necessary to replace all three bonds of a three-coordinated atom with two-coordinate ones, for a β-graphyne-like layer, two of the three bonds must be replaced, and to construct a γ-graphyne-like layer, one bond must be replaced. The analysis of graphyne-like boron nitride compounds showed that it is possible to build seven sp+sp^2 new boron nitride structures: one α-type, three β-types, and three γ-types, differing in the proportion of atoms in the sp-hybridized state and their spatial arrangement. Model construction was performed using the Quantum ESPRESSO software package [16]. The density functional theory method [17] in the generalized gradient approximation [18] was used to calculate the structures of three-dimensional crystals consisting of stacks of graphyne-like layers, the distance between which was 10 Å to exclude the influence of neighboring layers in the stacks. The calculations were carried out for k-point grids: 12×12×12, the cutoff energy on the basis of plane waves was 70 Rydbergs at a temperature of 0.01 K. The lengths of the elementary translation vectors (a, b), the lengths of interatomic bonds (Å) were determined as structural parameters and the angles between them (°). To determine the number of structural positions, the value of the ring Wells parameter (Rng) was determined; to determine the stability of the structures, the deformation parameter (Def) and sublimation energy (E_{sub}) were calculated. From the plots of the band structure and densities of electronic states, the numerical values of the band gap were determined.

3. RESULTS AND DISCUSSION

The density functional theory (DFT) method in the generalized gradient approximation (GGA) was used to perform geometric optimization

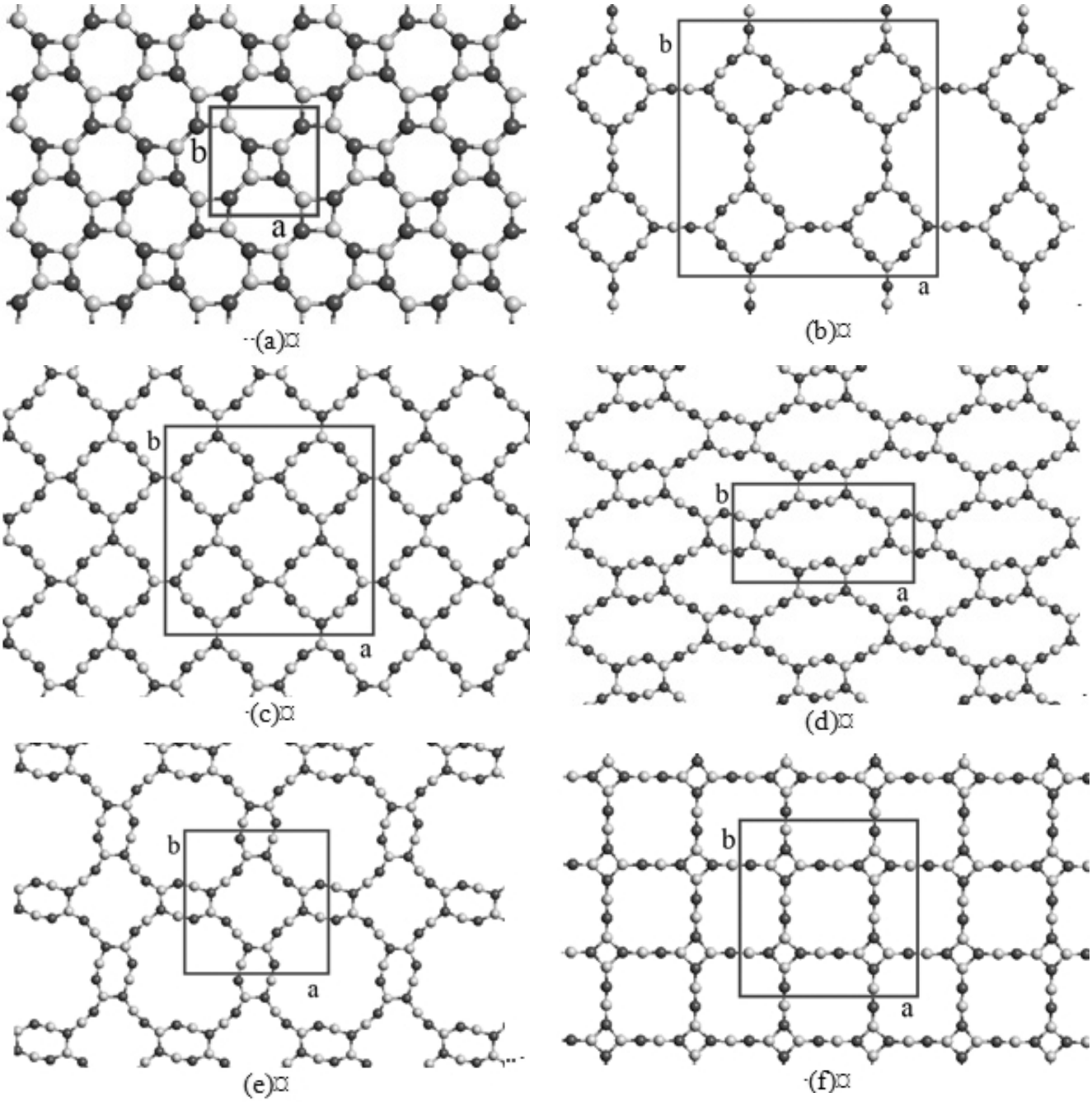

Fig. 1. *Geometrically optimized layer structures and unit cells of polymorphic varieties of boron nitride as a result of DFT-GGA calculations: (a) BN-L_{4-8}; (b) BN-L_{4-8}-a1; (c) BN-L_{4-8}-β1; (d) BN-L_{4-8}-β2; (e) BN-L_{4-8}-β3; (f) BN-L_{4-8}-γ1.*

of seven model-built layers of boron nitride with a grahyne-like structure. As a result of the performed calculations, the geometrically optimized structures of five new graphyne-like layers of boron nitride were determined. Monolayers with the smallest number of atoms in the sp-hybridized state BN-L_{4-8}-γ2 and BN-L_{4-8}-γ3 turned out to be unstable; in the process of geometric optimization, their structure was transformed into graphene-like compounds of boron nitride BN-L_{4-6-8} and BN-L_{4-8}, their structure was not considered further. The remaining five layers: BN-L_{4-8}-α1, BN-L_{4-8}-β1, BN-L_{4-8}-β2, BN-L_{4-8}-β3 and BN-L_{4-8}-γ1 have a stable structure, and their images are shown in **Fig. 1**. This figure shows images of a layer of graphene-like boron nitride BN-L_{4-8}, on the basis of which polymorphic varieties of graphyne-like

Table 1

Properties and structural parameters of polymorphic varieties of boron nitride with a graphyne-like structure

Laier	BN-L_6	BN-L_{4-8}	BN-L_{4-8}-α1	BN-L_{4-8}-β1	BN-L_{4-8}-β2	BN-L_{4-8}-β3	BN-L_{4-8}-γ1
Crystal system	Hex	Tetr	Tetr	Tetr	Rhomb	Tetr	Tetr
a, Å	2.512	4.942	19.689	14.307	14.868	11.096	12.286
b, Å					6.996		
c, Å	10.000	10.000	10.000	10.000	10.000	10.000	10.000
β, °	120	90	90	90	90	90	90
Rng_I	63	4182	242121	122161	20281	24116181	16241
Rng_{II}	-	-	242	161121	202	24181	162
N, atom	2	8	64	48	24	24	32
ρ, g/sm^2	0.754	0.675	0.3402	0.4832	0.4754	0.4017	0.4368
Def, °	0.325	50.55	14.04	22.73	39.79	27.62	60.00
E_{total}, eV/(el.c.)	-353.43	-1410.64	-11248.80	-8443.13	-4220.88	-4220.39	-5631.84
E_{total}, eV/(BN)	-353.43	-352.66	-351.52	-351.80	-351.74	-351.70	-351.99
E_{sub}, eV/(BN)	18.14	17.36	16.23	16.51	16.45	16.41	16.70
Δ, eV	4.686	3.894	3.878	3.877	3.853	3.868	3.777

boron nitride and their structures were built, and elementary cells were identified. In the BN-L_{4-8}-α1, BN-L_{4-8}-β1, BN-L_{4-8}-β3 and BN-L_{4-8}-γ1 layers, the unit cells belong to the tetragonal crystal system, which contain from 24 to 64 atoms (**Table 1**). The lengths of elementary translation vectors ($a = b$) are in the range from 11.096Å, observed for the BN-L_{4-8}-β3 layer, to 19.689Å, for the BN-L_{4-8}-α1 layer. The unit cell of the BN-L_{4-8}-β2 layer belongs to the rhombic crystal system, which contains 24 atoms. The lengths of elementary translation vectors are 14.868Å and 6.996Å.

In layers BN-L_{4-8}-α1, BN-L_{4-8}-β1 and BN-L_{4-8}-γ1 fragments of linear chains turned out to be straight, while in layers BN-L_{4-8}-β2 and BN-L_{4-8}-β3 - they turned out to be curved. Due to the fact that the graphyne-like layers of boron nitride are formed by atoms with different contents of *sp*- and *sp*^{2}-hybridized bonds, the structure of such layers will be characterized by two different structural positions, which are numerically expressed by the value of the Wells ring parameter (Rng). The first structural position is atoms in the *sp*^{2}-hybridized state, characterized by three bond lengths: L_1, L_2, L_3, the values of which are in the range from 1.370Å (BN-L_{4-8}-γ1) to 1.546Å (BN-L_{4-8}-β2). In addition, the first structural position is characterized by the values of three angles between bonds: φ_{1-2}, φ_{1-3} and φ_{2-3}, the values of which vary from 86.27° to 136.86° (BN-L_{4-8}-γ1).

Table 2

Interatomic bond lengths and angles between them in graphyne-like BN layers

Structure	Atom	L_1, Å	L_2, Å	L_3, Å	L_4, Å	φ_{1-2}, °	φ_{1-3}, °	φ_{2-3}, °	φ_{3-4}, °
BN-L_{4-8}	B	1.426	1.416	1.421	-	133.47	136.25	90.28	-
	N	1.410	1.387	1.403	-	135.42	134.58	90.01	-
BN-L_{4-8}-α1	B	1.421	1.435	1.436	1.261	122.15	121.89	115.97	179.52
	N	1.414	1.427	1.427	1.261	124.26	125.15	110.59	179.30
BN-L_{4-8}-β1	B	1.478	1.413	1.412	1.271	119.27	119.40	121.33	171.62
	N	1.478	1.410	1.411	1.271	123.81	124.02	112.18	161.24
BN-L_{4-8}- β2	B	1.397	1.414	1.546	1.279	128.43	113.84	117.73	167.39
	N	1.397	1.407	1.545	1.279	128.33	111.21	120.46	147.48
BN-L_{4-8}- β3	B	1.398	1.421	1.530	1.273	126.32	112.79	120.90	163.38
	N	1.398	1.412	1.530	1.273	127.49	110.41	122.11	175.00
BN-L_{4-8}-γ1	B	1.370	1.499	1.499	1.282	133.14	133.14	93.73	180.00
	N	1.372	1.499	1.499	1.282	136.86	136.86	86.27	180.00

The lengths of interatomic distances and the angles between them are given in **Table 2.** The second structural position is atoms in the *sp*-hybridized state, which is characterized by two bond lengths (L_3 and L_4). The L_3 bond connects the sp^2- and *sp*-hybridized atoms and is common to two structural positions. The interatomic bond L_4 characterizes the distance between atoms in a fragment of a linear chain. It is the shortest and its value ranges from 1.261Å (BN-$L_{4\text{-}8}$-α1) to 1.282Å (BN-$L_{4\text{-}8}$-γ1). Also, the second structural position is characterized by

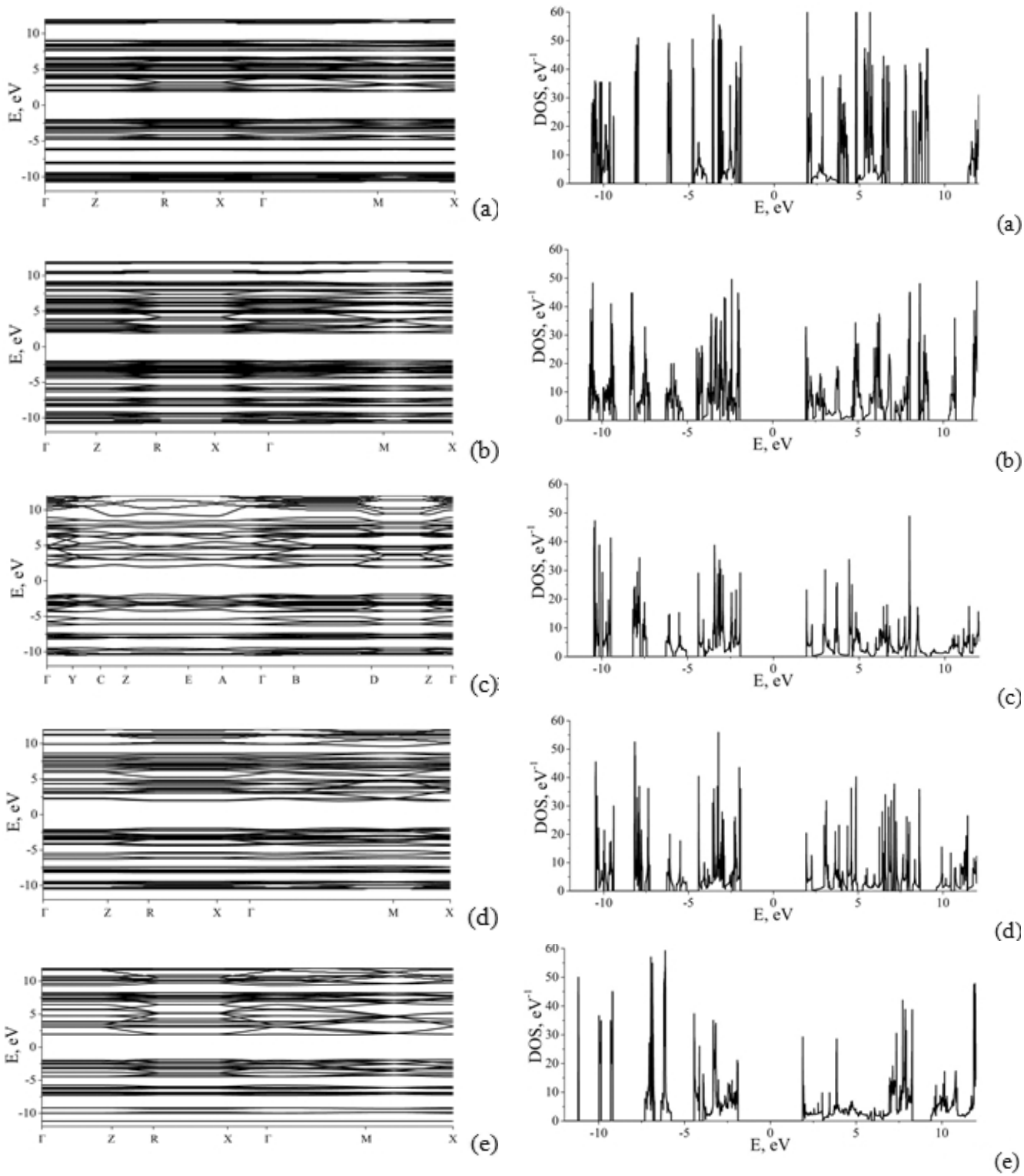

Fig. 2. *The band structure and density of electronic states of new layered BN polymorphs with a graphyne-like structure formed on the basis of the BN-$L_{4\text{-}8}$ layer: (a) BN-$L_{4\text{-}8}$-a1; (b) BN-$L_{4\text{-}8}$-β1; (c) BN-$L_{4\text{-}8}$-β2; (d) BN-$L_{4\text{-}8}$-β3; (e) BN-$L_{4\text{-}8}$-γ1.*

one value of the angle between the bonds L_3 and L_4 ($\varphi_{3\text{-}4}$), the values of which are in the range from 147.48° (BN-$L_{4\text{-}8}$-β2) to 180.00° (BN-$L_{4\text{-}8}$-γ1). Apparently, the differences in the lengths of interatomic bonds are explained by the different electron density in the interatomic space. Thus, the maximum electron density is observed in the L_4 bond.

The minimum layer density is observed for the layer with the maximum number of atoms in the *sp*-hybridized state, BN-$L_{4\text{-}8}$-α1, and is 0.3402 g/cm^2. The maximum layer density is observed for the BN-$L_{4\text{-}8}$-β1 layer and is 0.4832 g/cm^2, which is less than the calculated value for the hexagonal boron nitride (0.754 g/cm^2) and graphene-like BN-$L_{4\text{-}8}$ (0.675 g/cm^2) layer.

To assess the degree of deformation of the layer structure, the values of the deformation parameter were calculated (Table 1), which was determined as the sum of the modules of the angle differences between the bonds and the value of the angle of 120° in an ideal hexagonal structure. A comparative analysis of the numerical values of the deformation parameters of new boron nitride polymorphs with a graphyne-like structure showed that the values of this parameter are minimal for the BN-$L_{4\text{-}8}$-α1 layer and amount to 14.04°, the maximum value of the parameter is observed for the BN-$L_{4\text{-}8}$-γ1 layer (60.00°), which indicates strong deformations due to quadrangular fragments in the layer structure. The sublimation energy (E_{sub}) was calculated as the stability parameter of the structure, which was determined as the difference between the total energy per BN molecular group and the energy of isolated nitrogen and boron atoms. The minimum value of the sublimation energy is observed for the BN-$L_{4\text{-}8}$-α1 layer with the maximum number of atoms in the *sp*-hybridized state and is 16.23 eV/(BN), which indicates the low stability of this layer. The maximum sublimation energy is observed for the BN-$L_{4\text{-}8}$-γ1 polymorph with the minimum number of atoms in the *sp*-hybridized state and is 16.70 eV/(BN), which is lower than the sublimation energy of hexagonal boron nitride (18.14 eV/(BN)), the sublimation energy β-graphyne-like layers take an intermediate value.

The results of calculations of the band structure and densities of electronic states are shown in **Fig. 2.** The band gap (Δ) at the Fermi energy level is in the range from 3.777 eV to 3.878 eV, which indicates that all boron nitride polymorphs with a graphyne-like structure should exhibit semiconductor properties and it may vary depending on the features of the structure.

4. CONCLUSION

In this work, the density functional theory method using the generalized gradient approximation was used to calculate the structures, electronic and energy characteristics of polymorphic varieties of boron nitride with the structures of α-, β-, and γ-graphynes formed on the basis of graphene-like boron nitride BN-$L_{4\text{-}8}$. The highest sublimation energy is observed for the BN-$L_{4\text{-}8}$-γ1 layer and is 16.70 eV/(BN), which indicates that this layer should have a stable structure under normal conditions. In addition, there is a dependence between the values of the sublimation energy of polymorphic varieties and the fraction of atoms in the *sp*-hybridized state. As the fraction of atoms in the *sp*-hybridized state increases, the value of the sublimation energy decreases. The band gap of new polymorphic varieties ranges from 3.777 eV to 3.878 eV; therefore, all considered polymorphic varieties should exhibit semiconductor properties and can find wide practical application in creating heterostructures for nanoelectronic devices [19].

REFERENCES

1. Mohammad SN. Electrical characteristics of thin film cubic boron nitride. *Solid-state electronics*, 2002, 46:203-222.
2. Ji C, Levitans VI, Zhu H, Chaudhuri J, Marathe A, Ma Y. Shear-induced phase transition of nanocrystalline hexagonal boron nitride to wurtzitic structure at room temperature and lower pressur. *The Proceedings of the National Academy of Sciences*, 2012, 109:19108-19112.
3. Belenkov EA, Mavrinskii VV, Belenkova TE, Chernov VM. Structural varieties of graphyne layers, consisting of carbon atoms in the sp and sp² hybridization state. *Journal of experimental and theoretical physics*, 2015, 147(5):949-961 (in Russ.).
4. Mavrinskii VV, Belenkova TE, Chernov VM, Belenkov EA. The structure of polymorphic varieties of graphyne layers. *Bulletin of Chelyabinsk state university*, 2013, 18:31-39 (in Russ.).
5. Belenkova TE, Chernov VM Electronic structure of layers of sp+sp² hybridized carbon atoms obtained from hexagonal graphene. *Fundamental problems of modern materials science*, 2016, 13(2):149-154 (in Russ.).
6. Belenkov EA, Mavrinskii VV, Greshnyakov VA, Brzhezinskaya MM Structure and electronic properties of graphyne polymorphs formed from 4-8 graphene. IOP Conference Series: Materials Science and Engineering, 2019, 537: 022070.
7. Chen Z-G, Zou J, Liu G, Li F, Wang Y, Wang L, Yuan X-L, Sekiguchi T, Cheng H-M, Lu G. Novel Boron Nitride Hollow Nanoribbons. *ACS Nano,* 2008, 2:2183-2191.
8. Stephan O, Bando Y, Loiseau Y, Willaime F, Shramchenko N, Tamiya T, Sato T Formation of small single-layer and nested BN cages under electron irradiation of nanotubes and bulk material. *Applied Physics A*, 1998, 67:107-111.
9. Nagakubo A, Ogi H, Sumlya H, Kusakabe K, Hirao M Elastic constants of cubic and wurtzite boron nitrides. *Applied Physics Letters*, 2013, 102:241909.
10. Zhang Y, Yun J, Wang K, Chen X, Yang Z, Zhang Z, Yan J, Zhao W First-principle study of graphyne-like BN sheet: Electronic structure and optical properties. *Computational materials science,* 2017, 136:12-19.
11. Enyashin AN, Ivanovskii AL Graphene-like BN allotropes: Structural and electronic properties form DFTB calculations. *Chemical Physics Letters*, 2011, 509:143-147.
12. Ryashentsev DS, Belenkov EA Structure and electronic properties of 4-8 and 4-6-12 layered varieties of boron nitride. *Journal of Physics: Conference Series,* 2019, 1410:012016.
13. Ryashentsev DS, Belenkov EA. New BN polymorphs with two-dimensional structure. *IOP Conference Series: Materual Science and Engineering,* 2019, 537:022060.
14. Ryashentsev DS, Belenkov EA. Ab initio calculations of the structure and electronic properties of BN layered compounds from sp- and sp²-hybridized atoms. *Physicochemical aspects of studing clusters, nanostructures and nanomaterials,* 2019, 11:511-519 (in Russ.).
15. Ryashentsev DS, Belenkov EA. New polymorphic varieties of boron nitride with structure similar to graphyne. *Journal of Physics: Conference Series,* 2020, 1431:012051.
16. Gisnnozzi P, Baroni S, Bonini N, Calandra M, Car R, Cavazzoni C, Ceresoli D, Chiarotti GL, Cococcioni M, Dabo I, Corso AD, Gironcoli S, Fabris S, Fratesi G, Gebauer R, Gerstmann U, Gougoussis C, Kokalj A, Lazzeri M, Martin-Samos L, Marzari N, Mauri F, Mazzarello R, Paolini S, Pasquarello A, Paulatto L, Sbraccia C, Scandolo S, Sclauzero G, Seitsonen AP, Smogunov A, Umari P, Wentzcovitch RMM. Quantum Espresso: a modular and

open-source software project for quantum simulations of materials. *Journal of Physics: Condensed Matter*, 2009, 21:395502.

17. Koch WA, Holthausen MC. *Chemist's Guide to Density Functional Theory*. Weinheim, Wiley-VCH, 2002, 313 p.
18. Langreth DC, Mehl MJ. Beyond the local-density approximation in calculations of ground-state electronic properties. *Physical Review B*, 1983, 28(4):1809.
19. Katoch J, Ulstrup S, Koch RJ, Moser S, McCreary KM, Singh S, Xu J, Jonker BT, Kawakami RK, Bostwick A, Rotenberg E, Jozwiak C. Giant spin-splitting and gap renormalization driven by trions in single-layer WS2/h-BN heterostructures. *Nature Physics*, 2018, 14:355.

DOI: 10.17725/rensit.2023.15.401

Toward an Optimal Wavelet Filter and Decomposition Level for Noise Elimination of the ECG Signal

Anas Fouad Ahmed
Al-Iraqia University, Electrical Engineering Department, https://en.aliraqia.edu.iq/
Al Adhmia - Haiba Khaton, 6029, Baghdad, Iraq
E-mail: anasfuad33eng@yahoo.com

Ali Rasim Ibrahim
Alsalam University College, https://alsalam.edu.iq/
Baghdad - Sidiya, Iraq
E-mail: ali.r.ibrahim@alsalam.edu.iq

May Hatem Abood
Al-Iraqia University, Computer Engineering Department, https://en.aliraqia.edu.iq/
Al Adhmia - Haiba Khaton, 6029, Baghdad, Iraq
E-mail: may.hattim@gmail.com

Received March 28, 2023, peer-reviewed April 28, 2023, accepted May 05, 2023, published December 06, 2023.

Abstract: **The denoising process represents one of the most important preprocessing steps for Electrocardiogram (ECG) signal processing and assists the specialist in making the right diagnosis for the patient. Five wavelet filters (WFs) closest in morphology to the pattern of the ECG signal were nominated, and their performances were analyzed at different noise, and number of decomposition (No. Dec) levels to determine the optimum, among them for noise reduction task. These Filters are Daubechies 4 (DB4), Daubechies 6 (DB6), Coiflet 4 (Coif4), Symlet 6 (Sym6) and Symlet 8 (Sym8). The results of the standard ECG signals (downloaded from MIT-BIH) revealed that the DB6 filter with four decomposition levels is optimal for removing noise of the ECG signal in terms of three metrics "Mean Square Error" (MSE), "Output Signal to Noise Ratio" (SNRo), and "Correlation Coefficient Index" (CCI). In addition, a simple and efficient threshold rule was adapted to be used in the proposed method. The suggested approach was successfully applied to reduce the noise of the ECG signals recorded using a simple proposed electronic circuit. Finally, the performance of the introduced scheme was compared with that of the standard ECG equipment, the "Biocare iE300", and the outcomes were very close.**

Keywords: **electrocardiogram, wavelet denoising, wavelet filters; signal decomposition levels, thresholding**

UDC 519.67, 612.1, 53.083, 519.24, 004.93

For citation: Anas Fouad Ahmed, Ali Rasim Ibrahim, May Hatem Abood. Toward an Optimal Wavelet Filter and Decomposition Level for Noise Elimination of the ECG Signal. *RENSIT: Radioelectronics. Nanosystems. Information Technologies*, 2023, 15(4):401-410e. DOI: 10.17725/rensit.2023.15.401.

Contents

1. INTRODUCTION

An ECG is a graphical measurement of the electricity of the heart that indicates the prompt status for the health of the heart [1,2]. Therefore, it has been broadly utilized for diagnosing cardiovascular illness [3-6]. The traditional shape of the ECG signal with its most important distinguishing points is shown in **Fig. 1**. The noise cancellation is

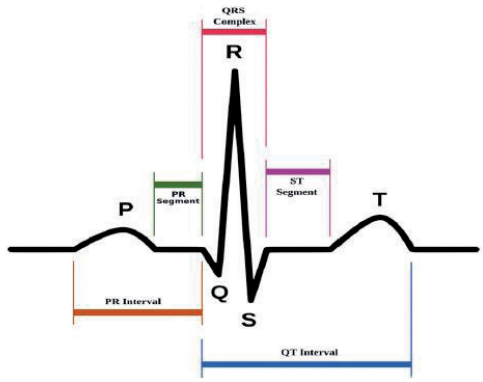

Fig. 1. *The principle components of a typical ECG waveform.*

one of the key processes that arise during the analysis of the heartbeat. The strength of the noise is low during the relaxation cases, while it becomes high when the person is under stress, and this makes the extraction of clinical information more difficult [7,8].

Different types of noise contaminate the ECG signal during acquisition and transmission, such as Electrode Movements (EM), Base-Line wanders (BL), Power-Line crosstalk (PL), Bad Electrode contact (BE), Inappropriate Measuring (IM) circumstances, and Electromyography (EMG) signals [9,10]. Most of the aforementioned types can be easily discarded using conventional filters, but the extraction of a clean heartbeat from an ECG signal that is corrupted with "Additive White Gaussian Noise" (AWGN) is a critical problem [11]. In spite of tremendous related works in this direction, there are numerous medical applications that need robust signal processing to abstract the clinical data in an efficient manner. Various approaches have been presented to improve the SNR of the noisy ECG signals [12-16]. The strategies that depend on Wavelet Transform (WT) surpassed the others because they showed good and stable performance in rejecting noise and exhibited high detection accuracy [17-20]. Nevertheless, which are the optimum WF and No. Dec levels for attaining these tasks remain prorated questions since it depends on the type and purpose of the specified application. This work attempts to answer the aforementioned question, specifically in the field of removing noise from the ECG signal using an effective methodology and a comprehensive analysis to determine the optimal WF and No. Dec levels. Also, this paper introduces a simple and efficient threshold rule. Finally, testing the reliability and robustness of the suggested scheme was performed using a simple, low-cost ECG acquisition system and standard ECG equipment, the "Biocare iE300".

2. A BRIEF OVERVIEW OF FILTERING BASED ON WAVELET

The aim of the wavelet filtering approach is to eliminate the AWGN $c(t)$ and to retrieve information signal $b(t)$. The idea is simply described in Eq. (1) [22]:

$$f(t) = b(t) + c(t) \tag{1}$$

The WT is an effective scheme with excellent time-frequency resolution, and it is perfect for signals of a non-stationary nature, such as ECG [3]. The WT divides the ECG signal into Detail coefficients (Dc) and Approximation coefficients (Ac) that can be formulated as the following [3]:

$$Dc[k] = \sum_{k=-\infty}^{\infty} f(s)H(2k-s), \tag{2}$$

$$Ac[k] = \sum_{k=-\infty}^{\infty} f(s)L(2k-s), \tag{3}$$

where s is a sampling data point, k is the No. Samples, $f(s)$ is the signal contaminated with noise, $H(2k - s)$ and $L(2k - s)$ are high-pass and low-pass filters, which alter based on the type of wavelet function [3]. The WT permits the abstraction of a specific frequency band from the signal. **Fig. 2** demonstrates the three levels of decomposition into Ac and Dc.

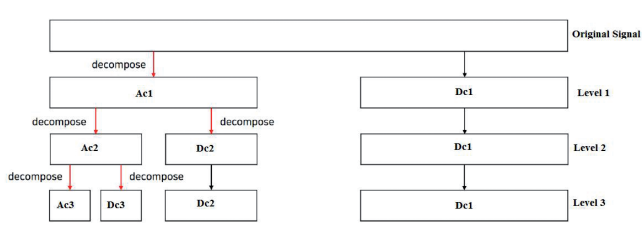

Fig. 2. *The three levels decomposition scheme.*

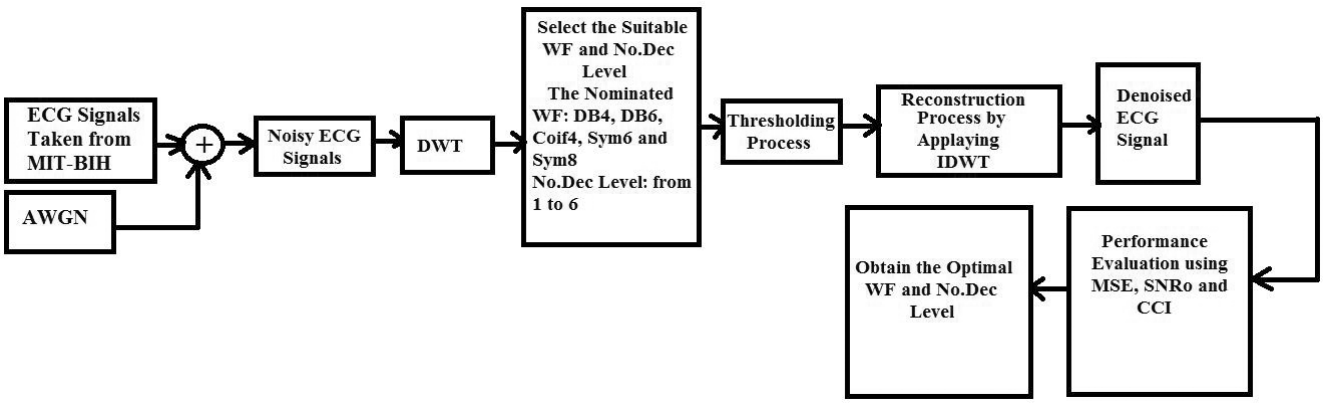

Fig. 3. *Block diagram of the investigative phase.*

The WF consists of scaled and dilated paradigms of the scaling function $\alpha(j)$ and wavelet function $\beta(j)$ [23]. The low-pass coefficients and high-pass coefficients are associated with $\alpha(j)$ and $\beta(j)$, respectively, as illustrated in Equations (4)-(6) [23]:

$$L(H) = (-1)^k H(1-k), \tag{4}$$

$$\alpha(2j-k) \rightarrow \alpha(j) = \sum_k H(k)\sqrt{2}, \tag{5}$$

$$\beta(2j-k) \rightarrow \beta(j) = \sum_k L(k)\sqrt{2}. \tag{6}$$

The high-pass and low-pass filters are featured parameters for each WF. Therefore, specifying the WF and No. Dec level has a significant impact on the performance of the denoising process.

3. SUGGESTED APPROACH

The proposed framework comprises two phases: the investigative phase, based on real standard ECG signals taken from MIT-BIH [24], and the verification phase, based on ECG signals recorded using the suggested Simple-design, Low-cost Acquisition system (SLA) and ECG signals collected using the standard ECG equipment, "Biocare iE300".

3.1. Investigative Phase

This phase aims to investigate to answer the following questions: The first is: what is the optimal WF? The second is: what is the optimal No. Dec level for minimizing the noise of the ECG signals? The steps of the investigative phase are displayed in **Fig. 3**. The real, standard ECG signals (46 records) from MIT-BIH were utilized and the AWGN was added to them to obtain the noisy ECG signals. Three levels of AWGN (15 dB, 20 dB, and 25 dB) were generated and added to the original signals using the MATLAB program. After that, the Discrete Wavelet Transform (DWT) was applied to the noisy ECG signals. Five filters whose patterns are the closest to the morphology of the ECG signal were nominated to compete with each other to discover the optimal one for the process of filtering ECG signals. In order to get the ideal reconstruction (as possible), only orthogonal filters were examined. Furthermore, the orthogonal property allows inexpensive calculations. To achieve the aforementioned factors, the following filters (as demonstrated in **Fig. 4**): DB4, DB6, Coif4, Sym6, and Sym8 put under investigation. The No. Dec levels varied from 1 to 6.

At each level, the signal under the test is subjected to a bank of filters, as described in section 2. The next step is the thresholding

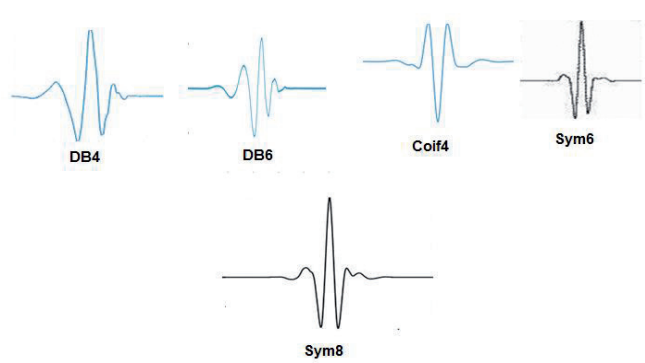

Fig. 4. *The patterns of the nominated wavelets.*

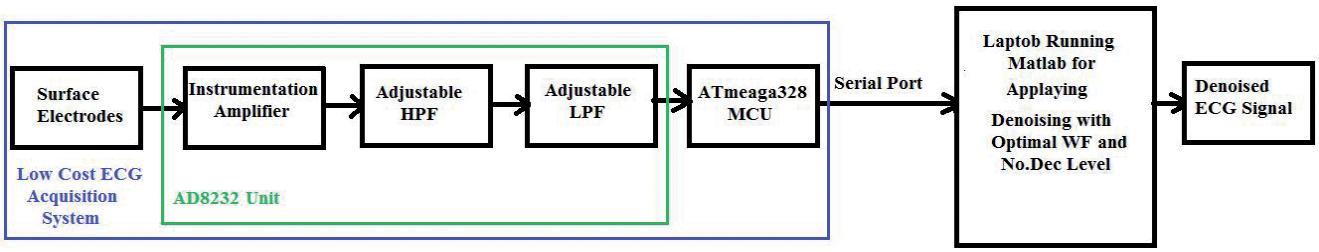

Fig. 5. *Block diagram of the SLA.*

process. There are two main thresholding methodologies, Soft thresholding (S_{th}) and Hard Thresholding (H_{th}). Many works [11,25,26,27] have proved the advantage of S_{th} in obtaining a smoother signal, as opposed to H_{th}, which causes discontinuities in the signal. Therefore, the S_{th} defined in Eq. (7) [28] is used in this paper.

$$S_{th}(D_c) = sign(D_c)(|D_c| - t_h) \; for \; |D_c| > t_h, \\ and \; 0 \; for \; |D_c| \le t_h, \tag{7}$$

where t_h is the threshold value.

Different threshold determination schemes have been suggested in the literature [14 and 29]. The universal approach (given in Eq. (8)) was used in this study for the straightforwardness of its calculations and its robust performance [22, 27].

$$t_h = ESD\sqrt{2\log(No.Samples)}, \\ ESD = MAD(D_c)/0.6745, \tag{8}$$

were ESD is the Estimation for the Standard Deviation of noise; MAD (Dc) is the Median Absolute Deviation for the Dc of the WT.

The thresholding process is followed by the reconstruction process, which is the inverse of the DWT, and then the denoised ECG signal is obtained. Finally, the performance was quantified using SNRo, MSE, and CCI. The WF and No. Dec levels that satisfied the highest SNR, CCI and lowest MSE were specified as the optimum.

3.2. Verification Phase

This phase includes the design of the SLA. The design of the SLA is composed of three units: surface electrodes that are placed on the human chest to record the signals, AD8232, and ATmega328 microcontroller as illustrated in **Fig. 5**. The AD8232 unit includes three components: Instrumentation Amplifier (IA) for signal amplification, amenable HPF for motion artifacts rejection, and amenable LPF for line interference cancellation. The board of the ATmega328 is equipped with a crystal of 16 MHz and 10 bits ADC. The f_s = 360 Hz. The computer, which runs the MATLAB R2020a is provided with digital signals via a USB port. Twenty signals (10 from males and 10 from females) were recorded. **Fig. 6** shows the collection process of ECG from a healthy male. The MATLAB 2020a program implements the denoising scheme with the optimal WF and No. Dec levels.

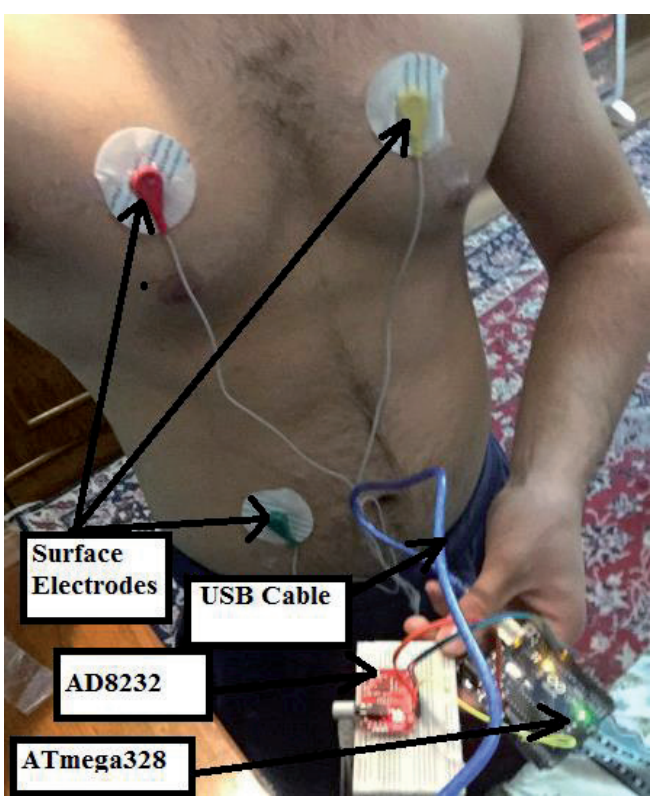

Fig. 6. *Recording ECG from a male.*

4. RESULTS AND DISCUSSION

The three main assessments metrics for specifying the optimal WF and No. Dec levels are the MSE, SNRo, and CCI, which are evaluated by equations (9), (10), and (11) respectively [2, 22]:

$$MSE = \sum_{p=1}^{z} \frac{1}{z}(v(p) - v^{-}(p))^2, \quad (9)$$

$$SNR = 10\log\left(\frac{\sum_{p=1}^{z}(v(p))^2}{\sum_{p=1}^{z}(v(p) - v(p)^{-})^2}\right), \quad (10)$$

$$CCL = \frac{\sum_{p=1}^{z}(v(p) - mean[v(p)])(v^{-}(p) - mean[v^{-}(p)])}{\sqrt{\sum_{p=1}^{z}(v(p) - mean[v(p)])^2 (v^{-}(p) - mean[v^{-}(p)])^2}}, \quad (11)$$

where $v(p)$ is the original signal, $v^{-}(p)$ is the denoised (filtered signal).

The comprehensive average results for each WF at different AWGN levels with various No. Dec levels are illustrated in **Tables 1-5**.

Table 1

The performance of the DB4 WF

Wavelet Filter: DB4								
AWGN with SNR=15 dB			AWGN with SNR=20 dB			AWGN with SNR=25 dB		
No. De composition Level	MSE	SNRo (db)	No. De composition Levell	MSE	SNRo (db)	No. De composition Level	MSE	SNRo (db)
1	0.1339	17.4668	1	0.0862	21.2932	1	0.0620	24.1475
2	0.1307	17.6727	2	0.0713	22.9378	2	0.0417	27.5974
3	0.1117	19.0418	3	0.0712	22.9454	3	0.0411	27.7129
4	0.1032	19.7304	4	0.0634	23.9631	4	0.0482	26.3364
5	0.1495	16.5063	5	0.1050	19.5767	5	0.0860	21.3083
6	0.1861	14.6066	6	0.1545	16.2236	6	0.1421	16.9466

Table 2

The performance of the DB6 WF

Wavelet Filter: DB6								
AWGN with SNR=15 dB			AWGN with SNR=20 dB			AWGN with SNR=25 dB		
No. De composition Level	MSE	SNRo (db)	No. De composition Levell	MSE	SNRo (db)	No. De composition Level	MSE	SNRo (db)
1	0.1248	18.0727	1	0.0803	21.9010	1	0.0674	23.4212
2	0.1232	18.1856	2	0.0670	23.4787	2	0.0494	26.1263
3	0.1042	19.6429	3	0.0597	24.4772	3	0.0389	28.2014
4	0.0929	20.6392	4	0.0535	25.4364	4	0.0403	27.8944
5	0.1856	14.6266	5	0.1480	16.5951	5	0.1375	17.2360
6	0.1999	13.9816	6	0.1670	15.5467	6	0.1579	16.0349

Table 3

The performance of the Coif4 WF

Wavelet Filter: Coif4								
AWGN with SNR=15 dB			AWGN with SNR=20 dB			AWGN with SNR=25 dB		
No. De composition Level	MSE	SNRo (db)	No. De composition Levell	MSE	SNRo (db)	No. De composition Level	MSE	SNRo (db)
1	0.1265	17.9599	1	0.0877	21.1427	1	0.0496	26.0950
2	0.1155	18.7516	2	0.0743	22.5788	2	0.0416	27.6133
3	0.1096	19.2016	3	0.0702	23.0692	3	0.0406	27.8317
4	0.0997	20.0242	4	0.0618	24.1855	4	0.0406	26.8911
5	0.1353	17.3728	5	0.1148	18.8027	5	0.0895	20.9625
6	0.1503	16.4603	6	0.1377	17.2243	6	0.1116	19.0493

Table 4

The performance of the Sym6 WF

Wavelet Filter: Sym6								
AWGN with SNR=15 dB			AWGN with SNR=20 dB			AWGN with SNR=25 dB		
No. De composition Level	MSE	SNRo (db)	No. De composition Levell	MSE	SNRo (db)	No. De composition Level	MSE	SNRo (db)
1	0.1258	18.0030	1	0.0894	20.9767	1	0.0634	23.9532
2	0.1186	18.5218	2	0.0776	22.2000	2	0.0502	25.9825
3	0.1065	19.4558	3	0.0732	22.7065	3	0.0413	27.8049
4	0.1004	19.9659	4	0.0653	23.6982	4	0.0407	27.6891
5	0.1347	17.4149	5	0.1111	19.0896	5	0.0927	20.6600
6	0.1517	16.3785	6	0.1357	17.3506	6	0.1205	18.3783

Table 5

The performance of the Sym8 WF

Wavelet Filter: Sym8								
AWGN with SNR=15 dB			AWGN with SNR=20 dB			AWGN with SNR=25 dB		
No. De composition Level	MSE	SNRo (db)	No. De composition Levell	MSE	SNRo (db)	No. De composition Level	MSE	SNRo (db)
1	0.1339	17.4668	1	0.0902	20.8939	1	0.0658	23.6371
2	0.1307	17.6727	2	0.0739	22.6253	2	0.0514	25.7737
3	0.1117	19.0418	3	0.0714	22.9212	3	0.0406	27.8189
4	0.1032	19.7304	4	0.0600	24.4331	4	0.0414	27.6697
5	0.1495	16.5063	5	0.1164	18.6835	5	0.0988	20.1048
6	0.1861	14.6066	6	0.1440	16.8333	6	0.1267	17.9459

In general, for each WF, the fourth decomposition level introduces the optimum results at very high noise (AWGN with SNR = 15 dB) and high noise (AWGN with SNR = 20 dB) environments, while the third decomposition level exhibits the best results at medium noise (AWGN with SNR = 25 dB) environments. The optimal WF achievement

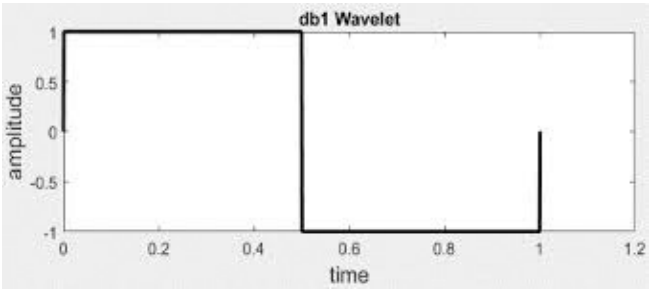

Fig. 7. *The DB1 (Haar) WF.*

is recorded for DB6. Here it is worth noting that the WFs were carefully nominated (as mentioned in section 3.1) to optimize the filtering process; in other words, all WFs have good and fairly close performance, and the study aims to discover the optimal WF. The wise choice for the WF grantees getting a good quality of the reconstruction, for instance, the selection of DB1 (Haar) is considered a bad decision because its shape (as displayed in **Fig. 7**) is very dissimilar to ECG, and thus worse reconstruction is obtained (much clinical information are lost) as appeared in **Fig. 8**. Since the difference is not significant between the third and fourth levels for medium noise environments, we have concluded that the No. Dec level = 4 is generally optimal for all noise environments. To enhance the produced results in terms of MSE, SNRo, a third assessment metric (CCI) was determined for each WF and it gave the same indication.

Since it agrees with the results of MSE and SNRo and to avoid the enormity of

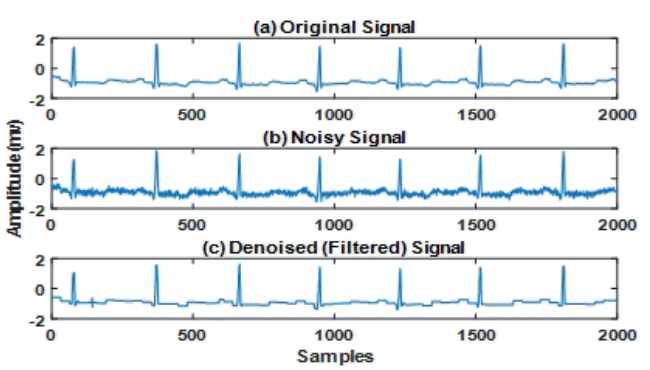

Fig. 8. *Denoising ECG using DB1 WF with No. Dec level = 4 in a high noise environment.*

Table 6
The average performance of the nominated WFs in terms of CCI at all noise environments with No. Dec level = 4

Wavelet Filter (WF)	Correlation Coefficient Index (CCI)
DB4	0.9829
DB6	0.9847
Coif4	0.9832
Sym6	0.9827
Sym8	0.9840

the results, only those cases with No. Dec level = 4 are shown in **Table 6**. Referring to the achievement of the WFs nominated in this study, DB6 is ranked first at all noise environments; for example, at high noise environments with No. Dec level = 4 (MSE = 0.0535, SNRo = 25.4364 dB and CCI = 0.9847) followed by Sym8 (MSE = 0.0600, SNRo = 24.4331 dB and CCI = 0.9840) then Coif4 (MSE = 0.0618, SNRo = 24.1855 dB and CCI = 0.9832), DB4 (MSE = 0.0634, SNRo = 23.9631 dB and CCI = 0.9829), and finally Sym6 (MSE = 0.0653, SNRo = 23.6982 dB, CCI = 0.9827). The detailed average results are demonstrated in the Tables 1-6.

Figures 9-11 demonstrate the attainment of denoising the ECG using the DB6 at various noise environments.

After conducting several experiments, Eq (8) has been developed with retaining its simplicity and improving the results. The improved threshold equation ($Th_{m,n}$) is defined in Eq. (12):

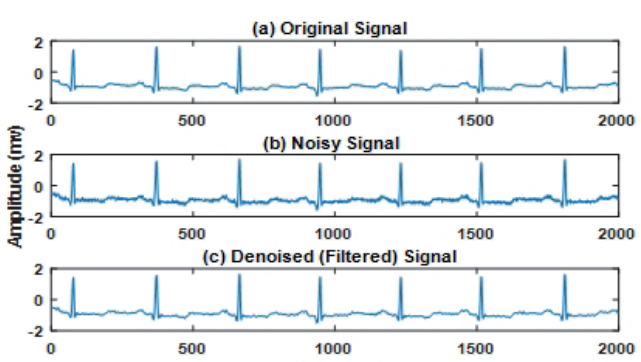

Fig. 9. *Denoising ECG using DB6 WF with No. Dec level = 4 in medium noise environment.*

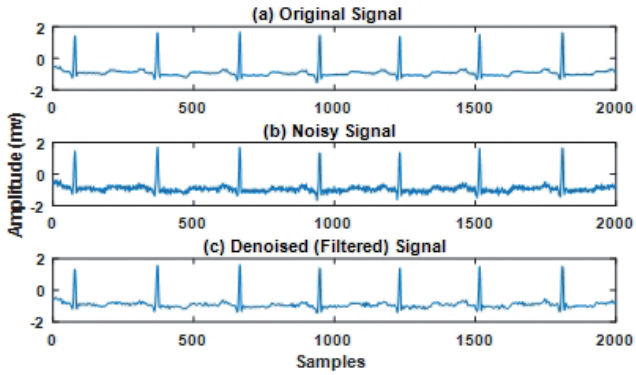

Fig. 10. *Denoising ECG using DB6 WF with No. Dec level = 4 in a high noise environment.*

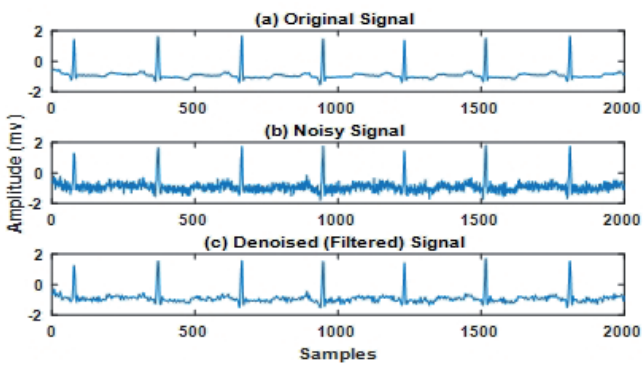

Fig. 11. *Denoising ECG using DB6 WF with No. Dec level = 4 in a very high noise environment.*

$$Th_{m,n} = 0.75\left(\frac{M}{N}\right)\frac{ESD_{n^*}\sqrt{2\log(No.Samples)}}{O_{m,n}+i}, \quad (12)$$

$$n = 1, 2, \ldots, m,$$

where $O_{m,n} = 2^{(M-(N/M))}$, M is the largest decomposition level, and N is the level at which the thresholding process is performed.

This paper introduces an adjustment factor (M/N). The adjustment factor M/N reduces progressively in response to the rise in No. Dec levels. This factor highlights the effect of the lower levels that are advantageous in the ECG signal by maximizing its value at the lower levels. Moreover, with this factor, the finest value of the tuning parameter (i) can improve the performance of the filter; this guarantees that the filtering is more effective; for instance, the achievements of the DB6 with No. Dec level = 4 using the $Th_{m,n}$ at very high noise environment are MSE = 0.0502, SNRo = 24.9810 dB, and CCI = 0.9861.

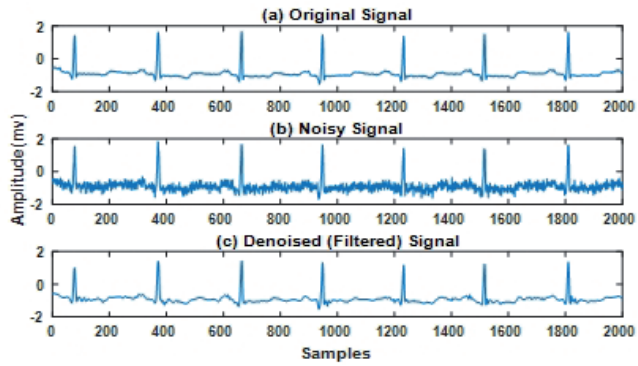

Fig. 12. *Denoising ECG using DB6 WF with No. Dec level = 4 using the $Th_{m,n}$ in a very high noise environment.*

Fig. 12 shows that the filtering process using the $Th_{m,n}$ is smoother, and the signal is reconstructed with less noise and this makes it closer to the original signal.

Based on the aforementioned analysis and the results from the investigative phase, the denoising approach using DB6-WF with No. Dec level = 4 was applied to the real ECG signals that were recorded by the SLA, which was designed in the verification phase. Excellent results were obtained, and this reflects the efficiency of the proposed framework in minimizing the noise of the ECG signals. **Fig. 13** illustrates a sample of applying this approach to the ECG signal recorded from a young male. For more testing of the reliability of the introduced denoising method, twenty ECG signals were collected using standard ECG equipment (Biocare iE300, specifications in [30]). The collected signals were saved (with and without applying the filtering option) into a USB flash memory

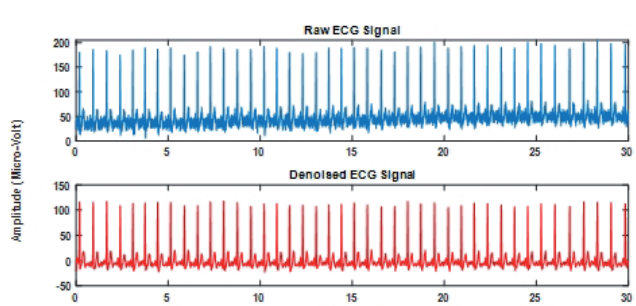

Fig. 13. *Sample of denoising ECG signal captured by SLA using the DB6 WF with No. Dec level = 4 and the $h_{m,n}$.*

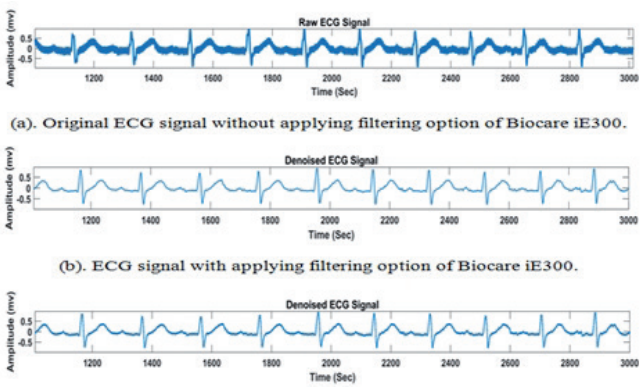

Fig. 14. *A sample of the visual performance comparison between Biocare iE300 and the proposed method.*

and then exported into MATLAB R2020a. The performance of the suggested denoising method is close to that of the Biocare iE300, as demonstrated in **Fig. 14**.

5. CONCLUSION

Noise that contaminates the ECG signal during its recording or transmission is an inevitable dilemma. This paper offered an excellent methodology based on WT for eliminating the noise of ECG signals by selecting the most appropriate WF and No. Dec levels; in addition, a simple and effective threshold calculation scheme was adapted to optimize the denoising process. The results revealed that the optimal WF was the DB6 with four levels of decomposition for both standard ECG signals taken from MIT-BIH and the ECG signals recorded using the suggested SLA and the standard ECG equipment, the "Biocare iE300". The filtered signal conserves critical features that can be utilized efficiently for medical diagnostic tasks.

REFERENCES

1. Ertuğrul ÖF, Acar E, Aldemir E, Öztekin A. Automatic diagnosis of cardiovascular disorders by sub images of the ECG signal using multi-feature extraction methods and randomized neural network. *Biomedical Signal Processing and Control*, 2022, 64:102260.
2. Liu B, Li Y. ECG signal denoising based on similar segments cooperative filtering. B*iomedical Signal Processing and Control,* 2021, 68:102751.
3. Jang YI, Sim JY, Yang J-R, Kwon NK. The Optimal Selection of Mother Wavelet Function and Decomposition Level for Denoising of DCG Signal. *Sensors*, 2021, 21(5):1851.
4. Ali AM, Ahmed AF, Najim AH. Efficient and Effective Scheme for ECG Compression. *IEEE Xplore,* Nov. 01, 2020.
5. Rodríguez R, Mexicano A, Bila J, Cervantes S, Ponce R. Feature Extraction of Electrocardiogram Signals by Applying Adaptive Threshold and Principal Component Analysis. *Journal of Applied Research and Technology,* 2015, 13(2):261-269.
6. Yang T, Gregg RE, Babaeizadeh S. Big data reveals insights for lead importance in ECG interpretation. *Journal of Electrocardiology*, 2021.
7. Jonkman AH, Juffermans R, Doorduin J, Heunks LMA, Harlaar J. Estimated ECG Subtraction method for removing ECG artifacts in esophageal recordings of diaphragm EMG. *Biomedical Signal Processing and Control*, 2021, 69:102861.
8. Xu B, Liu R, Shu M, Shang X, WangY. An ECG Denoising Method Based on the Generative Adversarial Residual Network. *Computational and Mathematical Methods in Medicine*, 2022, 2021:e5527904.
9. Kumar P, Sharma VK. Detection and classification of ECG noises using decomposition on mixed codebook for

quality analysis. *Healthcare Technology Letters*, 2020, 7(1):18-24.

10. Chatterjee S, Thakur RS, Yadav RN, Gupta L, Raghuvanshi DK. Review of noise removal techniques in ECG signals. *IET Signal Processing,* 2020, 14(9):569-590.
11. Zhang D et al. An ECG Signal De-Noising Approach Based on Wavelet Energy and Sub-Band Smoothing Filter. *Applied Sciences*, 2019, 9(22):4968.
12. AlMahamdy M, Riley HB. Performance Study of Different Denoising Methods for ECG Signals. *Procedia Computer Science*, 2014, 37:325-332.
13. Alickovic E, Babic Z. The effect of denoising on classification of ECG signals. *IEEE Xplore,* Oct. 01, 2015.
14. El B'charri O, Latif R, Elmansouri K, Abenaou A, Jenkal W. ECG signal performance de-noising assessment based on threshold tuning of dual-tree wavelet transform. *BioMedical Engineering OnLine*, 2017, 16(1).
15. Roy S, Chandra A. A new method for denoising ECG signal using sharp cut-off FIR filter. *IEEE Xplore,* Mar. 01, 2018.
16. Sraitih M, JabraneY. A denoising performance comparison based on ECG Signal Decomposition and local means filtering. *Biomedical Signal Processing and Control*, 2022, 69:102903.
17. Malik SA, Parah SA, Aljuaid H, Malik BA. An Iterative Filtering Based ECG Denoising Using Lifting Wavelet Transform Technique. *Electronics*, 2023, 12(2):387.
18. de Oliveira BR, Duarte MAQ, de Abreu CCE, Vieira Filho J. A wavelet-based method for power-line interference removal in ECG signals. *Research on Biomedical Engineering*, 2018, 34(1):73-86.
19. Kumar A, Komaragiri R, Kumar M. Design of wavelet transform based electrocardiogram monitoring system. *ISA Transactions,* 2018, 80:381-398.
20. Dwivedi AK, Ranjan H, Menon A, Periasamy P. Noise Reduction in ECG Signal Using Combined Ensemble Empirical Mode Decomposition Method with Stationary Wavelet Transform. *Circuits, Systems, and Signal Processing*, Jul. 2020.
21. T. R and V. B. A novel ECG signal compression using wavelet and discrete anamorphic stretch transforms. *Biomedical Signal Processing and Control,* 2022, p. 102773.
22. Zhang M, Wei G. An integrated EMD adaptive threshold denoising method for reduction of noise in ECG. *PLOS ONE*, 2020, 15(7):e0235330.
23. Mallat SG. A theory for multiresolution signal decomposition: the wavelet representation. *IEEE Transactions on Pattern Analysis and Machine Intelligence*, 1989, 11(7):674-693.
24. https://physionet.org/content/mitdb/.
25. He H, Wang Z, TanY. Noise reduction of ECG signals through genetic optimized wavelet threshold filtering. *IEEE Xplore*, Jun. 01, 2015.
26. Phinyomark A, Limsakul C, Phukpattaranont P. A Comparative Study of Wavelet Denoising for Multifunction Myoelectric Control. *IEEE Xplore*, Mar. 01, 2009.
27. Abbas EI, Rijab KSh, Fuad Ahmed A. Optimal Wavelet Filter for De-noising Surface Electromyographic Signal Captured From Biceps Brachii Muscle.

Engineering and Technology Journal, 2015, 33(1):198-207.

28. Donoho DL. De-noising by soft-thresholding. *IEEE Transactions on Information Theory*, 1995, 41(3):613-627.
29. Wang L, Sun W, Chen Y, Li P, Zhao L. Wavelet Transform Based ECG Denoising Using Adaptive Thresholding. *Proceedings of the 2018 7th International Conference on Bioinformatics and Biomedical Science – ICBBS'18*.
30. https://www.biocare.com.cn/html/en/Products/ECG/2015/1210/486.html.

DOI: 10.17725/rensit.2023.15.411

A nature-like anti-infective impregnation of a medical mask and a method for its application

Sergey N. Gaydamaka, Marina A. Gladchenko, Alla A. Kornilova
Lomonosov Moscow State University, https://www.msu.ru/
Moscow 119992, Russian Federation
E-mail: *s.gaidamaka@gmail.com, gladmarina@yandex.ru, prfnart@mail.ru*

Igor' V. Kornilov
Center Projection of Technologies
Moscow 115172, Russian Federation
E-mail: kiv@cdtch.ru

Received Ocrober 27, 2023, peer-reviewed November 03, 2023, accepted November 10, 2023, published December 06, 2023.

Abstract: **The potential for creating anti-infective impregnation based on aminopolysaccharide and silver ions is shown. Thanks to a unique water-insoluble complex of silver clusters (Ag 0.034 mg/cm^2 of mask material) in natural aminopolysaccharide, the impregnated material exhibits significant antibacterial properties. It has been shown that impregnation does not interfere with the effective removal of carbon dioxide, which can accumulate on the inside of the mask during breathing. It is noted that the use of a new nature-like anti-infective impregnation opens up the possibility of increasing the wear resistance of the impregnated material, while the impregnation is not removed from the surface of the mask material during intensive use of the mask.**

Keywords: **medical masks, impregnation, aminopolysaccharides, silver, antibacterial effect**

UDC 615.479.42; 677.494; 615.281.9

For citation: Sergey N. Gaydamaka, Igor' V. Kornilov, Marina A. Gladchenko, Alla A. Kornilova. A nature-like anti-infective impregnation of a medical mask and a method for its application. *RENSIT: Radioelectronics. Nanosystems. Information Technologies,* 2023, 15(4):411-414e. DOI: 10.17725/rensit.2023.15.411.

Contents

1. INTRODUCTION

Due to the numerous mutations of the new coronavirus infection COVID-19, the SARS-CoV-2 virus contains a lot of unpredictable complications. Despite the fact that the pandemic is over, today preventive measures for the non-proliferation of viral infections remain relevant [1-3]. The most common preventive measure is the wearing of a medical mask [4]. The medical mask is designed for an infected person and detains aerosols with viruses that he forms when talking, coughing and sneezing.
The disadvantages of using medical masks include the following factors:

- loose fit to the nose and mouth, the presence of gaps;
- touching the mask promotes the transfer of viruses to the skin of the face and hands, which increases the chances of their penetration into the body;
- wetting the mask significantly reduces its protective qualities;
- wearing a mask for more than the specified time, repeated use of disposable masks;
- significant accumulation of viruses on the mask promotes their penetration through the protective barrier.

Continuous wearing of one mask for more than 4 hours leads to oxygen deficiency and thus leads to headache, nausea, fatigue and loss of concentration. The gas permeability of the mask decreases over time and there is an accumulation of CO_2 in the undermask space, hence in the body, which negatively

affects the immune system, as well as the condition of the skin of the face, nasal mucosa and mouth.

Thus, when using medical masks, the following problems remain unresolved:

- Penetration of infectious agents through the pores of the mask during intensive breathing, including when using the mask by an infected person;
- Accumulation of infectious agents on the inside of the mask during breathing;
- Accumulation of carbon dioxide on the inside of the mask when breathing.

This work is devoted to the research of a new nature-like anti-infective mask impregnation, which is aimed at solving the existing problems of medical masks.

2. MATERIALS AND METHODS

The objects of research were disposable medical masks made of non-woven spunbond material. The spunbond was impregnated sequentially with two solutions by four procedures:

1. Application of an impregnating solution, a natural aminopolysaccharide with the inclusion of colloidal silver ions by the method of uniform micro-droplet spraying at the rate of 0.01 ml of solution per 1 cm^2 of spunbond.
2. Drying of spunbond in a hot air stream (80-120°C).
3. Application of the fixative (know-how), by the method of uniform micro-droplet spraying, after which the aminopolysaccharide takes it forms a water-insoluble form and forms clusters of silver that will not be removed from the spunbond when breathing.
4. Spunbond drying: wet spunbond is dried in a stream of hot air (80-120°C).

During drying, the aminopolysaccharide with silver ions is fixed at the pores, while the remnants of the fixative evaporate from the surface of the spunbond.

Then comparative physicochemical and microbiological studies were carried out with the masks. Atomic emission spectrometry with inductively coupled plasma of extracts from the mask material was carried out on the iCAP 6300 Duo device (Thermo Fisher Scientific, USA) by the method described in [5]. Energy dispersive *X*-ray spectroscopy based on a scanning electron microscope of mask material was performed on a Hitachi TM3030 scanning electron microscope (Hitachi Ltd., Japan) with an energy dispersive *X*-ray spectroscopy (EDS) Quantax system 70 (Bruker Nano GmbH, Germany) [6]. *X*-ray fluorescence analysis of the mask material was carried out using an Amptek semiconductor SDD Peltier cooled *X*-ray detector. The results were obtained under the following operating modes of the *X*-ray tube: 35 kV high voltage, the current is 20 mkA, the anode-Cr is a through-type. The irradiation area is 3 mm. The angle of incidence of *X*–ray radiation on the sample is 450, the sampling angle is 450. Physico-chemical quantitative determination CO_2 in the gas samples of the undermask space were carried out by the method described in [7].

Further, comparative tests of impregnated and non-impregnated masks for contamination with aerobic microorganisms when worn on the face and intensive breathing of a person for 1 hour were carried out. After use, the masks were placed in a hermetically sealed sterile plastic container and sent for microbiological analysis.

Microbiological determination of the total number of aerobic microorganisms on the mask tissue was determined by the method described in [8].

3. RESULTS AND DISCUSSIONS

A comparative analysis of microphotographs of impregnated and non-impregnated masks obtained using a scanning electron microscopy showed that the fibers of the studied material of the impregnated medical mask are everywhere covered with a gel-like colorless substance that does not violate the structure of the material and the size of the pores (**Fig. 1**).

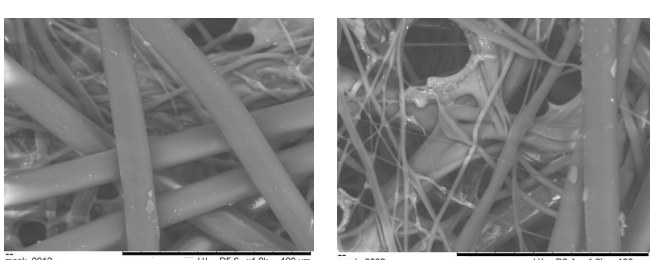

a *b*

Fig. 1. *Microphotographs of mask material obtained using a scanning electron microscope: a – non-impregnated mask, b - impregnated mask.*

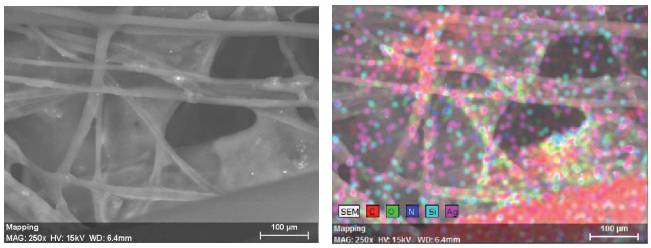

a *b*

Fig. 2. *Microphotography of the impregnated mask material obtained by energy dispersive X-ray spectroscopy (b) on the basis of a scanning electron microscope (a).*

Analysis of the material of the impregnated mask using energy dispersive *X*-ray spectroscopy based on a scanning electron microscopy showed the presence of silver and silicon ions (**Fig. 2**).

The data of energy dispersive X-ray spectroscopy based on a scanning electron microscopy were confirmed by *X*-ray fluorescence analysis (**Fig. 3**).

In addition to silver, zinc and traces of iron were found in the impregnated mask, in contrast to the non-impregnated mask. It is also noted that the impregnated mask has an increased titanium content compared to non-impregnated mask.

The analysis by atomic emission spectrometry with inductively coupled plasma of extracts from mask material showed the silver content on the impregnated mask in contrast to the non-impregnated mask (**Table 1**).

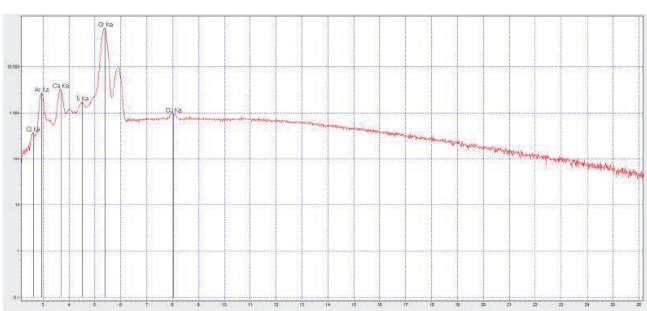

a

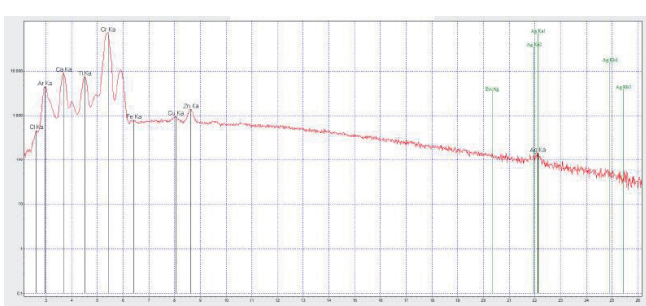

b

Fig. 3. *Spectra of X–ray fluorescence analysis of mask material: a – non-impregnated mask, b - impregnated mask.*

Table 1

Comparative content of silver, accumulation of carbon dioxide in exhaled air in non-impregnated and impregnated masks and the content of microorganisms on the mask material after 1 hour of use

The mask name	Ag mg/cm² of mask material	Carbon dioxide content, %	Total aerobic bacterial count, CFU/g mask
Non-impregnated mask	0.000	0.5	190
Impregnated mask	0.034±0.001	0.5	10

Studies on a stand with a breathing machine for determining the content of carbon dioxide in the undermask space were conducted up to the maximum value of carbon dioxide in the undermask space, with a well-established breathing cycle, until a stable value of the carbon dioxide content in the exhaled air was established. The retention of carbon dioxide in the undermask space depends on the permeability and density of the filter material. The permeability of the tested masks was 72-76%. With such permeability, fluctuations in carbon dioxide retention are insignificant.

As a result of the data obtained, it was concluded that there was no deterioration in the gas permeability of the impregnated mask compared to the non-impregnated one. At the same time, the removal of carbon dioxide from the undermask space remained at the same level, despite the impregnation and filling of the pores of the mask with natural anti-infective aminopolysaccharide (Table 1).

4. CONCLUSION

At the end of the research cycle, comparative tests of non-impregnated and impregnated masks for bacteriological contamination of the mask material adjacent to the face after 1 hour of use were carried out. The antibacterial effect of the impregnated mask was significantly increased (19 times) compared to the non-impregnated mask (Table 1).

These results show the potential to create a new anti-infective impregnation:

- due to the unique complex of silver clusters in the natural aminopolysaccharide, the impregnated material exhibits significant antibacterial properties;
- the impregnation does not prevent the effective removal of carbon dioxide, which can accumulate on the inside of the mask when breathing.

The use of a new nature-like anti-infective impregnation opens up the possibility of increasing the wear resistance of the impregnated material, while the water-insoluble impregnation is not removed with intensive use of the treated mask. In the future, it is planned to test the impregnated mask for resistance to washing in water, resistance to pathogenic microorganisms and viruses, as well as the absence of the release of harmful substances and allergens to human skin when used.

REFERENCES

1. Wu F, Zhao S, Yu B. et al. A new coronavirus associated with human respiratory disease in China. *Nature*, 2020, 579:265-269. DOI: 10.1038/ s41586-020-2008-3.
2. Alla A. Kornilova, Sergey N. Gaydamaka, Marina A. Gladchenko, Dmitry Ya Agasarov, Igor V. Kornilov, Maxim A. Gerasimov. Thermal waves and flow features of pulsed thermally stimulated biochemical reactions in viral particles interaction with cells. *RENSIT: Radioelectronics. Nanosystems. Information Technologies*, 2022, 14(1):87–96e. DOI: 10.17725/rensit.2022.14.087.
3. Alla A. Kornilova, Sergey N. Gaydamaka, Marina A. Gladchenko, Dmitry Ya Agasarov, Igor V. Kornilov, Maxim A. Gerasimov. Review of significant genome modifications cause of the new coronavirus infections (historical review). *History of science and technology,* 2022, 5:3-11. DOI: 10.25791/ INTSTG.5.2022.1352.
4. Tcharkhtchi A, Abbasnezhad N, Zarbini Seydani M, Zirak N, Farzaneh S, Shirinbayan M. An overview of filtration efficiency through the masks: Mechanisms of the aerosols penetration. *Bioactive Materials*, 2021, 6(1):106-122. DOI: 10.1016/j. bioactmat.2020.08.002.
5. GOST R 55845-2013 Reagents and especially pure substances. Determination of impurities of chemical elements by atomic emission spectrometry with inductively coupled plasma.
6. Gaydamaka S, Gladchenko M, Maslova O, Senko O, Kornilova A, Kornilov I. Application of the hybrid chemical-biocatalytic approach for conversion of nitrocellulose-containing sewage sludge. *Processes,* 2023, 11(7):2017. DOI: 10.3390/pr11072017.
7. GOST 12.4.294-2015 Personal respiratory protection equipment. Filter half masks for protection against aerosols. General technical conditions.
8. GOST R 58396-2019 item 5.2.5. MEDICAL MASKS. Requirements and test methods.

DOI: 10.17725/rensit.2023.15.415

Generation and detection of spin current in iridate/manganite heterostructure

Georgy D. Ulev, Gennady A. Ovsyannikov, Karen Y. Constantinian, Anton V. Shadrin, Ivan E. Moscal, Peter V. Lega

Kotel'nikov Institute of Radioengineering and Electronics of Russian Academy of Sciences, http://cplire.ru/
Moscow 125009, Russian Federation

E-mail: gdulev@edu.hse.ru, gena@hitech.cplire.ru, karen@hitech.cplire.ru, shadrinant@mail.ru, moskal@hitech.cplire.ru, lega_peter@list.ru

Received September 03, 2023, peer-reviewed September 10, 2023, accepted September 17, 2023, published December 06, 2023.

Abstract: **The results of experimental studies on spin current at the interface of iridate/manganite heterostructure $SrIrO_3/La_{0.7}Sr_{0.3}MnO_3$ consisted of oxide epitaxial films with nanometer thickness are presented. A pure spin current was induced by microwave irradiation in GHz frequency band under conditions of ferromagnetic resonance. The spin current was detected due to inverse spin-Hall effect measuring the spectral characteristics of charge current arising on electrically conductive $SrIrO_3$ film with strong spin-orbit interaction. The spin-Hall angle, which characterizes the efficiency of spin current conversion to the charge current, was determined by measurements of the angular dependences of spin magnetoresistance of the iridate/manganite interface.**

Keywords: **spin mixing conductance, spin magnetoresistance, spin-orbit interaction, thin film heterostructure, strontium iridate, manganite**

PACS: 75.47.Lx, 75.25.-j, 73.63.−b

Acknowledgments: The research was supported by a grant from the Russian Science Foundation (project No. 23-49-10006).

For citation: Georgy D. Ulev, Gennady A. Ovsyannikov, Karen Y. Constantinian, Anton V. Shadrin, Ivan E. Moscal, Peter V. Lega. Generation and detection of spin current in iridate/manganite heterostructure. *RENSIT: Radioelectronics. Nanosystems. Information Technologies*, 2023, 15(4):415-424e. DOI: 10.17725/rensit.2023.15.414.

Contents

1. INTRODUCTION

Spintronic devices of give opportunities to solve the problem of heating and energy dissipation in microelectronics, since the spin transfer (spin current) does not generate heat. In modern electronic systems the detection and generation of pure spin current (without charge transfer) require completely different approach to the problem and is based on usage of spin current. One of the possible techniques of generation of pure spin current at the ferromagnetic/normal (non-magnetic) metal interface is the precession of ferromagnetic magnetization (F) induced by microwave magnetic field under ferromagnetic resonance (FMR) conditions. The magnitude of the spin current is determined by the amplitude of magnetization precession and the spin-mixing conductance, which in general has both real and imaginary parts. The spin current could be recorded by charge current, induced by the inverse spin-Hall effect (ISHE) in a metal (N) with strong spin-orbit interaction [1-5]. The presence of both the spin-Hall effect (SHE) and the ISHE causes the spin-Hall magnetoresistance (SMR) in F/N heterostructure [6]. Measurement of the SMR angle dependences is a convenient

tool for determination of spin Hall angle θ_{SH}, which characterizes the efficiency of conversion of spin current into the charge current [6-8].

Experimental study of spin current excitation at the FMR (spin pumping) and its registration due to ISHE in F/N structures where carried out in [2,3] using platinum (Pt) as N metal and permalloy (NiFe) as F metal. Structures with N metal deposited on the top of insulating ferromagnet, the iron-yttrium garnet (YIG) were investigated as well [9,10]. It should be noted, mostly N-metal with strong spin-orbit interaction (SOI) was used [10,11].

In the present work, the 5d transition metal oxide $SrIrO_3$ [12,13] was used, which along with the strong SOI exhibits also electron-electron interaction. The combination of these effects leads to non-trivial quantum phases [14] and to the possibility of controlling of magnetic anisotropy [5]. The charge-spin coupling of $SrIrO_3$ been studied in structures with a metallic ferromagnet deposited on the top of $SrIrO_3$: $SrIrO_3$/Py [15,16], and $SrIrO_3$/$Co_{1-x}Tb_x$ [17]. In these works it was shown that an anomalously large spin-Hall angle is caused by the presence of SOI3 in $SrIrO_3$ which induces a curvature of Berry phase [15,16].

The usage of oxide materials allows to realize heterostructures with atomically smooth interface in the case of growth of thin epitaxial film of strontium iridate $SrIrO_3$ over the epitaxial film $La_{0.7}Sr_{0.3}MnO_3$, grown on $(LaAlO_3)_{0.3}(Sr_2AlTaO_6)_{0.7}$ (LSAT), $NdGaO_3$, or $SrTiO_3$ substrates. Technically, this is feasible by either laser ablation [18-20], or by magnetron sputtering at high temperature [12]. It has been demonstrated that an increase in Hilbert damping in $SrIrO_3$/$La_{0.7}Sr_{0.3}MnO_3$ heterostructure is caused by spin current which flows across the interface [12,18,19]. Experimental studies of spin current characteristics under influence of spin pumping showed that the anisotropic magnetoresistance of $La_{0.7}Sr_{0.3}MnO_3$ also contributes to the total response along with the component, caused by spin current generation [8,12,13,18].

2. MATERIALS AND METHODS

Thin epitaxial films of strontium iridate $SrIrO_3$ (further, SIO3) and manganite $La_{0.7}Sr_{0.3}MnO_3$ (LSMO) with thicknesses of 10-50 nm were grown on single crystal (110)$NdGaO_3$ (NGO) substrates using radio frequency magnetron sputtering at substrate temperatures of 770-800°C in a mixture of Ar and O_2 gases at a total gas pressure of 0.3-0.5 mbar [12].

The crystal structure of obtained heterostructures was investigated by *X*-ray diffraction analysis and the transmission electron microscopy (TEM). **Fig. 1** shows a TEM image of cross section of the heterostructure, demonstrating the SIO3/LSMO interface and the interface of the LSMO film with the NGO substrate. We will describe the crystal lattice of SIO and LSMO as a distorted pseudo-cube with parameters a_{SIO} = 0.396 nm and a_{LSMO} = 0.389 nm, as the growth of heterostructure is realized by cube-on-cube mechanism with the following ratios: $SrIrO_3$||(001)$La_{0.7}Sr_{0.3}MnO_3$||(110) $NdGaO_3$, and [100] $SrIrO_3$||[100] $La_{0.7}Sr_{0.3}MnO_3$||[001] $NdGaO_3$ [12].

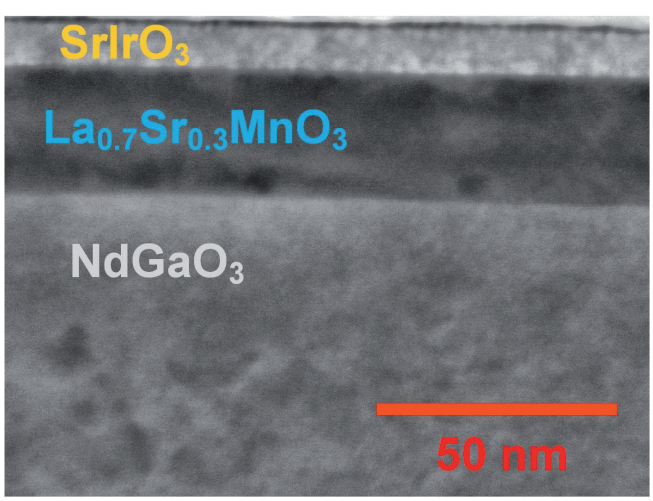

Fig. 1. *Cross section of $SrIrO_3$/$La_{0.7}Sr_{0.3}MnO_3$ heterostructure on $NdGaO_3$ substrate, obtained by transmission electron microscope. The additional Pt platinum film deposited for ion etching was removed.*

3. RESULTS AND DISCUSSION

In the SIO3/LSMO heterostructure, the paramagnetic SIO3 film plays role of a normal metal with strong SOI, while ferromagnetic LSMO is a half-metal with an almost 100% polarization at low temperatures.

In experiments with spin pumping at microwaves, the main decisive parameters are the spin diffusion length λ which characterizes spin current dissipation in N metal, and the spin-Hall angle θ_{SH} – the ratio of spin to charge currents at the N/F interface, and the spin mixing conductance $g^{\uparrow\downarrow}$, which is determined by the electron scattering matrix at N/F and characterizes the spin transfer transparency of angular magnetic momentum through the interface [4,5].

3.1. Spin current generation

At the FMR spin pumping, spin current j_S flows through the SIO3/LSMO interface, which is characterized by the spin mixing conductance $g^{\uparrow\downarrow}$, consisting of a real (Re $g^{\uparrow\downarrow}$) and an imaginary part (Im $g^{\uparrow\downarrow}$), as well by the amplitude of precession of magnetic moment m under influence of magnetic component of the microwave field [4,13]:

$$j_S = \frac{h}{4\pi}\left(\mathrm{Re}\, g^{\uparrow\downarrow}\ \mathrm{m}\frac{\mathrm{dm}}{\mathrm{dt}} + \mathrm{Im}\, g^{\uparrow\downarrow}\frac{\mathrm{dm}}{\mathrm{dt}}\right). \quad (1)$$

The spin current was recorded by measuring the voltage on a sample shaped ad s strip of SIO3/LSMO heterostructure grown on an NGO substrate with metal Pt contacts. To set the microwave magnetic field, the sample under the test was placed on a microstrip line, allowing to be carry out measurements in frequency band f = 2–20 GHz [10]. A constant magnetic H-field was set in the plane of the substrate and was directed perpendicular to the emerging charge current (along the Y axis), and the microwave magnetic field was excited by a short-circuited microstrip line with a microwave magnetic field component directed along the X axis. Precession of the magnetization of the LSMO film around the SIO3/LSMO strip induces a spin current perpendicular to the SIO3/LSMO interface (Z axis) and could be detected by voltage measurements due to ISHE (see inset in **Fig. 2**). The charge current j_Q is related to the spin current j_S through a dimensionless parameter – the spin Hall angle θ_{SH} [2,6]:

$$\vec{j}_Q = \theta_{SH}\frac{2e}{\hbar}\left[\vec{n}\times\vec{j}_S\right], \quad (2)$$

where $\vec{n}$ is the unit vector of the spin momentum direction.

Fig. 2 shows the magnetic-field dependence of the voltage appeared on the SIO3/LSMO heterostructure under the influence of microwave field at frequency f = 2.3 GHz and power 20 mW at T = 300 K. It is seen that the sign of the response $V(H)$ is reversed when the direction of dc magnetic field is changed. This caused by the change in the direction of induced charge current due to direction reversal of vector $\vec{n}$, reversing the direction of dc magnetic field. In experiment, caused by parasitic microwave detection by Pt contacts some asymmetry of response amplitudes for opposite directions

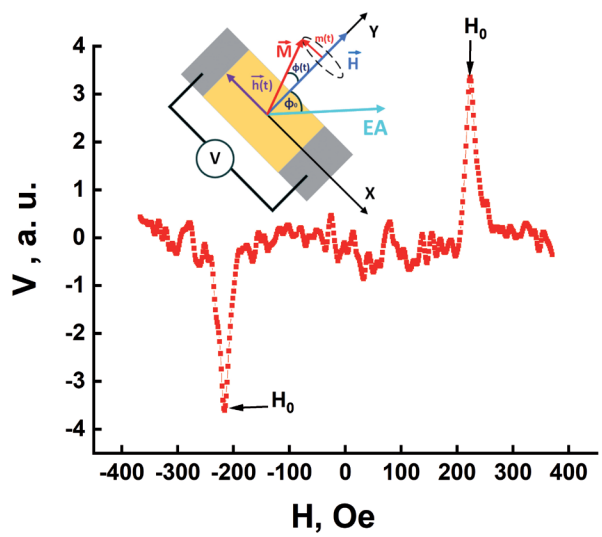

Fig. 2. *Magnetic-field dependence of the response of $SrIrO_3$/$La_{0.7}Sr_{0.3}MnO_3$ heterostructure to microwave field applied at frequency f = 2.3 GHz at T = 300 K with power of 30 mW. The inset shows the topology of the heterostructure indicating directions of microwave magnetic component h(t) and dc H magnetic field, as well as the direction of the charge current flow (registration of voltage V along the X axis) caused by the spin current.*

of *H*-field can be observed. An anisotropic magnetoresistance (AMR) response also contributes, which, however, under the certain conditions does not depend on direction of dc magnetic field [8,21].

Fig. 3 shows the voltage response caused by spin current at f = 2.3 GHz, T = 300 K, obtained from the half-difference of responses (Fig. 2) at opposite directions of *H*-field. The response shape is described well enough by the Lorentz function. The contribution caused by contacting phenomena and AMR was by an order in magnitude smaller, than amplitude of spin current response.

The flow of spin current through the interface causes an additional damping of spin precession. In experiment, this manifests itself in broadening of the FMR spectrum line , which is usually determined by the Hilbert spin damping coefficient α [4,11,22]. Parameters α and ΔH are coupled by a relation [23]: $\Delta H(f) = 4\alpha\pi f/\gamma + \Delta H_0$, where γ is the gyromagnetic ratio, and ΔH_0 – is broadening cased by magnetic inhomogeneity. Note, here we neglect the contributions of other damping sources (see, for example, [24]). The frequency-independent broadening ΔH_0 = 6±1 Oe is small and determined by the magnetic inhomogeneity of the LSMO film in the heterostructure. For LSMO films we get α_{LSMO} = (2.0±0.2)·10^{-4} and damping increases in heterostructure SIO3/LSMO $\alpha_{SIO/LSMO}$ = (6.7±0.8)·10^{-4}. The increase in Hilbert damping after deposition of SIO3 film makes it possible to estimate the real part of the spin mixing conductance Re$g^{\uparrow\downarrow}$ [4,21,25]. For LSMO magnetization M = 370 Oe and the thickness of the LSMO film d_{LSMO} = 30 nm, we obtain Re$g^{\uparrow\downarrow}$ = (3.5±0.5)·10^{18} m^{-2}. Note, that the obtained value coincides in order of magnitude with Re$g^{\uparrow\downarrow}$ = 1.3·10^{18} m^{-2}, determined in [19]. Changing thin film thickness of $SrIrO_3$ in SIO3/LSMO heterostructure from 1.5 nm to 12 nm value of Re$g^{\uparrow\downarrow}$ is changed from 0.5·10^{19} m^{-2} to 3.6·10^{19} m^{-2} [18].

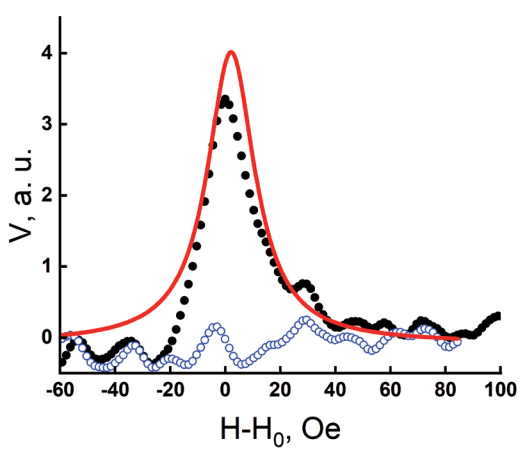

Fig. 3. *Voltage response induced by spin current at FMR pumping frequency f = 2.3 GHz, T = 300 K, obtained from the half difference of peaks at opposite directions of dc magnetic field. Filled circles are experimental, solid line is the Lorentz line approximation. Empty circles - response caused by parasitic contact phenomena and anisotropic magnetoresistance (half-sum of peaks at opposite directions of magnetic field).*

According to the theory based on the spin interaction between localized and conducting electrons the spin mixing conductance Re$g^{\uparrow\downarrow}$ is determined by resistivity ϱ_{SIO} and spin diffusion length λ_{SIO} of the normal metal with SOI, in our case SIO3 film [25]:

$$\mathrm{Re}g^{\uparrow\downarrow} \approx (h/e^2)/(\varrho_{SIO}\lambda_{SIO}). \quad (3)$$

Taking $h/e^2 \approx 25.8$ *kΩ* , for λ_{SIO} = 1 nm [19] and ϱ_{SIO} = 3·10^{-4} *Ω* cm [12] from relation (4)

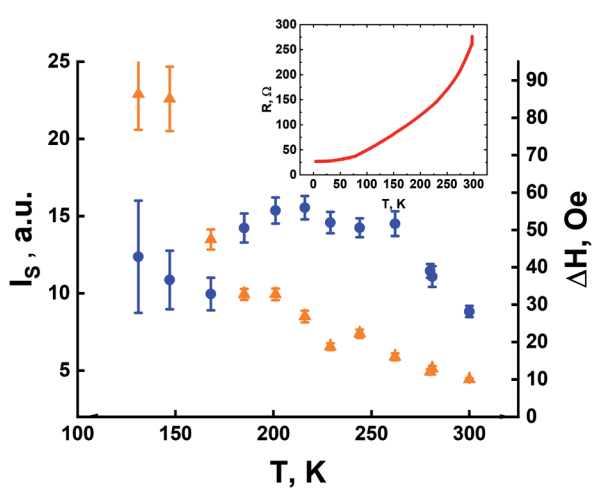

Fig. 4. *Temperature dependences of spin current amplitude (filled circles) and line-widths (filled triangles). The spin current value is obtained by dividing the voltage response by the resistance of heterostructure. Inset: temperature dependence of heterostructure's resistance at H = 0.*

we obtain $Reg^{\uparrow\downarrow} \approx 8.6 \cdot 10^{18}$ m^{-2}. The obtained value is consistent in order of magnitude with the experimental data for 3*d* transition metals, and for metallic ferromagnets Co, Ni, Fe the parameter $Reg^{\uparrow\downarrow}$ is in the range $6 \cdot 10^{18}$-$8 \cdot 10^{20}$ m^{-2} [25,26], although relation (3) is just a qualitative estimate of $Reg^{\uparrow\downarrow}$ and does not take into account the influence of spin-orbit interaction.

Assuming that the deviation of the $H_0(f)$ dependence for SIO3/LSMO heterostructure from $H_0(f)$ of the LSMO film can be described by a change in gyromagnetic ratio γ and attributed to a presence of an imaginary part of the spin mixing conductance, we obtain a value for significantly higher than estimated for ferromagnetic structures with Pt [4,22].

Closer to realistic experimental conditions, on our opinion, is $Img^{\uparrow\downarrow}$ 10^{19} m^{-2}, obtained taking into account the error of $H_0(f)$ function measurement. As shown in works [12,22], indeed, value of $Img^{\uparrow\downarrow}$ is comparable to the value of $Reg^{\uparrow\downarrow}$. Moreover, measurements of Hall magnetoresistance for Pt/EuS [27] and W/EuO [28] structures showed that $Img^{\uparrow\downarrow}$ exceeds $Reg^{\uparrow\downarrow}$ by a factor of 3 and 10 times, respectively. Note, the appearance of magnetization in the direction perpendicular to the plane, for example as in the case of superlattice made from SIO3/LSMO heterostructures may play a significant role [17].

Fig. 4 shows the temperature dependence of the spin current amplitude and response linewidth of the heterostructure. The spin current amplitude is obtained from response voltage division by the resistance of the heterostructure, shown in the inset to Fig. 4. It is seen that an increase of spin current observed with decreasing the temperature for the Pt/LSMO heterostructure [8] is not observed in our case, which is probably caused by the presence of a conducting layer at the SIO3/LSMO interface [13].

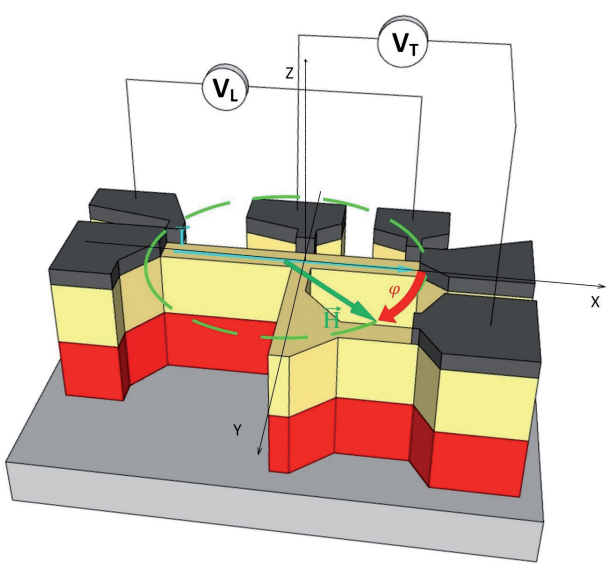

Fig. 5. *Schematic 3D image of $SrIrO_3/La_{0.7}Sr_{0.3}MnO_3$ heterostructure on (110)$NdGaO_3$ substrate with Pt contact pads. The current I is set along the X axis, the angle φ between the magnetic field H and the current I was varied by rotating the sample in the X-Y plane.*

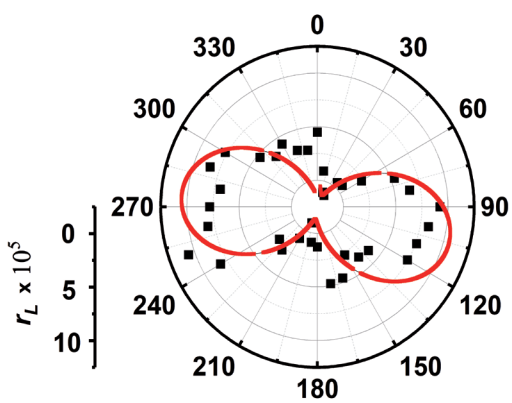

a

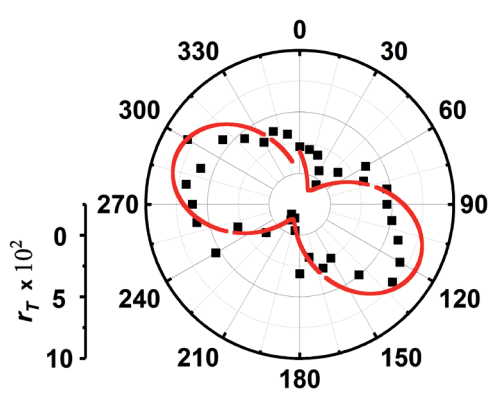

b

Fig. 6. *Angular dependences of normalized values of magnetoresistance of heterostructure $r_L(T)$ (squares) and approximation by sinusoidal dependence (solid line) in polar coordinates, taken at the field H = 100 Oe at T = 300 K. (a) transverse magnetoresistance, (b) longitudinal. The scale of magnetoresistance variation is shown on the left.*

3.2. Spin current detection using inverse spin Hall effect

The inverse spin Hall effect (ISHE) is used to detect the spin current [1,5]. In this case, the ratio of spin and charge currents is determined by a dimensionless parameter – spin Hall angle θ_{SH} (2) [2,6].

For determination the θ_{SH} value, the Hall geometry of the SIO3/LSMO heterostructure shown in **Fig. 5** and a 4-point measurement scheme was used. A constant magnetic field H was set in the plane of the SIO3/LSMO interface of heterostructure. The measured voltages were V_L, proportional to the longitudinal magnetoresistance, and V_T, proportional to the transverse (planar) Hall magnetoresistance. Along the X direction (see Fig. 5), a current I = 0.5 mA at frequency F = 1.1 kHz was set and a lock-in amplifier with high-sensitivity was used for voltage measurement. The substrate with the sample was rotated around the normal to the substrate in order to change the angle φ between the magnetic field H and the current I. The longitudinal magnetoresistance was determined from $R_L = V_L/I$, and the transverse magnetoresistance by $R_T = V_T/I$.

Magnetic-field dependences in normalized units of the change in magnetoresistance $r_{L(T)} = \Delta R_{L(T)}/R_0$ (longitudinal ΔR_L, and transverse ΔR_T) of SIO3/LSMO heterostructure, where $\Delta R_{L(T)} = R_{L(T)} - R_0$ (R_0 – magnetoresistance at $H = 0$) vs. angle φ between magnetic field H and current I were recorded. The obtained values were compared with magnetoresistance measurements for LSMO films, as well as for structures with a platinum film deposited on top of an epitaxial LSMO film on a substrate (Pt/LSMO). The measured longitudinal magnetoresistance $r_L(\varphi)$ contains in addition to the spin longitudinal magnetoresistance r_{LS} also a contribution from the anisotropic magnetoresistance (AMR) of the ferromagnetic LSMO film $r_A = R_A/R_0$. For the case of transverse magnetoresistance $r_T(\varphi)$ contains also a component of the planar Hall effect magnetoresistance.

Fig. 6a shows the angular dependence of the longitudinal magnetoresistance $r_L(\varphi)$ of the SIO3/LSMO heterostructure in polar coordinates. The dependence of $r_L(\varphi)$ observed in the experiment is a parallel connection of r_{LS} and r_A. In this case, the angular dependence of AMR is described by the function $r_A \cos 2\varphi$, which looks like a dependence of spin magnetoresistance of the SIO3/LSMO heterostructure [6]:

$$r_{LS} = r_1 \cos^2 \varphi, \quad (4)$$

where

$$r_1 = \theta_{SH}^2 \frac{\lambda_{SIO}}{d_{SIO}} \mathrm{Re} \frac{2\lambda_{SIO}\rho_{SIO}(\mathrm{ReG}^{\uparrow\downarrow} + i\,\mathrm{ImG}^{\uparrow\downarrow})}{1 + 2\lambda_{SIO}\rho_{SIO}(\mathrm{ReG}^{\uparrow\downarrow} + i\mathrm{ImG}^{\uparrow\downarrow})}. \quad (5)$$

$\mathrm{ReG}^{\uparrow\downarrow} = \mathrm{Reg}^{\uparrow\downarrow} e^2/h$, $\mathrm{ImG}^{\uparrow\downarrow} = \mathrm{Img}^{\uparrow\downarrow} e^2/h$, it is assumed that the spin diffusion length λ_{SIO} is much smaller than the SIO3 film thickness d_{SIO}. When current I flows longitudinally (along the X direction) we obtain a sinusoidal dependence $r_L(\varphi)$ (Fig. 6*a*). The phase shift in $r_L(\varphi)$ is caused by the difference between the coordinate of the substrate edge, from which the angle φ is counted, and the direction of the LSMO film magnetization easy axis, which is given by the crystallographic direction of the [001]$NdGaO_3$ substrate on which the LSMO film was epitaxially grown [12]. Using the values of SIO3 film resistivity $\varrho_{SIO} = 3 \cdot 10^{-4}$ Ω cm [12] and λ_{SIO} = 1

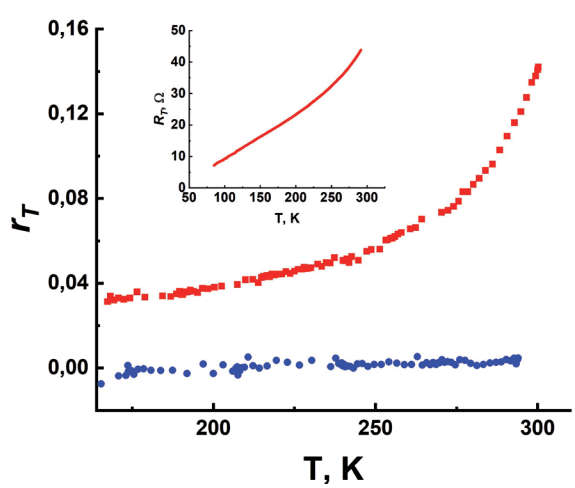

Fig. 7. *Temperature dependence of transverse (Hall) magnetoresistance r_T. Curve (1) corresponds to the angle φ = 210°, at which r_T is maximum, curve (2) was taken at the minimum value of r_T (φ = 275°). The inset shows the temperature dependence of the transverse (Hall) resistance at H = 0.*

nm [19] obtained at room temperature and the data for $Reg^{\uparrow\downarrow}$ и $Img^{\uparrow\downarrow}$ from the Part 3.1. of this paper, for thicknesses d_{SIO} = 10 nm and d_{LSMO} = 30 nm from amplitudes of magnetoresistance $r_L(\varphi)$ using eq. (4) and (5) we obtain $\theta_{SH} = 0.03\pm0.01$ for spin-Hall angle. Obtained value is an order of magnitude smaller than for the transverse case (Fig. 6*b*), but is about 4 times larger than the spin Hall angle for c Pt heterostructures [3,6,8].

Fig. 6*b* shows the angular dependence of the transverse magnetoresistance $r_T(\varphi)$ in polar coordinates of the SIO3/LSMO heterostructure which, in the general case, is the sum of the contributions from the spin-Hall magnetoresistance r_H and the contribution from the out-of-plane magnetoresistance r_2 [6].

$$r_{TS} = \frac{r_1}{2}\sin 2\varphi + r_2 \cos\theta, \qquad (6)$$

where θ is the angle between the current and magnetization along the Z axis perpendicular to the substrate plane (not shown in Fig. 5). The obtained values of r_T turn out are by an order of magnitude larger than in the case of the longitudinal magnetoresistance r_L even considering existence only the first term in (6) at $\theta = \pi/2$. As a result, from the data from $r_T(\varphi)$ we obtain $\theta_{SH} = 0.35\pm0.05$ for the SIO3/LSMO heterostructure. Thus, from the transverse magnetoresistance measurements, we obtained a value of θ_{SH} about 10 times larger than that from the longitudinal magnetoresistance, which, likely, caused by shunting of the longitudinal AMR magnetoresistance of the LSMO film [13]. Note, $\theta_{SH} \approx 0.3$ was obtained in SIO3/LSMO heterostructures [11,16] by other methods. The second term dependent on the imaginary part of the complex spin mixing conductance [6] in eq. (6) arises due to the magnetization directed perpendicular to the substrate plane and can cause an increase in magnetoresistance, which was observed in SIO3/LSMO superlattices [17]. High values of the spin Hall angle in structures with SIO3 films were reported earlier: θ_{SH} = 0.76 for Py/$SrIrO_3$ [15] and θ_{SH} = 1.1 for $SrIrO_3$/$Co_{1-x}Tb_x$ [29]. In order of magnitude, these values are close to θ_{SH}, observed in structures with topological insulators [30].

When the SIO3/LSMO heterostructure was cooled down to liquid nitrogen temperature T=77 K, the magnetoresistance value decreased. **Fig. 7** shows the temperature dependence of the normalized transverse value of r_T for two cases of $r_T(\varphi)$ at fixed values of the angle φ: when r_T is maximal (φ = 210º) and minimal (φ = 275º) at T = 300 K. At low temperatures (T < 150 K) the measurement error (not shown in Fig. 7) no longer allowed to extract reliable data. At T = 77 K, neither transverse, nor longitudinal magnetoresistance could be detected. The temperature dependence of the transverse resistivity of the SIO3/LSMO heterostructure R_T, taken at H = 0 is shown in the inset to Fig. 7. In general, the nature of the temperature dependence of $R_T(T)$ is similar to the temperature dependence of the planar Hall resistance $r_T(T)$. It is known that the magnetization M of an LSMO film increases with decreasing temperature, but relations (4)–(6) [6] do not imply a change in the Hall magnetoresistance with temperature. Note, that the temperature dependences of the characteristics of magnetoresistance, spin diffusion length, and spin Hall angle were considered in [30,31] for structures different from those considered in this work, as well as for the case of spin moment changes in SIO3/LSMO [20,32] under the influence of current pulses. Note also, that the observed increase in spin current with decreasing temperature for Pt/LSMO [8] is not observed in our case, which is probably due to the influence of the conducting layer at the SIO3/LSMO interface [12]. Note, that the changes of magnetoresistance with temperature can be caused by the temperature dependences of $Reg^{\uparrow\downarrow}$ and $Img^{\uparrow\downarrow}$. Varying the numerical value of the ratio $Img^{\uparrow\downarrow}/Reg^{\uparrow\downarrow}$ in (5) does not lead to a noticeable change in the parameter r_1, but can affect parameter r_2 in the case of the occurrence of out-of-plane magnetization in *F*-layer.

4. CONCLUSION

It is shown experimentally that under applied microwaves the spin current response in $SrIrO_3/La_{0.7}Sr_{0.3}MnO_3$ heterostructure exceeds the response caused by contributions due to parasitic detection at contacts and anisotropic magnetoresistance by an order in magnitude. It is shown that the imaginary part of the spin mixing conductance in $SrIrO_3/La_{0.7}Sr_{0.3}MnO_3$ interface turns out, by an order of magnitude, is equal to its real part. It was found out that the amplitude of the angular dependence of the transverse magnetoresistance significantly exceeds the amplitude of the longitudinal one, which is, most likely, affected by the shunting effect of the anisotropic magnetoresistance of the film $La_{0.7}Sr_{0.3}MnO_3$ and by the conducting layer at the interface of the heterostructure $SrIrO_3/La_{0.7}Sr_{0.3}MnO_3$. The spin-Hall angle (the ratio of spin and charge currents) determined from measurements of the longitudinal spin magnetoresistance was by an order of magnitude smaller than for the transverse (Hall) magnetoresistance, which is caused by the presence of a conducting layer at the heterostructure interface. As the temperature decreases below room temperature, we did not find any significant increase in spin current value, both from the direct detection of the spin current due to the inverse spin-Hall effect, and from the temperature dependence of the spin magnetoresistance.

REFERENCES

1. Dyakonov MI, and Perel VI. On possibility of orientation of spin by current. *JETP Lett.*, 1971, 13:467-469.
2. Saitoh E, Ueda M, Miyajima H, and Tatara S. Conversion of spin current into charge current at room temperature: Inverse spin-Hall effect. *Appl. Phys. Let.*, 2006, 88(18):182509-1-3.
3. Mosendz O, Vlaminck V, Pearson JE, Fradin FY, Bauer WGE, Bader SD, and Hoffmann A. Detection and quantification of inverse spin Hall effect from spin pumping in permalloy/normal metal bilayers. *Phys. Rev. B*, 2010, 82(21):214403-1-9.
4. Tserkovnyak Y, Brataas A, Bauer GEW. Enhanced Gilbert damping in thin ferromagnetic films. *Phys Rev. Lett.,* 2002, 88(11):117601-1-4.
5. Sinova J, Valenzuela SO, Wunderlich J, Back CH, Jungwirth T. Spin Hall effects. *Rev.Mod. Phys.*, 2015, 87(4):1213-1259.
6. Chen YT, Takahashi S, Nakayama H, Althammer M, Goennenwein ST, Saitoh E, Bauer GE. Theory of spin Hall magnetoresistance (SMR) and related phenomena. *J of Physics: Condensed Matter,* 2016, 28(10):103004-1-15.
7. Althammer M, Meyer S, Nakayama H, Schreier M, Altmannshofer S, Weiler M, Huebl H, Geprägs S, Opel M, Gross R, Meier D, Klewe C, Kuschel T, Schmalhorst J-M, Reiss G, Shen L, Gupta A, Chen Y-T, Bauer GEW, Saitoh E, Goennenwein ST. Quantitative study of the spin Hall magnetoresistance in ferromagnetic insulator/normal metal hybrids. *Phys. Rev. B,* 2016, 87(22):224401-1-15.
8. Azevedo A, Vilela-Leão LH, Rodríguez-Suárez RL, Santos AL, Rezende SM. Spin pumping and anisotropic magnetoresistance voltages in magnetic bilayers: Theory and experiment. *Phys. Rev. B,* 2011, 83(14):144402-1-6.
9. Sandweg CW, Kajiwara Y, Ando K, Saitoh E, Hillebrands B. Enhancement of the spin pumping efficiency by spin wave mode selection. *Appl. Phys. Lett.*, 2010, 97(25):252504-1-4.
10. Ovsyannikov GA, Constantinian KY, Stankevich KL, Shaikhulov TA, Klimov AA. Spin current and spin waves at a platinum/yttrium iron garnet interface: impact of microwave power and temperature. *J. of Physics D: Applied Physics,* 2021, 54(36):365002-1-11.
11. Nan T, Emori S, Boone CT, Wang X, Oxholm TM, Jones JG, Howe BM, Brown GJ, Sun NX. Comparison of spin-orbit

torques and spin pumping across NiFe/Pt and NiFe/Cu/Pt interfaces. *Phys. Rev.B,* 2015, 91(21):214416-1-9.
12. Ovsyannikov GA, Shaikhulov TA, Stankevich KL, Khaydukov Y, Andreev NV. Magnetism at an iridate/manganite interface: Influence of strong spin-orbit interaction. *Phys. Rev. B*, 2020, 102(14):144401-1-11.
13. Ovsyannikov GA, Constantinian KY, Shmakov VA, Klimov AL, Kalachev EA, Shadrin AV, Andreev NV, Milovich FO, Orlov AP, Lega PV. Spin mixing conductance and spin magnetoresistance of the iridate/manganite interface. *Phys. Rev. B,* 2023, 107(14):144419-1-12.
14. Qi XL, Zhang SC. Topological insulators and superconductors. *Rev. Mod. Phys.,* 2011, 83(4):1057-1103.
15. Nan T, Anderson TJ, Gibbons J, Hwang K, Campbell N, Zhou H, Dong YQ, Kim GY, Shao DF, Paudel TR, Reynolds N, Wang XJ, Sun NX, Tsymbal EY, Choi SY, Rzchowski MS, Kim YB, Eom CB. *Proc. Natl. Acad. Sci. USA,* 2019, 116(33):16186-16191.
16. Everhardt AS, Mahendra DC, Huang X, Sayed S, Gosavi TA, Tang Y, Lin CC, Manipatruni S, Young IA, Datta S, Wang J-P, Ramesh R. Tunable charge to spin conversion in strontium iridate thin films. *Phys. Rev. Materials*, 2019, 3(5):051201-1-18.
17. Yi D, Liu J, Hsu SL, Zhang L, Choi Y, Kim JW, Chen Z, Clarkson JD, Serrao CR, Arenholz E, Ryan PJ, Xu H, Birgeneau RJ, RameshR. Atomic-scale control of magnetic anisotropy via novel spin–orbit coupling effect in La2/3Sr1/3MnO3/SrIrO3 superlattices. *Proceedings of the National Academy of Sciences USA*, 2016, 113(23):6397-6402.
18. Huang X, Sayed S, Mittelstaedt J, Susarla S, Karimeddiny S, Caretta L, Zhang H, Stoica VA, Gosavi T, Mahfouzi F, Sun Q, Ercius P, Kioussis N, Salahuddin S, Ralph DC, Ramesh R. Novel Spin–Orbit Torque Generation at Room Temperature in an All-Oxide Epitaxial $La_{0.7}Sr_{0.3}MnO_3/SrIrO_3$ System. *Advanced Materials,* 2021, 33(24):2008269-1-7.
19. Crossley S, Swartz AG, Nishio K, Hikita Y, Hwang HY. All-oxide ferromagnetic resonance and spin pumping with $SrIrO_3$. *Physical Review B,* 2019, 100(11):115163-1-7.
20. Liu L, Zhou G, Shu X, Li C, Lin W, Ren L, Zhou C, Zhao T, Guo R, Xie Q, Wang H, Zhou J, Yang P, Pennycook SJ, Xu X, Chen J. Room-temperature spin-orbit torque switching in a manganite-based heterostructure. *Phys. Rev. B*, 2022, 105(14):144419-1-11.
21. Atsarkin VA, Borisenko IV, Demidov VV, Shaikhulov TA. Temperature dependence of pure spin current and spin-mixing conductance in the ferromagnetic—normal metal structure. *Journal of Physics D: Applied Physics*, 2018, 51(24):245002-245002.
22. Zwierzycki M, Tserkovnyak Y, Kelly PJ, Brataas A, Bauer GE. First-principles study of magnetization relaxation enhancement and spin transfer in thin magnetic films. *Phys. Rev. B*, 2005, 71(6):064420-1-11.
23. Yang F, Hammel PC. FMR-driven spin pumping in $Y_3Fe_5O_{12}$-based structures. *Journal Physics D: Applied Physics,* 2018, 51(25):253001-1-9.
24. Shaikhulov TA, Ovsyannikov GA. Attenuation of spin precession in manganite/normal metal heterostructures. *Physics of the Solid State,* 2018, 60:2231-2236.
25. Dubowik J, Graczyk P, Krysztofik A, Głowiński H, Coy E, Załęski K, Gościańska I. Non-Negligible Imaginary Part of the Spin-Mixing Conductance and its Impact on Magnetization Dynamics in Heavy-Metal–Ferromagnet Bilayers. *Physical Review Applied,* 2020, 13(5):054011-1-13.
26. Czeschka FD, Dreher L, Brandt MS, Weiler M, Althammer M, Imort IM, Reiss G, Thomas A, Schoch W, Limmer W, Huebl H, Goennenwein ST. Scaling behavior of the spin pumping effect in ferromagnet-platinum bilayers. *Phys. Rev. Lett.*, 2011, 107(4):046601-1-4.

27. Gomez-Perez JM, Zhang XP, Calavalle F, Ilyn M, González-Orellana C, Gobbi M,Rogero C, Chuvilin A, Golovach VN, Hueso LE, Bergeret FS, Casanova F. Strong interfacial exchange field in a heavy metal/ferromagnetic insulator system determined by spin Hall magnetoresistance. *Nano Letters*, 2020, 20(9):6815-6823.
28. Rosenberger P, Opel M, Geprägs S, Huebl H, Gross R, Müller M, Althammer M. Quantifying the spin mixing conductance of EuO/W heterostructures by spin Hall magnetoresistance experiments. *Applied Physics Letters,* 2021, 118(19):192401-1-5.
29. Wang H, Meng KY, Zhang P, Hou JT, Finley J, Han J, Yang F, Liu L. Large spin-orbit torque observed in epitaxial $SrIrO_3$ thin films. *Applied Physics Letters,* 2019, 114, 23:232406-1-5.
30. Yi D, Liu J, Hsu SL, Zhang L, Choi Y, Kim JW, Chen Z, Clarkson JD, Serrao CR, Arenholz E, Ryan PJ, Xu H, Birgeneau RJ, Ramesh R. Atomic-scale control of magnetic anisotropy via novel spin–orbit coupling effect in $La_{2/3}Sr_{1/3}MnO_3/SrIrO_3$ superlattices. *Proceedings of the National Academy of Sciences*, 2016, 113(23):6397-6402.
31. Marmion SR, Ali M, McLaren M, Williams DA, Hickey BJ. Temperature dependence of spin Hall magnetoresistance in thin YIG/Pt films. *Phys. Rev. B*, 2014, 89(22):220404-1-5.
32. Wang Y, Deorani P, Qiu X, Kwon JH, Yang H. Determination of intrinsic spin Hall angle in Pt. *Applied Physics Letters,* 2014, 105(15):152412-1-4.
33. Yi D, Amari H, Balakrishnan PP, Klewe C, Shafer P, Browning N, Suzuki Y. Enhanced interface-driven perpendicular magnetic anisotropy by symmetry control in oxide superlattices. *Physical Review Applied,* 2021, 15(2):024001-1-9.

DOI: 10.17725/rensit.2023.15.425

Sound reflection from an elastic finite cylindrical shell of different relative lengths

Sergey L. Ilmenkov
St. Petersburg State Marine Technical University, http://www.smtu.ru/
St. Petersburg 190121, Russian Federation
E-mail: sl_ilmenkov@mail.ru

Sergey A. Pereselkov, Nikolay V. Ladykin
Voronezh State University, http://www.vsu.ru/
Voronezh 394006, Russian Federation
E-mail: pereselkov@yandex.ru, ladykin.edu@yandex.ru

Vladimir I. Grachev
Kotel'nikov Institute of Radioengineering and Electronics of RAS, http://www.cplire.ru/
Moscow 125009, Russian Federation
E-mail: grachev@cplire.ru

Received November 28, 2023, peer-reviewed December 01, 2023, accepted December 03, 2023, published December 06, 2023.

Abstract: **A calculation of the sound pressure frequency dependences scattered by a finite elastic cylindrical shell placed in a liquid medium is presented. The shell has hemispherical ends and is considered either hollow or filled with gas or liquid. The scattered sound pressure under conditions of hydroelastic contact on the shell surfaces is found by jointly using the Kirchhoff integral and the integral equation for the elastic medium displacement vector, obeying the Lamé equation. Boundary conditions regarding stresses and displacements are formulated for each of the shell contact surfaces with the external and internal environments. Considerating approach is based on the numerical transformation of continuous integral equations into a system of linear algebraic equations using curvilinear isoparametric boundary elements. In this case, the elements geometry and the main variables (displacements and stresses) are specified using the same interpolating relations (shape functions). The scattered sound pressure frequency dependences are calculated and analyzed for various ratios of the length and shell diameter.**

Keywords: **finite elastic cylindrical shell, Kirchhoff integral equation, displacement vector, boundary elements, scattered sound pressure**

UDC 534.26

Acknowledgments: The study was supported by the Russian Science Foundation grant No. 23-61-10024, https://rscf.ru/project/23-61-10024/.

For citation: Sergey L. Ilmenkov, Sergey A. Pereselkov, Vladimir I. Grachev, Nikolay V. Ladykin. Sound reflection from an elastic finite cylindrical shell of different relative lengths. *RENSIT: Radioelectronics. Nanosystems. Information Technologies,* 2023, 15(4):425-432e. DOI: 10.17725/rensit.2023.15.425.

Contents

1. INTRODUCTION

It is known that the target detection range of modern sonar systems significantly depends on the energy losses of probing and reflected signals. The increase in such losses with frequency dictates the need to reduce the location signal frequency. In addition, discrete signal components in the low-frequency range are less sensitive to fluctuations in the marine environment parameters and are very informative in identifying individual characteristics of objects. In the context of the principles of a deformable solid mechanics, it is possible to obtain solutions to boundary value problems for objects of non-analytical shape using numerical methods: finite differences, T-matrices, finite and boundary elements. Algorithms based on these methods form the basis of common software packages for solving boundary value problems (ANSYS, NASTRAN, COSMOS/M, COMSOL Multiphysics [1-5], etc.).

With all the undoubted advantages of such packages, specially developed individual software can have significant advantages in practice, having: compactness, speed, uniqueness, interaction with analytical and approximate approaches, accessibility, absence of an expensive license, etc. The solution presented in this article is based on the use of a boundary integral equation with respect to unknown surface displacements and stresses, interpolated by identical polynomial functions through their values at the nodal points of curvilinear isoparametric boundary elements. The calculation algorithm implementation was carried out using software specially developed by the author.

2. PROBLEM FORMULATION

The sound pressure p_s scattered by an elastic body can be found using the Kirchhoff integral and the Green's function for free space, which is the point source field placed at a far-field point [6-9]:

$$p(\mathbf{r}_1) = 1/4\pi \int_S [p(\mathbf{r}_0)\frac{\partial}{\partial n}G(\mathbf{r}_1;\mathbf{r}_0) - \frac{\partial}{\partial n}p(\mathbf{r}_0)G(\mathbf{r}_1;\mathbf{r}_0)]dS, \quad (1)$$

where $p(\mathbf{r}_1)$ is the sound pressure in the far field of the object (Fraunhofer zone); $\mathbf{r}_1$ – radius vector of the far field point; S – closed surface surrounding an object with a continuous external normal $\mathbf{n}$; $p(\mathbf{r}_0)$ and $\partial p(\mathbf{r}_0)/\partial n$ – amplitude-phase distributions of sound pressure and its gradient on the surface S; $\mathbf{r}_0$ – radius vector of a point on the surface S; $G(\mathbf{r}_1; \mathbf{r}_0)$ is the Green's function satisfying the inhomogeneous Helmholtz equation.

The transition from ideal boundary conditions on the diffuser surface to the conditions of hydroelastic contact adds to (1) the integral equation for the displacement vector $\mathbf{u}$ and the boundary conditions for contact of an ideal compressible fluid with an elastic medium [10-12]:

$$\mathbf{u} = \iint_S \left\{\mathbf{t}(\mathbf{r}_0)G_t(\mathbf{r};\mathbf{r}_0) - \mathbf{u}(\mathbf{r}_0)[\mathbf{n}\sum(\mathbf{r};\mathbf{r}_0)]\right\} dS, \quad (2)$$

where $\mathbf{t}(\mathbf{r}_0) = \mathbf{n}\mathbf{T}(\mathbf{r}_0)$ – voltage vector; $\mathbf{n}$ is the unit vector of the external normal to S; $\mathbf{T}(\mathbf{r}_0)$ – stress tensor of an isotropic material; $G_t(\mathbf{r}; \mathbf{r}_0)$ – Green's displacement tensor; $\sum(\mathbf{r}; \mathbf{r}_0)$ – Green's stress tensor.

In equation (2), the stress vectors $\mathbf{t}(\mathbf{r}_0)$ and displacement $\mathbf{u}(\mathbf{r}_0)$ on the surface of the body S are unknown, and in equation (1) in this case, $p(\mathbf{r}_0)$ and $\partial p(\mathbf{r}_0)/\partial n$ on the same surface are unknown. The displacement vector of the elastic medium $\mathbf{u}$, with a harmonic dependence on time, obeys the Lamé equation and can be represented, as

is known, as a combination of scalar and vector potentials [12].

The following boundary conditions must be satisfied on the surfaces of the shell, based on the complete system of equations of the linear theory of elasticity, which determines the state of dynamic equilibrium of the elastic body [11,12]:

1) the normal component of the displacement vector u_n is continuous and related to the normal derivative of the diffracted pressure $p_\Sigma = p_i + p_s$ (p_i is the sound pressure in the incident wave):

$$u_n = \left(1/\rho_0\omega^2\right)\left(\partial p_\Sigma/\partial n\right)\Big|_s, \quad (3)$$

where ϱ_0 is the density of the liquid medium, kg/m^3; $\omega = 2\pi f$, f – sound signal frequency, Hz;

2) normal stress σ_n:

– on the outer surface of the shell is equal to the acoustic pressure in the liquid

$$\sigma_n|_s = p_\Sigma, \quad (4)$$

- on the inner surface of the shell it is either absent (hollow shell) or equal to the sound pressure of the gaseous or liquid filler;

3) there are no tangential stresses:

$$\tau_i|_s = 0. \quad (5)$$

Using (3)-(5), one group of unknowns on S can be eliminated from equations (1) and (2), and the two remaining unknowns can be found from a joint solution of these equations [12,13].

The approach under consideration is based on the numerical transformation of continuous integral equations (1) and (2) into a system of linear algebraic equations using quadratic isoparametric elements. The use of curved boundary elements provides a more detailed discretization of the boundary surface and increases the accuracy of the result while reducing computation time. When constructing a mesh of boundary elements, the sampling step Δ of the surface S in the direction of any of the coordinates should not exceed $(0.25\div0.5)\cdot\lambda_0$ (λ_0 is the length of the sound wave in the liquid). Near the edges and corners of the surface, the calculation algorithm provides for condensation of nodal points with a decrease in the sampling step up to values $\Delta \sim(0.025\div0.05)\cdot\lambda_0$. With such discretization, the three-dimensional boundary of the region S is divided into triangular and quadrangular elements (**Fig. 1**), at the nodes of which some coefficients are specified, and the continuous integrand function is approximately represented as a series of basic (interpolating) shape functions multiplied by these coefficients. The nodal coordinates of any point of the original elements x_{i_α} are transformed into the corresponding curvilinear coordinates x_i (i = 1,2,3), and the geometry of the element $x_i(\xi)$, displacement $u_i(\xi)$ and stress $t_i(\xi)$ are specified using the same shape functions [12,13].

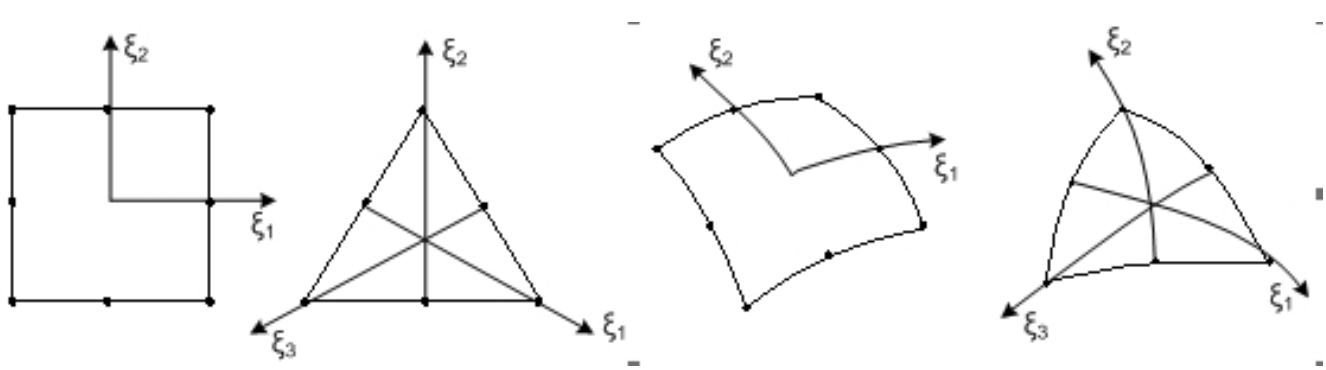

a *b*

Fig. 1. *Initial flat (a) and corresponding curvilinear isoparametric (b) boundary elements*

Using such relations allows us to obtain the matrix equation based on (2):

$$[H]\{u\} = [\tilde{G}]\{t\}, \quad (6)$$

where H and $\tilde{G}$ are matrices of coefficients obtained as a result of numerical integration.

Integral (1) will take the form [11-13]:

$$p_s(P) = \\ = 1/4\pi \int_S [p_\Sigma(Q)\frac{\partial}{\partial n}\left(e^{ikr}/r\right) - (e^{ikr}/r)\rho_0\omega^2(\mathbf{u}\cdot\mathbf{n})]dS + \\ +4\pi p_i(P), \quad (7)$$

where $p_\Sigma(Q)$ is the diffracted sound pressure at point Q of the surface S.

Having performed numerical integration (7) and expressing part of the unknown stresses in (6) in terms of pressure in accordance with the boundary condition (4), we obtain:

$$[T]\{u\} = [D]\{p_\Sigma\} + 4\pi\{p_\Sigma\}, \quad (8)$$

$$[H]\{u\} = [G]\{t\} + F\{p_\Sigma\}, \quad (9)$$

where *T, D, G* and *F* are coefficient matrices.

Next, from equations (6) and (8), the distributions $p_\Sigma(Q)$ and $(\mathbf{u}\cdot\mathbf{n})$ on the surface S are found, and then, based on (7), $p_\Sigma(P)$ in a liquid medium is determined using quadrature formulas.

Let us consider the practical implementation of this approach in relation to an isotropic circular cylindrical shell of length L and thickness h, limited at the ends by hemispheres of radius a at different values of the relative length L/a (**Fig. 2**):

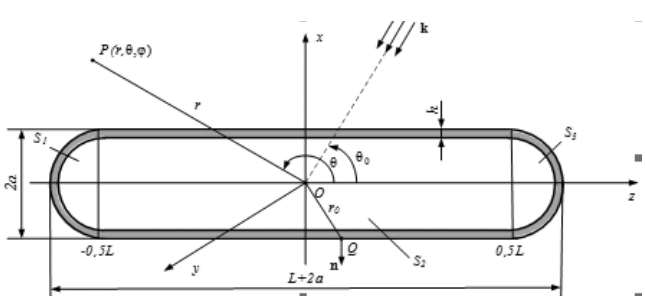

Fig. 2. *Elastic finite cylindrical shell with hemispheres at the ends; S2 is the area of the lateral surface of the cylinder, S1 and S3 are the surface areas of the hemispheres.*

We will assume that the shell is thin ($h/a \leq 0.05$). As is known, for such shells it is possible, based on the Kirchhoff–Love hypothesis, to move from three-dimensional relations of the theory of elasticity to two-dimensional ones. In this case, the exclusion of tangential and shear forces allows, when describing small bending vibrations of the shell, to use a system of two differential equations and determine the projections of all forces and stresses on the direction of the normal to the middle surface of the shell (the wave vector **k** is perpendicular to the z-axis of the cylinder).

Let us introduce coordinate systems associated with each part of the surface S, for which, at $\theta_0 = 90°$, all the main physical variables are functions of only two coordinates, so the displacement vector will also have two components. For the cylindrical part of the surface S_2 they will have the form [9,14]:

$$u_r = -\frac{\partial\Phi}{\partial r} + \frac{1}{r}\frac{\partial\Psi}{\partial\varphi};\ u_\varphi = -\frac{1}{r}\frac{\partial\Phi}{\partial\varphi} - \frac{\partial\Psi}{\partial r}. \quad (10)$$

Using the representations of the strain components ε_r, ε_φ through the components of the displacement vector, as well as the generalized Hooke's law for an isotropic medium, it is possible to express the elastic stresses on the surface S_2 through the scalar Φ and vector $\mathbf{\Psi}$ potentials [12,15]:

$$\left.\begin{aligned}\sigma_r &= \lambda\vartheta + 2\mu\varepsilon_r = \lambda k_1^2\Phi + \left(-\frac{\partial^2\Phi}{\partial r^2} - \frac{1}{r^2}\frac{\partial\Psi}{\partial\varphi} + \frac{1}{r}\frac{\partial^2\Psi}{\partial r\partial\varphi}\right),\\ \tau_{r\varphi} &= 2\mu\gamma_{r\varphi} = \mu\left(-\frac{2}{r}\frac{\partial^2\Phi}{\partial r\partial\varphi} + \frac{2}{r^2}\frac{\partial\Phi}{\partial\varphi} - k_2^2\Psi - 2\frac{\partial^2\Psi}{\partial r^2}\right).\end{aligned}\right\} \quad (11)$$

where r, φ – cylindrical coordinates of point Q; $\vartheta = \varepsilon_r + \varepsilon_\varphi = \mathrm{div}\mathbf{u}$; k_1 and k_2 are the wave numbers of longitudinal and transverse waves in the elastic shell material.

Similar relations for the hemispherical parts of the shell S_1 and S_3 will have the form:

$$\left.\begin{aligned} u_r &= -\frac{\partial\Phi}{\partial r}+\frac{1}{r}ctg\theta\Psi+\frac{1}{r}\frac{\partial\Psi}{\partial\theta};\\ \sigma_r &= \lambda\vartheta+2\mu\varepsilon_r=\lambda k_1^2\Phi+\\ &+2\mu\left(-\frac{\partial^2\Phi}{\partial r^2}+\frac{1}{r}ctg\theta\frac{\partial\Psi}{\partial r}-\frac{1}{r^2}ctg\theta\Psi+\frac{1}{r}\frac{\partial^2\Psi}{\partial r\partial\theta}-\frac{1}{r^2}\frac{\partial\Psi}{\partial\theta}\right);\\ \tau_{r\theta} &= 2\mu\gamma_{r\theta}=\\ &=\mu\left(\frac{1}{r^2}ctg\theta\frac{\partial\Psi}{\partial\theta}+\frac{1}{r^2}\frac{\partial^2\Psi}{\partial\theta^2}-\frac{\partial^2\Psi}{\partial r^2}-\frac{2}{r^2}\frac{\partial\Phi}{\partial\theta}-\frac{1}{r^2\sin^2\theta}\Psi\right);\\ &, \end{aligned}\right\} \quad (12)$$

where r, θ – spherical coordinates of point Q; $\vartheta=\varepsilon_r+\varepsilon_\theta=div\mathbf{u}$.

Substituting relations for the components of the displacement vector and elastic stresses into the boundary conditions (3)-(5), we obtain for each point Q of the surface S a system of algebraic equations for finding unknown coefficients in the expansions of elastic potentials, and then we find the distributions $p_\Sigma Q$ and u_r at the boundary element nodes (points Q) on the surface S.

3. RESULTS OF NUMERICAL ANALYSIS OF CHARACTERISTICS SOUND REFLECTIONS

Let us consider the main results of calculations of the frequency characteristics of sound reflection by a steel shell of the shape under consideration in the range of wave radii ka = 0.95÷25.0. **Fig. 3** shows the frequency dependences of the modulus levels $p_\Sigma(P)$ at traverse location (θ_0 = 90°) for a shell filled with air (curve 1), water (curve 2) and vacuum (curve 3). The geometric parameters of the shell are: L/a = 20; h/a = 0.01.

As can be seen from the figure, the levels of modules $p_\Sigma(P)$ for a hollow shell exceed the corresponding values for an air-filled shell on average over the range by 1...1.5 dB (≈20%...50%). For a shell filled with water, the added mass can lead to the interaction of vibration modes and, accordingly, to an increase in the likelihood of resonance phenomena occurring. The latter can also be determined by the propagation of Scholte-Stoneley type waves in the liquid and elastic waves of the Lamb type in the shell material [11,12,14], which is observed mainly for ka > 3. The values of the resonant frequencies are determined by the integer number of lengths of these half-waves, which fit along the closed contour of the shell. In the presence of a liquid filler, the probability of phase matching for such half-waves at the excitation point increases.

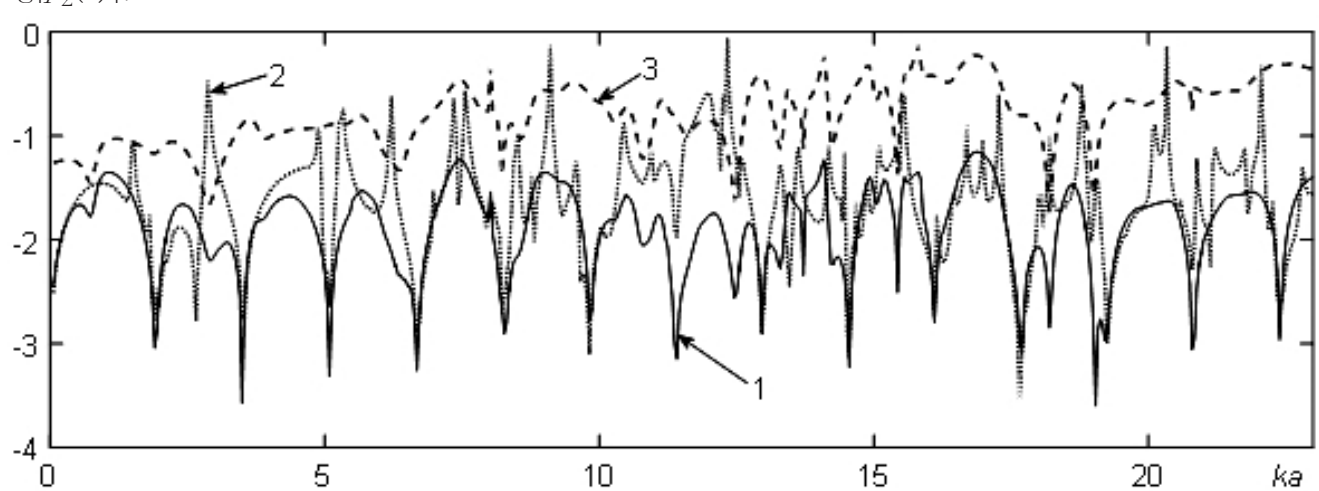

Fig. 3. *Levels of modules of frequency dependences of an audio signal reflected by a shell filled with: air (1), water (2) and vacuum (3) at θ0 = 90°; L/a = 20; h/a = 0.01.*

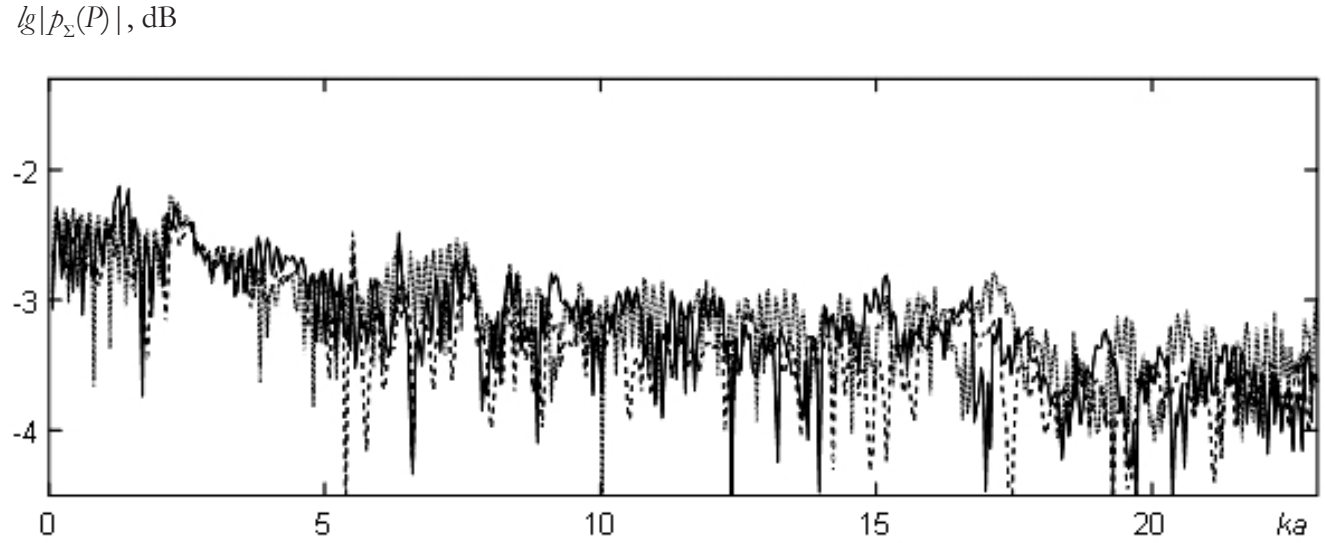

Fig. 4. *Levels of modules of frequency dependences of an audio signal reflected by a shell filled with air, at $L/a = 20$; $-\theta_0 = 0°$; $-\theta_0 = 30°$; $-\theta_0 = 60°$.*

In addition, in this case, compared to an air-filled shell, at a number of resonant frequencies ($ka \approx$ 5-10, 17-22, etc.) there is a tendency to double the frequency spectrum of the reflected signal. Lower in frequency ($ka \leq 3$) spatial coincidence resonances may occur.

Figures 4-7 show the frequency dependences of $\lg|p_\Sigma(P)|$, dB for location angles $\theta_0 = 0°$; 30°; 60° of a shell filled with air, at $h/a = 0.01$ and relative elongations $L/a = 20$; 10; 5 and 2.

The presented results show that at non-averse location angles, the levels of the reflected signal are generally 1...2 dB lower than at $\theta_0 = 90°$. When L/a decreases by a factor of two, the repetition frequency of elastic resonances caused by the rounding of the shell contour by waves of the Scholte-Stoneley and Lamb type decreases by a factor of 2...3. When $L/a < 10$, the role of spatial coincidence resonances increases (up to ≈30%...50%), which manifest themselves predominantly in the range $ka < 2$ and location angles $\theta_0 = 30°$, 60°.

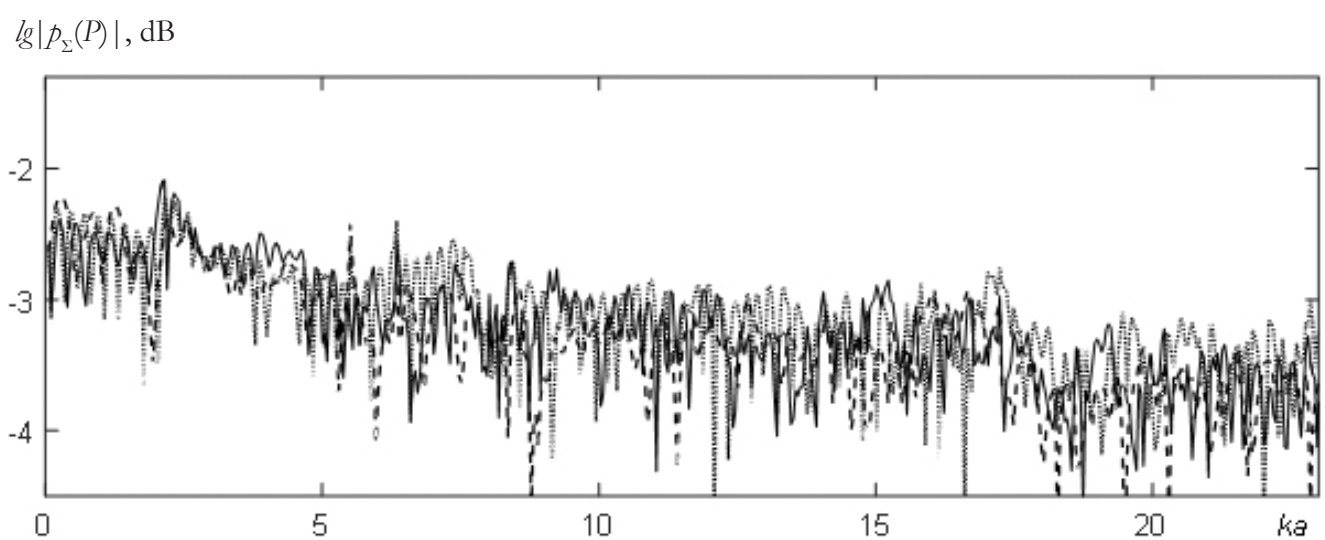

Fig. 5. *Levels of modules of frequency dependences of an audio signal reflected by a shell filled with air, at $L/a = 10$; $-\theta_0 = 0°$; $-\theta_0 = 30°$; $-\theta_0 = 60°$.*

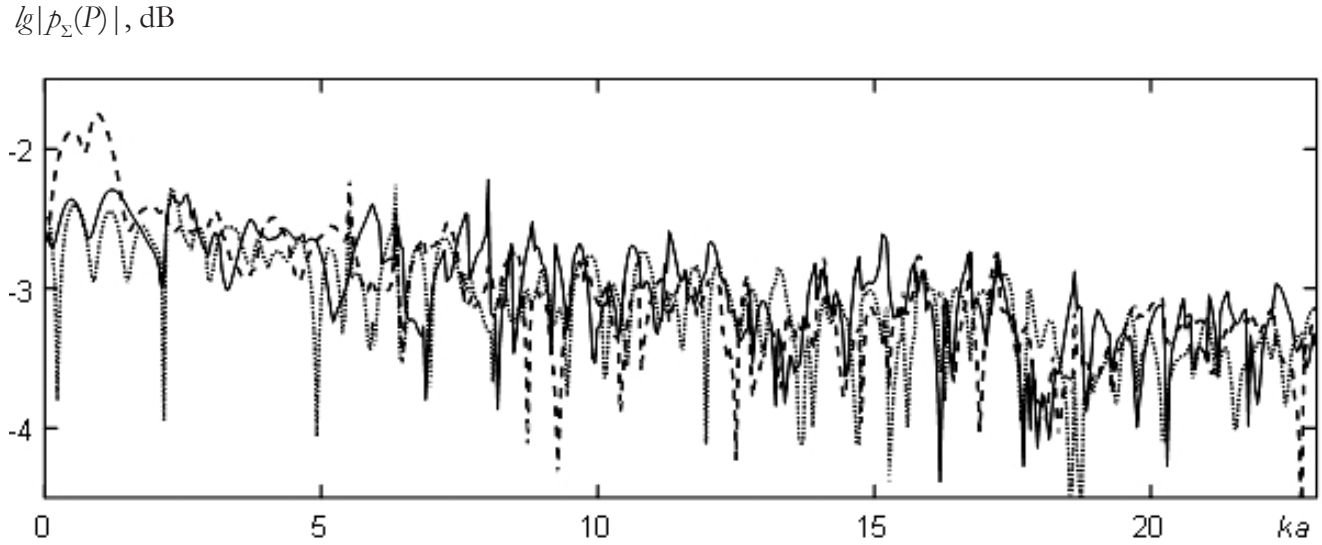

Fig. 6. *Levels of modules of frequency dependences of an audio signal reflected by a shell filled with air, at L/a = 5; -θ_0 = 0°; -θ_0 = 30°; -θ_0 = 60°.*

4. CONCLUSION

The use of a numerical transformation of continuous integral equations into a system of linear algebraic equations for unknown displacements and stresses, determined by their values at the nodal points of curvilinear boundary elements, made it possible to calculate the levels of sound pressure dissipated by a finite elastic cylindrical shell. The latter has hemispherical ends, is placed in a liquid medium and is considered both hollow and filled with gas or liquid. The scattered sound pressure on the surfaces of the shell is found by combining the Kirchhoff integral and the integral equation for the displacement vector of the elastic medium, which obeys the Lamé equation. The frequency dependences of the modulus levels of a stationary sound signal reflected by the shell are calculated and analyzed at various location angles, relative elongations, and options for filling its internal volume. The implementation of the calculation algorithm was carried out using software specially developed by the author

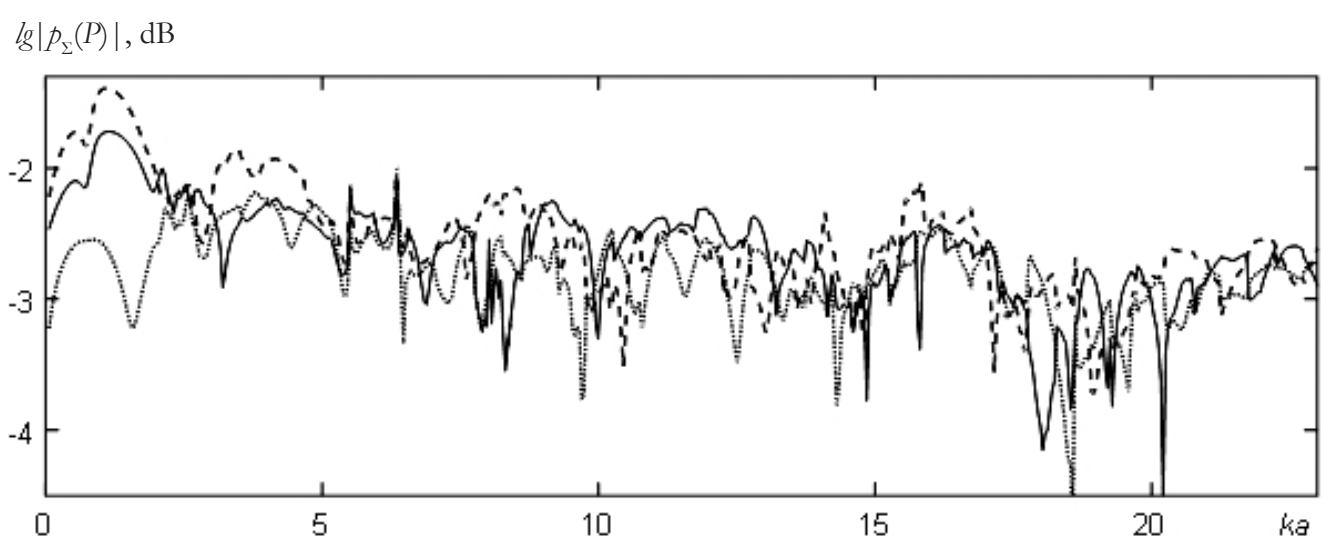

Fig. 7. *Levels of modules of frequency dependences of an audio signal reflected by a shell filled with air, at L/a = 2; -θ_0 = 0°; -θ_0 = 30°; -θ_0 = 60°.*

REFERENCES

1. Kudin MV. *Solving acoustics problems in the ANSYS software package: an electronic manual.* Nizhny Novgorod, Nizhny Novgorod State University, 2011, 27 p.
2. A.SYS 11.0. Documentation. Theory Reference for ANSYS and ANSYS Workbench. Acoustics// ANSYS, Inc. Southpointe Technology Drive Canonsburg, 2004, 1067 p.
3. Shatrov BV, Bukharov SA, Martynenko YUR, et al. *General-purpose finite element analysis system MSC Nastran: methodological manual.* Moscow, MSC Software Corporation, 2020, 50 p.
4. Shimkovich DG. *Structural analysis in MSC Nastran: methodological manual.* Moscow, DMK Press, 2003, 448 p.
5. Krasnikov GE, Nagornov OV, Starostin NV. *Modeling physical processes using the Comsol Multiphysics package: a methodological manual.* Moscow, MEPhI Publishing House, 2012, 184 p.
6. Ilmenkov SL. On the application of the Green's function method for calculating sound fields. *Proceedings of the IV Far Eastern Acoustic Conference, p. 73-75*. Vladivostok, Publishing house of the Far Eastern Polytechnic Institute, 1986.
7. Ilmenkov SL. On the accuracy of the Green's function method for calculating sound fields of radiators of complex shape. *Abstracts of reports of the All-Union meeting-seminar "Deep-sea systems and complexes." Part 1*, p.75. Cherkassy, 1986.
8. Ilmenkov SL. Green's function method in the problem of sound diffraction on bodies of non-analytical shape. *Marine Intelligent Technologies,* 2014, 2:32-36.
9. Shenderov EL. *Radiation and scattering of sound.* Leningrad, Sudostroenie Publ., 1989, 301 p.
10. Brebbia K, Walker S. *Application of the boundary element method in engineering.* Moscow, Mir Publ., 1981, 248 p.
11. Ilmenkov SL. Solving the problem of sound diffraction on an elastic body of non-analytical shape using the boundary element method. *Marine Intelligent Technologies*, 2015, 1, 1(27):30-36.
12. Kleshchev AA. *Hydroacoustic diffusers*. St. Petersburg, Sudoctroenie Publ., 1991, 248 p.
13. Seybert AF, Wu TW, Wu XF. Radiation and Scattering of acoustic waves from elastic solids and shells using the boundary element method. *Journal of the Acoustical Society of America,* 1988, 84(I.5)1906-1911.
14. Kleshchev AA, Klyukin II. *Fundamentals of hydroacoustics*. Leningrad, Sudostroenie Publ., 1987, 224 p.
15. Ilmenkov SL. *Development of methods for solving boundary problems of hydroacoustics.* St. Petersburg, St. Petersburg State Medical University, 2020, 190 p.

DOI: 10.17725/rensit.2023.15.433

Localization of the geological layer boundaries using the reverse time migration method

Alexey V. Shevchenko, Vasily I. Golubev
Moscow Institute of Physics and Technology, https://mipt.ru/
Dolgoprudny 141700, Moscow region, Russian Federation
E-mail: alexshevchenko@phystech.edu, golubev.vi@mipt.ru
Anton V. Ekimenko
Gazpromneft's Research and Development Center, https://ntc.gazprom-neft.com/
St.-Petersburg 190000, Russian Federation
E-mail: ekimenko.av@gazpromneft-ntc.ru

Received October 09, 2023, peer-reviewed October 16, 2023, accepted October 23, 2023, published December 06, 2023.

Abstract: **The article is devoted to solving an important practical problem - determining the structure of the subsurface space of the geological environment based on surface seismic data. Thanks to the registration of seismic waves reflected from the boundaries of geological layers, it is possible to delineate hydrocarbon deposits, which makes it possible to effectively plan a field development scheme. Optimizing the production process makes it possible to make it profitable, including when developing unconventional hydrocarbon deposits. The paper discusses the technology of constructing a migration image using the reverse time migration method. In the general case, an analytical derivation of the calculation formulas was carried out. For the practically significant case of an acoustic environment, simplified calculation formulas are explicitly written out and implemented in the form of a software algorithm. The issue of improving the quality of the migration image without significantly increasing the computational complexity of the problem is discussed separately. The authors demonstrated the performance of this approach using the widely used Marmousi geological model.**

Keywords: **mathematical modeling, seismic survey, reverse-time migration**

UDC 004.94

Acknowledgments: This work was financially supported by the Russian Science Foundation, project 21-11-00139, https://rscf.ru/en/project/21-11-00139/.

For citation: Alexey V. Shevchenko, Vasily I. Golubev, Anton V. Ekimenko. Determination of the boundaries of geological layers using the reverse time migration method. *RENSIT: Radioelectronics. Nanosystems. Information Technologies,* 2023, 15(4):433-440e. DOI: 10.17725/rensit.2023.15.433.

Contents

1. INTRODUCTION

Seismic exploration is the main method for detailed study of the geological medium structure. Most of the work is carried out using the reflected wave method in the modification of the common depth point

(CDP). The seismic cross-sections obtained are interpreted by geologists. Based on them, they construct geological models and assess the resource base of minerals.

CDP seismic cross-sections have several disadvantages: diffracted waves associated with faults and small objects are displayed as diffraction hyperbolas, inclined boundaries are not displayed in their true position, synclinal structures are displayed as loops. In cases where there are velocity anomalies in the geological model, the underlying reflecting horizons are less well focused, and their relief is distorted. The seismic data migration procedure is aimed at minimizing these shortcomings and constructing a reliable seismic image.

One of the advanced migration methods is the reverse-time migration method (RTM). The foundations of this method were laid in fundamental works [1-3]. The method was subsequently developed and generalized to more complex media models using various parameterizations, integral formulas, and post-processing techniques by various researchers [4-8].

This article presents successful experience in using the RTM method to construct a migration image of a complex geological medium in a two-dimensional setting. In the general case, a detailed derivation of the fundamental formulas is presented, as well as a method for reducing them to the special case of an acoustic model. The results of the work contain a description of the computer experiments performed and the constructed migration images.

2. MATERIALS AND METHODS

2.1. Basic idea of RTM

Let the data $D = \vec{D}(t)$ be recorded as a result of seismic exploration: a time-dependent signal at the receivers at points $\vec{x}_i$, Having denoted the wave field (generally speaking, unknown) in the entire geological massif by u, we can write that $D = Ru$, where R is the restriction operator. Moreover, $u \in U$, where U is the space of admissible functions of coordinates and time. Let the physical and mathematical model of the medium be described by the differential equation

$$F[m]u = f, \tag{1}$$

where f is the known right-hand side, $m \in M$ are the parameters of the medium from a certain space of admissible parameters M, $F[m]$ is a differential operator acting on functions from the space U. The differential problem based on equation (1) is well-posed when specifying suitable initial and boundary conditions. We can assume that these conditions are included in the definition of the space U.

Then we can write the following residual function:

$$\begin{aligned}\Psi(m) &= \frac{1}{2}\left\|(Ru)(t) - \vec{D}(t)\right\|^2_{R^n(t)} = \\ &= \frac{1}{2}\int_0^T \left\|\left(\overrightarrow{Ru}\right)(t) - \vec{D}(t)\right\|^2_{R^n} dt = \\ &= \frac{1}{2}\sum_{i=0}^{n}\int_0^T \left(\left(\overrightarrow{Ru}\right)(t) - \vec{D}(t)\right)_i^2 dt.\end{aligned} \tag{2}$$

In this formula, the wave field u is the only solution to equation (1), therefore, $u = u[m]$ and $\Psi = \Psi[m]$.

Let us write down the definitions of several concepts used later in the article.

The Frechet derivative of a functional A acting from a normed space E into R^1 ($A:E \to R^1$) at the point $x_0 \in E$ is a linear functional

$$\left.\frac{\partial A}{\partial x}\right|_{x_0} : E \to R^1 \left(\left.\frac{\partial A}{\partial x}\right|_{x_0}(\tilde{x}) = y,\ \tilde{x} \in E, y \in R \right)$$

such that

$$\begin{aligned}&\mathrm{A}(x) - A(x_0) = \left.\frac{\partial A}{\partial x}\right|_{x_0}(x - x_0) + \alpha(x)\|x - x_0\|, \\ &\lim_{x \to x_0} \alpha(x) = 0.\end{aligned} \tag{3}$$

Also, we will use the definition of the adjoint operator A^* to the operator A for spaces with the scalar product $\langle\cdot,\cdot\rangle$:

$$\langle Ax, y\rangle = \langle x, A^* y\rangle. \quad (4)$$

The distribution of medium parameters $m_* = \operatorname{argmin}\Psi[m]$ can be considered a solution to the inverse problem of finding medium parameters m using the known equation (1), the known right-hand side f and the known recorded data D. To find m_*, we can use various optimization methods, for example, gradient methods using derivatives in the Frechet sense (3) are often used. It was noted that if the initial approximate distribution of parameters is a smoothed version of the true one (this is often the case due to the estimate of the average value of the velocity), then the desired increment of medium parameters $m_* - m_{\text{initial}}$ corresponds to the migration image of the medium. Based on this observation, the RTM method was proposed, which consists of finding the gradient $\partial\Psi/\partial m$ and then processing it to obtain a migration image.

2.2. RTM IN THE OPERATOR FORM

In this subsection, we consider a method for finding the derivative $\partial\Psi/\partial m$. Direct differentiation of the residual functional (2) with respect to the parameters of the medium m will require finding the derivatives $\partial(Ru)/\partial m$, which in the discrete case corresponds to the Jacobian matrix of the first derivatives $\left\|\frac{\partial(\mathrm{Ru})_i}{\partial m_j}\right\|$, the calculation of which is extremely expensive. Therefore, to calculate the derivative $\partial\Psi/\partial m$, the technique of solving the adjoint equation is used, which does not require explicit calculation of $\partial(Ru)/\partial$m. The corresponding formulas can be derived in several ways [5]. We chose the Lagrange multiplier method for the continuous optimization problem with constraints, presented below.

To optimize the residual functional $\frac{1}{2}\left\|(\mathrm{Ru})(\mathrm{t}) - \vec{\mathrm{D}}(\mathrm{t})\right\|^2_{\mathrm{R}^n(\mathrm{t})}$ under the additional constraint $F[m]u = f$, consider the Lagrange functional

$$L\left[m, \tilde{u}, \tilde{\lambda}\right] = \frac{1}{2}\left\|(R\tilde{u})(t) - \vec{D}(t)\right\|^2_{R^n(t)} + \left\langle \tilde{\lambda}, F[m]\tilde{u} - f\right\rangle \quad (5)$$

with arbitrary $m \in \mathcal{M}$, $\tilde{u} \in U$, $\tilde{\lambda} \in U^*$, where the space U^* defines functions of the same smoothness as in the space U, with the same boundary conditions, but with conditions at the final time instead of initial conditions. From optimization theory it is known that the minimum of the functional is achieved at the point where the derivatives of the Lagrangian are equal to zero [9]. First, we write down the Frechet differentials of the functional L with respect to $\tilde{u}$ and $\tilde{\lambda}$, using the definition of the adjoint operator (4):

$$\left.\frac{\partial L}{\partial \tilde{\lambda}}\right|_{m,\tilde{u},\tilde{\lambda}} \left(\tilde{\lambda}\right) = 0 + \left\langle \tilde{\lambda}, F\left[m\right]u - f\right\rangle, \quad (6)$$

$$\left.\frac{\partial L}{\partial \tilde{u}}\right|_{m,\tilde{u},\tilde{\lambda}} \left(\tilde{u}\right) = \left\langle R\tilde{u} + D, R\hat{u}\right\rangle + \left\langle F[m]^*\lambda, \hat{u}\right\rangle = \left\langle R^*(R\tilde{u}) + D\right\rangle + F[m^*\lambda, \hat{u}]. \quad (7)$$

Equating the derivatives above to zero, we get a direct problem with respect to u and an adjoint problem with respect to λ:

$$\frac{\partial L}{\partial \tilde{\lambda}} = 0 \Leftrightarrow F\left[m\right]u - f = 0, \quad (8)$$

$$\frac{\partial L}{\partial \tilde{u}} = 0 \Leftrightarrow R^*\left(R\tilde{u} + D\right) + F[m]^*\lambda = 0. \quad (9)$$

Equation (8) is a direct problem that can be solved by a numerical method. Many different approaches have been developed for seismic problems, for example [10-12]. Equation (9) is an adjoint problem with respect to λ, which can also be solved numerically. In the next section it will be shown that for the acoustic model the operator F and its conjugate F^* are

such that to solve the conjugate problem it is possible to use the same solver as for the direct problem.

Now consider the Frechet differential L with respect to the parameters of the medium m under the assumption that the terms of the operator F are linear with respect to m ($\tilde{u}$, $\tilde{\lambda}$, do not depend on m):

$$\begin{aligned}&\left.\frac{\partial L}{\partial m}\right|_{m,\tilde{u},\tilde{\lambda}}(\hat{m})=\left.\frac{\partial}{\partial m}\left\langle\tilde{\lambda},F[m]u\right\rangle\right|_{m,\tilde{u},\tilde{\lambda}}(\hat{m})=\\&=\left\langle\tilde{\lambda},F[m+\hat{m}]-F[m](u)\right\rangle_U=\\&=\left\langle I(\vec{x}),\hat{m}\right\rangle_M.\end{aligned}\tag{10}$$

Thus, the derivative of the functional with respect to the parameters m is an integral operator on the space $\mathcal{M}$ with kernel I:

$$\left\langle I(\vec{x}),\hat{m}\right\rangle_M=\int_\Omega\int_0^T\lambda\cdot\left(F[m+\hat{m}]-F[m]\right)u\,dtd\vec{x}.\tag{11}$$

The kernel $I=I(\vec{x})$ defines the integral operator defining the Frechet derivative, so I is usually called the gradient $\partial\Psi/\partial m$. This kernel is the desired derivative.

So, the algorithm for calculating $\partial\Psi/\partial m$ is as follows:

1. Solve direct problem (8) – find u.
2. Solve the conjugate problem (9) – find λ.
3. Calculate the gradient $I=I(\vec{x})$ using the integral formula (11) based on the calculated u and λ.

2.3. Acoustic model

In this work, acoustic equations were used to describe the seismic wave propagation in the geological media. This model correctly describes the propagation of P-waves, their multiple passage and reflection at the interfaces between layers. Mathematically, the model can be written as a scalar wave equation

$$u_{tt}=c^2\Delta u+f.\tag{12}$$

In this equation, $u=u(\vec{x},t)$ is the deviation of pressure in the medium from equilibrium state; $c=c(\vec{x})>0$ is the propagation velocity of longitudinal waves, Δ is the Laplace operator. Thus, the operator F can be written as

$$\mathrm{F}[\mathrm{m}]=\frac{\partial^2}{\partial \mathrm{t}^2}-\mathrm{c}^2\sum_{\mathrm{i}=1}^{\mathrm{d}}\frac{\partial^2}{\partial \mathrm{x}_\mathrm{i}^2}.\tag{13}$$

The problem is considered with zero initial conditions, since before the start of seismic exploration the medium was at rest. On the only physical boundary – the free surface – a zero boundary condition is set. Thus, we can define the spaces $\mathcal{U},\mathcal{U}^*$:

$$\mathcal{U}=\left\{f\in C^2:f\big|_{t=0}=0,f_{t\big|_{t=n}}=0,f\big|_{\vec{x}\in\partial\Omega}=0\right\},\tag{14}$$

$$\mathcal{U}^*=\left\{f\in C^2:f\big|_{t=T}=0,f_{t\big|_{t=T}}=0,f\big|_{\vec{x}\in\partial\Omega}=0\right\},\tag{15}$$

From this we can obtain the self-adjoint condition $F=F^*$:

$$\begin{aligned}&\forall u\in\mathcal{U}\circ\forall\lambda\in\mathcal{U}^*\to\left\langle F[m]u,\lambda\right\rangle_{L_2}=\\&=\left\langle u,F[m]\lambda\right\rangle_{L_2}.\end{aligned}\tag{16}$$

The restriction operator R represents taking values at points $\vec{x}_i$, , and its conjugate R^* is an operator that reduces the time signal at a set of points to the sum of delta functions over a coordinate at that set of points. Thus, the right side of the conjugate equation (9) $-R^*(Ru-D)$ is the sum of the point sources located at the data receiver locations D.

To calculate I using formula (11), it remains to express in explicit form the expression $\left(\mathrm{F}[\mathrm{m}+\hat{\mathrm{m}}]-\mathrm{F}[\mathrm{m}]\right)\mathrm{u}$. In this case, $\hat{m}$ will not be included in the final formula, being transferred to another factor of the scalar product according to formula (10). Considering the parameter m to be the square of the velocity, from (13) we obtain

$$\left(\mathrm{F}[\mathrm{m}+\hat{\mathrm{m}}]-\mathrm{F}[\mathrm{m}]\right)\mathrm{u}=\hat{\mathrm{c}}^2\Delta\mathrm{u},\tag{17}$$

$$I(\vec{x})=\int_0^T\lambda\cdot\Delta u\,dt.\tag{18}$$

However, it should be noted that for other parameterizations of the model under

consideration the result will be different. For example, considering the slowness $\beta = 1/c^2$ as a medium parameter, we can write $F_1 = \beta u_{tt} - \Delta u$, from which it follows $\left(F_1[m+\hat{m}] - F_1[m]\right)u = \beta u_{tt}$ and formula

$$I_1(\vec{x}) = \int_0^T \lambda \cdot u_{tt}\, dt. \tag{19}$$

The last formula, taking into account the zero initial conditions on u and the final conditions on λ, according to the rule of integration by parts, can easily be rewritten in the form

$$I_1(\vec{x}) = \int_0^T \lambda \cdot u_{tt}\, dt = -\int_0^T \lambda_t \cdot u_t\, dt = \int_0^T \lambda_{tt} \cdot u\, dt. \tag{20}$$

In this work, we used the simplified formula widely used in practice

$$I(\vec{x}) = \int_0^T \lambda \cdot u\, dt. \tag{21}$$

2.4. Gradient post-processing for the migration image calculation

For some real problems, the resulting gradient $\partial\Psi/\partial m$ is quite far from the desired migration image. There are several approaches to improve the result. For example, Least-Squares RTM performs a gradient descent procedure to achieve $dm \approx m_* - m_{\text{initial}}$, but this method is computationally expensive. In this work, we used several simpler techniques that allow us to significantly improve the final migration image in a short computational time.

The first such method is the seismic signal attenuation compensation. It is known that the amplitude of waves decreases due to geometric divergence even in a model of the geological media without dissipation. Consequently, the amplitude of the gradient obtained using integral (21) decays with depth, because the sources of both the direct and conjugate problems are located near the surface. To compensate for this effect, it was proposed to replace the integral formula (21) with the following:

$$\text{Image}(\vec{x}) = \frac{\sum_{\text{s:sources}} \int_0^T u_s \lambda_s dt}{\sum_{\text{s:sources}} \int_0^T u_s^2 dt + \delta}. \tag{22}$$

The non-negative denominator is separated from zero using the small constant δ. We also explicitly added summation over all sources to this formula: for each source there is its own set of data D, and its own calculation of the direct and conjugate problems is carried out.

A standard Laplace filter is used to suppress low-frequency noise components in the resulting image.

Since the amplitudes of $I(\vec{x})$ in the immediate vicinity of sources and receivers are extremely large, but are not of significant interest, when displaying I for visual analysis, values near the surface (down to depths of the order of 100 m) are set to zero.

3. RESULTS

The computational algorithm described in the work was implemented by the authors as a computer program in Python. To numerically solve the governing equations of the direct and adjoint problems, the open-source solver SpecFem2D, based on the spectral element method, was used [13]. Fourth order elements were used as a basis for expanding the solution. Near the lateral and lower boundaries, absorbing PML layers were additionally used [14]. During the modeling process, the calculated pressure fields were saved to the hard disk, after which they were used to calculate the integral using formula (22).

A two-dimensional formulation of the problem with the widely used test geological model Marmousi [15] in a monoparametric acoustic formulation (13) was considered. **Fig. 1** shows the *P*-wave velocity distribution in the true media model. To build an initial guess model, this distribution was smoothed using the gaussian_filter function of the

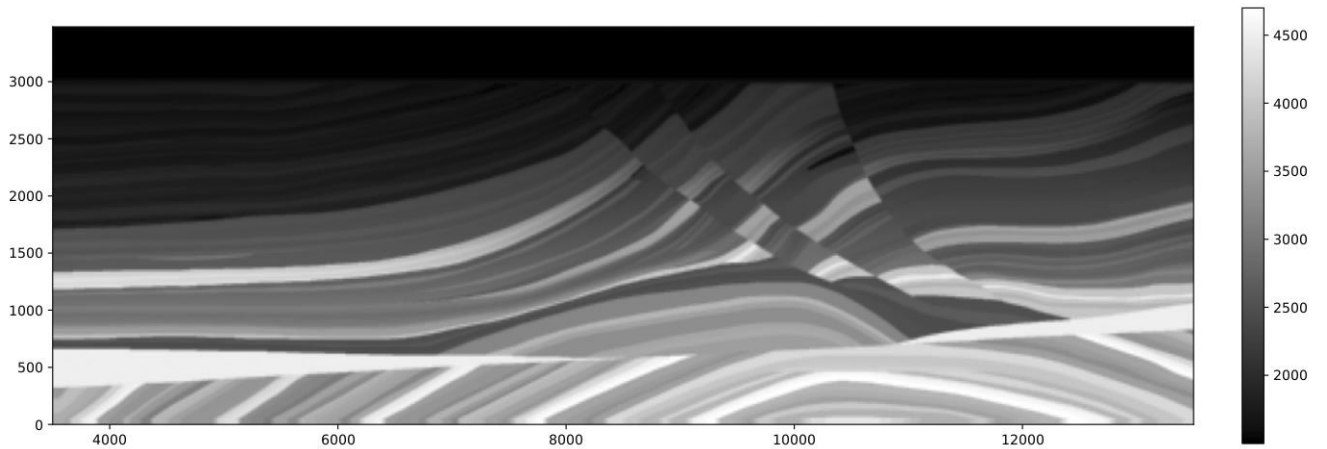

Fig. 1. *Spatial distribution of the P-wave velocity in the Marmousi model.*

SciPy.ndimage library. For clarity, the difference between the initial guess and the true distribution $m_* - m_{\text{initial}}$ is presented in **Fig. 2**.

When carrying out computer calculations, a square computational grid with a step of 20 m was used, covering a geological model with dimensions of 10×3.5 km. The total time of the computer experiment was 3.5 *s*, the time step was chosen equal to $3.5 \cdot 10^{-4}$ s. The source function was a Ricker pulse with a peak frequency of 25 Hz. On the day surface, data were recorded by 491 receivers, uniformly located with a step of 20 m at a depth of 10 m. To construct a migration image, 61 sources were used with a step of 150 m at a depth of 10 m. **Fig. 3** shows the result of the RTM method.

4. CONCLUSIONS

The work considers the seismic exploration inverse problem – determination of the boundary positions between the geological layers. The derivation of a calculation algorithm for the reverse time migration of seismic data in the general case is presented. Simplified calculation formulas for the acoustic model of the geological media were obtained. The computational algorithm was implemented as a computer program. It was successfully used to solve the migration problem for the Marmousi test model. Analysis of the resulting migration image confirms the possibility of localizing reflective horizons and suppressing noise.

As a further continuation of the research, the generalization of the considered approach

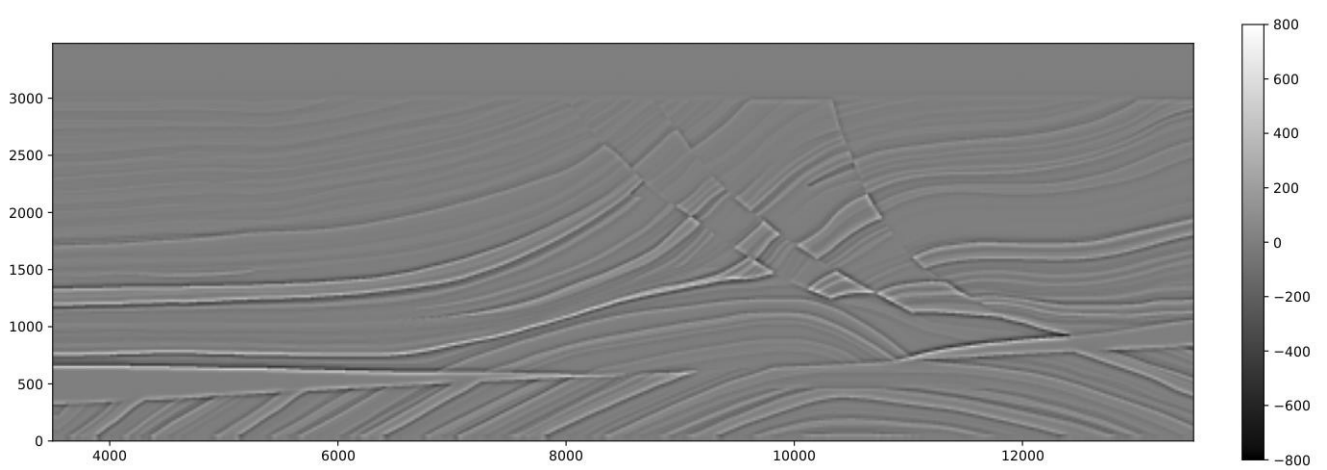

Fig. 2. *The difference between true model and used initial guess model.*

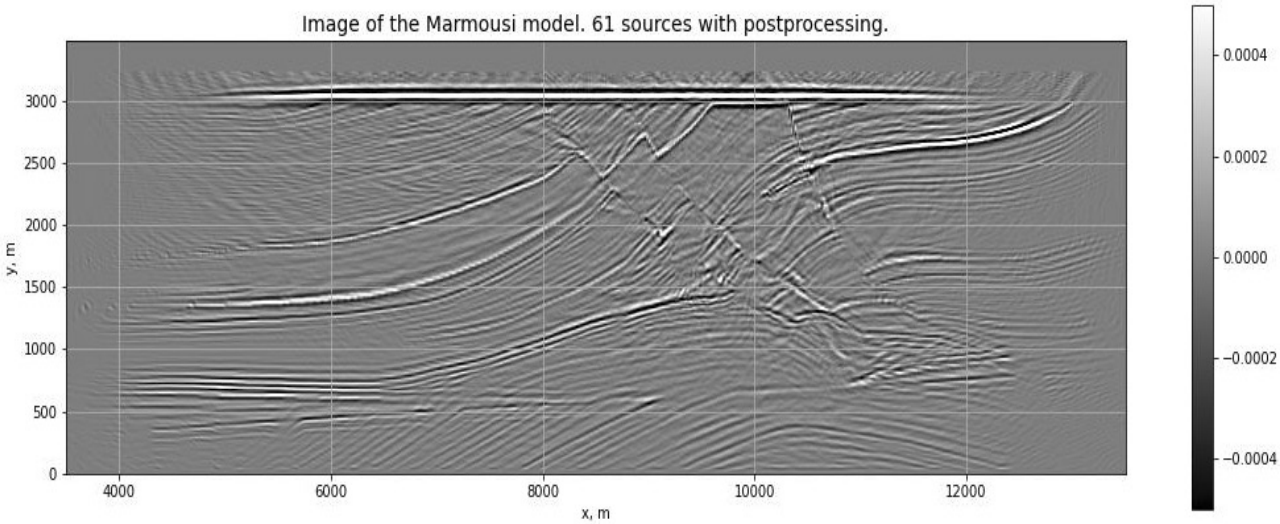

Fig. 3. *Obtained migration image.*

to more complex models of geological media, for example, isotropic and anisotropic linear elastic models is prominent.

REFERENCES

1. Lailly P. The Seismic Inverse Problem as a Sequence of before Stack Migrations. In: Bednar JB, Robinson E, Weglein A. (eds.). *Conference on Inverse Scattering – Theory and Application*, SIAM, Philadelphia, 1983, pp. 206-220.
2. Tarantola A. Inversion of seismic reflection data in the acoustic approximation. *Geophysics*, 1984, 49:1259-1266.
3. Baysal E, Kosloff DD, Sherwood JWC. Reverse time migration. *Geophysics*, 1983, 48:1514-1524.
4. Plessix RE, Mulder WA. Frequency-domain finite-difference amplitude-preserving migration. *Geophys. J. Int.*, 2004, 157:975-987.
5. Plessix RE. A review of the adjoint-state method for computing the gradient of a functional with geophysical applications. *Geophys. J. Int.*, 2006, 167(2):495-502.
6. Yang J, Liu Y, Dong L. Least-squares reverse time migration in the presence of density variations. *Geophysics*, 2016, 81(6):497-509.
7. Sun M, Dong L, Yang J, Huang C, Liu Y. Elastic least-squares reverse-time migration with density variations. *Geophysics*, 2018, 83(6):1-62.
8. Malovichko MS, Shevchenko AV, Golubev VI. On imaging conditions for elastic reverse-time migration. *Conference Quasilinear Equations, Inverse Problems and Their Applications (QIPA)*, 2022.
9. Ciarlet PG. *Introduction to Numerical Linear Algebra and Optimization*. Cambridge University Press, New York, 1989.
10. Virieux J, Calandra H, Plessix RE. A review of the spectral, pseudo-spectral, finite-difference and finite-element modelling techniques for geophysical imaging. *Geophysical Prospecting*, 2011, 59(5):794-813.
11. Golubev V, Shevchenko AV, Petrov I. Raising convergence order of grid-characteristic schemes for 2D linear elasticity problems using operator splitting. *Computer Research and Modeling*, 2022, 14(4):899-910.
12. Golubev V, Shevchenko A, Khokhlov N, Petrov I, Malovichko M. Compact Grid-Characteristic Scheme for the Acoustic System with the Piece-Wise Constant Coefficients. *International Journal of Applied Mechanics*, 2022, 14(02). DOI: 10.1142/S1758825122500028.
13. Peter D, Komatitsch D, Luo Y, Martin R et al. Forward and Adjoint Simulations

of Seismic Wave Propagation on Fully Unstructured Hexahedral Meshes. *Geophys. J. Int.*, 2011, 186(2):721-39. DOI: 10.1111/J.1365-246X.2011.05044.X.

14. Zhinan X, Komatitsch D, Martin R, et al. Improved Forward Wave Propagation and Adjoint-Based Sensitivity Kernel Calculations Using a Numerically Stable Finite-Element PML. *Geophys. J. Int.*, 2014, 198(3):1714-1747.
15. Brougois A, Bourget M, Lailly P, Poulet M, Ricarte P, Versteeg R. Marmousi, model and data. *Conference: EAGE Workshop - Practical Aspects of Seismic Data Inversion,* 1990. DOI: 10.3997/2214-4609.201411190.

DOI: 10.17725/rensit.2023.15.441

Evaluation of noise immunity of multi-user mimo systems with imperfect channel estimation and other distortions

Artem Shinkevich, Dmitry A. Pokamestov, Yakov V. Kryukov, Evgeny V. Rogozhnikov, Georgy N. Shalin, Andrey A. Brovkin

Tomsk State University of Control Systems and Radioelectronics, https://tusur.ru/
Tomsk 634050, Russian Federation

E-mail: a.shinkevich00@gmail.com, dmaltomsk@mail.ru, kryukov.tusur@gmail.com, udzhon@mail.ru, shalingn1120@gmail.com, soldierbrovkin@gmail.com

Received August 09, 2023, peer-reviewed August 16, 2023, accepted August 23, 2023, published December 06, 2023.

Abstract: **The technology of multi-antenna MIMO (Multiple Input Multiple Output) systems is actively used in modern wireless communication systems. MIMO can enhance the performance of wireless data transmission systems, but their effectiveness depends on the transmission conditions. Ideal conditions are represented as a channel with a large number of possible signal propagation paths and an error-free estimation of its parameters. The estimation error significantly affects the performance of the beamforming algorithms used to mitigate inter-user interference in multi-user MIMO (MU-MIMO) systems. Spatial correlation of the channel results in a decrease in the number of independent information transmission streams. These factors can significantly reduce the performance of multi-antenna systems. For this reason, operating MIMO communication systems under non-ideal conditions is a topical issue. The paper examines the performance of various beamforming algorithms in such conditions. It describes the communication systems with MIMO, beamforming algorithms, and distorting effects. The paper includes a developed simulation model of the communication channel with MU-MIMO accounting for a variety of distorting factors. The results demonstrate the bit-error probability dependences for different simulation scenarios**

Keywords: **MIMO, MU-MIMO, gigital precoding, hybrid beamforming, imperfect CSI, Los channel, spatial correlation**

UDC 621.396.4

Acknowledgments: The research was carried out at the expense of the grant of the Russian Science Foundation No. 22-79-10148, https://rscf.ru/project/22-79-10148/.

For citation: Artem Shinkevich, Dmitry A. Pokamestov, Yakov V. Kryukov, Evgeny V. Rogozhnikov, Georgy N. Shalin, Andrey A. Brovkin. Evaluation of noise immunity of multi-user mimo systems with imperfect channel estimation and other distortions. *RENSIT: Radioelectronics. Nanosystems. Information Technologies*, 2023, 15(4):441-452e. DOI: 10.17725/rensit.2023.15.441.

Contents

1. INTRODUCTION

Wireless communication systems are widely used nowadays. The growing transmitted

data volumes and the development of new applications led to increased demands for modern communication systems: spectral and energy efficiency, data rate, noise immunity, mitigation of delays, the ability to connect a large number of subscribers, etc.

Multi-antenna Multiple Input Multiple Output (MIMO) systems are one of the key technologies for increasing spectral efficiency, and, accordingly, data rate and noise immunity of the transmission. Unlike traditional single-antenna Single Input Single Output (SISO) systems, MIMO uses multiple antennas both on the transmitting and receiving sides. Ideally for systems with MIMO, the number of independent streams is a multiple of the number of antennas. This is achieved in an uncorrelated multipath channel with non-line-of-sight, where the receiver is synchronous with the transmitter and ideally evaluates the frequency response (FR) of the channel. However, in real systems, due to the physical proximity of antenna elements, there is a spatial correlation of signals, and noise does not allow for an accurate assessment of the channel frequency response. Some scenarios are characterized by the line of sight, which also leads to signal correlation. These factors significantly affect the MIMO performance, impairing the efficiency of multiplexing and channel noise immunity.

There are two types of MIMO: single-user (SU-MIMO) and multi-user (MU-MIMO). In multi-user systems, a base station with multiple antennas can simultaneously transmit a signal to several subscriber stations with one or more antennas (broadcast channel) [1]. It is also possible that many subscribers with one or more antennas transmit a signal to one base station with several antennas (multiple access channel) [1].

Inter-user interference, caused by signals intended for other subscribers, should be mitigated. Different types of beamforming are used to tackle this issue with MU-MIMO systems making it possible to perform this procedure in a digital, analog or hybrid (digital and analog) form.

Analog beamforming, which originated in the middle of the 20th century, is directly related to phased arrays. In modern systems employing analog beamforming, signals from the radio frequency (RF) circuit are fed to phase shifters before reaching the antenna elements, which allows for real-time adjustments to the antenna pattern [2].

In the case of digital beamforming, the signal from the modulator output arrives at a digital preliminary coder (precoder), where it is multiplied by the calculated coefficients. This operation results in changing both the signal amplitude and its phase. There are different precoding algorithms, for example, Block Diagonalization (BD) [3], Channel Inversion (ChI) [4], Dirty-Paper Coding (DPC) [5], Tomlinson–Harashima (TH) [6], and others [7–8].

Hybrid beamforming combines analog beamforming and digital precoding. In this case, signal is processed in the time and frequency domain. Currently, hybrid beamforming is the main technology for massive MIMO (mMIMO) systems, as well as communication systems in the mmWave range [9].

Even though the algorithms used in MU-MIMO have been known for a long time, the evaluation and comparison of various beamforming methods are poorly represented in the literature. This article addresses the impact of various distorting factors on the signal noise immunity, including frequency response estimation errors, spatial correlation, and Rice *K*-factor,

when using different beamforming methods. It also describes the obtained dependences of the bit error probabilities and the ratio of energy per bit of information to spectral power density of noise. There are conclusions about the effectiveness and applicability of the considered methods presented.

2. BEAMFORMING IN MU-MIMO

Fig. 1 shows the structural schemes of systems employing different variants of beamforming. For digital and hybrid adaptive beamforming on the transmitting side, it is required to have the channel state information (CSI), which is transmitted via the feedback channel. In real systems, the presence of noise often hinders the accurate estimation of the channel parameters. The CSI discreteness also affects the performance of MIMO systems, underscoring the need to take into account the imperfection of the estimation when considering the effectiveness of beamforming algorithms.

As the problem statement, let us consider a mathematical model of the MU-MIMO system with digital beamforming (precoding). Its block diagram is presented in **Fig. 2**.

Let $\mathbf{s}^1$, …, $\mathbf{s}^K$ be the modulation symbols of K subscribers. $\mathbf{S}=\left[\left(\mathbf{s}^1\right)^{\mathrm{T}},\cdots,\left(\mathbf{s}^k\right)^{\mathrm{T}}\right]^{\mathrm{T}}$, — the transposition operation, $\mathbf{V}_1$, …, $\mathbf{V}_K$ are

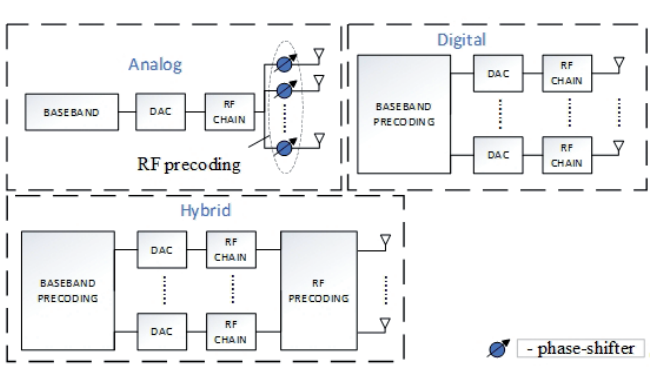

Fig. 1. *Beamforming types.*

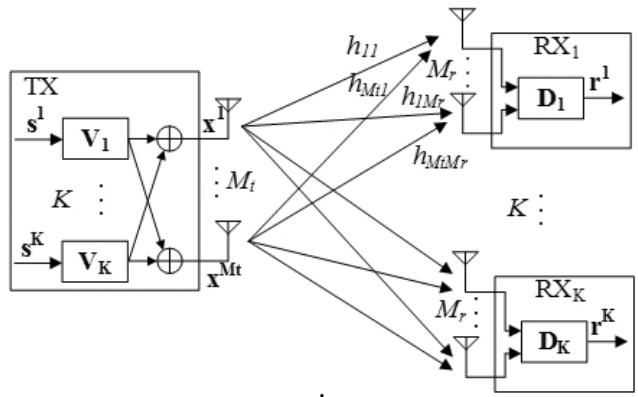

Fig. 2. *Block diagram of MU-MIMO system with precoding.*

precoding matrices. $\mathbf{V}=\left[\mathbf{V}_1,\cdots,\mathbf{V}_K\right]$, $\mathbf{x}^{\mathrm{k}}$ are symbol vectors transmitted through M_{t} antennas,

$$\mathbf{X}=\left[\left(\mathbf{x}^1\right)^{\mathrm{T}},\cdots,\left(\mathbf{x}^k\right)^{\mathrm{T}}\right]^{\mathrm{T}},$$

$$\mathbf{X}=\mathbf{VS}=\sum_{k=1}^{K}\mathbf{x}^k=\sum_{k=1}^{K}\mathbf{V}_k\mathbf{s}^k.$$

Let $\mathbf{y}^{\mathrm{k}}$ represent the signal sample vector at the input of the kth receiver, and $\mathbf{n}^{\mathrm{k}}$ represent the sample vector of noise implementations at the input of the kth receiver; $\mathbf{H}_{\mathrm{k}}$ is the matrix of channel coefficients for the kth receiver, $\mathbf{H}=\left[\mathbf{H}_1{}^{\mathrm{T}},\ldots,\mathbf{H}_K{}^{\mathrm{T}}\right]^{\mathrm{T}}$.

$$\mathbf{y}^k=\mathbf{H}_k\mathbf{X}+\mathbf{n}^k=\mathbf{H}_k\mathbf{x}^k+\sum_{i=1,i\neq k}^{K}\mathbf{H}_k\mathbf{x}^i+\mathbf{n}^k=$$

$$=\mathbf{H}_k\mathbf{V}_k\mathbf{s}^k+\sum_{i=1,i\neq k}^{K}\mathbf{H}_k\mathbf{V}_i\mathbf{s}^i+\mathbf{n}^k,$$

$$\mathbf{Y}=\mathbf{HX}+\mathbf{N},$$

$$\mathbf{N}=\begin{bmatrix}\mathbf{n}^1\\ \vdots\\ \mathbf{n}^K\end{bmatrix}=\begin{bmatrix}n_1\\ \vdots\\ n_{KMr}\end{bmatrix}.$$

In each of the K receivers, the signal is postprocessed using matrices $\mathbf{D}_{\mathrm{k}}$, and the reconstructed signal for the kth user $\mathbf{r}^{\mathrm{k}}$ is described by the following expressions:

$$\mathbf{r}^k=\mathbf{D}_k\mathbf{y}^k,$$

$$\mathbf{r}^k=\mathbf{D}_k\left(\mathbf{H}_k\mathbf{V}_k\mathbf{s}^k+\sum_{i=1,i\neq k}^{K}\mathbf{H}_k\mathbf{V}_i\mathbf{s}^i+\mathbf{n}^k\right).$$

Thus, $\mathbf{D}_k\mathbf{H}_k\mathbf{V}_k\mathbf{s}^k$ is a desired signal intended for the *k*th subscriber, and $\sum_{i=1,i\neq k}^{K}\mathbf{D}_k\mathbf{H}_k\mathbf{V}_i\mathbf{s}^i$ is an interference component.

The problem of digital beamforming can be formulated as the problem of mitigating the interference component, which is equivalent to the expression:

$$\sum_{i=1,i\neq k}^{K}\mathbf{D}_k\mathbf{H}_k\mathbf{V}_i\mathbf{s}^i \equiv \mathbf{\Theta},$$

where $\mathbf{\Theta}$ is the zero vector.

Therefore, the problem is reduced to finding precoding matrices $\mathbf{V}_i$ and postprocessing matrices $\mathbf{D}_k$.

Let us examine the precoding types mentioned earlier, along with the hybrid beamforming.

2.1. Block Diagonalization

To form a precoding matrix for the *k*th user, it is required to have information about the status of channels of other users, that is, the interference matrix, which includes channel matrices between the base station and other users [3]:

$$\hat{\mathbf{H}}_k = \left[\hat{\mathbf{H}}_1^{\mathrm{T}},\cdots,\hat{\mathbf{H}}_{k-1}^{\mathrm{T}},,\hat{\mathbf{H}}_{k+1}^{\mathrm{T}}\cdots\hat{\mathbf{H}}_k^{\mathrm{T}}\right]^{\mathrm{T}}. \quad (1)$$

After that, the singular value decomposition (SVD) of the resulting matrix is performed and the matrix rank is calculated:

$$\hat{L}_k = \mathrm{rank}\left(\hat{\mathbf{H}}_k\right),$$

$$\hat{\mathbf{H}}_k = \hat{\mathbf{U}}_k\hat{\mathbf{\Lambda}}_k\left[\hat{\mathbf{V}}_k^{(1)}\hat{\mathbf{V}}_k^{(0)}\right]^{\mathrm{H}},$$

where $\mathbf{U}_k$ are left singular vectors; $\mathbf{\Lambda}_k$ is a diagonal matrix containing the singular numbers of matrix $\mathbf{H}_k$; $\mathbf{V}_k^{(1)}$ are the first L_k of the right singular vectors of matrix $\mathbf{V}_k$; $\mathbf{V}_k^{(0)}$ are $(N_{tx} - L_k)$ of the right singular vectors of matrix $\mathbf{V}_k$; and $\mathbf{V}_k^{(0)}$ forms an orthogonal basis for the space of (1) [3]. And in what follows, $(\bullet)^{\mathrm{H}}$ is the Hermitian transpose.

The next step is to perform SVD of the product of the channel matrix for the kth user and $\hat{\mathbf{V}}_k^{(0)}$:

$$\mathbf{H}_k\hat{\mathbf{V}}_k^{(0)} = \mathbf{U}\mathbf{\Lambda}\left[\mathbf{V}_k^{(1)}\mathbf{V}_k^{(0)}\right]^{\mathrm{H}}.$$

As a result, the general precoding matrix can be represented as: $\mathbf{V} = \left[\hat{\mathbf{V}}_1^{(0)}\mathbf{V}_1^{(1)},\hat{\mathbf{V}}_2^{(0)}\mathbf{V}_2^{(1)},\ldots,\hat{\mathbf{V}}_K^{(0)}\mathbf{V}_K^{(1)}\right]$.

The postprocessing matrix can be expressed as follows [3]:

$$\mathbf{D} = \begin{bmatrix} \mathbf{U}_1^{\mathrm{H}} & \cdots & \mathbf{0} \\ \vdots & \ddots & \vdots \\ \mathbf{0} & \cdots & \mathbf{U}_K^{\mathrm{H}} \end{bmatrix}.$$

2.2. Dirty-Paper Coding

The DPC algorithm is based on an *LQ* decomposition of the channel matrix [1], which is, in turn, associated with a *QR* decomposition:

$$\mathbf{H} = \mathbf{L}\mathbf{Q}, \quad (2)$$

where $\mathbf{L}$ is a lower triangular matrix (with elements above the main diagonal being zero), and $\mathbf{Q}$ is the orthogonal matrix ($\mathbf{Q}\mathbf{Q}^{\mathrm{H}} = \mathbf{Q}^{\mathrm{H}}\cdot\mathrm{Q} = \mathbf{I}$).

$$\mathbf{H} = \mathbf{Q}\mathbf{R}, \quad (3)$$

where $\mathbf{R}$ is an upper triangular matrix (with elements below the main diagonal being zero), and $\mathbf{Q}$ is the orthogonal matrix.

Let us derive the relation of the *LQ* and *QR* decompositions (2) and (3):

$$(\mathbf{Q}\mathbf{R})^{\mathrm{H}} = \mathbf{R}^{\mathrm{H}}\mathbf{Q}^{\mathrm{H}} = \mathbf{L}\mathbf{Q}^{\mathrm{H}} = \mathbf{H}^{\mathrm{H}}. \quad (4)$$

From equation (4), it follows that the *QR* decomposition of matrix $\mathbf{H}^{\mathrm{H}}$ will be the Hermitian-transposed *LQ* decomposition of matrix $\mathbf{H}$.

The precoding matrix is calculated based on matrix $\mathbf{L}$. Multiplying the precoded signal by $\mathbf{Q}^{\mathrm{H}}$ eliminates the impact of $\mathbf{Q}$ [1]. Considering this, the received signal can be written as follows [1]:

$$\mathbf{Y} = \mathbf{HQ}^{\mathrm{H}}\mathbf{X} + \mathbf{Z} = \mathbf{LQQ}^{\mathrm{H}}\mathbf{X} + \mathbf{Z} = \\ = \mathbf{LX} + \mathbf{Z} = \begin{pmatrix} l_{11} & 0 & \cdots & 0 \\ l_{21} & l_{22} & \cdots & 0 \\ \vdots & \vdots & \ddots & \vdots \\ l_{m1} & l_{m2} & \cdots & l_{mm} \end{pmatrix} \begin{pmatrix} x_1 \\ x_2 \\ \vdots \\ x_m \end{pmatrix} + \begin{pmatrix} z_1 \\ z_2 \\ \vdots \\ z_m \end{pmatrix}, \quad (5)$$

where $\mathbf{X}$ is the precoded signal and $\mathbf{Z}$ is the noise.

Let us express the reception conditions without interference from (5).

For the first antenna, it is expressed as:

$$x_1 = \tilde{x}_1, \quad (6)$$

where $\tilde{x}_1$ is the signal at the precoder input.

From (5), the condition for the 2nd antenna can be expressed as:

$$x_2 = \tilde{x}_2 - \frac{l_{21}}{l_{22}} x_1, \quad (7)$$

from equations (6) and (7), the condition for the ith antenna is represented as:

$$x_i = \tilde{x}_i + \sum_{k=1}^{i-1} (-1) \frac{l_{ik}}{l_{ii}} x_k.$$

Therefore, the precoding matrix can be described using the following expression [1]:

$$\begin{pmatrix} 1 & 0 & \cdots & 0 \\ -\frac{l_{21}}{l_{22}} & 1 & \cdots & 0 \\ \vdots & \vdots & \ddots & \vdots \\ -\frac{l_{m1}}{l_{mm}} & -\frac{l_{m2}}{l_{mm}} & \cdots & 1 \end{pmatrix} = \\ = \begin{pmatrix} l_{11} & 0 & \cdots & 0 \\ l_{21} & l_{22} & \cdots & 0 \\ \vdots & \vdots & \ddots & \vdots \\ l_{m1} & l_{m2} & \cdots & l_{mm} \end{pmatrix}^{-1} \begin{pmatrix} l_{11} & 0 & \cdots & 0 \\ 0 & l_{12} & \cdots & 0 \\ \vdots & \vdots & \ddots & \vdots \\ 0 & 0 & \cdots & l_{mm} \end{pmatrix}. \quad (8)$$

The precoded signal can be expressed using the following formula:

$$\mathbf{X} = \mathbf{L}^{-1} \operatorname{diag}(\mathbf{L}) \tilde{\mathbf{X}}, \quad (9)$$

where $\mathbf{L}$ is the matrix resulting from the LQ decomposition of matrix $\mathbf{H}$, $\tilde{\mathbf{X}}$ is the signal from the output of the modulator, and *diag* are the elements of the main diagonal.

The postprocessing for this algorithm is expressed as follows [1]:

$$\hat{\mathbf{X}} = \begin{pmatrix} l_{11} & 0 & \cdots & 0 \\ 0 & l_{12} & \cdots & 0 \\ \vdots & \vdots & \ddots & \vdots \\ 0 & 0 & \cdots & l_{mm} \end{pmatrix}^{-1} \mathbf{Y}, \quad (10)$$

where $\hat{\mathbf{X}}$ is the reconstructed signal.

DPC is a non-linear algorithm enabling the maximum possible bandwidth in MIMO systems. However, this algorithm is of limited practical utility, due to its high computational complexity and the associated increase in transmission power caused by the algorithm peculiarities.

2.3. Tomlinson-Harashima

The TH algorithm can be considered as a variant of DPC with a symmetric modulo operation. Initially, TH was introduced to diminish peak or average power in the Decision Feedback Equalizer (DFE). The concept behind applying TH in DFE is to mitigate the impact of postcursor intersymbol interference (ISI) [10] on the transmitting side, where the transmitted symbols are known a priori [11,12].

Let us denote the signal precoded by the DPC algorithm (9) as $\mathbf{C}$.

The symmetric modulo operation for a signal can be expressed as follows:

$$\mathbf{X} = \mathbf{C} - 2A \left\lfloor \frac{(\mathbf{C} + A + jA)}{2A} \right\rfloor, \quad (11)$$

where $A = \sqrt{M}$, M is the modulation order, $\mathbf{X}$ is the precoded signal, and $\lfloor\ \rfloor$ is the operation of rounding down to the nearest integer.

Expression 11 can be transformed as follows:

$$\mathbf{X} = \mathbf{C} - 2A \left(\left\lfloor \frac{\mathrm{Re}(\mathbf{C}) + A}{2A} \right\rfloor + j \left\lfloor \frac{\mathrm{Im}(\mathbf{C}) + A}{2A} \right\rfloor \right), \quad (12)$$

where Re is the real part of the number, Im is the imaginary part of the number, and j denotes the imaginary unit.

The postprocessing problem is simplified to expression 10 from DPC and the subsequent modulo operation (12).

2.4. Channel Inversion

Precoding that uses the ChI algorithm for MU-MIMO systems essentially amounts to a pre-equalization operation [13] used in SU-MIMO systems, which is based on the same expressions.

In the case of zero-forcing (ZF), the precoding matrix is expressed as follows:

$$\mathbf{W}_{ZF} = \beta \mathbf{H}^{-1}, \quad (13)$$

where $\mathbf{H}$ is the channel matrix, β is the coefficient used to limit the total transmitted power after pre-equalization.

Coefficient β is calculated using the formula:

$$\beta = \sqrt{\frac{N_{TX}}{\mathrm{Tr}\left(\mathbf{H}^{-1}\left(\mathbf{H}^{-1}\right)^{H}\right)}},$$

where N_{TX} is the number of transmitting antennas, $\mathbf{H}$ is the channel matrix, and Tr is the matrix trace, that is, the sum of elements on the main diagonal.

This coefficient allows for normalizing the output power to 1 watt.

Postprocessing is simplified to dividing the received signal by β:

$$\hat{\mathbf{X}} = \frac{\mathbf{Y}}{\beta},$$

where $\mathbf{Y}$ is the received signal and $\hat{\mathbf{X}}$ is the reconstructed signal.

By definition, β is the gain factor for an automatic gain control (AGC) system.

In the case of the Minimum Mean Squared Error (MMSE) equalizer, equation (13) takes the following form:

$$\mathbf{W} = \beta \mathbf{H}^{H}\left(\mathbf{H}\mathbf{H}^{H} + \frac{N_{TX} \cdot 10^{\left(\frac{-SNR}{10}\right)}}{2}\mathbf{I}\right)^{-1},$$

where $\mathbf{I}$ is the identity matrix with ones on the main diagonal, and SNR is the signal-to-noise ratio measured in dB.

2.5. Hybrid Beamforming

Hybrid beamforming is a combined method that employs analog beamforming while using phase shifters. In numeric simulation, the analog beamforming matrix contains shift coefficients for each RF circuit. The digital precoding matrix, in turn, contains specific weights for signal processing in the frequency domain. This method allows combining the advantages of digital and analog beamforming to achieve the best performance with minimal complexity of equipment and energy consumption [14].

To calculate the precoding and postprocessing matrices, approximation is used, involving the decomposition of a signal into basic functions from a predefined set (codebook), where these functions are called atoms. Sparse approximation, in turn, aims to approximate the signal using the smallest number of elements, while maintaining the number of errors lower than a specified threshold level, i.e.

$$f(t) = \sum_{m=0}^{N-1} a_m g_m(t) + \mathbf{r}_N,$$
$$\|\mathbf{r}_N\| \to \min, \quad \|\mathbf{a}\|_0 \to \min,$$

where a_m is the decomposition coefficient; $g_m(t)$ is the codebook atom $\mathbf{D}$; N is the number of decomposition elements; $\mathbf{r}_N$ is the approximation error; $\|\bullet\|$ —the norm; and $\|\bullet\|_0$ is pseudonorm L_{-0}, equal to the number of non–zero elements of the vector.

The problem of determining digital ($\mathbf{F}_{bb}$) and analog ($\mathbf{F}_{rf}$) precoding matrices can be formulated as maximizing mutual

information, $\arg\max_{(\mathbf{F}_{rf},\mathbf{F}_{bb})}\left(\mathrm{I}\left(\mathbf{F}_{rf},\mathbf{F}_{bb}\right)\right)$, expressed by the following formula:

$$\mathrm{I}\left(\mathbf{F}_{rf},\mathbf{F}_{bb}\right)= \\ =\log_2\left(\det\left(\mathbf{I}+\frac{\rho}{N_s\sigma^2}\mathbf{H}\mathbf{F}_{rf}\mathbf{F}_{bb}\mathbf{F}_{bb}^{\mathrm{H}}\mathbf{F}_{rf}^{\mathrm{H}}\mathbf{H}^{\mathrm{H}}\right)\right). \quad (14)$$

At the same time, by using SVD and its properties [15], equation (14) can be transformed as follows:

$$\mathrm{I}\left(\mathbf{F}_{rf},\mathbf{F}_{bb}\right)= \\ =\log_2\left(\det\left(\mathbf{I}+\frac{\rho}{N_s\sigma^2}\mathbf{\Sigma}^2\mathbf{V}^{\mathrm{H}}\mathbf{F}_{rf}\mathbf{F}_{bb}\mathbf{F}_{bb}^{\mathrm{H}}\mathbf{F}_{rf}^{\mathrm{H}}\mathbf{V}\right)\right), \quad (15)$$

where $\mathbf{V}$ and $\mathbf{\Sigma}$ are the matrices from the singular decomposition of matrix $\mathbf{H}$; ρ is the average power of the transmitter; N_S is the number of digital streams; and σ^2 is the noise variance.

In addition, $\mathbf{V} = [\mathbf{V}_1\mathbf{V}_2]$. Through mathematical substitutions in (15), as elaborated in [16], the optimal precoding matrix is represented as $\mathbf{F}_{\mathrm{opt}}=\mathbf{V}_1$. Furthermore, based on these transformations, the problem of determining precoding matrices can be reformulated as follows:

$$\left[\mathbf{F}_{bb},\mathbf{F}_{rf}\right]=\arg\min_{(\mathbf{F}_{bb},\mathbf{F}_{rf})}\left(\left\|\mathbf{F}_{opt}-\mathbf{F}_{rf}\mathbf{F}_{bb}\right\|_{\mathrm{F}}\right), \quad (16)$$

where $\|\bullet\|_{\mathrm{F}}$ is the Frobenius norm.

The mathematical apparatus of sparse approximation is well-developed and highly suitable for calculating precoding and postprocessing matrices in the context of hybrid beamforming. In particular, equation (16) can be solved using the Orthogonal Matching Pursuit (OMP) algorithm [17]. Although there are other algorithms, for example, manifold optimization-based AltMin (MO-AltMin) [18], OMP offers significantly lower computational complexity with a slight decrease in spectral efficiency gain [19]. For this reason, this algorithm was used in the simulation.

The signal at the input of the receiving antenna can be recorded as follows:

$$\mathbf{y}=\mathbf{H}\mathbf{F}_{rf}\mathbf{F}_{bb}\mathbf{x}+\mathbf{n}.$$

The postprocessing problem is to minimize the Mean Squared Error (MSE) between the signal from the modulator output and the received signal after processing $\arg\min_{(\mathbf{W}_{rf},\mathbf{W}_{bb})}\left(\mathrm{E}\left\{\left\|\mathbf{x}-\mathbf{W}_{bb}^{\mathrm{H}}\mathbf{W}_{rf}^{\mathrm{H}}\mathbf{y}\right\|_2^2\right\}\right)$, hereafter, E{...} is the averaging operator.

Consequently, the optimal postprocessing matrix is the MMSE equalization matrix, which in this case can be expressed as follows:

$$\mathbf{W}_{MMSE}^{\mathrm{H}}=\mathrm{E}\left\{\mathbf{s}\mathbf{y}^{\mathrm{H}}\right\}\mathrm{E}\left\{\mathbf{y}\mathbf{y}^{\mathrm{H}}\right\}^{-1}= \\ =\frac{1}{\sqrt{\rho}}\left(\mathbf{F}_{bb}^{\mathrm{H}}\mathbf{F}_{rf}^{\mathrm{H}}\mathbf{H}^{\mathrm{H}}\mathbf{H}\mathbf{F}_{rf}\mathbf{F}_{bb}+\frac{\sigma^2N_s}{\rho}\mathbf{I}\right)^{-1}\mathbf{F}_{bb}^{\mathrm{H}}\mathbf{F}_{rf}^{\mathrm{H}}\mathbf{H}^{\mathrm{H}}. \quad (17)$$

Taking into account (17) and using transformations, the determination of digital and analog postprocessing matrices can be simplified to the following expression:

$$\left[\mathbf{W}_{rf},\mathbf{W}_{bb}\right]= \\ =\arg\min_{(\mathbf{W}_{rf},\mathbf{W}_{bb})}\left(\left\|\mathrm{E}\left\{\mathbf{y}\mathbf{y}^{\mathrm{H}}\right\}^{\frac{1}{2}}\left(\mathbf{W}_{MMSE}-\mathbf{W}_{rf}\mathbf{W}_{bb}\right)\right\|_{\mathrm{F}}\right).$$

The OMP algorithm [17] can also used to solve this problem.

The reconstructed signal can be written as follows:

$$\hat{\mathbf{x}}=\mathbf{W}_{bb}\mathbf{W}_{rf}\mathbf{y}.$$

3. SIMULATION RESULTS

To assess the noise immunity ensured by using different types of beamforming, a mathematical model of a broadcast MU-MIMO communication system has been developed. **Table 1** contains the main simulation parameters.

The simulation has been carried out under different scenarios. The results are the dependences of BER on E_0/N_0.

In the first scenario, the channel coefficients obey the Rayleigh distribution.

Table 1

Simulation parameters

Modulation	QPSK
Transmitting antennas number	16
Number of users	4
Number of receiving antennas per user	4
Message size	320 bits per user
Signal-to-noise ratio range	[0-30]
Iterations number	1000

The simulation in this scenario has been carried out for the BD, ChI, DPC, TH algorithms with perfect and imperfect CSI estimation.

Perfect estimation assumes that the transmitter knows the instantaneous values of the channel matrix. It is important to note that the channel is stationary, and CSI perfectly aligns with the channel matrix. Imperfect estimation implies the presence of noise due to which the receiver cannot accurately estimate both the channel and the temporary non-stationarity of the channel frequency response.

Fig. 3 shows the obtained dependences of the BER estimation on the ratio of the energy per bit of information to the noise power spectral density E_b/N_0 for different root-mean-square error (MSE) estimates.

The second scenario considers the influence of the line of sight on the noise immunity. The presence of line of sight impairs the performance of multi-antenna systems because it leads to a decrease in the channel matrix rank. Channel coefficients obey the Rice distribution. In this scenario, the channel matrix can be described by the following formula:

$$\mathbf{H} = \sqrt{\frac{K}{1+K}}\mathbf{H}_{LoS} + \sqrt{\frac{1}{1+K}}\mathbf{H}_{NLoS},$$

where $\mathbf{H}_{LoS}$ is the line-of-sight component, $\mathbf{H}_{NLoS}$ is a random component of the channel matrix, and K is the Rice factor (the ratio of the direct ray power to the power of the other rays).

The line-of-sight component can be represented as follows:

$$\mathbf{H}_{LoS} = \mathbf{a}_{rx}(\theta_{rx})\left(\mathbf{a}_{tx}(\theta_{tx})\right)^{\mathrm{T}},$$

where $\mathbf{a}_{\mathrm{rx}}(\theta_{\mathrm{rx}})$ and $\mathbf{a}_{\mathrm{tx}}(\theta_{\mathrm{tx}})$ are the responses of the receiving and transmitting antenna arrays, respectively; θ_{rx} and θ_{tx} are the receiving and transmitting angles, respectively.

Fig. 4 shows the obtained dependences of BER on E_b/N_0 at different values of the Rice coefficient K.

The K = 2 coefficient indicates a weak line of sight, K = 100 implies a weakly expressed multipath nature, K = 10 suggests the presence of both multipath and line-of-sight components.

The simulation for the third scenario has been performed in a correlated Rayleigh channel. In this scenario, the channel coefficients follow the Rayleigh distribution,

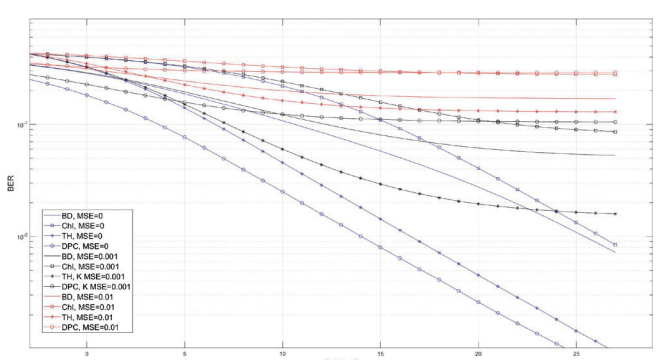

Fig. 3. *Dependences of BER on E_b/N_0 in the Rayleigh channel with different estimation errors*

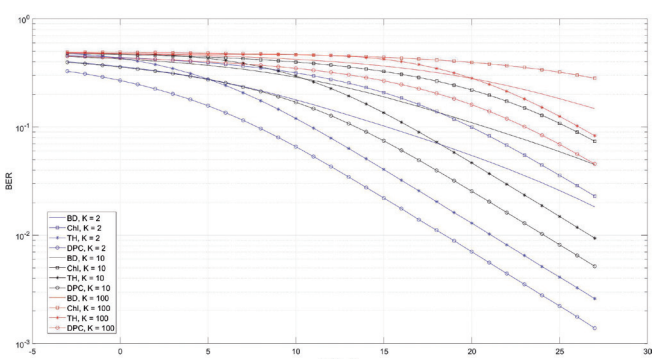

Fig. 4. *Dependences of BER on E_b/N_0 in the Rice channel with different values of coefficient K.*

but it is characterized by spatial correlation on both the receiving and transmitting sides caused by the physical proximity of antenna elements and the limited diversity of the propagation medium. Considering this, the channel matrix can be written as follows [1]:

$$\mathbf{H} = \mathbf{R}_{rx}^{1/2}\mathbf{H}_{\omega}\mathbf{R}_{tx}^{1/2},$$

where $\mathbf{R}_{rx}$, $\mathbf{R}_{tx}$ are the correlation matrices on the receiving and transmitting sides, respectively, and $\mathbf{H}_{\omega}$ is the uncorrelated channel matrix.

Correlation matrices take the following form:

$$\mathbf{R}_{tx} = \begin{bmatrix} 1 & \rho_{tx} & \rho_{tx}^4 & \cdots & \rho_{tx}^{(N-1)^2} \\ \rho_{tx} & 1 & \rho_{tx} & \cdots & \vdots \\ \rho_{tx}^4 & \rho_{tx} & 1 & \cdots & \rho_{tx}^4 \\ \vdots & \vdots & \vdots & \ddots & \rho_{tx} \\ \rho_{tx}^{(N-1)^2} & \cdots & \rho_{tx}^4 & \rho_{tx} & 1 \end{bmatrix},$$

$$\mathbf{R}_{rx}^k = \begin{bmatrix} 1 & \rho_{rx} & \rho_{rx}^4 & \cdots & \rho_{rx}^{(N-1)^2} \\ \rho_{rx} & 1 & \rho_{rx} & \cdots & \vdots \\ \rho_{rx}^4 & \rho_{rx} & 1 & \cdots & \rho_{rx}^4 \\ \vdots & \vdots & \vdots & \ddots & \rho_{rx} \\ \rho_{rx}^{(N-1)^2} & \cdots & \rho_{rx}^4 & \rho_{rx} & 1 \end{bmatrix},$$

$$\mathbf{R}_{rx} = \begin{bmatrix} \mathbf{R}_{rx}^1 & 0 & \cdots & 0 \\ 0 & \mathbf{R}_{rx}^2 & \cdots & 0 \\ \vdots & \vdots & \ddots & \vdots \\ 0 & 0 & \cdots & \mathbf{R}_{rx}^K \end{bmatrix},$$

where $\mathbf{R}_{rx}^k$ is the correlation matrix for the kth user, while ρ_{tx} and ρ_{rx} are the correlation coefficients on the transmitting and receiving sides. **Fig. 5** shows the obtained dependences.

The selection of these correlation coefficient values is justified as follows: when $\rho = 0.5$ is true, the correlation introduces minimal distortions, whereas when $\rho = 0.8$ holds true, the correlation already has a strong impact.

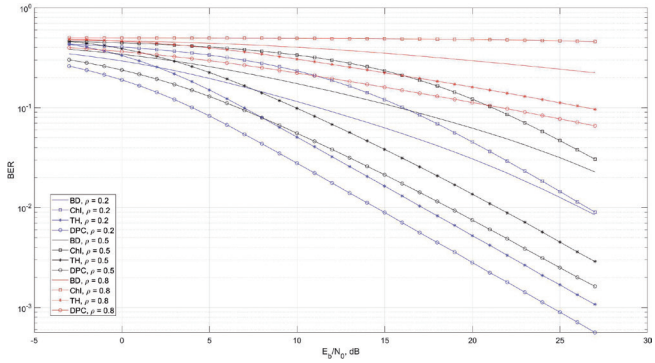

Fig. 5. *Dependences of BER on E_b/N_0 in the Rayleigh channel for various spatial correlation coefficient values*

The last scenario considers hybrid beamforming and takes into account the spatial separation of subscribers. Number of digital streams Ns = 4, the architecture is fully connected. Users are evenly distributed around the base station. The distance between BS and UEs is in the range of 200–4000 wavelengths, which corresponds to a distance of up to 570 meters at 1800 MHz and up to 200 meters at 6 GHz. Such coverage areas are common for small cells where MIMO technology is actively used. **Fig. 6** illustrates the obtained dependences for a different number of RF circuits (NTRF) on the transmitting side, considering both perfect and imperfect estimation of the channel matrix.

Figs 3–6 demonstrate that imperfect estimation, the presence of a line of sight, and the correlation contribute to a significant

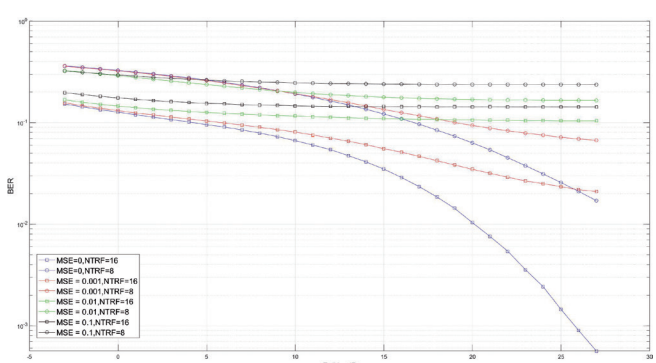

Fig. 6. *Dependences of BER on E_b/N_0 – for hybrid beamforming with varying estimation errors and different number of RF circuits.*

decrease in the noise immunity of MIMO systems.

Fig. 3 illustrates that among digital algorithms, DPC shows the best noise immunity performance, but only with perfect estimation. Even a small estimation error (MSE = 0.001) results in a sharp decrease in noise immunity, with BER > 0.1. The TH algorithm is behind the DPC algorithm in performance by about 2.5 dB (with perfect estimation), but it is less sensitive to estimation errors. Even with a small estimation error, the value of BER < 0.1 can be achieved via only TH or BD algorithms (BER is 0.02 and 0.06, respectively). With MSE = 0.01, none of the precoding algorithms can achieve a bit error probability of 0.1. With perfect estimation, the ChI algorithm is behind BD by about 1 dB in terms of BER = 0.01, but a small estimation error also leads to a significant decrease in noise immunity, with BER > 0.1.

For Figs 4, 5, the performance degradation is considered relative to the uncorrelated Rayleigh channel with perfect estimation. Fig. 4 shows that even a weak line of sight (K = 2) significantly diminishes the system noise immunity. At E_b/N_0 = 27 dB, BER increases by about 3 times for all types of precoding. At K = 10, BER increases by about 10 times for the DPC and TH algorithms, by about 7 times for BD, and by 9 times for ChI (at E_b/N_0 = 27 dB). The explicit line of sight (K = 100) increases BER by about 90 times for DPC and TH, by 21 times for BD, and by 32 times for ChI at E_b/N_0 = 27 dB. Only the DPC and TH algorithms allow achieving BER < 0.1 (0.05 and 0.08, respectively). Thus, DPC is most resistant to the presence of line of sight in the channel.

Fig. 5 shows that a weak spatial correlation has almost no effect on noise immunity. Correlation at level $\rho = 0.5$ leads to an increase in BER by about 3–4 times at E_b/N_0 = 27 dB. At $\rho = 0.8$ and E_b/N_0 = 27 dB, BER increases by 128, 101, 32, and 52 times for DPC, TH, BD and ChI, respectively. At the same time, DPC and TH make it possible to achieve BER < 0.1 (0.06 and 0.09, respectively), whereas when using BD and ChI, BER values are 0.2 and 0.5. Consequently, DPC is most resistant to spatial correlation.

As can be seen from Fig. 6, with perfect estimation and NTRF = 8, the noise immunity is lower than that achieved with the ChI algorithm, and with NTRF = 16, the hybrid beamforming approaches the noise immunity performance of DPC, but it is slightly inferior to it. At NTRF = 16, a small estimation error (MSE = 0.001) leads to a significant decrease in noise immunity, BER increases by about 40 times; while at NTRF = 8, such an error leads to a deterioration in noise immunity by about 4 times (at E_b/N_0 =27 dB). At MSE = 0.01, E_b/N_0 = 27 dB; when NTRF = 16, BER ≈ 0.1; and when NTRF = 8, BER exceeds 0.1. With a larger estimation error (MSE = 0.1), BER exceeds 0.1 even when NTRF = 16.

4. CONCLUSIONS

The article considers the influence of transmission channel parameters on the noise immunity of MIMO systems. The obtained results highlight that MIMO shows robust performance with perfect estimation and a wide variety of channels. However, real conditions often deviate significantly from ideal conditions. The presence of noise, partial or complete absence of multipathing, physical proximity of antenna elements can lead to a significant decrease in the performance of multi-antenna systems. For this reason, the work of MIMO

systems in the light of new technologies, such as machine learning, metamaterials, reconfigurable surfaces, is a significant research issue. For example, reconfigurable surfaces can enhance channel diversity, and machine-learning algorithms can improve the accuracy of channel estimation. Additionally, there is a need for further improvement of the existing beamforming algorithms and the development of new ones, especially in the millimeter and terahertz ranges, to mitigate the consequences of the strong signal attenuation. Research in these areas has the potential to become the basis for enhancements in basic characteristics of forthcoming communication systems. In addition, the integration of MU-MIMO systems with existing multiple-access methods, such as [20, 21], will further improve the communication system performance.

REFERENCES

1. Cho YS, Kim J, Yang WY, & Kang CG. *MIMO-OFDM wireless communications with MATLAB*. Hoboken., NJ, USA,Wiley, 2010: 439.
2. Heath RW, Gonzalez-Prelcic N, Rangan S, Roh W, & Sayeed AM. An overview of signal processing techniques for millimeter wave MIMO systems. *IEEE journal of selected topics in signal processing*, 2016, 10(3):436-453.
3. Spencer QH, Swindlehurst AL, & Haardt M. Zero-forcing methods for downlink spatial multiplexing in multiuser MIMO channels. *IEEE transactions on signal processing,* 2004, 52(2):461-471.
4. Peel CB, Hochwald BM, & Swindlehurst AL. A vector-perturbation technique for near-capacity multiantenna multiuser communication-part I: channel inversion and regularization. *IEEE Transactions on Communications*, 2005, 53(1):195-202.
5. Costa M. Writing on dirty paper (corresp.). *IEEE transactions on information theory,* 1983, 29(3):439-441.
6. Fischer RF, Windpassinger C, Lampe A, & Huber JB. Space-time transmission using Tomlinson-Harashima precoding. *ITG FACHBERICHT,* 2002:139-148.
7. Sadek M, Tarighat A, & Sayed, AH. A leakage-based precoding scheme for downlink multi-user MIMO channels. *IEEE transactions on Wireless Communications,* 2007, 6(5):1711-1721.
8. Gao X, Edfors O, Rusek F, & Tufvesson F. Linear pre-coding performance in measured very-large MIMO channels. *Proc. IEEE vehicular technology conference* (*VTC Fall*), 2011:1-5.
9. Heath RW, Gonzalez-Prelcic N, Rangan S, Roh W, & Sayeed AM. An overview of signal processing techniques for millimeter wave MIMO systems. *IEEE journal of selected topics in signal processing*, 2016, 10(3):436-453.
10. Shahramian S, Yasotharan H, & Carusone AC. Decision feedback equalizer architectures with multiple continuous-time infinite impulse response filters. *IEEE Transactions on Circuits and Systems II: Express Briefs,* 2012, 59(6):326-330.
11. Tomlinson, M. New automatic equaliser employing modulo arithmetic. *Electronics letters,* 1971, 7(5):138-139.
12. Harashima H, & Miyakawa H. Matched-transmission technique for channels with intersymbol interference. I*EEE Transactions on Communications*, 1972, 20(4):774-780.
13. Joham M, Utschick W, & Nossek, JA. Linear transmit processing in MIMO communications systems. *IEEE*

Transactions on signal Processing, 2005, 53(8):2700-2712.

14. Molisch AF, Ratnam VV, Han S, Li Z, Nguyen SLH, Li L, & Haneda K. Hybrid beamforming for massive MIMO: A survey. *IEEE Communications magazine*, 2017, 55(9):134-141.
15. Tyrtyshnikov EE. *Matrichnyi analiz i lineynaya algebra* [Matrix analysis and linear algebra.]. Mocsow, Fizmatlit Publ., 2007, 480 p.
16. El Ayach O, Rajagopal S, Abu-Surra S, Pi Z, & Heath RW. Spatially sparse precoding in millimeter wave MIMO systems. *IEEE transactions on wireless communications*, 2014, 13(3):1499-1513.
17. Tropp JA, & Gilbert AC. Signal recovery from random measurements via orthogonal matching pursuit. *IEEE Transactions on information theory*, 2007, 53(12):4655-4666.
18. Yu X, Shen JC, Zhang J, & Letaief, KB. Alternating minimization algorithms for hybrid precoding in millimeter wave MIMO systems. *IEEE Journal of Selected Topics in Signal Processing,* 2016, 10(3):485-500.
19. Zhang J, Yu X, & Letaief KB. Hybrid beamforming for 5G and beyond millimeter-wave systems: A holistic view. *IEEE Open Journal of the Communications Society*, 2019, 1:77-91.
20. Pokamestov DA, Kryukov YV, Rogozhnikov EV, & Kanatbekuli I., Adapting SCMA Codebooks to Channel State. *Proc. 3rd International Youth Conference on Radio Electronics, Electrical and Power Engineering* (*REEPE*), 2021:1-4.
21. Kryukov YV, Pokamestov DA, Rogozhnikov EV, Demidov AY, & Gromova YS. Experimental research of PD/NOMA. *Proc. 19th International Conference of Young Specialists on Micro/Nanotechnologies and Electron Devices* (*EDM*), 2018:176-179.

DOI: 10.17725/rensit.2023.15.453

Flat Panel Display Controller Driver Architecture for Linux OS

Konstantin V. Pugin, Kirill Mamrosenko, Alexander Giatsintov

Scientific Research Institute of System Analysis of RAS, https://niisi.ru/

Moscow 117218, Russian Federation

E-mail: rilian@niisi.ras.ru, mamrosenko_k@niisi.ras.ru, algts@niisi.ras.ru

Received May 25, 2023, peer-reviewed June 01, 2023, accepted June 08, 2023, published December 06, 2023.

Abstract: **This paper discusses the development of a driver architecture for display transmitter link controller. The architecture ensures the implementation of protocols for interaction with flat panel displays in the case when the controller has its own registers and configuration system. Unlike the known solutions, the proposed architecture makes it possible to reduce the amount of changes in the implementation code in the event of hardware upgrade, and also does not require the use of automatic driver code generation based on high-level descriptions or the development of special tools, such as domain-specific languages. This paper analyses drivers that are based on Direct Rendering Management subsystem and available in open source, as well as previously described approaches to the development of display transmitter link controller drivers. The paper also presents a logical comparator model for testing phase-locked loop devices, which are an integral part of all display output stacks. Based on this model, an IP block was developed, which was used to test the Display Serial Interface driver. Evaluation of the results was carried out in the development of the MIPI Display Serial Interface driver for a promising controller. This driver was tested together with a device prototype and a panel that supports the MIPI Display Serial Interface 1.3 standard. The results provided in this paper can be used both to develop new drivers for existing controllers and new controllers with new drivers.**

Keywords: **driver, architecture, MIPI DSI, embedded systems**

UDC 004.454

Acknowledgments: The work was carried out within the framework of the state task of the Federal State Institution FNTs NIISI RAS "Conducting fundamental scientific research (47 GP)" on topic No. FNEF-2022-0022 "Mathematical support and tools for modeling, designing and developing elements of complex technical systems, software systems and telecommunication networks in various problem-oriented areas".

For citation: Konstantin V. Pugin, Kirill A. Mamrosenko, Alexander M. Giatsintov. Flat Panel Display Controller Driver Architecture for Linux OS. *RENSIT: Radioelectronics. Nanosystems. Information Technologies*, 2023, 15(4):453-462e. DOI: 10.17725/rensit.2023.15.453.

Contents

1. INTRODUCTION

Currently, graphic display units for mobile devices are developing at a high pace. Many new display devices are characterized by resolutions up to 2560x1600 and dynamic refresh rates from 60 to 120 Hz. In this regard, it becomes relevant to use new standards in developing display interface controllers that can stream video at high speed. To solve this problem, there are several existing protocols that require using separate devices, so called display transmitter link controllers (here and afterwards referred to as DTLC), which complement the display controller by converting the output in the form required by the display. Many protocols that transmit video at high speed (1 Gbit/s and higher) require both to interact dynamically and agree on acceptable transmission parameters. Controllers for such protocols require complex program control that is specific for every type of device. Protocols for flat panel displays that transfer smaller amounts of data often do not require such complex control and feedback. If these protocols are used, flat panel display configuration does not change when display is up and running, and dynamic configuration is not supported. Like [1], let's call complex DTLC a DTLC that require program control with feedback. As the number of mobile devices with displays that require new ways of interacting and new controllers increases, it is necessary to have approaches at hand to develop drivers for such (complex) devices [2]. If the DTLC driver for interacting with flat panel displays is developed in parallel with the device, then several problems are encountered, some of which are identical to those described in [1], and some are unique, related to the essence of these protocols:

1. There is a need to compute compatible frequencies for the FPGA and select flat panels that will be used during the design of a controller.
2. Possible incompatibility of allowed frequencies of panels and controllers, to bypass which additional hardware and software is required.
3. The need to test several frequencies and panel operation modes with no possibility to replace device hardware.
4. The need to bypass OS interfaces if they are not compatible with the protocol version that is implemented in hardware.

To address these problems, different hardware and software-based approaches are used: use of verifiers [3], creation of the Domain Specific Languages (DSLs) [4], automatic generation of driver code based on the common pattern [5], and development of drivers that define the unchangeable main features of a series of devices until the end of its production, while other features are parametristic and dynamically fetched from configuration file entries. This paper is an attempt to answer what approaches to the development of the DTLC driver for interacting with flat

panel displays should be applied, given the proposed conditions. The contribution of the study is as follows:

- This paper improves the DTLC driver architecture created earlier by ([1]) for cases where DTLC is used to interact with the flat panel display.
- To test the correctness of programming an interface of phase-locked loop driver (afterwards referred to as PLL), at the early stages of the development of the IP block, the logical comparator model was created and implemented on FPGA, which is used in conjunction with built-in PLLs. This model made it possible to test the correctness of programming of phase-locked loop devices for DTLC in FPGA states similar to the real device application case.

The developed architecture ensures the implementation of protocols for interaction with flat panel displays in the case when the controller has its own registers and configuration system. Unlike the known solutions, the proposed architecture makes it possible to reduce the amount of changes in the implementation code in the event of hardware upgrade, and also does not require the use of automatic driver code generation based on high-level descriptions or the development of special tools, such as domain-specific languages.

Section 3.1 describes approaches to developing drivers for Linux OS, on the basis of which the study was carried out. Section 3.3 describes the architecture of the DTLC driver for flat panel displays, which contains two loosely bound components – a hard-ware binding component and an OS interaction component, which are linked by an internal API. The hardware binding component performs most of the necessary conversions of incoming data into those formats that are required for programming of a particular device, programs its registers and ensures feedback. The OS interaction component converts requests from other parts of the system and transmits them with an internal API, which is a system of functions and structures common to all hardware binding modules. Section 4 describes how to use the above mentioned architecture when developing a driver for the MIPI Display Serial Interface (MIPI DSI), which is one of the DTLC protocols for interacting with flat panel displays. Section 5 describes the logical model of the comparator for testing the driver using FPGA PLL generator. This model allows testing the correctness of programming the real hardware PLL drivers when it is necessary by using emulation of real hardware PLL interface in FPGA instruments.

2. RELATED WORK

Some recent papers [6] offer to create systems with several DTLCs for interacting with the flat panel display that have a common physical interface layer (afterwards referred to as PHY), which can be used by only one DTLC at a time. One may try to get round this limitation using the DTLC driver architecture described in [7]. In this architecture frequency synthsizer in the shared device, but in the architecture, described in [6], PHY will be the shared device in this architecture and not the frequency synthesiser. Or it is possible to preserve the limitation on simultaneous operations but separate out the frequency synthesiser (FS) together

with PHY into an independent module with a common part of the driver. Since PHY described in [6] is used in DTLC to interact with the flat panel display, the driver architecture described in this paper can also be used for controllers with such a PHY (taking into account the paper by [7]).

The article [8] describes approaches to designing DTLC drivers for real-time operating systems. The description of the RTOS subsystem provided in this article allows applying the models for driver development like those used for DRM in Linux with minimal modification in terms of component names replacement. This allows developing DRM-compatible models for DTLC drivers to interact with the flat panel display not only for Linux but also for other OS, which is also reported in [9]. This paper cites that DRM is also used for writing graphics drivers for FreeBSD OS. So it is possible to use the models developed for DRM to write DTLC drivers in these OS.

3. RESEARCH APPROACHES

3.1 Approaches to the development of graphics controller drivers on the example of Linux OS

Several approaches to the use of certain popular graphics subsystem tools used in the development of DTLC drivers for Linux are known. The most popular of them are the following:

1. DRM. As mentioned in [10], the DTLC interface is part of the Direct Rendering Management (DRM) framework. If to consider the DRM subsystem as a software model of the real output device, then all flat panel displays and interfaces for their interaction with DTLC match the panel type because they determine how graphics output works with fixed frequencies. However, the panel type implementation requires that each type of panel has its own driver, even if the controllers match. Therefore, most often DTLC drivers for fixed panels are implemented as a bridge + panel bundle, or, less often as encoder + panel bundle. The second option, in contrast to the first one, does not correlate with the external model, although it is practically possible [11].
2. User Mode Setting (UMS) or the implementation of setting modes and interacting with hardware inside the X server. Problems with the implementation and the use of UMS were reported in 2006 [12], whereafter no drivers for DTLC were developed using this approach.
3. FrameBuffer device (fbdev). This kernel interface preceded the KMS DRM module and was most common until 2008-2009, when the first version of KMS was adopted. The fbdev interface did not provide for the implementation of mode configuration in the kernel, and, therefore, required the implementation of UMS, which led to the above problems. No drivers, specifically for DTLC devices, were developed using this approach after the appearance of KMS.
4. There are driver implementations for the Android Display Framework (ADF). However, they are standard, hardware-independent, protocol functions must be developed from scratch in each driver, which increases the likelihood

of errors and increases the complexity of the task. Also, due to the use of the ADF architecture (the development of fbdev), it becomes necessary to combine DTLC drivers and display controller drivers. Implementations of controller drivers in a number of other Unix-compatible systems (for example, FreeBSD) are also created with DRM ([9]), as the most advanced open system for implementing complex output tools.

3.2 Methods used to study DTLC drivers

When preparing the paper, the authors analysed the existing open DTLC drivers for Linux OS. The special emphasis was placed on drivers for mobile platforms. Based on this analysis, the novel Display Serial Interface (DSI) driver architecture was developed. It allows quickly creating the driver for a device prototype and, after hardware release, port this driver to a serial device. Through previous analysis and case study, and using materials from [1], the proposed architecture has been further extended to all complex DTLC drivers to interact with flat panel displays.

3.3 Differences in the DTLC driver architecture for interacting with the flat panel display

For DTLC with a dynamic panel, the architecture offered by [1], **Fig. 1**, is currently the most applicable one. To adapt this architecture for use in flat panel display systems, the drm_panel structure must be used, which will only work with DRM model interfaces, and the panel driver must be fully compatible with the DRM model. The improved architecture is shown in **Fig. 2**. In this version, the drive rarchitecture also retains all the advantages

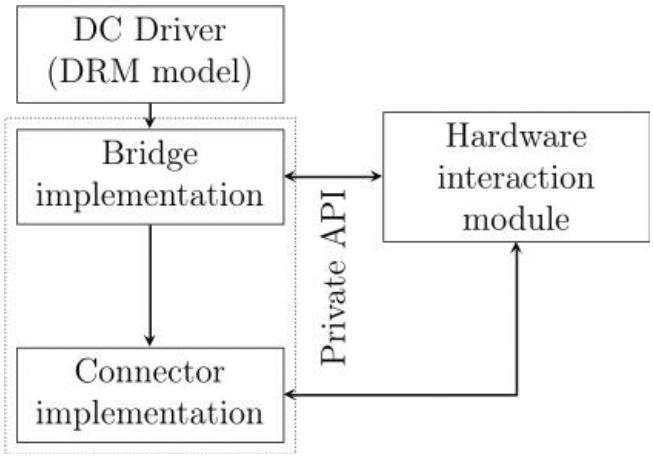

Fig. 1. *DTLC driver architecture for implementation within the DRM subsystem.*

described in [1], while being able to work with flat panel displays in cases where the feedback implementation in the panel complies with the relevant protocol clauses. However, this architecture needs to be improved in cases where non-standard extensions are required to interact with the panel interface.

4. ANALYSIS OF THE MIPI DISPLAY SERIAL INTERFACE PROTOCOL

Along with eDP (embedded DisplayPort, the development of drivers for which was described in [1]), MIPI DSI, used by leading Android mobile device manufacturers, is one of the most used protocols for transmitting data

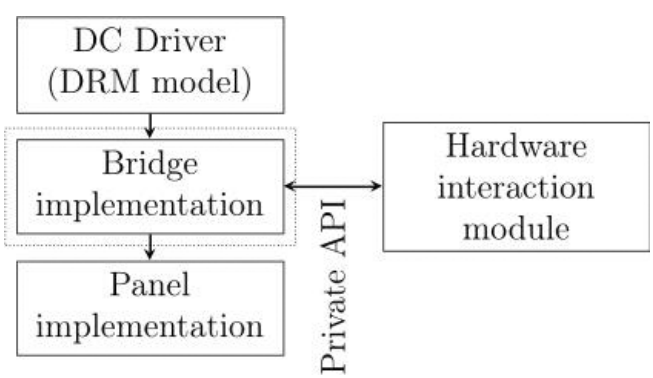

Fig. 2. *DTLC driver architecture for interacting with flat panel displays for implementation within the DRM subsystem.*

to displays. The important part of this protocol is a feedback protocol that is implemented through the Display Command Set (DCS), which defines the format of commands and responses of interaction participants, as well as a list of standard commands that must be supported by all compatible devices. To implement the MIPI DSI protocol, DRM uses drm_encoder (to implement the controller driver), drm_panel (to implement the panel driver), and drm_connector or drm_bridge (to implement panel interaction with the controller) [11].

There is a program model in the Linux kernel for DRM-based MIPI DSI drivers that complements the general DRM model as follows: MIPI DSI, like similar eDP standard implements not only the basic image output, but also additional functions (for example, the transfer of various data via the DCS protocol). To implement these functions from the MIPI DSI controller side, the DRM has a MIPI DSI Host object (mipi_dsi_host), and to implement these functions from the panel side, there is the MIPI DSI Device object (mipi_dsi_device), as well as several auxiliary functions only for MIPI DSI controllers and panels. MIPI DSI DRM model is shown on **Fig. 3**.

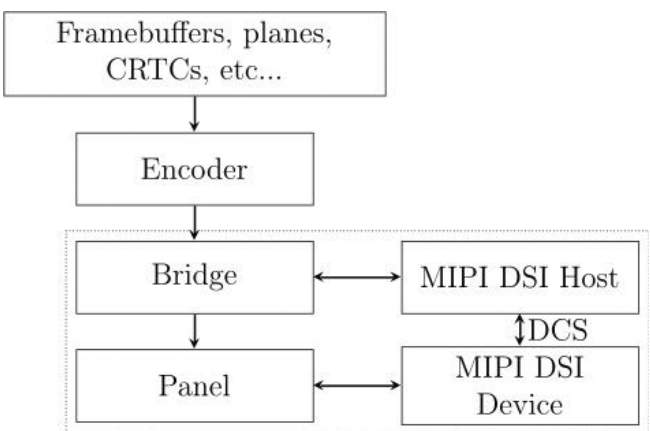

Fig. 3. *MIPI DSI program model within the common DRM model.*

4.1 Peculiarities of working with MIPI DSI displays

The vast majority of PHY for MIPI DSI (afterwards referred to as D-PHY) [13] either use burst mode or require certain constants for the MIPI DSI protocol to be taken into account. This leads to the fact that, unlike other DTLC, in MIPI DSI it is necessary to recalculate the time and frequency characteristics for all the modes. Also, unlike the DisplayPort protocol, the data transfer frequency in DSI is not constant but is derived from the pixel frequency using the formula

$$clk_{hs} = clk_{pix} \cdot BPP \cdot lanes,$$

where lanes is the number of active transmission lines (from 1 to 4), BPP is the number of bits per pixel, and clkpix is pixel clock. It is the bit frequency that must be transmitted to the PLL of the DSI controller [14]. The DSI protocol uses the Display Monitor Timings (DMT, see [15]) definition of screen resolution. However, unlike other protocols, DSI needs to recalculate all the characteristics of horizontal lines in order for the invisible part of the screen to fit the packet headers. Let us denote the horizontal characteristics as: HBP – Front Porch, HFP – Back Porch, HSA – Hsync Active, HACT – H Active, PULSE_CLK – pulse synchronisation value, – число битов в пикселе. number of bits in a pixel. For each characteristic (denoted as X) let's XDPI be input characteristic of X, XDSI be recalculated characteristic of X. Protocol constants, such as HDR = 6 (packet header, one per each timing, must

be in the invisible area), HSS = 4 horizontal synchronisation start header), HSE = 4 (horizontal synchronisation end header), are also important for recalculation. The following formulas are used to recalculate timings:

$$HBP_{DSI} = (HBP_{DPI} \cdot BPP/8) - HDR_{HBP}$$
$$HFP_{DSI} = (HFP_{DPI} \cdot BPP/8) - HDR_{HACT} - HDR_{HFP}$$
$$HSA_{DSI} = (HSA_{DPI} \cdot BPP/8) - HSS - HDR_{HSA} - HSE$$
$$HACT_{DSI} = HACT_{DPI} \cdot BPP/8$$
$$PULSE\_CLK = ((HACT_{DPI} + HSA_{DPI} + HBP_{DPI} + HFP_{DSI}) \cdot BPP/8) - HSA_{DSI} - 20.$$

Calculations in accordance with the above formulas must always deliver integers. If the figure turns out to be non-integer, then the driver must choose an alternative. Since there is no resources for this in the common DRM stack, this should be redirected to the controller driver. Different controller models may have different additional restrictions, such as the inability to select certain bit rates or the need to select specific vertical timings. To be able to determine additional restrictions on controller values, a module originally proposed in [1] for hardware interaction is used. However, an improvement is required for use with the fixed panel (2). It is also possible to reduce Vertical Front Porch (VFP, see [15]) to reduce power consumption with high-speed operation, which is performed depending on the model of the controller and panel. Therefore, work on reducing VFP is done in the hardware module interactions. To test the correctness of programming the transmission frequency generator, a testing comparator (5) was used, which made it possible to avoid PLL programming errors when testing the DTLC driver for the MIPI DSI controller.

5. COMPARATOR-BASED LOGIC MODEL FOR TESTING PLL DRIVERS

For most DTLC, the driver needs to correctly program PLL frequencies directly related to the image output. On some controllers, the PLL data programming interface can be built directly into the controller's program interface and performed in the same way as all other setup operations. Despite the development of phase-locked loop devices with reduced size [16], FPGA and emulators often lack the ability to dynamically tune PLL, which makes it very difficult to test DTLC controllers with changing the connected monitor without powering off the controller, for example, DisplayPort or HDMI. Each frequency value required project rewiring for FPGA. For DTLC with fixed panels, this problem is less relevant, since panels support a small frequency range and, thereore, a small number of supported display modes. Such systems have another problem with FPGA drivers. Often, the programmable value of the PLL drivers is not taken into account by FPGA, which allows FPGA-based controller prototypes to display an image with incorrectly programmed PLL. In this case, the fact of incorrect programming would manifest on production devices. To solve this problem, it was proposed to develop a testing block for FPGA-based implementation, the logical model of which consists of the following elements (**Fig. 4**):

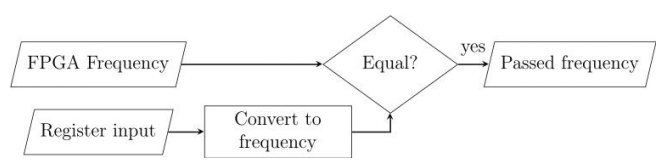

Fig. 4 . *Comparator-based PLL mock-up model.*

- Input that receives the frequency specified during FPGA wiring.
- Calculation block that converts the input to a frequency value (rounded to the nearest whole number). The exact structure of the calculation block is determined by the PLL programming interface or the part of the controller programming interface that programs PLL.
- Comparator that compares the calculation block output with the frequency specified during FPGA wiring. If the comparison result is positive, the comparator sends the enabling signal to the frequency skip switch. The allowed deviation of the estimated frequency from the incoming one depends on the device under development (it often does not exceed 1 kHz for DTLC).
- Frequency skip switch, which is turned on by the enabling signal from the comparator.

This model was implemented as an IP block on FPGA. The use of this model to test DTLC drivers for interaction with the flat panel display made it possible to achieve correct PLL programming for the DTLC controller even before the first prototype was made. The correctness of programming has been confirmed already at the testing stage with the use of emulators and FPGA.

6. CONCLUSION

The approaches proposed in this paper make it possible to reduce the amount of changes in the implementation code in case of hardware upgrade. Also, these approaches make it possible to reduce the number of driver modifications to support device families (including for one device with differences in various blocks, for example, different PLL). The PLL model described above, when implemented, will allow testing drivers at the early stages of PLL development, as well as device drivers that use PLL.

Further developments may deal with determining the applicability of the resulting architecture to the development of DTLC drivers for embedded systems with external buses (for example, using DTLC on PCI Express), researching specific DTLC protocols (over HDMI), and also determining the possibilities of using the comparator to test PLL drivers, used in other SoC parts.

REFERENCES

1. Pugin KV, Mamrosenko KA, Reshetnikov VN. Display Transmitter Link Controller Design Technology for Linux OS. *Software Journal:Theory and Applications*, 2019, 4:10-17, doi: 10.15827/2311-6749.33.406.
2. Jonathan Corbet, Alessandro Rubini, Greg Kroah-Hartman. *Linux Device Drivers*. O'Reilly Media, Inc., 2005. ISBN: 0-596-00590-3.
3. Dileep KP, Raghavendra A, Suman M, Devesh G, Srikanth SV. Rules Based Automatic Linux Device Driver Verifier and Code Assistance. *Proc. IEEE International Conference on Recent Advances and Innovations in Engineering*. Jaipur, India: IEEE, 2014. ISBN: 978-1-4799-4040-0.
4. Lisboa EB, Silva L, Lima T, Chaves I, Barros E. An Approach to Concurrent Development of Device Drivers

and Device Controller. *Proc. 11th International Conference on Advanced Communication Technology, pp.* 571-575. Phoenix Park: IEEE, 2009. ISBN: 978-89-5519-139-4.

5. Jung Choon Park, Yong Hoon Choi, Tae Ho Kim. Domain Specific Code Generation For Linux Device Driver. *Proc. 10th International Conference Advanced Communication Technology, pp.* 101-104. Gangwon-Do, Korea (South): IEEE, Feb, 2008. ISBN: 978-89-5519-136-3. DOI: 10.1109/ICACT.2008.4493721.12.
6. Sunil Kumar CR, Aruna Kumar, Sanjib Basu. Novel Circuit Architecture for Configurable eDP and MIPI DPHY IO. *Proc. 2022 35th International Conference on VLSI Design and 2022 21st International Conference on Embedded Systems* (*VLSID*), pp. 98-101. Bangalore, India: IEEE, 2022. DOI: 10.1109/VLSID2022.2022.00030.
7. Konstantin V. Pugin, Kirill A. Mamrosenko, Alexander M. Giatsintov. Software Architecture for Display Controller and Operating System Interaction. *RENSIT: Radioelektronika. Nanosistemy. Informacionnye Tehnologii*, 2021, 13(1):87-94. DOI: 10.17725/rensit.2021.13.087.
8. Bazhenov PS, Giatsintov AM, Mamrosenko KA. Approaches to providing data visualization on devices using modern real time operating systems. *Software & Systems,* 2021, 3:433-439. DOI: 10.15827/0236-235X.135.433-439.
9. Emmanuel Vadot. Adventure in DRMland Or How to Write a FreeBSD ARM64 DRM Driver. *Proceedings AsiaBSDCon*, 2019, pp. 9-13, (AsiaBSDCon. Tokyo, Japan: BSD Research, 2019). DOI: 10.25263/asiabsdcon2019/p01a.
10. Konstantin V. Pugin, Kirill A. Mamrosenko, Alexander M. Giatsintov. Visualization of Graphic Information in General-Purpose Operating Systems. *RENSIT: Radioelektronika. Nanosistemy. Informacionnye Tehnologii*, 2019, 11(2):217-224e. DOI: 10.17725/rensit.2019.11.217.
11. Linux GPU Driver Developer's Guide. 2019. URL: https://dri.freedesktop.org/docs/drm/gpu/index.html (Access mode: 06.03.2019).
12. Verhaegen Luc. X and Modesetting: Atrophy Illustrated. 2006. URL: https://people.freedesktop.org/~libv/X_and_Modesetting_–_Atrophy_illustrated_(paper).pdf.
13. Kiyong Kwon, Dongwon Kang, Geon-Woo Ko, Seok-Young Kim, Seon-WookKim. Low-Cost Unified Pixel Converter from the MIPI DSI Packets intoArbitrary Pixel Sizes. *Electronics,* 2022, 11(8):1221. DOI:10.3390/electronics11081221.
14. Yeming Liu, Chengyue He. A Design of MIPI DSI Interface for LCD Display Driver. *Journal of Physics: Conference Series,* 2022, 2221(1):012015. DOI: 10.1088/1742-6596/2221/1/012015.
15. VESA and Industry Standards and Guidelines for Computer Display Monitor Timing (DMT), Version 1.0, Rev. 13. 39899 *Video Electronics Standards Association,* 2013, 105 p.

16. Hye-Hyun Lee, Yeon-Seob Song, Kang-Yoon Lee. Modeling of Nano-Scale PLL Using Verilog HDL. *Proc. 13th International Conference on Information and Communication Technology Convergence* (ICTC). IEEE, 2022, pp. 2101-2104. DOI: 10.1109/ICTC55196.2022.9952654.

DOI: 10.17725/rensit.2023.15.463

Vladimir I. Vernadsky and the new paradigm

Gennady V. Mishinsky
Joint Institute for Nuclear Research, http://www.jinr.ru/
Dubna 141980, Moscow Region, Russian Federation
E-mail: mysh@jinr.ru

Received October 09, 2023, peer-reviewed October 16, 2023, accepted October 23, 2023, published December 06, 2023.

Abstract: **The main directions of V.I. Vernadsky's scientific activity during the period of the scientific revolution occurred at the end of the 19th and until the middle of the20th centuries are briefly listed. His decisive contribution to the initial research and practical application of the phenomenon of radioactivity and nuclear physics is shown. Based on the discovery of low-energy nuclear reactions more than 30 years ago, the development of Vernadsky's ideas about the role of radioactivity − the transformation of some chemical elements into other chemical elements − in geology, in the thermal balance of the Earth, in the prevalence of trace chemical elements is presented. Main provisions of the theory of low-energy nuclear reactions in condensed matter are listed: the threshold for excitation of the medium is indicated; shown is the possibility of generating a strong magnetic field in a unidirectional flow of electrons in a quasineutral plasma with the pairing of free electrons, and, subsequently, the pairing of atomic electrons into orthobosons with the latter forming a Bose-Einstein condensate, in which a new state of matter is formed − transatoms, which are combined, due to their ultra-strong magnetic fields, into nuclear transmolecule, in which multinuclear transmutation reactions occur with non-radioactive products; with the transformation of transmolecules into different sets of stable nuclei, subject to all conservation laws. In this case, the collective parameter that characterizes the quasi-equilibrium distribution of the mass numbers of isotopes – reaction products – is the "thermodynamic" coefficient of the energy content of the medium. Natural nucleosynthesis in the era of recombination of the Universe, which gave rise to the formation and development of organic chemical, and subsequently biochemical synthesis, is described. The development of Vernadsky's doctrine of the biosphere and noosphere of the Earth is supplemented by the concept of fractality of material, including biological structures with the further evolution of living matter, as well as by the concept of planetary nucleosynthesis. Starting from the idea of planetary nucleosynthesis, based on the mechanism of multinuclear quantum transitions of some atomic nuclei to others, a new doctrine of the geological development of the Earth and the foundations of quantum planetology were formulated, which explained the strict temporal cyclicity observed in the geological activity of the Earth associated with galactic jet energy flows. The issues discussed may become a basis for those directions in scientific research that will form a new paradigm, a new worldview.**

Keywords: **Vladimir I. Vernadsky, paradigm, low-energy nuclear reactions, nucleosynthesis, fractals, living matter, biosphere, noosphere, philosophy of science**

PACS: 01.70.+w; 03.75.Mn; 25.60.Pj; 25.70.Hi; 52.25.Xz; 91.35.Nm; 96.12.je; 98.70.Sa

For citation: Gennady V. Mishinsky. Vladimir I. Vernadsky and the new paradigm. *RENSIT: Radioelectronics. Nanosystems. Information Technologies,* 2023, 15(4):463-482e. DOI: 10.17725/rensit.2023.15.463.

Contents

1. INTRODUCTION

1.1. V.I. Vernadsky and his activities

On February 28, 2023 have passed 160 years since the birth of the outstanding Russian and Soviet scientist, academician Vladimir Ivanovich Vernadsky (1863-1945) [1]. That date not only reminded us of the role of V.I. Vernadsky in the development of science in the first half of the last century, but also stimulated us to turn again to his scientific heritage, including rereading his, according to Vernadsky himself, "main" book – "Chemical structure of the Earth's biosphere and of its environment" [2].

The range of Vernadsky's scientific interests was incredibly wide. His legacy contains works on geology, mineralogy, crystallography, and analytical chemistry. He studied soil science, biology, radiology, paleontology, and meteorology. His work made a huge contribution to the development of geochemistry. Vernadsky founded a new science – biogeochemistry. Vernadsky knew the history and philosophy of science well. He laid the foundations for the study of the noosphere known as a new period in the development of the biosphere.

V.I. Vernadsky was one of the first who appreciated the discovery of the phenomenon of radioactivity in 1896, who understood the power hidden in the atomic nucleus [3]. Having studied the works of A. Becquerel, W.C. Roentgen, M. Sklodovskaya-Curie, E. Rutherford and F. Soddy, Vernadsky came to the conclusion that the study of radioactivity and "uranium issues" could open new horizons in the development of mankind. Back in the fall of 1908, three years before Rutherford's discovery of the atomic nucleus, he gave a report on radioactivity research at the Department of Physical and Mathematical Sciences of the Academy of Sciences. The following year, he organized a radium expedition to Fergana, and subsequently compiled a review of deposits of radioactive minerals. 1911, V.I. Vernadsky organized in Saint-Petersburg the Mineralogical Laboratory, in which a radiological research department was created in 1914. On the basis of this department in 1915, the Radiological Laboratory was formed, which became the first scientific center in Russia for the study of radioactivity, and later, of the atomic nucleus.

1922, the Radiological Laboratory was transformed into the State Radium Institute, V.I. Vernadsky was appointed the first director of the Institute. The State Radium Institute consisted, at that time, of three departments: chemical department (in the future – department of radiochemistry), which was headed by V.G. Khlopin; physical department (nuclear physics), led by L.V. Mysovsky, and the mineralogical and geochemical department (radiology), which was headed by V.I. Vernadsky. Such outstanding scientists as academicians A.I. Alikhanov, A.P. Vinogradov, P.I. Kapitsa, I.V. Kurchatov, B.P. Nikolsky, A.E. Fersman, V.G. Khlopin, D.I. Shcherbakov; corresponding members of the Academy of Sciences V.V. Belousov, K.A. Nenadkevich, L.N. Bogoyavlensky, I.E. Starik; professors E.K. Gerling, L.V. Komlev and many other prominent specialists in the field of research and practical application of the phenomenon of radioactivity and nuclear physics worked at the Institute.

V.I. Vernadsky wrote in the same 1922: "... we are approaching a great revolution in the life of mankind that cannot be compared with anything it has previously experienced. The time is not far away when a man gets his hands on atomic energy, a source of power that gives him a capability to build his life as he wants. Will a man be able to use this power, direct it to good, and not to self-destruction?" [4]. This prophecy was made by V.I. Vernadsky 16 years before the discovery, in 1938, of uranium fission by thermal neutrons by German scientists O. Hahn and F. Strassmann.

It clearly follows from all of the above that V.I. Vernadsky can fully be considered the founder of nuclear research in Russia and in the Soviet Union.

Vernadsky was confident that the phenomenon of radioactivity, as the transformation of some chemical elements into other chemical elements accompanied by the release of enormous energy, would help to solve problems related to nuclear energy, geochronology, the thermal balance of the Earth, the state of trace chemical elements and related features of their migration and concentration in the earth's crust.

1.2. Modern development of V.I. Vernadsky's heritage

Our attention to the works of V.I. Vernadsky is associated, first of all, with the discovery of low-energy nuclear reactions (LENR) in 1989-1992 [5-8]. This discovery made it possible to formulate a new, Natural mechanism for the synthesis of chemical elements in the Universe [9] and, thereby, to try to answer many questions formulated by V.I. Vernadsky in the course of his investigation of the Earth's biosphere and its environment.

By Natural nucleosynthesis in the Universe we mean the transformation of some stable chemical elements into other stable chemical elements in low-energy nuclear reactions (LENR). Natural nucleosynthesis is an alternative mechanism to the synthesis of chemical elements, both in stars, as a result of thermonuclear reactions that require temperatures of hundreds of millions degrees, and to the synthesis of elements through the sequential capture of neutrons by atomic nuclei in the *s*- and *r*-processes with further beta decay of the nuclei. Nucleosynthesis in *r*-processes occurs at the stage of star death: at explosions of supernovae and neutron stars.

Low-energy nuclear reactions are divided into two types: cold nuclear fusion (CF) reactions and low-energy transmutation reactions of chemical elements (LET or transmutation).

Cold fusion reactions include reactions that involve hydrogen or deuterium, namely: protons or deuterons, and nuclei of the main element, for example: palladium, nickel, titanium. These reactions can occur spontaneously, without external influence. In solids, they occur preferentially in samples that have a size of the order of several nanometers. This sample size makes it possible to create a concentration of 2-3 hydrogen or deuterium atoms per one atom of the main element. CF reactions can also occur in solutions and melts. For the first time, the implementation of cold nuclear fusion reactions at room temperature was announced by M. Fleischmann and S. Pons in 1989 [10]. They realized the cold nuclear fusion reaction by electrolysis of a solution of deuterated lithium hydroxide in heavy water with a palladium cathode (0.1M LiOD in a solution of 99.5% D_2O + 0.5% H_2O).

Transmutation reactions occur for all chemical elements, starting with hydrogen, and occur, as a rule, with a simultaneous participation of a large number of atomic nuclei. LET reactions include both nuclear fusion and decay [18]. They occur in weakly excited condensed matter with an excitation energy in the reaction range of ~ 1 eV/atom. In ordinary nuclear reactions, in order to bring atomic nuclei closer to the distance of action of nuclear forces, it is necessary to overcome the Coulomb barrier that exists between them, which has values from tens of keV to hundreds of MeV. Transmutation reactions occur only as a result of external influences. Transmutation reactions predominantly occur in melts, solutions and dense gases, i.e. on free atoms and molecules. It is noteworthy that the products of transmutation reactions – isotopes of chemical elements – are non-radioactive.

Transmutation reactions were discovered in 1992 by A.B. Karabut, Y.R. Kucherov and I.B. Savvatimova in experiments on stimulation of cold nuclear fusion reactions in the method with a glowing gas discharge in deuterium with a palladium cathode [11]. Subsequently, transmutation reactions were discovered and reproduced many times in other numerous and varied experiments. For example, in a glowing gas

discharge [11-13]; at industrial, electronic, zone melting of zirconium ingots in a vacuum furnace [14]; at explosions of metal targets irradiated with a powerful electron pulse [15,16]; at explosions in liquid dielectric media of metal foils through which a powerful pulse of electric current was passed [17,18]; when exposed to a pulsed current on a lead-copper melt [19]; at the passage of electric current in water-mineral media [20]; at ultrasonic treatment of aqueous salt solutions [7]; when irradiated with braking gamma rays of condensed gases [21-23]; in growing biological structures [24-26] and in many others [1-3]. From the above list of transmutation experiments it is clear that their methods are extremely diverse and fundamentally different from the methods of nuclear physics.

Low-energy nuclear reactions occur due to exchange and resonance interference exchange interactions [27].

The discovery of low-energy nuclear reactions in 1989-1992 marked the beginning of a paradigm shift in science or a new scientific revolution [28-30].

The scientific revolution that currently takes place allows us to take a fresh look at the teachings of V.I. Vernadsky about the Earth's biosphere, to confirm and develop his hypotheses and foreknowledge.

2. "THERMODYNAMIC" QUASI-EQUILIBRIUM DISTRIBUTION

One of the main properties of matter, the way of its existence, is continuous movement. The movement can be chaotic or directed. For the most part, we see directional movement of particles of matter everywhere.

The unidirectional, collective movement of free electrons in a quasi-neutral plasma creates a magnetic field $\mathbf{B}_\mu$ (**Fig. 1***b*). This magnetic field owes its origin to the magnetic moments of electrons $\boldsymbol{\mu}_e$, which, in a unidirectional flow, due to the helicity property of electrons $\mathbf{p}_e\uparrow\uparrow\boldsymbol{\mu}_e(\mathbf{s}_e\downarrow\uparrow\mathbf{p}_e)$, are parallel to each other,

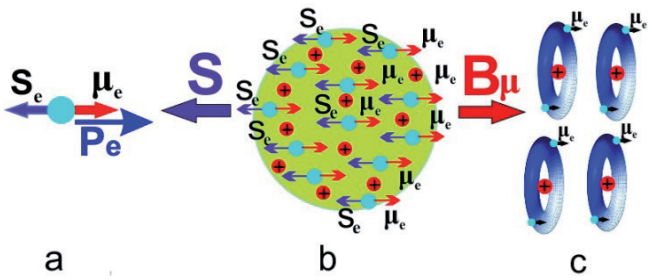

Fig. 1. *a – electron helicity, b – exchange* **S** *and magnetic* $\mathbf{B}_\mu$ *fields, c – orthobosons.*

where $\mathbf{p}_e$ is the momentum of the electron (Fig. 1*a,b*). At electron density $\rho > 10^{21}$ см$^{-3}$ (distance between electrons $< 10^{-7}$cm), the magnetic field $\mathbf{B}_\mu$ generates a Coulomb exchange field **S**, which is associated with the parallelism of electron spins $\mathbf{s}_e$ (Fig. 1*b*). In the Coulomb exchange field **S** in a quasi-neutral plasma, electrons are attracted to each other, which leads to the pairing of free electrons into orthobosons (Fig. 1*c*) [31].The Coulomb repulsion between electrons disappears in a quasi-neutral plasma with $\rho > 10^{21}$ cm^{-3}, due to the small Debye radius $r_D = 69(T/\rho)^{1/2} \sim 10^{-8}$ cm. The electron spins ($\mathbf{s}_e = 1\hbar/2$) are parallel in an orthoboson pair, and their total spin is equal to unity, $\mathbf{S}_{2e} = 1\hbar$. The pairing of electrons into an orthoboson is due to the appearance of a new quantum number in an electron in a strong magnetic field, generated by the oscillations of the electron around its orbital, and which did not manifest itself in any way in the absence of a magnetic field. The magnetic moments of the electrons $\boldsymbol{\mu}_e$ in the orthoboson are also parallel, and they create a strong magnetic field $\mathbf{B}_{2e}$ >30 *T* (**Fig. 2***a*).

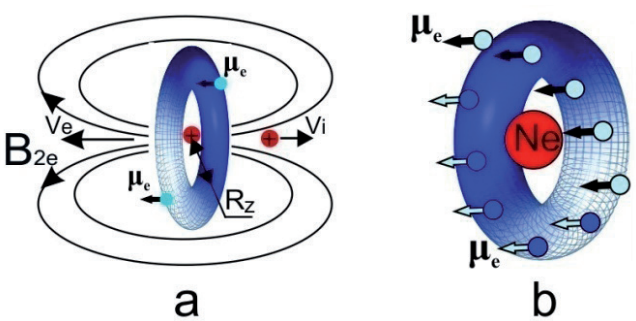

Fig. 2. *a – orthoboson, b – Neon transatom.*

Atoms turn into transatoms in magnetic fields >30 *T*. In a transatom, its orbital electrons are also pairwise bound into orthobosons [32]. Atomic electron orthobosones merge into a Bose-Einstein condensate, in which all electron spins and, accordingly, their magnetic moments are parallel to each other (Fig. 2*b*). The magnetic moments of electrons generate ultra-strong magnetic fields up to $\mathbf{B}_S \sim 10^5$-10^{10} T inside and around transatoms [33].

This mechanism explains the existence of strong and superstrong magnetic fields in cosmic plasma.

The internal ultra-strong magnetic field interacts with the magnetic spin and magnetic orbital moments of the nucleons in the nucleus, changes the structure of the nucleus and turns it into a transnucleus. Nucleons in the transnucleus: pairs of protons and neutrons (fermions with spin equal to s = 1ħ/2), also form orthobosons with $S_{2p,2n}$ = 1ħ, but they are already nuclear orthobosons. The transnucleus with surrounding electron orthoboson Bose-Einstein condensate forms a new state of matter – a spin nuclide electron condensate [33,34].

External ultra-strong magnetic fields of transatoms connect their electron Bose condensates into one, common electron condensate. And their nuclei form a nuclear transmolecule, in which multinuclear transmutation reactions occur [27,35] (**Fig. 3,4**). Transmutation reactions can occur with the participation of electron orthobosons. Thus, strong and weak interactions occur simultaneously in transmutation reactions. Therefore, the products of nuclear transmutation reactions are non-radioactive. These reactions release nuclear energy. The reaction products scatter in different directions. And if the atoms of the reaction products are not in a strong magnetic field, then they become ordinary atoms with ordinary nuclei. As a result of transmutation reactions, the nuclear transmolecule is transformed with the appropriate probability into different sets of stable nuclei, subject to conservation laws: energy, electric, baryon and lepton charges conservation, etc. **Fig. 4** shows a diagram of eight of the twenty-two possible transitions of an aluminum transmolecule, that consists of transatoms of helium, boron and carbon, into two or three stable nuclei. Multinuclear reactions can be considered as a simultaneous, multinucleon exchange between transnuclei that make up a transmolecule [36].

The energy is released during transmutation due to the positive difference between the sums of the masses of the initial and newly formed nuclei, taking into account the binding energy of their electron shells. This difference arises due to different binding energies of nucleons in nuclei (nuclei mass defect) (**Fig. 5**). Transmutation reactions that continuously occur in a condensed matter lead to a quasi-equilibrium distribution of isotopes – reaction products – by mass numbers.

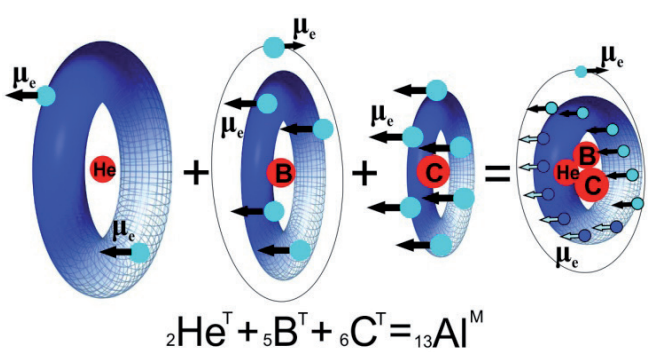

Fig. 3. *Formation of aluminum transmolecules from helium, boron and carbon transatoms.*

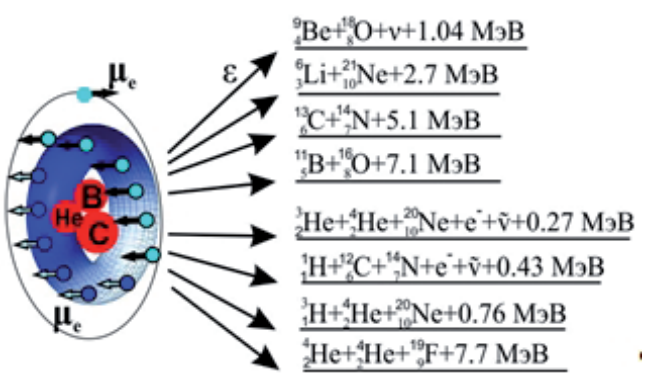

Fig. 4. *Scheme of transitions of an aluminum transmolecule into two or three stable nuclei.*

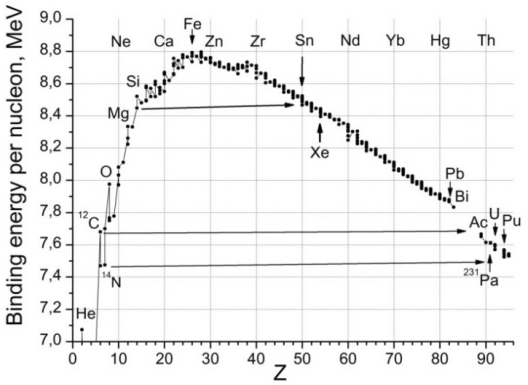

Fig. 5. *Coupling energy per nucleon in stable atomic nuclei.*

The laws of statistical physics can be applied to transmutation processes on the basis that transmutation can be represented not as an exchange of energy between particles, but as an exchange of nucleon portions between nuclides ($E = mc^2$). As a statistical ensemble, we can use all types of sets of a limited number of 286 stable nuclides.

In statistical physics, the energy distribution E for colliding gas atoms at temperature T is described by the Maxwell distribution:

$$f_E = \frac{2\pi}{\sqrt{(\pi kT)^3}}\sqrt{E}\exp(-E/kT).$$

For transmutation processes, we replace the energy in the Maxwell distribution with the masses of isotopes M_A or with the mass numbers of isotopes A: $E \to A$, and kT with the energy content coefficient of the medium G, which characterize the transmutation process: $kT \to 2G$:

$$f_A = \frac{C}{\sqrt{(2G)^3}}\sqrt{A}\exp(-A/2G), \quad (1)$$

where C is the normalization coefficient. Just as the temperature of a system T is a collective parameter of its constituent particles, so the number G determines the collective energy content of the medium [37]. The energy content coefficient of a medium depends on the total binding energy of its constituent nuclei (Fig. 5). The lower the total binding energy of all nuclei, the greater the energy content of the medium, the greater the coefficient G. It is noteworthy that the energy content of systems that consist of atoms, for example: carbon-nitrogen and thorium-uranium, is approximately the same (Fig. 5). The energy content coefficient has a maximum value in a medium that consists of hydrogen atoms, whose binding energy is zero. Transmutation reactions do not occur in a medium made up exclusively from iron and nickel isotopes with the maximum binding energy per nucleon: ^{56}Fe-8.790 MeV, ^{58}Fe-8.792 MeV and ^{62}Ni-8.794 MeV (Fig. 5). The mass number of A varies from 1 to 250, from hydrogen to californium-250 isotope in the "thermodynamic" distributions corresponding to formula (1) (**Fig. 6**). Energy content coefficient G in Fig. 6 has three, arbitrarily chosen, values G = 8, 12 and 24. These values correspond in the distributions to the maximum values of the mass number Amax, which determines the physical meaning of the coefficient $G = A_{max}$. Since transmutation reactions occur with a loss of internal energy of the atomic nuclei of the medium, the energy content coefficient G will constantly decrease during the transmutation process.

Thus, the resulting distribution, firstly, will be quasi-equilibrium distribution; secondly, all chemical elements, including heavy and superheavy ones, will be synthesized at high

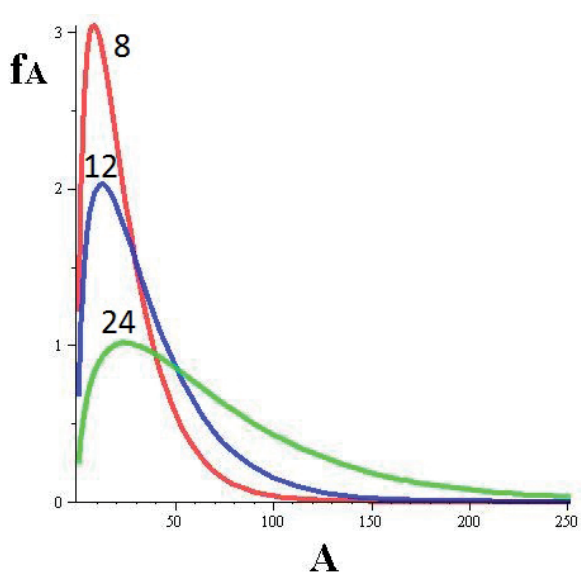

Fig. 6. *"Thermodynamic" mass number distributions A for transmutation processes.*

values of the energy content coefficient G, thirdly, as the coefficient G decreases, the distribution, conditionally, will change from the distribution described by the line with $A_{max} = 24$ in Fig. 6, to the distribution described by the line with $A_{max} = 8$. Consequently, chemical elements with small and medium mass numbers will be mainly synthesized. And heavy and superheavy elements will be transformed into lighter elements; fourthly, the presence of iron and nickel, that do not participate in transmutation reactions, will increase in the distribution over time. By the content of these elements in an object, by its mass density, one can judge the duration of the transmutation processes that occur in this object.

Consequently, quasi-equilibrium distributions reflect the occurrence of chemical elements and their isotopes in different objects and regions of the Universe.

Vernadsky V.I. wrote in the book [2]: "It turned out that the quantitative atomic composition of the Earth's crust is not a random phenomenon. It is closely related to the diverse properties of atoms in the physical, primarily thermodynamic, field to which the Earth's crust responds. The Earth's crust in the Phillips-Clark-Focht table (a table of concentrations of chemical elements) quantitatively corresponds to some important *planetary manifestation of atoms*. As a result of astrophysical research, it turned out that the surface layers of stars, including the Sun, reflect, approximately, the same quantitative atomic composition, which is expressed in the P-C-F table. …There can hardly be any doubt that as geological processes are deeply studied, their not only terrestrial, but planetary character will be revealed with ever increasing sharpness".

3. NUCLEOSYNTHESIS. LIVING MATTER

Since the transformation of chemical elements in transmutation reactions occurs at low excitation energies of condensed matter ~ 1 eV/atom, natural nucleosynthesis started in the Universe during the Recombination Era approximately 50 thousand years after the Big Bang (BB). At the same time, matter began to dominate over electromagnetic radiation, "light was separated from darkness", which led to a change in the expansion regime of the Universe. The Recombination Era began approximately 18 thousand years after BB, when electrons began to combine with helium nuclei to form He^+ ions. At that time, matter consisted mainly of electrons, protons, deuterons (0.5% of nuclei) and helium nuclei (6% of nuclei).The beginning of nucleosynthesis is associated with two circumstances: firstly, directed electromagnetic radiation that comes from the hot center of the Universe generated directed flows of free electrons, which create strong magnetic fields. And, secondly, 50 thousand years after the BB, there was already a sufficient number of neutral helium atoms in the cosmic plasma, which were the first to participate in transmutation reactions [38]. It is noteworthy that the isomer of the helium atom, namely, orthohelium, is the only one of all atoms of chemical elements, which, due to the parallelism of the magnetic moments of the electrons, has a strong magnetic field of ~ 70 T at the radius of the atom. This property of orthohelium radically increases the intensity of nucleosynthesis processes [21,38]. Due to the strong magnetic field, orthohelium atoms are attracted to each other and form helium transatoms (Fig. 3). Helium transatoms, which combine due to an ultra-strong magnetic field, form multinuclear molecules. The creation of such transmolecules leads to multinuclear transmutation reactions, with the emission of protons, neutrons, alpha particles and the formation of heavy chemical elements with a nuclear charge $Z \geq 6$ (**Fig. 8**).

100 thousand years later, electrons recombined with all the helium nuclei to form neutral helium atoms and with half of the protons to form hydrogen atoms. The temperature of the cosmic plasma at that time was ~ 4000 K or ~ 0.4 eV. The Recombination

Era ended 380,000 years after the Big Bang with the neutralization of all hydrogen atoms. It can be assumed that nucleosynthesis due to transmutation reactions did not stop with the end of the Recombination Era, but continued due to the always available hydrogen and helium atoms and energy flows that comes from the center of the Universe and creates cosmic plasma.

As a result of transmutation reactions, the onset of nucleosynthesis led to the appearance, first of all, of light chemical elements in cosmic hydrogen-helium plasma: carbon, nitrogen and oxygen, the atomic content of which was more than two orders of magnitude higher than the production of other chemical elements (**Fig. 7, 8**) [21,22,39]. It is obvious that the appearance of carbon *C*, nitrogen *N* and oxygen *O*, when they are overwhelmingly surrounded by

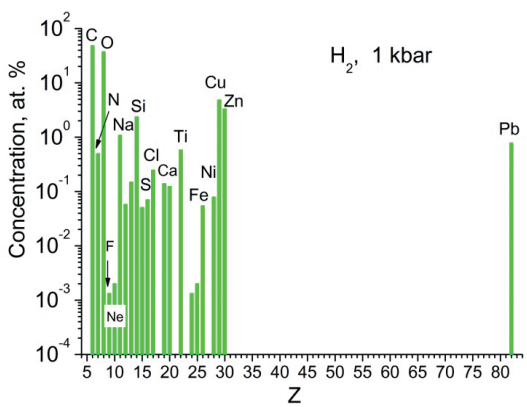

Fig. 7. *The average concentrations of chemical elements over 15 measurements of different objects.*

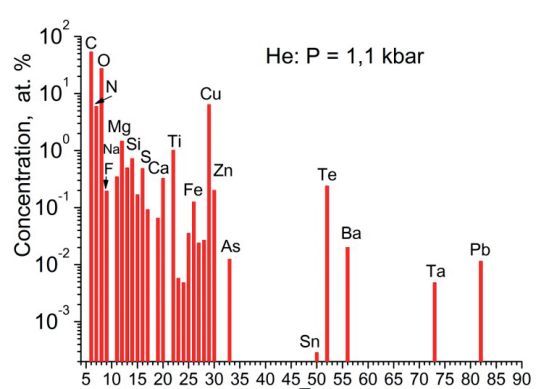

Fig. 8. *The average concentrations of chemical elements over 11 measurements in an experiment with He at P=1.1 kbar.*

hydrogen ions H^+ and its *H* atoms, immediately leads to the launch of organic world reactions with the production of molecules: methane CH_4 and other hydrocarbons, including those that contain *C = O* and *COOH* groups, ammonia NH_3, cyanide *HCN*, water H_2O, carbon dioxide CO_2, etc. Hydrogen, carbon, nitrogen and oxygen are the basic elements in diverse organic world.

Thus, the nucleosynthesis that began simultaneously gave rise to the processes of inorganic chemistry, but, to a greater extent, organic chemistry, and, ultimately, the parallel formation and development of Inert matter and Living matter. Organic matter after nucleosynthesis during the Recombination Era many times prevailed over inorganic matter (excluding hydrogen and helium). The subsequent transition of organic matter into inorganic matter is associated with the destructive action of the external environment and transmutation reactions that occur in condensed matter.

Figures 7 and 8 show the results of experiments performed by A.Yu. Didyk and R. Wiśniewski on the synthesis of chemical elements during irradiation of condensed gases hydrogen and helium with braking gamma rays with a boundary energy of 10 MeV [21-23,39]. A unidirectional flow of braking gamma quanta creates a unidirectional flow of free electrons, which generate strong magnetic fields, Fig. 1*b*. The orthohelium atom itself has a strong magnetic field [38]. Atoms are transformed into transatoms in strong magnetic fields, and transmutation reactions induce nucleosynthesis. In addition, after the end of irradiation, newly created objects were discovered in the reaction chambers in all experiments: particles and other simple and complex microstructures.

Eight particles with sizes of ~ 1 mm were discovered in the reaction chamber in an experiment with hydrogen at a pressure of *P* = 1 kbar. A photo of one of these particles measuring ~700×630 μm is shown in **Fig. 9***a*.

a *b*

Fig. 9. *Particles synthesized in experiments with hydrogen at pressures: a – P = 1 kbar; b – P = 3.4 kbar.*

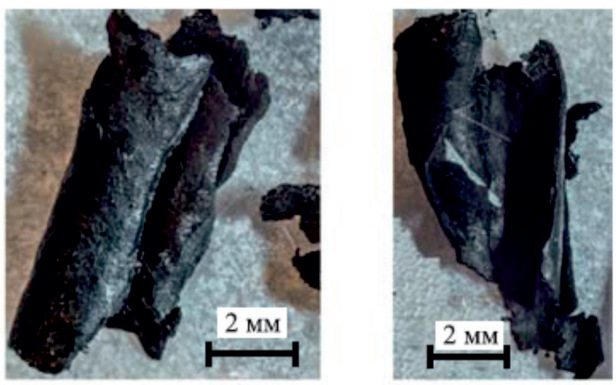

Fig. 10. *Photo of graphite foils.*

One black particle was found in the chamber in another experiment with a pressure of P = 3.4 kbar (Fig. 9*b*). The particles consisted primarily of carbon and oxygen.

Thin, cylindrical, black foils of considerable size were discovered in the inner part of the reaction chamber in an experiment with helium at a pressure of 1.1 kbar. The foils (**Fig. 10**) contained mainly carbon and oxygen and left an oily residue on the paper. The latter indicates the presence of liquid oils in the form of hydrocarbons on the foils and the synthesis of hydrogen.

It follows from the experiments presented above and numerous other experiments that a synthesis of not only new chemical elements, but also the synthesis of extraneous solid structures that contains these new elements occurs in the process of transmutation.

There are several mechanisms for the formation of solid structures in condensed matter. This is, first of all, the chemical combination of particles, the formation of structures as a result of resonant interference exchange interaction between different objects and the formation of structures due to the fractal geometry of nature.

One of the fundamental properties of objects is that they all have wave properties described by de Broglie waves λ. This property is of fundamental importance, since without it the following would be impossible: exchange interaction between identical objects and resonant interference exchange interaction between objects that have common resonant states [27]. For a particle, the de Broglie wavelength is $\lambda = h/mV$, where h is Planck's constant, mV is the momentum of the particle: the product of its mass m and velocity V. A hydrogen atom with a mass of 1 amu at room temperature 300K has the de Broglie wavelength λ_H = 0.145 nm (the diameter of the hydrogen atom is 0.106 nm). The lower the velocity V of a particle, the longer the de Broglie wavelength λ, the greater the distance it interacts with other identical particles in an exchange manner.

3.1. "Boson body"

Boson particles tend to occupy one state, and thereby to form a Bose-Einstein condensate. Consequently, boson atoms and boson molecules can concentrate in one place and form a "boson body". The thermal speed of the "boson body" decreases with an increase in the mass of the "boson body" and its crystallization, when bosons bind. From thermodynamics $V = \sqrt{\frac{3kT}{N \cdot m}} \left(\frac{3}{2} kT = \frac{N \cdot m \cdot V^2}{2} \right)$, where k is Boltzmann's constant, T is temperature, N is the number of identical bosons of mass m in the "boson body". Consequently, the "boson body" reduces the speed of bosons by a factor $1/\sqrt{N}$ and increases the de Broglie wavelength $\lambda = \frac{h}{mV} = h\sqrt{\frac{N}{3kT \cdot m}}$ by a factor $\sqrt{N}$. The force that attracts other identical bosons is proportional to the number of bosons N that make up the "boson body". Let us remember that one mole contains $6 \cdot 10^{23}$ particles. For this reason, the "boson body"

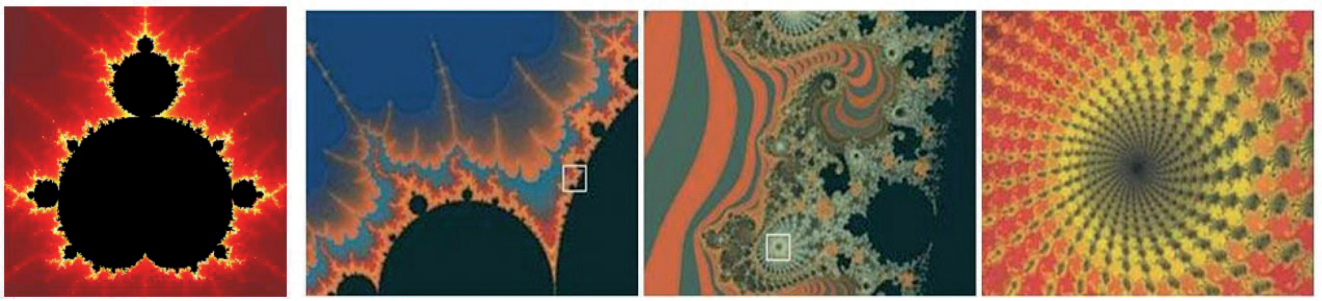

Fig. 11. *Mandelbrot set.*

constantly increases its size due to the addition of identical bosons to itself.

In a "boson body" that consists mainly of hydrogen, carbon, nitrogen and oxygen, intense reactions, including organic chemical reactions, begin under the influence of electromagnetic radiation and other external influences. Organic chemical synthesis leads to the formation of a variety of organic molecules, and, subsequently, biochemical molecules. Thus, recently a group of scientists identified chemical reactions that could lead to the emergence of life [40]. These chemical reactions occur with the participation of only four chemical elements that represent the inert matter: keto acids (hydrocarbon derivatives that contain $C = O$ and $COOH$ groups), cyanide HCN, ammonia NH_3 and carbon dioxide CO_2, and the products are: amino acids and nucleic acids, which are the building blocks for proteins and DNA of Living matter.

3.2. Fractals

All matter consists of a multitude of both diverse and similar identical systems. In turn, any system consists of its constituent connected objects. The same objects can be in a free state in the space that surround the system.

One of the main properties of systems is the ability to form other, self-similar systems within themselves or from free objects that surround them. "If each of the parts of a certain form is geometrically similar to the whole, then this form and the cascade that generates it are called self-similar structures" (Mandelbrot, [41]).

This property of systems is called *Fractal geometry of nature* [41]. This geometry describes both mathematical space and, what is fundamentally important, the physical Universe (**Fig. 11, 12**). Fig. 11 shows the Mandelbrot set, which is a classic example of an algebraic fractal. Three successive enlargements of fragments (marked with squares) shown in Fig. 11 allow us to see similar, repeating structures of the Mandelbrot set with the addition of many new and previously non-repeating elements. The Mandelbrot set reflects the self-similarity that forms a basis for infinite diversity!

Building fractals in physical space is one of main properties of the Matter that makes up any Structures.

Fractal geometry is inherent in all material structures, from atomic nuclei to stars and galaxies. Even the characteristics that describe Chaos are subject to the law of fractal geometry [42]. We should go further and see that Intellectual images, constructions and structures associated with Consciousness and Mental activity in the field of art, humanities, social and political sciences also obey the laws of fractal

Fig. 12. *Fractals of mountains, clouds, rivers and Living matter.*

self-similarity. This property is especially evident in music and architecture.

Fractals are created by both Inert matter and biological, Living matter. Thus, Inert matter and Living matter reproduce themselves, i.e. MULTIPLY. Biological organisms proliferate particularly intensively. Living matter are biological structures and organisms capable of self-similarity and reproduction due to the processing of inert matter, consisting of organic and inorganic molecules and structures. Living matter differs from Living substance, which Vernadsky defined as follows: "I will call Living substance the totality of organisms that participate in geochemical processes. The organisms that make up the totality will be elements of Living substance" [43].

It is noteworthy that large structures that are capable of creating more stable substructures within themselves can "spontaneously" disintegrate into them. This property of systems is also reproduction. It is characteristic of nuclei: cell nuclei and nuclei of transuranium chemical elements. In politics, this phenomenon is observed during the collapse of empires. Probably, the decay phenomenon is also characteristic of the nuclei of some planets.

The condensed substance changes its internal state and internal structure under the influence of external environmental factors. Inert matter in strong magnetic fields is transformed through transMutations of chemical elements, and the development of Living matter occurs due to Mutations in its biochemical structures.

The difference between transmutations and mutations is determined by the energy of these processes and, as a consequence, their intensity. To transform Inert matter, it is necessary to exert a strong action on it, and a weak action is sufficient for the transformation of Living substance. Therefore, Living matter evolves through intensive mutations several orders of magnitude faster than Inert matter.

Thus, from the very beginning of nucleosynthesis, the development of Inert matter and the evolution of Living matter were always going and are going in parallel and interpenetrating each other. Since they consist of identical atoms, Living matter grows due to the processing of Inert matter, and Inert matter is replenished at the expense of Living matter after its death.

In the Universe, "boson bodies" began, starting from the Recombination Era to form, first of all, from light chemical elements, from which organic and biological planets were later formed. Thanks to mutations and the fractal geometry of nature, primitive organic life must first have appeared, and subsequently intelligent life must have developed on these organic planets [44]. It is difficult to imagine the capabilities of a Supreme Intelligence aged more than 12 billion years.

From the above, two important statements can be made:

- Life is eternal in a physically eternal Universe.
- The Universe is filled with Living matter.

V.I. Vernadsky wrote: "The spreading of life, expressed in the omnipresence of life, is a manifestation of its internal energy" [1]. These statements are consistent with three points made by V.I. Vernadsky, who believed that, firstly, "life is eternal insofar as the cosmos is eternal" [45], and secondly, "living things are generated only by living things." And, therefore, thirdly, "only cosmos is the source of terrestrial life". Vernadsky opposed mechanical theories of the spontaneous generation of life on Earth through the arbitrary transformation of inorganic matter into organic and biotic. "Life, eternal in the Universe, appeared New on Earth. The germs of Life were constantly brought into it from the outside, but they strengthened on Earth only when there were favorable opportunities for this on Earth" [45]. This statement, a confirmation by V.I. Vernadsky, we consider to be valid for any object in the Universe.

4. PLANETARY NUCLEOSYNTHESIS AND GALACTIC JET STREAMS OF MATTER AND ENERGY. LIVING EARTH

The first stars and galaxies began to form after ~0.5 billion years of development of the Universe. At this stage, when the density of matter and the directional movement of free electrons reached values sufficient for the generation of magnetic fields and the pairing of electrons in them, low-energy transmutation reactions of chemical elements similar to those that had been taking place since Recombination Era began again.

And again, first of all, light chemical elements were synthesized from hydrogen and helium: carbon, nitrogen and oxygen. These chemical elements that created a cosmic, condensed environment, were a fertile "soil" for the "embryos of life" − Living matter, the entire cosmos of which by that time was already contaminated. Therefore, the formation of the Earth and the formation of its Biosphere occurred simultaneously from the very beginning. "For our planet, the existence of life in the most ancient sediments accessible to us, known to us on our planet, has been empirically established. On the other hand, we have not found rocks anywhere in the biosphere that would indicate their formation over geological time in the absence of living substance. …The biosphere is geologically eternal", − wrote V.I. Vernadsky – "If the amount of living substance is lost on the background of inert and bioinert masses of the biosphere, then biogenic rocks (i.e. created by living substance) make up a huge part of its mass, and go far beyond the biosphere. Taking into account the phenomena of metamorphism, they transform, losing all traces of life, into a granite shell and leave the biosphere. The granite shell of the Earth is the region of former biospheres" [2].

Since the transformation of chemical elements in low-energy transmutation reactions occurs under fairly "soft" physical conditions of ~ 1 eV/atom and reproduces a quasi-equilibrium distribution, it can be concluded that the process of nucleosynthesis carries out on planets and shapes their elemental composition [8,46-49]. Now, in the Earth's magma, transmutation processes continue, and the colossal energy released during this process is observed by us in the constant movement of lithospheric plates and in volcanic eruptions. Experts know that intraplate tectonic activity and volcanism cannot be explained within the framework of plate tectonics. The most common hypothesis that satisfactorily explains volcanism and tectonic activity within both the oceanic and continental lithosphere is associated with the ideas of hot spots and mantle plumes [50]. Apparently, it is in these hot spots and mantle plumes that transmutation processes occur.

V.I. Vernadsky wrote: "Everything indicates that the radioactive decay of chemical elements − the transformation of one isotope into another − is not a special case, but a general property of terrestrial matter. All chemical elements of the Earth are in the state of radioactive decay. This is the basic physical and chemical process, which is the root cause of all geological phenomena. The chemical degeneration of the planet is, in the end, its consequence... It is characteristic of trace elements, at least for their main mass, that the regularities of their distribution cannot be explained by chemical processes. They are continuously created and transformed into new isotopes of other elements throughout the matter of our planet. The phenomenon of trace elements − a large terrestrial exothermic process − introduces probably more heat into our planet than the "spontaneous" decay of radioactive atoms" [2].

Judging from the idea of planetary nucleosynthesis, based on the mechanism of multinuclear quantum transitions of one atomic nuclei to another, we have formulated a new doctrine of the geological development of the Earth:

1. The geological development of the Earth is a monotonous, evolutionary process, which is superimposed by revolutionary, stepwise periods.

2. The evolutionary process is determined by internal energy sources: low-energy nuclear reactions, radioactive decays, gravitational compression, etc. Since the energy coming from internal sources monotonically decreases, geological processes monotonically slow down.

3. Abrupt, including cyclical periods in the development of the Earth are generated by external energy sources that stimulate geological activity on Earth. During these periods, geological processes accelerate, sometimes in revolutionary, explosive ways.

4. External energy sources are the Sun, jet streams of energy and matter from the Galaxy and outer cosmos. Perhaps there are other, external energy sources available. External energy sources can influence the Earth directly or indirectly through the Sun and the giant planets of the solar system.

V.I. Vernadsky emphasized in the book [2]: "We are in geology − in the history of planet Earth − are continuously, really confronted with the energetic and material manifestation of the Milky Way − in the form of cosmic matter − meteorites and dust and material-energetic, penetrating cosmic radiation invisible to the eye and not consciously perceived by humans. Cosmic rays come to us from the Galaxy continuously. I proceed from the scientific hypothesis that these rays, on their way, break up the atoms of most chemical elements, transform them into others, and constantly there is a synthesis of enormous released thermal energy, which should have great geological significance and which is still, taken as a whole, is not taken into account by geologists. ...Solar energy, which creates life on our planet, pales in its power on the background of the so-called cosmic penetrating radiation. We will see the geological significance of these radiations and their role in the thermal regime of the planet".

The idea of planetary nucleosynthesis led us to the creation of a new scientific discipline − Quantum planetology (geology) [47-49]. Within the framework of quantum geology and the new doctrine of geological development of the Earth, the strict temporal cyclicity observed in the geological activity of the Earth has been explained.

According to a study published in the journal Geoscience Frontiers [51], geological activity on Earth follows a well-traced cycle of approximately 27.5 million years. Previously, it was believed that geological events were random. But the analysis of geological events over the past 260 million years showed that, in fact, there is a strict cyclicity in geological activity. **Fig. 13** presents the results of an analysis of 89 geological events using a 10 million year sliding window centered every 0.5 million years. The number of events that fell into the sliding window was calculated at intervals of 1 million years. Ten peaks are clearly visible. This analysis was carried out thanks to significant improvements in radioisotope dating techniques and in methods for measuring time on the geological scale.

The fact of presence of cyclical fluctuations in the Earth's geological activity is a serious deviation from generally accepted views. However, the observed cyclicity fits perfectly into the above new doctrine of the geological development of the Earth. The galactic year

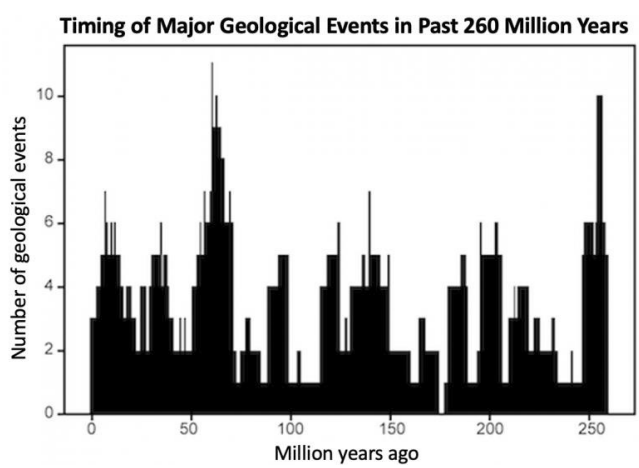

Fig. 13. *Cyclicity of the Earth's geological activity* [51].

amounts, according to various estimates, from 180 to 250 million years. The Sun and its planets are believed periodically, four times per galactic year, approximately every 60 million years, cross the visible jet streams of matter and energy ejected from the center of the Galaxy disk [19,52]. If the cycle of geological activity on Earth of 27.5 million years is associated with galactic energy flows, then we should assume the existence of four additional, invisible, jet energy flows located between the visible flows. Based on these considerations and on a cycle of 27.5 million years, the Galactic year will be equal to 220 million years.

In our opinion, jet energy streams (JES) of the Galaxy trigger transmutation reactions in stars and planets. The nuclear energy released in these reactions, colossal in scale, causes super-powerful activity of matter in the volumes of stars and planets. These phases of activity of the solar system (PASS), associated with the JESs of the Galaxy, lead to huge changes in the structure of the Sun and planets.

Scientists called the 27.5 million year cycle as the "pulse" of the Earth. It is obvious that the "pulse" of the Earth is set by the JESs – the rhythm of the energetic "heartbeat" of our Galaxy. An interesting challenge for planetary science and astronomy is to record the invisible, jet energy flows of the Galaxy by detecting their impact on stars and their planetary systems. If the JESs of the Galaxy are constant during the formation of the entire solar system, then since the formation of the Earth 4.54 billion years ago as an independent planet, it has been exposed to these flows 165 times.

If the explosive transmutations that regularly occur in the history of the Earth are equated to mutations in Living matter, then it can be argued that the geological shells of the Earth and the biosphere are constantly adapting to the impact of cosmic radiation. Thus, the geosphere and biosphere co-evolve and become more and more structurally and functionally interconnected with each other, ultimately becoming a Unified System. It is obvious that dramatic changes in one of these areas can lead to catastrophic changes in others. For this reason, planet Earth should be perceived as entirely Alive planet. "Throughout the entire period of geological phenomena, which we scientifically cover during the period of 2-3 billion years, we see the existence of life, the existence of the biosphere on the planet Earth" [2].

Due to the "shake-up" of the entire solar system every 27.5 million years, "lifeless" planets have a chance to restart their history with the possibility of the emergence of life, if there was no life on these planets or it disappeared.

In other cases, if vegetable life, animal life, and, especially, intelligent life in the form of highly developed civilizations existed on the planets, then during periods of destructive planetary activity, the vegetable and animal parts of the biosphere, if would not have disappeared, then had to be radically transformed. And highly developed civilizations were forced to leave their "living" planets and move to "dead" or artificially created planets on which transmutation reactions would be impossible. After the end of the activity phase of the solar system, highly developed civilizations could return to their home planets or put them under observation, if, for example, the conditions of existence of their civilization changed on them (the composition of the atmosphere, the temperature on the surface of the planet, etc.) or another life appeared with a changed structure, different from their genetic structure. Therefore, if we assume that highly developed civilizations in the intervals between the phases of activity of the solar system closest to our time existed on Earth, then during the period of geological activity of the Earth they had to leave it. And now they regularly visit our common planet, but not as Aliens, but as AlienEarthmen.

The last phase of solar system activity ended approximately 7 million years ago. This allows us to assume and hope that the peak intensity of the next catastrophic geological activity on Earth will occur in 20 million years. And, if the Humanity does not self-destruct themselves before that time, then in approximately 17 million years they will be forced to leave the Earth!

5. CONCLUSION

Nowadays, a paradigm shift in science occurs or in other words, a new scientific revolution takes place associated with the discovery of low-energy nuclear reactions and the discovery of fundamental resonant interference exchange interaction. The previous scientific revolution began in 1896 with the discovery, by A. Becquerel, of the natural radioactivity of uranium salts. This event was followed by the creation of quantum mechanics, atomic and nuclear physics, special and general relativity theories, and the discovery of electromagnetic, strong and weak interactions.

The whole scientific activity of V.I. Vernadsky took place during a paradigm shift. Vernadsky wrote: "We are currently experiencing a revolutionary movement in science that has nothing comparable; only the 17th century, with its victory of the ideas of Copernicus, with great discoveries of Kepler, Galileo, and Newton, may, perhaps, have a distant analogy with our time. Before the change in scientific thinking, which is taking place before our eyes steadily and at an increasingly rapid pace, surprisingly little noticeable to contemporaries, the entire 19th century with its scientific development will probably seem in the history of thought to be a mere preparation for the great revolutionary movement of the 20th century" [1]. Having made this conclusion, V.I. Vernadsky practically anticipated the discovery of the law of paradigm shift made by T.S. Kuhn in 1962 [28]. At the same time, Vernadsky pointed out that the formation of a new worldview is preceded by a stage of scientific research conducted within the framework of the old paradigm. After the integration period, which is the confirmation of a new worldview, the era of the most extensive, differential research in emerging, new scientific directions and disciplines begins again. It is obvious that the integral and differential periods of scientific research during the operation of the paradigm are its components.

With the discovery of low-energy nuclear transmutation reactions, we have proposed a new mechanism for the nucleosynthesis of chemical elements, which occurs both at the stage of formation of the very early Universe, and in stars and planets. Transmutation reactions occur with the participation of many atoms and many nuclei. This approach allowed us to take a new look at various processes that occur in the Universe.

Transmutation reactions that continuously occur in a condensed matter lead to a quasi-equilibrium distribution of isotopes − reaction products − by mass numbers. The collective parameter that characterizes the quasi-equilibrium distribution is the "thermodynamic" coefficient of energy content G of the matter. Quasi-equilibrium distributions reflect the occurrence of chemical elements and their isotopes in different objects and regions of the Universe.

The implementation of nucleosynthesis of chemical elements in the Recombination Era allowed us to understand that the development of Inert substance and the evolution of Living matter have always been going and are going in parallel and interpenetrate each other. Thus, Life revealed itself to be eternal in a physically eternal Universe. Since the evolution of Living matter was much more intense compared to the development of Inert substance, then it filled the entire early Universe, and formed the Seeds of Life for future planets in star systems.

The discovery of fractal geometry made it clear that the existence and evolution of the Universe occurs due to one of main

properties of structured Matter and intellectual forms of Consciousness − the ability to build fractals. Moreover, the fundamental law of the Development of matter and consciousness has been identified from this property of fractal geometry − The creation of self-similar structures and their reproduction is the basis of infinite Diversity!

Judging from the idea of planetary nucleosynthesis, based on the low-energy mechanism of multinuclear quantum transitions of one atomic nuclei to another, we created a new scientific discipline − Quantum planetology (geology) and formulated a new doctrine of the geological development of the Earth. The new doctrine allowed us to explain the cyclicity observed in the geological activity of the Earth, thereby suggesting the existence of visible and invisible jet energy flows coming from the center of our Galaxy. It is obvious that Galactic jet energy flows, that stimulate geological activity on Earth, determine the beginning and end of geological eras and periods in the evolution of the geosphere and biosphere of the Earth.

The geosphere and biosphere evolved together throughout the formation of the Earth and became more and more structurally and functionally interconnected with each other, and, eventually they have become a Single Living System − the Earth.

Vernadsky believed that the biosphere, due to ongoing scientific and technological progress, made the transition to the noosphere at the beginning of the 20th century. As main reasons for the emergence of the noosphere, V.I. Vernadsky indicated: human population of the entire planet; development of planetary communication systems and communications, creation of a unified information system; discovery of new energy sources such as nuclear energy; access to the management of states by the broad masses of people; predominance of the geological role of man over other geological processes that occur in the biosphere. V.I. Vernadsky pointed out in 1944 [2]: "In the twentieth century, a man recognized and embraced the entire biosphere for the first time in the history of the Earth. Humanity, taken as a whole, have become a powerful, ever growing geological force. The question of restructuring the biosphere in the interests of free-thinking humanity as a single whole arises before humanity, before their thought and work. This new state of the biosphere is exactly the noosphere".

In addition to the fact that Humanity have turned into a powerful geological force capable of destroying the biosphere and itself, due to publicly available means of communication, it has been transformed into a Single Whole with a single world production, with a world economy, with a world but diverse culture, with a world diverse art, with a world science, with a world history. V.I. Vernadsky wrote in 1912: "This has never happened before, and in vain we would look for analogies of the era of the 17th-20th centuries in the past of mankind. It is not without reason that this is recognized now, when before our eyes, world history is emerging more and more clearly and powerfully, and embraces, as a single whole, the entire globe, completely putting an end to the secluded cultural historical areas of the past, that little depend on each other" [53].

Vernadsky possessed a huge amount of knowledge, formed a new worldview, synthesized various directions in science, which had previously developed within the narrow framework of their specialization. Many of Vernadsky's studies were ahead of his time, and some ideas became prophetic and are only understood by us at the present time. The ideas of V.I. Vernadsky and a large number of quotes from his original works given in this article made him the inspirer and co-author of this work. We tried, in this article, to answer those few questions, a huge number of which Vernadsky formulated in his fundamental scientific and philosophical works. According to the law of fractal geometry, the issues discussed have multiplied several times, thereby indicating

directions in scientific research that will form a new paradigm, a new worldview.

"The great process of the collapse of the old and the creation of new understandings of the surrounding world is going on around us, whether we want and realize it or not; things that seemed to be completely strong and established for us are being undermined at the very foundation − the century-old foundations of scientific thinking are crumbling, the covers that were accepted by us for completed creations are demystified, and under old names, new, unexpected content is revealed to the surprised gaze of contemporaries... What has always seemed scientifically impossible, tomorrow may turn out to be scientifically necessary" [1]. Yesterday's tomorrow – today – is already here.

REFERENCES

1. *Vernadsky Vladimir Ivanovich. Materials for the Biography*. [Prometey. Historical and Biographical Almanakh. Ser. "Life of Outstanding People". Compiled by Aksenov G., Scientific editor. Mochalov I.I. Vol. 15]. Moscow, Molodaya gvardiya Publ., 1988, 352 p.
2. Vernadsky VI. *Chemical Structure of the Earth's Biosphere and Its Environment*. Moscow, Nauka Publ, 1965, 374 p.
3. Tarasova NP, Mustafin DI. V.I. Vernadsky and the Problems of Radioactivity. *Voprosy sovremennoy nauki i praktiki,* 2013, 3(47):38-50 (in Russ.).
4. Vernadsky VI. *Ocherki i rechi* [Essays and Speeches]. Issue 1:159 p.; issue 2:124 p. Petrograd, Nauchnoe khim.-tekhnich. izd-vo Publ, 1922, (in Russ.).
5. Proceedings of the 1-27th Russian Conferences on Cold Transmutation of Nuclei of Chemical Elements (RCCTNCE). Dagomys-Sochi-Moscow, RUDN, 1993-2022.
6. Proceedings of the 1-25th International Conferences on Condensed Matter Nuclear Science (Cold Fusion, ICCF).
7. Balakirev VF, Krymsky VV, Bolotov BV, Vasilieva NV, Vachaev AV, Ivanov NI, Kazbanov VI, Pavlova GA, Solin MI, Trofimov VI, Urutskoev LI. *Vzaimoprevrashcheniya khimicheskikh elementov* [Mutual Transformation of chemical Elements]. Ekaterinburg, Urals Branch of RAS Publ., 2003, 96 p.
8. Mishinsky GV, Kuznetsov VD, Penkov FM. Nizkoenergeticheskaya transmutatsiya atomnykh yader khimicheskikh elementov. Raspredelenie po elementam v produktakh transmutatsii. nukleosintez [Low energy transmutation of atomic nuclei of chemical elements. Element distribution in the products of low energy transmutation. Nucleosynthesis]. *Journal formiruyushchikhsya napravleniy nauki* (*JFNN*), 2017, 17-18(5):61-81 (in Russ).
9. Mishinsky GV, Kuznetsov VD, Starostin VI. Natural nucleosynthesis. *RENSIT: Radioelectronics. Nanosystems. Information Technologies,* 2022, 14(4):461-484. DOI: 10.17725/rensit.2022.14.461.
10. Fleishmann M, Pons S, Hawkins M. Electrochemically induced nuclear fusion of deuterium. *J. Electroanal. Chem.*, 1989, 261:301-308.
11. Karabut AB, Kucherov YaR, Savvatimova IB. Nuclear product ratio for glow discharge in deuterium. *Phys. Letters A*, 1992, 170:265-272.
12. Savvatimova IB, Karabut AB. The products of nuclear reactions recorded at the cathode after experiments in a glow discharge in deuterium. *Poverhnoct'* [Surface Investigation: X-Ray, Synchrotron and Neutron Techniques], 1996, 1:63-75; 78-81 (in Russ.).
13. Savvatimova IB. Transmutation Effects in the Cathode Exposed Glow Discharge. Nuclear Phenomena Or Ion Irradiation Results? *Proc. 7th Int. Conf. on Cold Fusion* (ICCF),

Canada, 1998: 342-350; Reproducibility of Experiments in Glow Discharge and Processes Accompanying Deuterium ions Bombardment. *Proc. 8th ICCF,* Italy, 2000: 277-283.

14. Solin MI. Experimental facts of spontaneous appearance of condensate of soliton charges with the formation of nuclear fusion products in liquid zirconium. *Fizicheskaya mysl' Rossii* [Physical Idea in Russia], 2001, 1:43-5. (in Russ.).
15. Controlled Nucleosynthesis Breakthroughs in Experiment and Theory. Editors Adamenko SV, Selleri F, A. van der Merwe. Series: *Fundamental Theories in Physics,* Springer, 2007, v. 156, 780 p., http://www.springer.com/physics/elementary/book/978-1-4020-5873-8.
16. Adamenko SV. The concept of artificially initiated collapse of matter and the main results of the first stage of its experimental implementation. Preprint, 2004, Kiev (in Russ.), http://proton-21.com.ua/publ/Preprint_ru.pdf.
17. Urutskoev LI, Liksonov VI, Tsinoev VG. Observation of Transformation of Chemical Elements during Electric Discharge. *Annales de la Fondation Louis de Broglie* (*AFLB*), 2002, 27(4):701-726.
18. Kuznetsov VD, Mishinsky GV, Penkov FM, Arbuzov VI, Zhemenik VI. Low energy transmutation of atomic nuclei of chemical elements. *AFLB*, 2003, 28(2):173-214.
19. Krivitsky VA. *Paradoksy Transmutatsii i Razvitie Zemli* [Paradoxes of Transmutation and the Development of the Earth]. Moscow, NITs "Academica" Publ., 2016, 238 p.
20. Kladov AF. Cavitation destruction of matter (in Russ.); http://roslo.narod.ru/rao/rao1.htm.
21. Didyk AYu, Wiśniewski R and Wilczynska-Kitowska T. The carbon-based structures synthesized through nuclear reactions in helium at 1.1 kbar pressure under irradiation with braking γ-rays of 10 MeV threshold energy. *Euro. Phys. Lett.*, 2015, 109: P.22001-P.1-22001-P.6.
22. Didyk AYu, Wiśniewski R, Wilczyńska-Kitowska T, Mishinsky GV, Semin VA. Synthesis of chemical elements under irradiation by bremsstrahlung gamma-rays of palladium in condensed gases. *RENSIT: Radioelectronics. Nanosystems. Information Technologies,* 2019, 11(2):143-160. DOI: 10.17725/rensit.2019.11.143.
23. Wisniewski R, Mishinsky GV, Wilczynska-Kitowska T, Zukowska Z, Rostocki A. Graphite-like structures, synthesized from gaseous He under high pressure, by braking irradiation of maximum energy of 10 MeV – modeling of the process. *Acta Physica Polonica B, Proceedings Supplement*, 2020, 13(4).
24. Vysotskii VI, Kornilova AA. *Nuclear Fusion and Transmutation of Isotopes in Biological Systems*. Moscow, Mir Publ., 2003, 304 p.
25. Vysotskii VI, Kornilova AA. Transmutation of stable isotopes and deactivation of radioactive waste in growing biological systems. *Annals of Nuclear Energy*, 2013, 62:626–633.
26. Kornilova AA, Vysotskii VI. Synthesis and transmutation of stable and radioactive isotopes in biological systems. *RENSIT: Radioelectronics. Nanosystems. Information Technologies,* 2017, 9(1):52-64. DOI: 10.17725/rensit.2017.09.052.
27. Mishinsky GV. Resonant interference exchange interaction. *RENSIT: Radioelectronics. Nanosystems. Information technologies,* 2019, 11(3):261-278. DOI: 10.17725/rensit.2019.11.261.
28. Kuhn TS. *The Structure of scientific revolutions.* University of Chicago Press, 1962, 172 p.
29. Mishinsky GV. Towards a new paradigm. *RENSIT: Radioelectronics. Nanosystems. Information Technologies*, 2020, 12(4):529-544. DOI: 10.17725/rensit.2020.12.529.

30. Mishinsky GV. New Paradigm and Parametry. *RENSIT: Radioelectronics. Nanosystems. Information Technologies*, 2021, 13(4):509-520. DOI: 10.17725/rensit.2021.13.509.
31. Mishinsky GV. Magnetic fields and high-temperature superconductivity in excited liquids. Unknown particles. *RENSIT: Radioelectronics. Nanosystems. Information Technologies,* 2021, 13(3):303-318. DOI: 10.17725/rensit.2021.13.303.
32. Mishinsky GV. Atom in a strong magnetic field. Transformation of atoms to transatoms. *RENSIT: Radioelectronics. Nanosystems. Information Technologies,* 2017, 9(2):147-160. DOI: 10.17725/ rensit.2017.09.147
33. Mishinsky GV. Magnitnye polya transatomov. Spinovy-nuklidny-elektronny kondensat [Magnetic fields of transatoms. Spin-nuclide-electronic condensate]. *Journal formiruyushchikhsya napravleniy nauki* (*JFNN*), 2017, № 15-16 (5):6-25 (in Russ), http://www.unconv-science.org/.
34. Mishinsky GV. Spin electron condensate. Spin nuclide electron condensate. *RENSIT: Radioelectronics. Nanosystems. Information Technologies,* 2018, 10(3):411-424. DOI: 10.17725/ rensit.2018.10.411.
35. Mishinsky GV. Non-Coulomb nuclear reactions of transatoms. Stellar energy and nucleosynthesis. *RENSIT: Radioelectronics. Nanosystems. Information Technologies,* 2018, 10(1):35-52. DOI: 10.17725/ rensit.2018.10.035.
36. Volkov VV. *Nuclear Reactions of deep inelastic Transfers*. Moscow, Energoizdat Publ., 1982, 182 p.
37. Pavlov AN. Quantum principles of the development of the Earth – a new paradigm of geology. *Prinzipy razvitiya i istorizma v geologii i paleobiologii* [Principles of development and historicism in geology and paleobiology]. Novosibirsk, Nauka Publ., 1990, pp. 115-122 (in Russ.).
38. Mishinsky GV. Multinuclear reactions in condensed helium. *RENSIT: Radioelectronics. Nanosystems. Information Technologies,* 2017, 9(1):94-105. DOI: 10.17725/ rensit.2017.09.094.
39. Wiśniewski R, Mishinsky GV, Gulbekian GG, Wilczyńska-Kitowska T, Semin VA. Sintez khimicheskikh elementov i tverdotelnukh struktur pri obluchenii γ-kvantami kondensirovannykh gazov [Synthesis of chemical elements and solid-state structures under irradiation by γ-quanta in condensed gases]. *JFNN*, 2017, 17-18(5):6-15 (in Russ).
40. Pulletikurti S, Yadav M, Springsteen G. Prebiotic synthesis of α-amino acids and orotate from α-ketoacids potentiates transition to extant metabolic pathways. *Nature Chemistry,* 2022, 14(10):1142-1150. DOI: 10.1038/s41557-022-00999-w.
41. Mandelbrot BB. *The Fractal Geometry of Nature*. Henry Holt and Company, 1983, 468 p.
42. Mandelbrot BB. *Fractals and Chaos: The Mandelbrot Set and Beyond*. Springer Science & Business Media, 2004, 308 p.
43. Vernadsky VI. *Living Matter*. Moscow, Nauka Publ., 1978, 219 p.
44. Turchin VF. *The Phenomenon of Science. Cybernetic approach to human evolution*. New York, Columbia University Press, 1977, 368 p.
45. Vernadsky VI. *Selected Works*. Moscow, Nauka Publ., 1960, vol. 5, 140 p.
46. Mishinsky GV, Kuznetsov VD. Element distribution in the products of low energy transmutation. Nucleosynthesis. *AFLB,* 2008, 33(3-4):331-356.
47. Krivitsky VA, Mishinsky GV, Starostin VI. Planetary nucleosynthesis and ore formation. Bose-Einstein spin condensate of atomic electrons and atomic nuclei. *Smirnovsky sbornik-2019* [Smirnov collection-2019] pp. 246-265. Moscow, "MAKS Press" Publ., 2019 (in Russ.).

48. Mishinsky GV, Krivitsky VA, Starostin VI. Quantum geology. The feasibility of nucleosynthesis not only in stars, but also on planets in the process of their evolution. *Smirnovsky sbornik-2020*, pp. 96-136. Moscow, "MAKS Press" Publ., 2020 (in Russ.).
49. Mishinsky GV, Starostin VI. Quantum geology is a scientific discipline born of a new scientific revolution. Planetary nucleosynthesis and ore formation. *Smirnovsky sbornik-2021*, pp. 155-192. Moscow, "MAKS Press" Publ., 2021 (in Russ.).
50. Grachev AF. Osnovnue problemy sovremennoy tektoniki i geidinamiki Severnoy Evrazii [Main problems of modern tectonics and geodynamics of Northern Eurasia]. *Fizika Zemli,* 1996, 12:3-32.
51. Rampino MR, Caldeira K, Zhu Yu. A pulse of the Earth: A 27.5-Myr underlying cycle in coordinated geological events over the last 260 Myr. *Geoscience Frontiers,* 2021, 12:101245.
52. Barenbaum AA. *Galaktika. Solnechnaya sistema. Zemlya* [Galaxy. Solar System. Earth]. Moscow, GEOS Publ., 2002, 392 p.
53. Vernadsky VI. *Iz istorii idey. Izbrannye trudy po istorii nauki* [From the History of Ideas. Selected works on the history of science]. Moscow, Nauka Publ., 1981, 215 p.